Investigation of Travelling-wave Thermoacoustic Engines with Different Configurations

By
Ali Abbas Hameed Al-Kayiem
BSc & MSc

Submitted in fulfilment of the requirements for the degree of
Doctor of Philosophy (PhD)

System, Power & Energy Research Division
School of Science and Engineering
College of Engineering
University of Glasgow
Glasgow, UK

July 2017

Abstract

Thermoacoustic systems can either generate acoustic work (i.e., p-v work) from thermal energy, or consume acoustic work to transfer heat from low to high temperature sources. They are the so-called thermoacoustic prime movers or heat pumps, essentially acting as the acoustical equivalents of Stirling engines or coolers. If a travelling sound wave propagates through a regenerator with a positive temperature gradient along the direction of sound wave propagation, the gas parcels experience a Stirling-like thermodynamic cycle. As such, thermal energy can be converted to acoustic power. Similar to Stirling engines and thermo-fluidic oscillators, thermoacoustic engines can be externally heated with various heat sources and are capable of utilising low-grade thermal energy such as industrial waste heat and solar thermal energy. Both the simplicity, and even the absence of moving parts of thermoacoustic engines demonstrate that they have the potential for developing low-cost power generators therefore, they have attracted significant research effort for developing coolers or electric generators.

The target design principle of a thermoacoustic engine is to maximise acoustic power production within the thermoacoustic core whilst minimising the acoustic losses in the resonator. One of the main issues with current thermoacoustic systems is low efficiency, which is largely attributed to acoustic losses in the resonator and the regenerator. There would be a significant impact on the thermoacoustic field if a suitable travelling wave resonator were developed with the least losses. Despite the different engine configurations for developing these engines, they all work on the same thermodynamic principle, i.e., the Stirling cycle. In this study, the first issue is resolved by employing a by-pass configuration, and the second is addressed by using a side-branched volume technique.

The current study focuses on the investigation of looped-tube travelling-wave thermoacoustic engines with a by-pass pipe. The novelty of such a by-pass configuration is that the by-pass and feedback pipes actually create a pure travelling

Abstract

wave resonator. The engine unit extracts a small amount of acoustic work from the resonator, amplifies it and sends it back to it. As the pure travelling wave resonator has very low losses, it requires very little acoustic power to sustain an acoustic resonance. This idea is analogous to children playing on swings, where a small push could sustain the swinging for a long time. The present research demonstrates that travelling wave thermoacoustic engines with such a by-pass configuration can achieve comparable performances with other types of travelling wave thermoacoustic engines which have been intensively researched.

According to the results, this type of engine essentially operates on the same thermodynamic principle as other travelling wave thermoacoustic engines, differing only in the design of the acoustic resonator. The looped-tube travelling-wave thermoacoustic engine with a by-pass pipe was then implemented in the design of an engine with a much longer regenerator and higher mean pressure to increase its power density. A thermoacoustic cooler was also coupled to the engine to utilise its acoustic power, allowing evaluation of thermal efficiency. A linear alternator has also been coupled to the tested engine to develop an electric generator.

This research additionally addresses the effect of a side-branched Helmholtz resonator to tune the phase in looped-tube travelling wave thermoacoustic engine. This action is performed in order to obtain the correct time-phasing between the acoustic velocity and pressure oscillations within the regenerator, to force gas parcels to execute a Stirling-like thermodynamic cycle, so that thermal energy can be converted to mechanical work (i.e., high-intensity pressure waves). By changing its volume one can change the acoustic impedance at the opening of the Helmholtz resonator, and thus adjust the acoustic field within the loop-tubed engine. It can essentially shunt away part of the volumetric velocity at the low impedance region of the engine, so that the acoustic loss can be reduced within the engine. Both the simulations and the experimental results have demonstrated that the proposed side-branched volume can effectively adjust the acoustic field within the looped-tube engine and affect its performance. There is

Abstract

an optimal acoustic compliance corresponding to the best performance in terms of acoustic power output and energy efficiency when the heating power input is fixed.

Table of Contents

Table of contents

List of Tables

List of Figures

List of Figures

List of Figures

List of Figures

List of Figures

List of Symbols

Symbol	Description and Unit
A	Cross-sectional area (m^2)
A_g	Cross-sectional occupied by working gas (m^2)
a	Speed of sound (m/sec)
BL	Force factor (--)
C_p	Isobaric specific heat ($J\ kg^{-1}K^{-1}$)
C_v	Isochoric specific heat ($J\ kg^{-1}K^{-1}$)
C_s	Acoustic compliance (m^3/Pa)
d	Diameter (m)
D_r	Drive ratio (--)
$\dot{E}$	Net production acoustic power (W)
f	Frequency (Hz)
f_m	Mean Frequency (Hz)
f_v	Spatially averaged viscous functions of h_v (--)
f_k	Spatially averaged thermal function of h_k (--)
g	The complex gain constant for the volume flow rate (--)
h_v	Function dependant on geometry and δ_v (thermoviscous function) (--)
h_k	Function dependant on geometry and δ_k (thermoviscous function) (--)
$\dot{H}$	Total powers flux (W)
h	Enthalpy ($J\ kg^{-1}$)
Im [•]	Imaginary part of • (--)
J	Bessel function
k_m	Stiffness ($mm\ N^{-1}$)
k	Thermal conductivity ($W\ K^{-1}m^{-1}$)
L	Length (m)
L_e	Electric Inductance (Henry)
m	Mesh number of the screen (--)
$\dot{m}$	Flow rate (kg/sec)

List of Symbols

M_m	Moving mass (g)
p	Charging pressure (Pa)
p_m	Mean pressure (Pa)
p_{atm}	Atmospheric pressure (Pa)
Q	Heat energy (W)
Q_H	Heat source at high temperature (W)
Q_C	Heat sink at low temperature or cooling load of cooler (W)
$\dot{Q}$	Heat flow per unit time (W)
q	Heat flux (W m^{-2})
R	Acoustic resistance (Pa s m^{-3})
Re	Electric resistance (Ω)
Re [•]	Real part of • (--)
Re	Reynold number (--)
R_m	Mechanical resistance (kg s^{-1})
Rl	Load resistor (Ω)
r	Radius (m)
r_h	Hydraulic radius (m)
S	Entropy (J K^{-1})
s	Specific entropy (J $kg^{-1}K^{-1}$)
s_m	Mean entropy (J K^{-1})
S	Effective area of alternator (m^2)
T	Temperature (K, °C)
T_m	Mean Temperature (K, °C)
T_H	High temperature (hot) (K, °C)
T_C	Low temperature (cold) (K, °C)
T_h	Solid Temperature of HHX (K, °C)
T_a	Solid Temperature of AHX (K, °C)
T_c	Solid Temperature of CHX (K, °C)
t	Time (sec)
u	Acoustic velocity oscillation (m s^{-1})
U	Volumetric velocity (m^3 s^{-1})

List of Symbols

V	Volume of Helmholtz resonator (m^3)
V	Volume of compliance (m^3)
V	Voltage (Volt)
W	Work (W)
$\dot{W}$	Acoustic power (W)
W_{in}	Electricity produced by ALT (W)
$W_{a,\,in}$	Acoustic power inlet (W)
$W_{a,\,out}$	Acoustic power outlet (W)
$W_{a,\,net}$	Net acoustic power (W)
$W_{a,c}$	Acoustic power consumed in cooler (W)
X	Aperture width (m)
X_{max}	Maximum excursion (mm)
y_0	Half of the plate spacing (m)
Z	Impedance (Pa s/ m^3)
Z_c	Compliance impedance (Pa s/ m^3)
ξ	Gas parcel displacement (m)
Θ_{BC}	Phase angle difference between two pressure signals (rad, °)
β	Thermal expansion coefficient (K^{-1})
β_m	Mean thermal expansion coefficient (K^{-1})
δ	Penetration depth (m)
δ_k	Thermal penetration depth (m)
δ_v	Viscous penetration depth (m)
λ	Wave length (m)
Π	Perimeter (m)
$\mathcal{E}, E$	Internal energy (J)
μ	Dynamic (shear) viscosity (Pa s)
μ_m	Mean Dynamic (shear) viscosity (Pa s)
ρ	Density (kg m^{-3})
ρ_m	Mean density (kg m^{-3})
ω	Angular frequency of the acoustic oscillations (rad s^{-1})

List of Symbols

θ	Phase angle (rad or °)
$\emptyset$	Porosity (--)
γ	Ratio of specific heat capacity (--)
ε_s	Correction factor for finite solid heat capacity (--)
∇	Gradient operator (--)
γ_m	Mean Ratio of specific heat capacity (--)
γ_{pf}	Effective thickness (--)
σ	Prandtl number (--)
σ'	Fluid stress tensor (Pa)
∂	Partial derivative (--)
$\langle \bullet \rangle$	Spatial average of • (--)
$[\bar{\ }]$	Average value (--)
[~]	Complex conjugate (--)
| |	Magnitude of complex number
η	Efficiency (%)
η_e	Engine efficiency (%)
η_i	Efficiency for each Engine (%)
η_R	Relative efficiency (%)
η_C	Carnot efficiency (%)
η_m	Average engine efficiency (%)
η_{h-a}	Thermal to acoustic efficiency (engine efficiency) (%)
η_{h-e}	Thermal to electricity efficiency (generator efficiency) (%)
η_{a-e}	Acoustic to electricity efficiency (alternator efficiency (%)

Acknowledgement

First and foremost, all the praises be to Allah (God), the Most Merciful and Beneficent. I wish to express my huge gratitude to my supervisor, Dr Zhibin Yu, for giving me constant and invaluable support throughout the long years with his academic expertise, patience, encouragement and understanding. His support has contributed to my academic development, in particular my confidence in undertaking independent and rigorous research. With his skilled supervision and inspirational advice, my PhD research has become an enjoyable experience. In addition, his wisdom made it easier for me to accomplish my work, despite the hard circumstances I faced throughout my study. Without his supervision during the period, this research would not have been possible.

My special gratitude goes to the Iraqi government, especially the Ministry of Higher Education and Scientific Research for nominating me to study aboard and supporting me and my family with a fully-funded scholarship.

Special thanks to my wife for her patience and providing me comfort, and my lovely children Aya, Mohammed, Rukya and Hussain, for their affectionate support and love during this period of study.

I would like to thank my best friend from Iraq Prof. Hussein A. Lafta from the bottom of my heart for his continuing support, without his contribution I would not have been able to continue this study.

Moreover, I wish to express my warm thanks and appreciation to the most helpful people in Iraq during my studies, to the spirit of my beloved father who passed away, my loving mother and every person who had a direct and indirect contact with me during my studies and who had a positive influence on my progress and outcomes.

I wish to thank all tecnicians at the Univesity of Glasgow for their help and support. They were very friendly in their treatment when any problem arose. Special thanks to

Acknowledgement

Mr. Stephen Monaghan for his assistance with the experimental works, he was really helpful and very friendly in manufacturing all the parts which were used in my rig. Also, I wish to express my thanks to Mr. Denis Kearns, Mr.Brian Robb, for their assistance. I am also grateful to Mr. Bernard Hoer and Neil Owen in the electronics workshop for their assistance. Also, I wish to express my thanks to the members of IT support team, especially Mr Chris Nicol, Mr Walter Robinson and Mr Ken McColl for their help in fixing any problems with my computer.

I give special thanks to my colleagues, friends and the department staff for their generous help and assistance; Andrew Mckeown, Peter Collings, Jim Blunn, Douglas Iron, Ian Scouller, and every person who had a contact with me during my studies and who had a positive influence on my progress.

Finally, I wish to deliver my sincere thanks to the University of Glasgow for giving me the opportunity to develop my research skills in a great working environment

Author's Declaration

This thesis is entirely my own work, except where mentioned and acknowledged. This work has not been previously submitted for other degree or qualification in any university.

Ali Al-Kayiem
July 2017

Definitions/Abbreviations

ALT	Alternator
AHX	Ambient heat exchanger
AHX_C	Ambient heat exchanger for cooler
CHX	Cold heat exchanger
CHX_C	Cold heat exchanger for cooler
COP	Coefficient of performance
COPC	Carnot coefficient of performance
COPR	Percentage of Carnot COP
COP_m	Average coefficient of performance
DeltaEC	Design Environment for Low-Amplitude ThermoAcoustic Energy Conversion
FBP	Feedback pipe
HHX	Hot heat exchanger
HR	Helmholtz resonator
LANL	Los Alamos National Laboratory
REG	Regenerator
REG_C	Regenerator for cooler
RPA	Relative pressure amplitude
RPN	Reverse Polish Notation
RC	RC-acoustic load
SAHX	Secondary ambient heat exchanger
SWR	Standing wave ratio
SWE	Standing wave engine
SX	Screen-type heat exchangers
TX	Shell-and-Tube-type heat exchangers
TADTAR	Thermoacoustically Driven Thermoacoustic Refrigerator
TWE	Travelling wave engine
TBT	Thermal buffer tube
TA	Thermoacoustic

Definitions/Abbreviations

Θ_{REGC}	Phase angle at the cold end of the regenerator
Θ_{REGH}	Phase angle at the hot end of the regenerator
Z_{REGC}	Normalised impedance at the cold end of the regenerator
Z_{REGH}	Normalised impedance at the hot end of the regenerator

Chapter 1 Introduction

1.1 Overview of thermoacoustics

Thermoacoustic technology deals with the interactions between acoustic fields and heat transfer, and ultimately, the resultant thermoacoustic energy conversion effects. Thermoacousic engines convert thermal energy to acoustic energy, and normally consist of a porous material (regenerator or stack) sandwiched between two heat exchangers (hot and ambient heat exchanger). The regenerator is made from a porous material such as steel wool, metal gauze or metal foam, in which heat can be stored for a period of time.

It should be noted that the regenerator is generally referred to as a "stack" in standing-wave thermoacoustic devices (where the phase difference between pressure and velocity is close to 90°), and as a "regenerator" in travelling-wave devices (where the phase difference between pressure and velocity is close to 0°) [1]. Two heat exchangers impose a temperature gradient along the porous material, which is required to amplify the acoustic wave that is spontaneously generated. A thermoacoustic heat engine or heat pump can operate at power levels ranging from a few hundred Watts up to one megawatt [2].

Thermoacoustic systems can either generate acoustic work (i.e., p-v work) from thermal energy, or consume acoustic work to transfer heat from low to high temperature. Thus, there are two types of thermoacoustic device: the prime mover (heat engine) and the heat pump (refrigerator/cooler). Heat engines deal with heat power and convert it into acoustic power, while a heat pump consumes acoustic power to pump heat from a low to high temperature level. It should be noted that there is a difference between a heat pump and a refrigerator; a heat pump keeps the temperature of a given space above that of its surroundings, but a refrigerator keeps the temperature of given space below that of the surroundings Tijani [3].

In a travelling wave thermoacoustic engine, when a modulated sound wave propagates through a regenerator from the cold to the hot end, the gas parcels undergo a Stirling-like thermodynamic cycle at a microscopic level. This is due to the complicated interactions between their displacement and heat transfer with the solid porous material of the regenerator. Based on this principle, a travelling wave thermoacoustic engine can be built by employing a delicately designed acoustic network to tune the pressure oscillation to be virtually in phase with the velocity oscillation within the regenerator, so that thermal energy can be converted to mechanical work (i.e., high-intensity pressure waves) at macroscopic level.

In general, thermoacoustic technology has many advantages. The lack of moving parts means that little maintenance is required. In addition, it is environmentally friendly since it uses noble gases as the working gas, and can utilise low-temperature heat sources. These advantages have attracted many researchers and companies across the world to research in this field. The overwhelming benefit of these systems is that they can utilise low-temperature energy sources, such as industrial waste heat, to generate acoustic power that in turn can be converted into useful power. Furthermore, they can be used to generate power from solar energy, which has particular promise in countries which have abundant solar energy, such as the Middle East.

1.2 Thermoacoustic engine

A thermoacoustic engine converts some heat from a high-temperature heat source into acoustic power, rejecting waste heat to a low-temperature heat sink [4]. Figure 1.1 demonstrates the basic principles of the process.

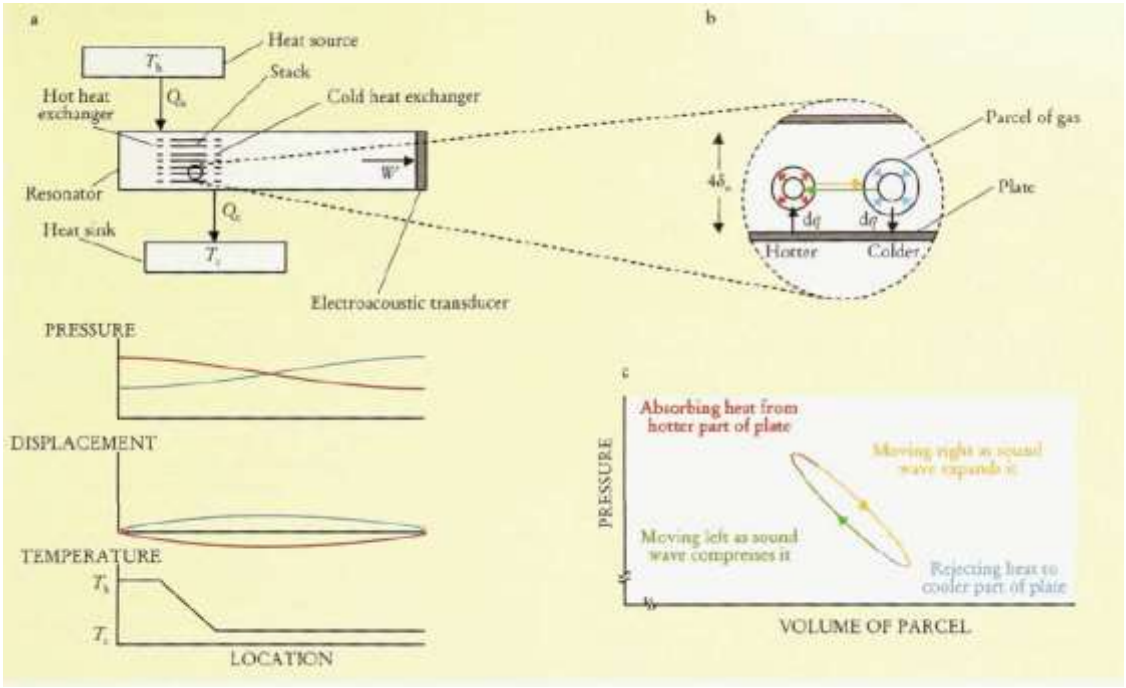

Figure 1.1: Demonstrates the basic principles of the thermoacoustic engine process [4].

a: Heat exchangers and a stack in a half-wavelength acoustic resonator (Plots below show gas pressure and gas displacement in the horizontal direction and average temperature as functions of location in the resonator), b: Magnified view of part of the stack shows a typical parcel of gas, c : Pressure-volume (p-V) diagram for the parcel of gas.

It can be seen that the gas parcels absorb heat (Q_h) from a heat source at high temperature T_h, reject heat (Q_c) to a heat sink at low temperature T_c and then generates acoustic power W [4]. The thermoacoustic effect can be defined as the energy transfer between a compressible fluid and a solid material in the presence of any acoustic wave. The effect of thermoacoustics is demonstrated by imposing a temperature gradient within the solid material, by supplying heat energy which in turn results in spontaneous generation of an acoustic wave along the direction of the temperature gradient in its vicinity [5]. Over 100 years ago, Rayleigh [6] understood that heating and cooling could create acoustic power. He set out the criterion for the production of any type of thermoacoustic oscillation as follows:

"If heat be given to the air at the moment of greatest condensation, or be taken from it at the moment of greatest rarefaction, the vibration is encouraged".

The Rayleigh's criterion has been generally accepted as an explanation of sustaining the thermoacoustic oscillations [7].

If the temperature gradient in the stack exceeds the onset temperature (which is the difference between the temperature of hot and cold side of the stack) an acoustic wave in the stack is spontaneously generated.

1.3 Thermoacoustic refrigerator

A thermoacoustic refrigerator device uses acoustic power to absorb heat from a low-temperature medium and reject it to a high-temperature medium. The main objective of the refrigerator is to maintain the temperature of the low-temperature medium by constantly removing heat that leaks into the cold space from the surroundings at a higher temperature [5].

The basic principle of operation is very similar to that of thermoacoustic engines (see Figure 1.2), but the temperature gradient in the stack is much lower. The reason behind that is that the working fluid experiences changes in temperature when it oscillates along the stack. This change comes from adiabatic compression and expansion of the gas by the acoustic pressure, resulting in heat transfer with the stack [4]

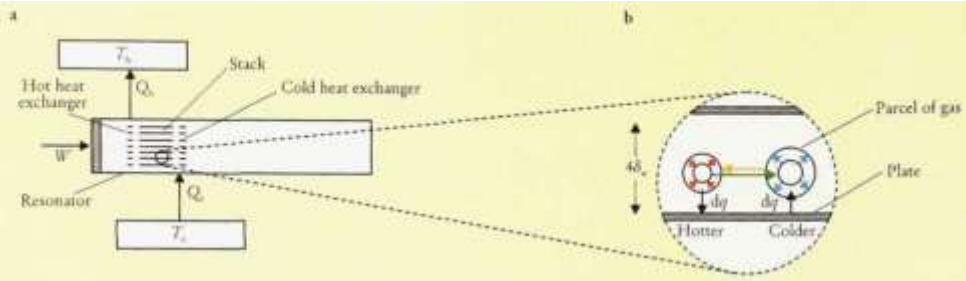

Figure 1.2: Demonstrate the basic principle of process of the thermoacoustic refrigerator [4].

a: Electroacoustic transducer at the left end delivers acoustic power to theresonator, b: Magnified view of part of the stack shows a typical parcel of gas as it moves heat up the temperature gradient.

1.4 Travelling-wave and standing-wave thermoacoustic systems

Standing wave is a vibration of a system in which some particular points remain fixed while others between them vibrate with the maximum amplitude. Travelling wave is a

wave in which the positions of maximum and minimum amplitude travel through the medium [8].

The thermoacoustic devices can be categorised into standing wave and travelling wave devices. This categorisation is based on whether acoustic pressure and acoustic velocity are in phase or 90° out of phase. In the standing wave devices, the gas parcel movement is comparable to the Brayton cycle, consisting of two reversible adiabatic and two constant pressure processes, while the cycle in the travelling wave devices is similar to the Stirling cycle, comprising two constant temperature processes and two reversible constant volume processes [7].

1.4.1 Standing-Wave-Engine (SWE)

The configuration of the Standing-Wave-Engine is often simple, but their efficiency is low. In standing-wave feedback configurations pressure and velocity oscillation are out of phase by 90°, as shown in Figure 1.3. However, in a real standing-wave thermoacoustic device, the phase difference drops slightly below 90° to permit power flow to the acoustic load. It is worth mentioning here that there is a thermal contact imperfection between the working gas and the stack. This has the effect of creating the desired phase difference, by delaying the heating and cooling processes so that heating follows compression and cooling follows expansion. The spacing in the stack of a standing-wave device should be greater than that for the regenerator in a travelling-wave device, in the order of δ_k, which provides imperfect heat transfer between the gas parcels and the solid surface of the stack, thus causing the necessary phase shift between the pressure and velocity waves [9].

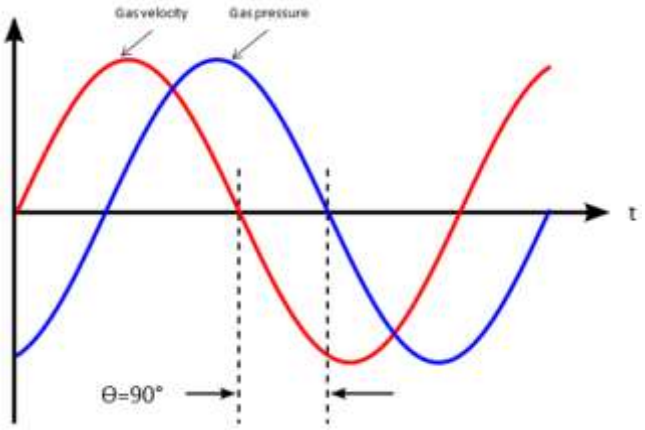

Figure 1.3: Standing-wave feedback configurations pressure and velocity amplitude are out of phase by 90°.

1.4.2 Travelling-Wave-Engine (TWE)

The configuration of Travelling-Wave-Engines is complex, and their efficiency is higher than Standing-Wave-Engines efficiency, because they operate in a nearly reversible manner in terms of heat transfer within the engine core. This is because, in an ideal thermodynamically reversible process, the work done by the system would be maximised, and the heat consumed by the system would be minimised, leading to a maximum efficiency. In travelling-wave feedback configurations pressure and velocity oscillations are nearly in phase within the regenerator, as shown in Figure 1.4. The maximum efficiency (thermal to acoustic efficiency) reached by a standing-wave thermoacoustic engine was 18%, while a travelling-wave thermoacoustic engine reached a maximum efficiency of 30%, corresponding to 41% of the Carnot efficiency of the system developed by the researchers [10, 11].

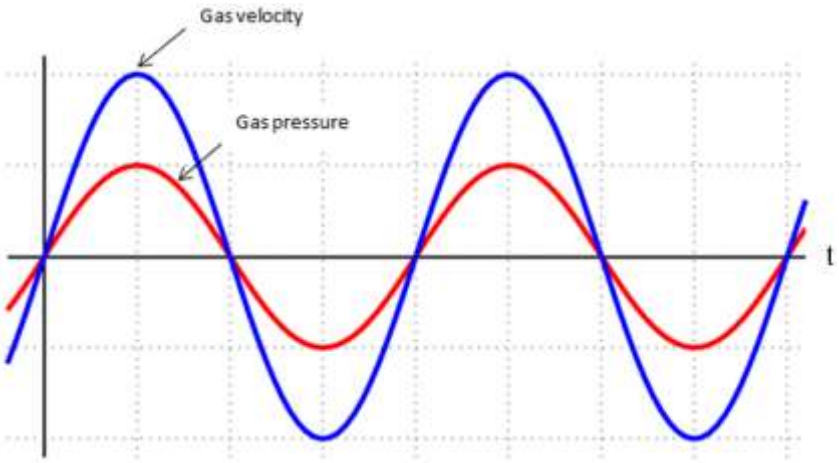

Figure 1.4: Travelling-wave feedback configurations pressure and velocity amplitude are nearly in phase.

Generally, in the standing wave engine, the heat transfer is delayed due to the pressure and velocity not being in phase. The thermal transfer processes in the standing wave engine are lagging behind the acoustic velocity by 90°. This thermal delay is not required in the travelling wave engine. Moreover, the pore size of the regenerator in the travelling wave devices is much smaller than the thermal penetration depth (the thermal penetration depth is the thickness of the layer of gas within a stack plate through which the heat diffuses, and it gives an idea about heat diffusion, according to the distance between the working gas and solid surface of the stack or regenerator), Thus the small pore size of the regenerator definitely leads to small thermal penetration depth, which gives a almost uniform temperature between the gas bulk temperature and the gas located at the regenerator surface [7].

In general, the travelling wave thermoacoustic engine usually consists of a pair of cold and hot heat exchangers, a regenerator, and the acoustic resonator. The regenerator of the travelling wave thermoacoustic engine is a section of porous material which is similar to that of the conventional Stirling engine. Perfect thermal contact between the gas and solid material is maintained, and therefore the gas has the same temperature as the local solid material within the regenerator. The hot heat exchanger extracts heat from heat sources and transfers it to the working gas within the thermoacoustic engine, while the ambient heat exchanger removes the heat from the working gas and rejects it

to the external heat sink. This pair of heat exchangers builds up and maintain a steep temperature gradient along the axle of the regenerator where the thermodynamic cycle takes place and converts the thermal energy to acoustic power [12]. Thermoacoustic systems require an acoustic resonator to keep an acoustic wave; the resonator determines the operating frequency of the system and confines the pressurized working gas [13].

1.5 Motivation for the present research

The motivation behind the current study is to improve the thermoacoustic system performance in terms of maximising acoustic power production within the engine core and minimising acoustic losses in the FBP. These goals are achieved in two ways by the current work. First, a by-pass configuration that shunts a part of the volumetric velocity away from the engine core leads to decreased velocity, an increase in the pressure and acoustic impedance, which ultimately increases the system's efficiency. Second, the design forces the phase angle between pressure and velocity oscillation to an ideal phase using a side-branched volume. This technique helps to create a pure travelling-wave, leading to a high acoustic power production.

DeltaEC software [14] has been employed to simulate and analyse this by-pass configuration. Thereafter, a linear alternator or cooler is coupled to the by-pass configuration to further check the working principle.

As for the side-branched volume configuration, it is investigated numerically and experimentally. It is also simulated numerically using DeltaEC software. Based on the obtained model, an experimental rig is designed, constructed and then tested.

1.6 Aims and objectives of this research

The objective of this research is twofold: 1) to analyse different configurations of thermoacoustic engine; and 2) to design, construct and test a prototype of looped-tube travelling-wave thermoacoustic engine with a side-branched Helmholtz resonator

for phase tuning. The simulation part is carried out using DeltaEC software and the experiment part employed an experimental rig, which was designed and built during this PhD project. Finally, the results from the two parts will be compared to each other to validate the numerical model.

One of the main challenges to any thermoacoustic system is low efficiency, which is mainly due to acoustic losses in the resonator. It is important to develop a resonator with very low acoustic losses. Based on this, a comprehensive simulation effort will be conducted in this research, with the aim to decrease acoustic losses at the resonator. The phase angle difference between the acoustic velocity and the pressure oscillations within the regenerator has significant impact on the acoustic losses. From the thermoacoustic point of view, reducing the phase angle towards zero leads to low reflection (SWR=1) and very low acoustic losses. This mainly happens in the travelling-wave thermoacoustic engine. This issue has been addressed in the second part of this research.

Based on the above challenges, the main goals of this work are:

- To simulate a looped-tube travelling-wave thermoacoustic engine with a by-pass configuration
- To analyse the looped-tube travelling-wave thermoacoustic engine with a by-pass configuration, and reveal its advantages and disadvantages
- To find out whether this new configuration operates on the same thermodynamic principle
- To understand how the by-pass configuration decreases the acoustic losses, leading to improving the thermoacoustic system performance
- To analyse the application of this configuration for a cooler
- To analyse the application of this configuration for a electric generator
- To investigate a two-stage travelling wave thermoacoustic engine with a by-pass configuration to find out how the new resonator affects the thermoacoustic system performance

- To investigate a two-stage travelling wave thermoacoustic engine with a by-pass configuration without acoustic load
- To investigate a two-stage travelling wave thermoacoustic engine with a by-pass configuration with acoustic loads
- To tune the phase between the pressure amplitude and the volumetric velocity of the sound wave towards zero by using a side-branched Helmholtz resonator
- To investigate the affect of a side-branched Helmholtz resonator to tune the phase in looped-tube travelling wave thermoacoustic engine with RC-load
- To design, construct and test a prototype thermoacoustic engine of the side-branched Helmholtz resonator in looped-tube travelling wave thermoacoustic engine

1.7 Outline of the thesis

Following the introduction as shown in this section, Chapter 2 reviews the previous experimental and numerical studies to gain a comprehensive understanding of the physics of thermoacoustic process, providing the context and technical background for this PhD research project. Chapter 3 then describes the theory of thermoacoustic, and the equations which govern this thermoacoustic process.

Chapter 4 presents a comprehensive numerical analyse of a by-pass type (a looped-tube with a by-pass pipe) travelling wave thermoacoustic engine, which was recently proposed for low temperature applications. The research results show that an engine with such a by-pass configuration essentially operates on the same thermodynamic principle as other travelling wave thermoacoustic engines, differing only in the design of the acoustic resonator. The model was then applied to design an engine with a much longer regenerator and higher mean pressure to increase its power density.

Chapter 5 demonstrates the application of a looped-tube travelling-wave thermoacoustic engine with a by-pass configuration to the cooler. In this chapter, a thermoacoustic

cooler is coupled to the engine to utilise its acoustic power, allowing for evaluation of thermal efficiency. It also investigates how to improve the power density and thermal efficiency of this by-pass type engine without violating its working principle.

Chapter 6 shows the application of a looped-tube travelling-wave thermoacoustic engine with a by-pass configuration to electric generator. A linear alternator has been coupled to the engine to develop an electric generator. This research demonstrates that a travelling wave thermoacoustic engine with such a new by-pass configuration can achieve comparable performances as other types of travelling wave thermoacoustic engines.

Chapter 7 presents the numerical investigation of a two-stage travelling-wave thermoacoustic engine with a by-pass configuration. This study consists of two numerical sections: 1) a numerical investigation of such a system without acoustic load; and 2) a numerical investigation of a two-stage thermally driven travelling-wave thermoacoustic heat pump. It introduces a new configuration to reduce the acoustic losses without violating the working principle. By-pass configuration travelling-wave thermoacoustic engines essentially employ a near pure-travelling wave acoustic resonator to provide acoustic resonance to the engine unit.

Chapter 8 summarises the design, construction, and test of the experimental rig used in this thesis. In addition, all the instrumentation and equipment are described in detail. Furthermore, this chapter investigates how to use a side-branched Helmholtz resonator to tune phase in looped-tube travelling wave thermoacoustic engine. This chapter reports a new phase tuning method, i.e., using a side-branched volume to tune the time-phasing within a looped-tube travelling wave thermoacoustic engine. This concept has been investigated both numerically and experimentally.

Chapter 9 summarises the research of this thesis, and points out future work to be done.

Chapter 2 Literature review

2.1 Introduction

The thermoacoustic effect was probably first observed by glass blowers, who noticed the generation of a loud sound when connecting a long and narrow pipe to a molten glass blob. This phenomenon was noticed and studied more than 200 years ago; however, the research on thermoacoustic phenomena has progressed over the recent decades. There have been many developments in this field, including theoretical models, numerical simulations, experimental apparatus etc. However, the most important studies relevant to the present work are reviewed and summariesed in this chapter.

2.2 Review of developments in thermoacoustics

2.2.1 A historical perspective and developments in thermoacoustics engine

In 1777, Dr Bryan Higgins produced an acoustic standing wave by placing a hydrogen flame inside an open vertical glass tube, which was the so-called singing flame [15].

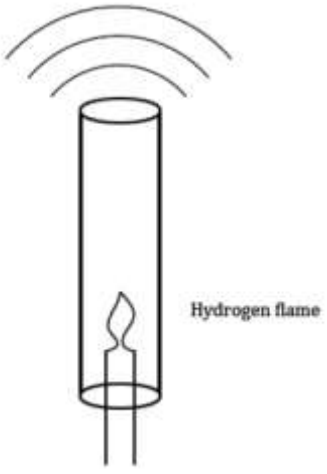

Figure 2.1: Higgins' singing flame [15].

In 1850, Soundhauss [16] conducted an experiment, which was different from previous research. He kept the tube open at one end, closed (with a glass bulb) at the other, and rotated it horizontally. When the gas flame is placed in the bulb, the temperature at the closed end of the tube rises and emits a sound from the open end of the tube.

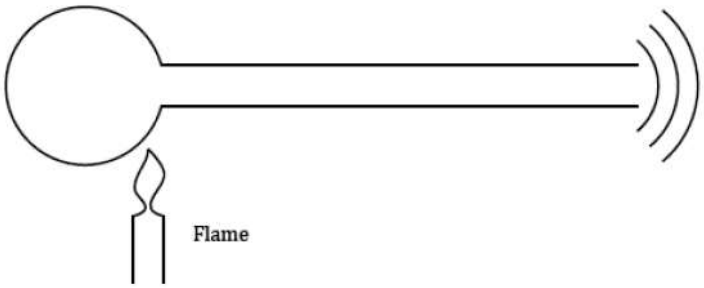

Figure 2.2: Sondhaus's tube [16].

In 1859, Rijke [17] reported a similar observation, but he replaced the hydrogen flame with a hot iron mesh disc, Rijke noted that the maximum density of sound may be located where the distance of the disc from the lower end of the glass is one-fourth of its length. In addition, he pointed out that closing the tube would stop the sound, meaning the air contained within the tube influenced the acoustic phenomenon acting as a working fluid as will explained in next chapter.

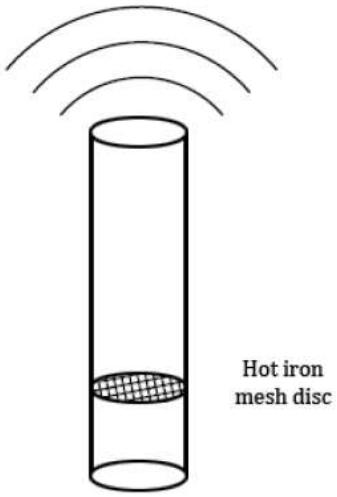

Figure 2.3: Rijke's tube [17]

In 1896, Rayleigh [6], a British physicist, qualitatively understood that these heat-driven tones (thermoacoustic pressure oscillations) would occur if heat flowed into the gas while its density is high, and out of the gas while its density is low. However, through the mid-20th century these coupled pressure and temperature oscillations in a Soundhauss tube were considered to be nothing more than a science demonstration that could make a loud noise [18].

In 1949, Kramers [19] made the first attempt to study thermoacoustic phenomena, his work being based on boundary-layer approximation. While he did not obtain acceptable results when he compared the numerical results with experimental data, he encouraged others to study the thermoacoustic phenomenon in depth. This study was followed by Taconis's research who suggested that the spontaneous vibrations may occur in gas columns if the temperature of the tube containing the column varies along its length especially in low-temperature experiments. Kramers investigated in detail the sign of the damping of the small oscillations which the gas may perform. To study Taconis's idea (occurrence of spontaneous vibrations in gas columns) more a rigorously, the vibrations of a gas in a cylindrical tube were investigated taking into account; on one hand the existence of a temperature gradient along the tube and on the other hand the influence both of the heat conductivity and of the internal friction of the gas. After a long numerical analysis, the final result of the study of the very small vibrations which a gas column can perform in a tube along which there exists a temperature gradient, cannot satisfactorily account for the spontaneous vibrations so often observed. The reason for this is that only extremely small vibration amplitudes were considered. It should be mentioned that Rott and Swift did not take the boundary layer effect into account in their research, as it will be explained in the next section.

In 1951 and 1958, Bell Telephone Laboratories proposed that they would use the thermoacoustic phenomenon to produce electricity. The proposed concept would convert heat into a pressure wave (acoustic power) with a thermoacoustic engine, and then the acoustic power would be converted into electricity. These concepts were very encouraging in their attempts to convert heat energy into electricity, but they were not

considered applicable because the conversion of heat into acoustic power was not very efficient [20, 21].

In 1962, the Sondhauss tube was greatly improved by Carter et al. [22] who placed a stack of parallel plates inside the tube which made the heat transfer with the working gas more efficiently. Thereafter, in order to create a large temperature gradient across the stack, hot and cold heat exchangers are placed on both sides of the stack to exchange heat with external reservoirs. Thereby, part of the supplied heat from the hot to the cold side will be converted to work in the form of an acoustic standing wave. This work can be conducted with a piston to drive a flywheel, or it can be used to run a thermoacoustic heat pump or refrigerator.

The first successful attempt to establish a thermoacoustic theory was done by Rott [23-28] between 1969 and 1980. He introduced a linear theory which is based on linearisation of continuity, momentum and energy equations, and wrote an impressive series of articles in which a linear theory of thermoacoustics was derived. Rott abandoned the boundary-layer approximation as used by Kramers [19], and formulated the mathematical framework for small-amplitude damped and excited oscillations in wide and narrow tubes with an axial temperature gradient, only assuming that the tube radius was much smaller than the length of the tube. In 1980, Rott summarised his results in a review work, which became the cornerstone for the subsequent intensified interest in thermoacoustics.

Merkli and Thomann in 1975 [29] discovereda thermoacoustic cooling effect in the resonator tube at a velocity antinode. This discovery stimulated intense research at the Los Alamos National Laboratory (LANL) during the 1980s. The results showed cooling in the section of the tube with maximum velocity amplitude (dissipation) and heating in the region of the velocity nodes. A strong dependence of these effects on the Prandtl number was noted. This study gave an idea on what happens when nonlinear effects dominate and laminar flow was assumed. The important result from this research was that cooling exists in the region of greatest dissipation due to friction.

In 1979 and 1985, Ceperley [30, 31] improved the efficiency of thermoacoustic devices by using a toroidal geometry which permits the propagation of a travelling wave inside the device instead of a standing wave. The propagation of acoustical waves through a heated regenerator results in gas in the regenerator experiencing a Stirling thermodynamic cycle. This results in; amplification of the waves and conversion of thermal energy into acoustical energy with the acoustical energy being used to pump heat. The basic energy conversion process involves an acoustical traveling wave propagating through a differentially heated regenerator, as shown in Figure 2.4. This device is similar to a singing pipe except in its use of traveling waves instead of standing waves. Acoustical traveling waves propagating through the differentially heated regenerator from cold to hot are amplified. This device is reversible and promises higher efficiency than the singing pipe.

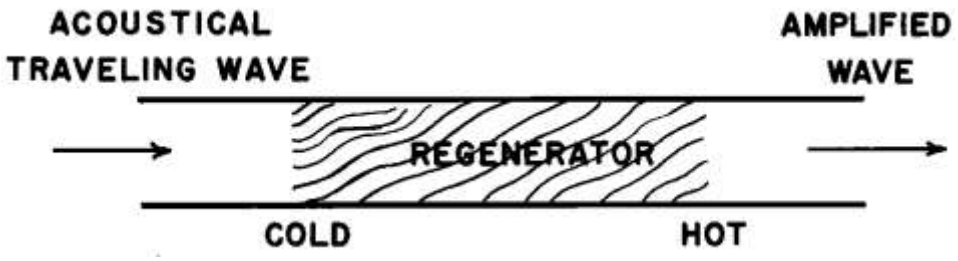

Figure 2.4 Traveling wave heat engine [30].

One reason for this improvement in efficiency is that a standing wave is the result of positive interference between two travelling waves, so that the pressure and velocity local amplitudes can be nearly twice the amplitudes of the initial travelling wave generated in the engine, resulting in high acoustic losses [32], as shown in Figure 2.5. It can be seen that inertance and compliance are required to maintain the travelling wave phasing in a single-stage engine. The thermal buffer tube helps thermally isolate the hot heat exchanger from ambient-temperature components below, thus limiting heat losses [33].

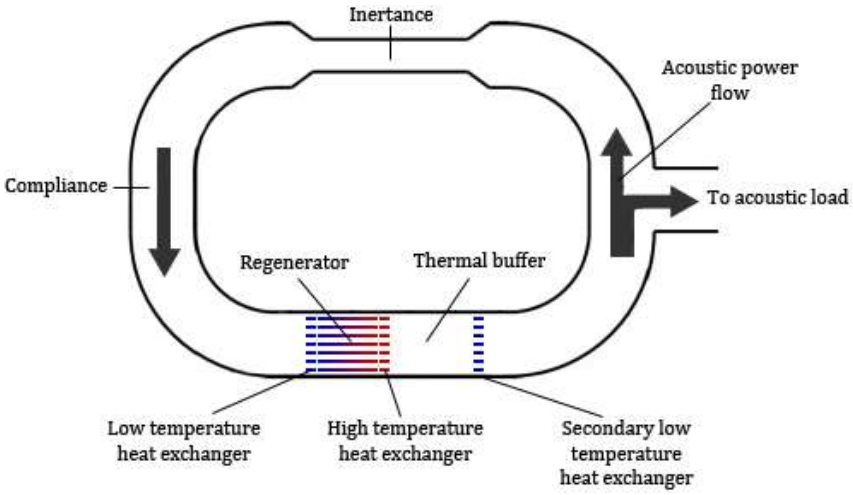

Figure 2.5: Travelling wave thermoacoustic engine [33].

In 1988, Swift [34] published a review article, showing how Rott's thermoacoustic theory can be implemented to create practical thermoacoustic engines and refrigerators. Historical details, theoretical calculations and discussions on how to build these devices as well as experimental results were presented. The governing equations were derived starting from the single plate to the stack. He also described the components of the thermoacoustic engine, such as heat exchangers and resonators.

In 1995, Olson and Swift [35] presented the measurements and analysis of the performance of a thermoacoustic engine driving a dissipative load, and investigated the effect of a thermoacoustic load on a thermoacoustic engine. They reported that the effect of the acoustic load can be explained using a simple low amplitude approximation. The heater power and the hot temperature were measured as a function of the complex impedance of the acoustic load. They pointed out that the acoustic load increases the engine's hot temperature and the ratio of input heater power to the square of the pressure amplitude. As for the numerical calculations, DeltaEC software was employed. The experimental rig is shown in Figure 2.6 below, the working fluid was helium at 3.1 MPa mean pressure.

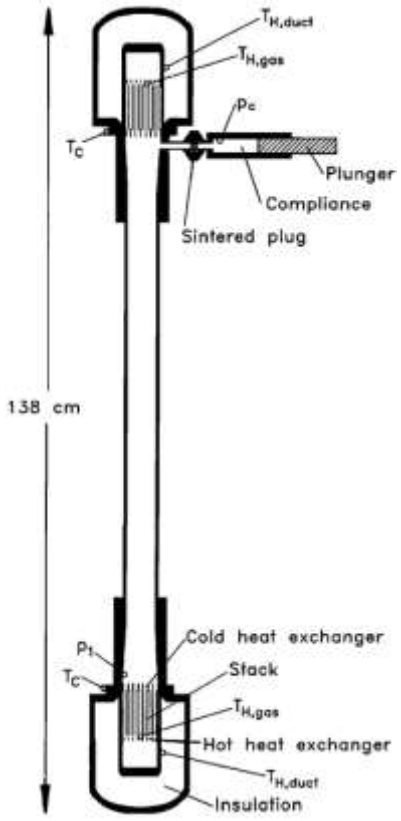

Figure 2.6: Longitudinal cross section of the apparatus. All dimensions are to scale, except for the pore sizes in the heat exchangers and stacks which have been exaggerated by a factor of 5 for clarity. Sensor locations are indicated by small circles [35].

Heat exchangers were cooled by water at their ends, with a cooling water temperature of 17°C. The temperatures were assured using thermocouples with an accuracy of ±2°C, and the pressures amplitude and its phase were measured by using a piezoresistive pressure sensor and lock-in amplifier to an accuracy of 2%. This experimental study showed that the dummy acoustic load consumed 5% of the supplied heat. The experimental and simulation results were shown in Figure 2.7. It should be mentioned here that this analysis is not sufficient to describe the engine because it assumed that the thermal penetration depth, pressure amplitude, and gas velocity are uniform throughout the entire length of the stack, which is not the case.

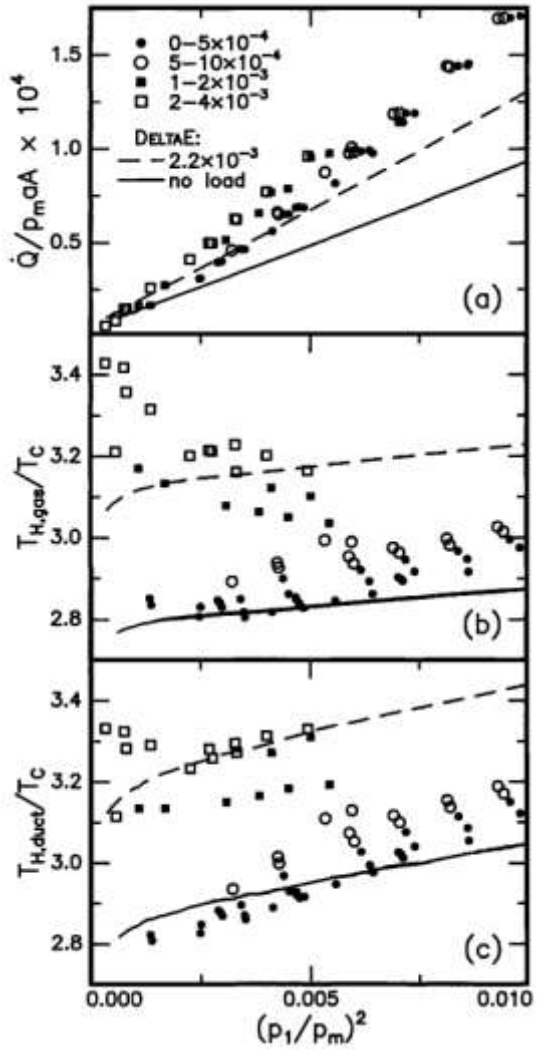

Figure 2.7: Normalized measurements of heater power and hot temperatures carded out over a range of load values [35].

In 1998, Yzaki et al. [36] demonstrated a practical travelling-wave thermoacoustic engine for the first time. They had relatively low efficiency because of a low acoustic impedance within the thermoacoustic core, the latter being caused by large viscous losses resulting from high acoustic velocities in the regenerator and the resonator feedback. The experimental rig is schematically shown in Figure 2.8. The purpose of Yazaki's study was overcoming the problems that Ceperley had faced, which was generating acoustic power in travelling-wave mode. The experimental results of this study concluded that a travelling-wave device could perform significantly better than a standing-wave device at the same frequency and wavelength. One of the excellent

advantages of such a system is that the onset temperature (which is the difference between the hot and cold sides of the regenerator) would be lower than that in anonset standing wave devices, leading to better utilisation of the low temperature difference resources. This group found that the phase difference between the pressure oscillation and the velocity oscillation was neither 90° nor 0° but between these limits and closer to zero, resulting in a travelling-wave in the looped tube.

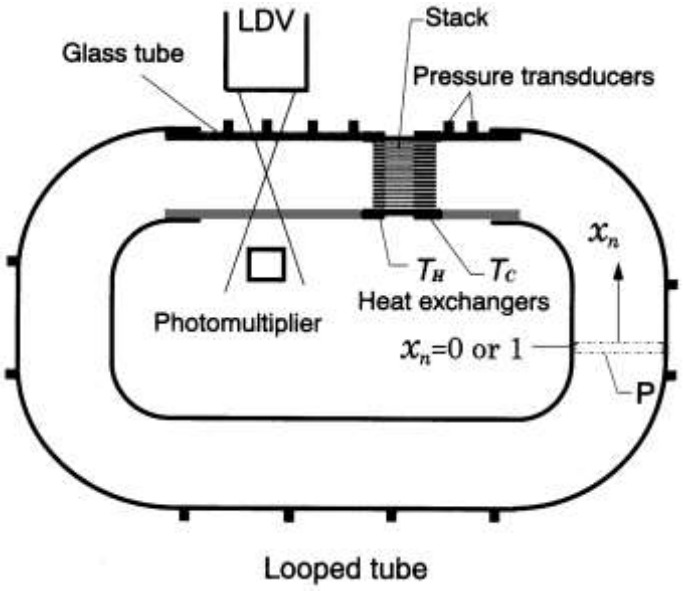

Figure 2.8: Schematic view of the experimental device used by Yazaki et al. [36].

Backhaus and Swift [10, 37] tried to solve Yazaki's problem by proposing a new type of thermoacoustic engine consisting of a loop tube connected to a long resonator pipe. The working fluid of this system was helium at the mean pressure of 30 bar and frequency of 80 Hz. They found out from the first round of results that there was a big difference between the measured and estimated value of the temperature at the midpoint of the regenerator. This is mainly due to the acoustic streaming processes i.e. Gedeon streaming and Rayleigh streaming.

This group made several changes to improve the thermoacoustic engine under study and overcome the viscosity losses which Yazaki had encountered in the previous study. The first change they made was to force the phase angle between the pressure and velocity

oscillations in the regenerator by employing an inertance in the torus part. Secondly, they reduced the acoustic losses and achieved high acoustic impedance in the regenerator by designing the compact acoustic configuration. Finally, they suppressed acoustic streaming by using a jet pump and a tapered thermal buffer tube. The new thermoacoustic engine configuration reached a higher thermal efficiency (30%), equivalent to 41% of the Carnot efficiency.

In 2006, Bao [38] studied the effect of the RC-load (it is a resistance-compliance acoustic load which is used to consume the acoustic power) impedance on the performance of a symmetric standing-wave thermoacoustic engine experimentally and numerically. He found that maximum acoustic power may be obtained when the acoustic resistance is equal to its compliance impedance for the RC-load, and a low compliance impedance Z_c of RC-load causes a higher acoustic power. The experimental apparatus is schematically shown in Figure 2.9.

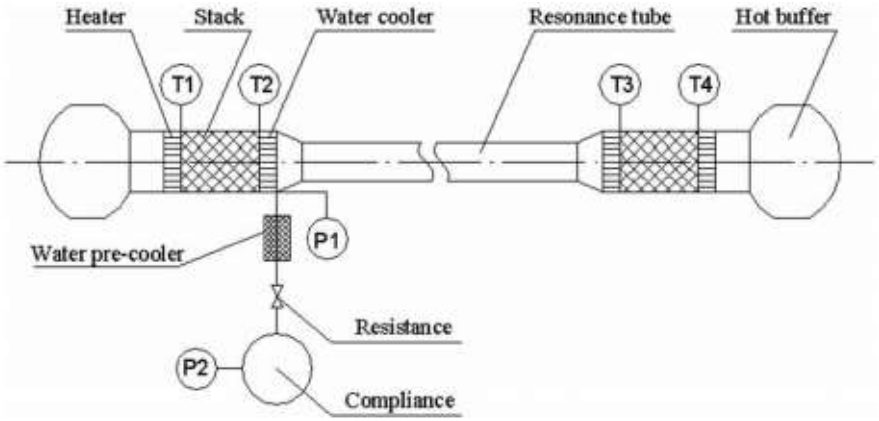

Figure 2.9: Schematic of experimental apparatus [38].

In 2008, Ward and Swift [14] another important development in thermoacoustics is the numerical simulation tool named DeltaEC (Design Environment for Low-Amplitude ThermoAcoustic Energy Conversion) was developed at LANL DeltaEC is a tool implementing the linear theory for the design of the real devices, to achieve a desired performance. Currently, it is widely used in the design, analysis, assessment and prediction of the performance of thermoacoustic systems [7].

Since we know that the wasted heat energy in factories is often at low temperatures, a significant proportion of research in thermoacoustic systems in focused on this low temperature heat application. The most significant development in this area is by Kees [39] who developed in 2008 a thermoacoustic system for utilising low temperature differences from solar collectors or waste heat, with a temperature in the range of 70-200°C. In order to increase the power of the thermoacoustic system at low operator temperature it is necessary to cascade multi engine stages. He also noticed that the viscous losses must be reduced by enlarging the regenerator cross-section with respect to the FBP. He experimentally studied a novel acoustic geometry based on travelling wave thermoacoustic engine with by-pass configuration, as shown in Figure 2.10. His prototype using atmosphere air as the working gas achieved an onset temperature difference as low as 65 K. Kees concluded that; firstly, in standing wave type resonators high acoustic loses (as compared to loop) is the fundamental limitation at low operating temperature and high regenerator impedance. Secondly, the new hybrid configuration is more suitable for low operating temperatures with the low onset temperature giving an indication for low acoustic loss. Thirdly, the proposed hybrid configuration allows for simple cascading multiple regenerator units including a heat pump.

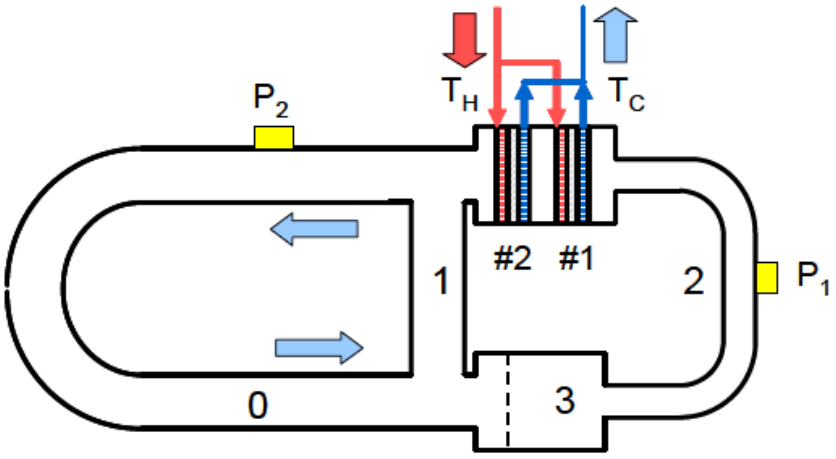

Figure 2.10: By-pass configuration of two stages engines [39].

In addition, Kees published two papers that support the same trend in his previous research in terms of utilization of low-temperature energy sources. In 2010 and 2012, Kees de Blok [32, 40] developed a four stage self-matching travelling wave

thermoacoustic engine that can operate at a temperature difference as low as 40 K at each stage. As utilizing low temperature differences from solar vacuum tube collectors or waste heat in such a range seems to be the most promising and commercial interesting field of applications for thermoacoustic systems. He enlarged the regenerator cross-sectional area with respect to the FBP diameter in order to reduce the velocity in the regenerator, leading to a reduction in viscous losses. It should be mentioned here that the travelling wave resonator is not only to have low acoustic losses but also has to be capable of handling an arbitrary number of regenerator units. Also in standing wave configuration adding any additional engine to the system requires additional loops or branches, increasing the acoustic losses. The four regenerator units were placed on a mutual distance of ¼ λ, as shown in Figure 2.11.

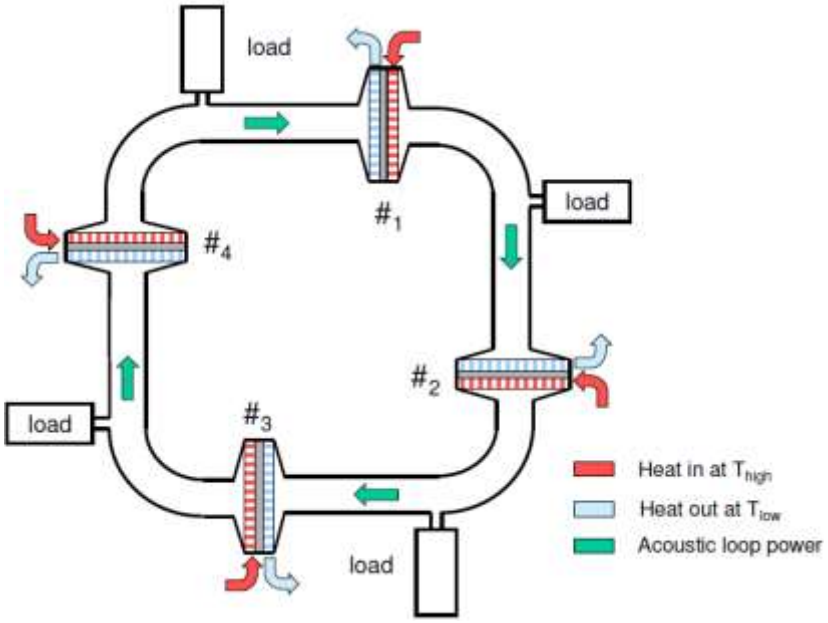

Figure 2.11: 4-stage Atmospheric test rig [32]

This study showed that thermoacoustic engines have the potential for utilising waste heat sources, which is a hot research topic, and has attracted much attention with regard to the development of innovative thermal energy technologies.

In the past three decades, thermoacoustic devices including, refrigerators/coolers or generators have been developed rapidly in many institutes around the world. Owing to their

simplicity and absence of moving parts, travelling wave thermoacoustic engines have the potential to develop low-cost power generators, and therefore have attracted much research effort for developing coolers or electric generators.

2.2.2 Themoacoustic coolers/refrigerators

In 1986, a first successful attempt of a standing wave thermoacoustic refrigerator was demonstrated by Hofler [41] by using a loudspeaker as acoustic source. The COP of Hofler's refrigerator was 12% relative to the Carnot COP. He designed the thermoacoustic refrigerator by employing Root's linear thermoacoustic theory. A comparison between theoretical and experimental results was made, which showed a good agreement between them.

In 1999, Hofler [42] built a thermoacoustically driven thermoacoustic refrigerator (TADTAR). The unit had a total COP of 15% and delivered a cooling power of 91 W across a temperature span of 25^{o}C with the hot side heat addition temperature being 450^{o}C. A helium-Argon mixture was used as the working fluid.

In 2000, Adeff and Hofler [43] demonstrated experimentally a standing wave engine powered by solar energy and coupled to a refrigerator. The working fluid was argon-helium mixture at 6 bar. Few watts of cooling load were obtained from this device. The largest temperature span of 18°C and 2.5 W of cooling power at cold end temperature of 5°C were observed in such a thermoacoustic refrigerator [7].

In 2001, Chen [44] built a thermoacoustic cooler using solar power to generate acoustic power. A device based on harnessing solar power in combination with thermoacoustic principles was built and tested. A solar collector was used to focus radiation from the sun to the engine side to convert it into acoustic power and then produce the refrigeration effect. The working gas was argon at mean pressure of 6.8 bar. The achieved cooling power was computed as 5.7 W.

The bulky shape of the thermoacoustic-Stirling refrigerator leads to discomfort in practical use. A coaxial configuration is an alternative which is more compact and has relatively high performance [7]. Therefore, in 2004; Poese et al. [45] investigated the first systematic study of the coaxial thermoacoustic refrigerator to avoid the bulky shape in the previous research. The main purpose of this study was to develop an environmentally friendly ice-cream freezer. It was an acoustic network based on the same principle as a torus-shaped design. The system was filled with helium at 10 bar, and the frequency was100 Hz. The maximum cooling capacity was about 119 W at the temperature of -24.6°C.

In 2006, Dai et al. [46] designed and constructed a travelling wave thermoacoustic refrigerator driven by a travelling wave thermoacoustic engine, as shown in Figure 2.12. The device reached a lowest temperature of -66^{o}C. 250 W of cooling power at -22^{o}C was obtained when using helium gas at 3 MPa mean pressure, 220 W of input power, and the operating frequency was 57.7 Hz. The results showed good application potential for the system in the field of domestic refrigeration, particularly when the cooling power required is around −20°C or lower.

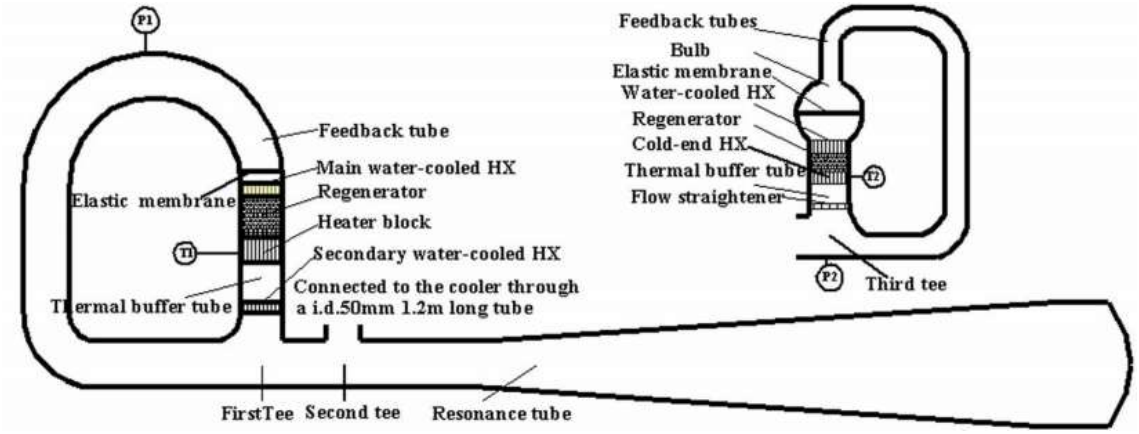

Figure 2.12: Schematic diagram of the traveling wave thermoacoustic refrigerator driven by the traveling wave thermoacoustic engine [46].

In order for the measurements to be comprehensive, it is better to take those measurements with different mean pressures and heating powers.

In 2008, Tijani and Spoelstra [47] developed another coaxial thermoacoustic refrigerator. The linear motor was employed to produce acoustic power for the heat pumping effect. The experimental configuration has a compliance and inertance which are important to create the travelling wave phasing for the operation in a Stirling-like cycle. The operating frequency was 60 Hz, and the working gas was argon at 15 bar. The cooler achieved a coefficient of performance relative to Carnot of 25% at cooling load Q_c=25 W and T_c= -11°C of cooling temperature and a low temperature of -54°C without heat load. The experimental system of the thermoacoustic-Stirling cooler is shown in Figure 2.13.

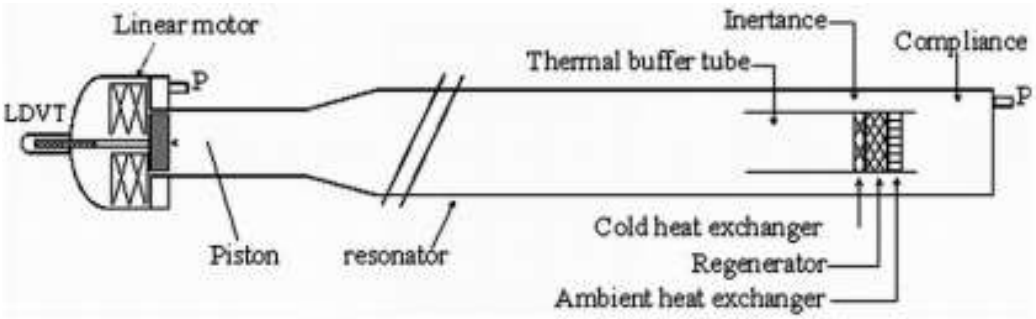

Figure 2.13: Schematic diagram of the thermoacoustic-Stirling cooler [47].

Travelling wave resonator reduces the acoustic losses, and the multi-stage thermoacoustic engine allows utilization of a heat source with a low temperature difference. These two points are described in the next two papers.

In 2013, Yu [48] studied the design and analysis of a thermally driven thermoacoustic cooler. The goal of this study was to utilise industrial waste heat to provide air-conditioning for buildings. The working gas was helium at 3.0 MPa, and the operating frequency was around 100 Hz. A three-stage travelling wave thermoacoustic engine was designed to convert waste heat to acoustic power, and a single stage travelling wave thermoacoustic cooler connected to the engine to provide cold water at temperature of 0-5°C for air conditioning. The ambient temperature was set as 40°C. The simulation results showed that the engine could convert 9.9% of the 15 kW heat input to 1.5 kW acoustic power, and that the cooler could deliver 2.6 kW cooling power at 0°C with a

coefficient of performance (COP) of 2.25. This system is schematically shown in Figure 2.14.

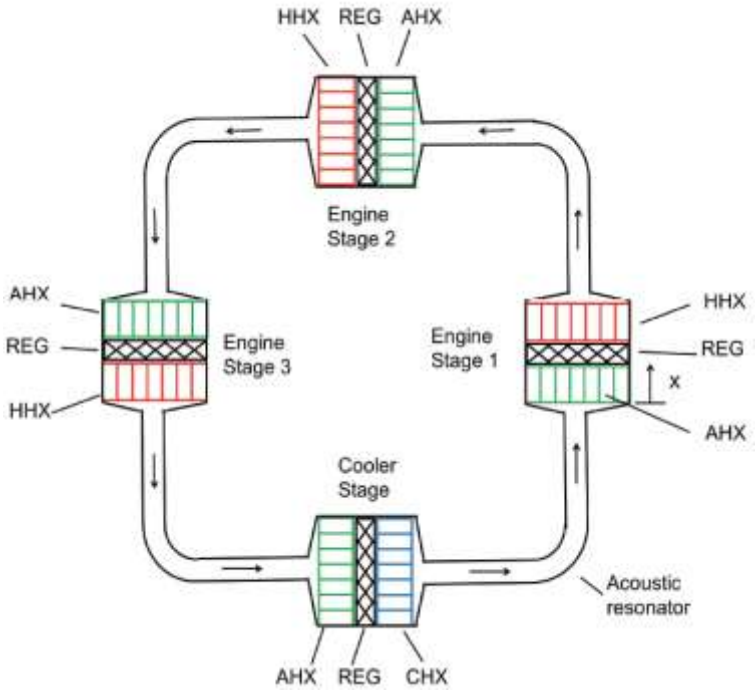

Figure 2.14: Schematic diagram of the waste heat-powered thermoacoustic air conditioner [48].

In 2014, Yu and Al-Kayiem [12] improved this research [48], and investigated numerically a 4-staged system to utilise industrial waste heat to provide air conditioning for buildings where waste heat is abundant but air conditioning is required. A three-stage travelling wave thermoacoustic engine was designed to convert waste heat to acoustic power, and a single-stage travelling wave thermoacoustic cooler connected to the engine to provide cooling at a temperature of 0°C for air conditioning. The ambient temperature was set as 40°C. A system with symmetric geometric configuration was initially modelled and validated using published experimental data. The author introduced an asymmetric impedance distribution and the asymmetric system, which has different geometric dimensions at each stage modelled to improve the acoustic conditions within the system. The simulation results showed that the overall energy efficiency of the tested system for the given temperature range could reach 15–17%,

which showed the feasibility of and potential in developing thermally driven thermoacoustic heat pump systems for utilising waste heat to produce air conditioning.

In 2015, Xu et al. [49] introduced a looped-tube three-stage thermoacoustically-driven cryocooler system. Simulations were performed to investigate the effects of three representative coupling positions of the resonance tube the inlet, middle, and outlet respectively. Their efficiency was found to depend on the dimensions of the resonance tube, indicating the importance of this parameter. The results showed that better phase distribution in the regenerator and less exergy loss in the resonance tube contribute significantly to the superior performance of the system. The system which was investigated is shown in Figure 2.15.

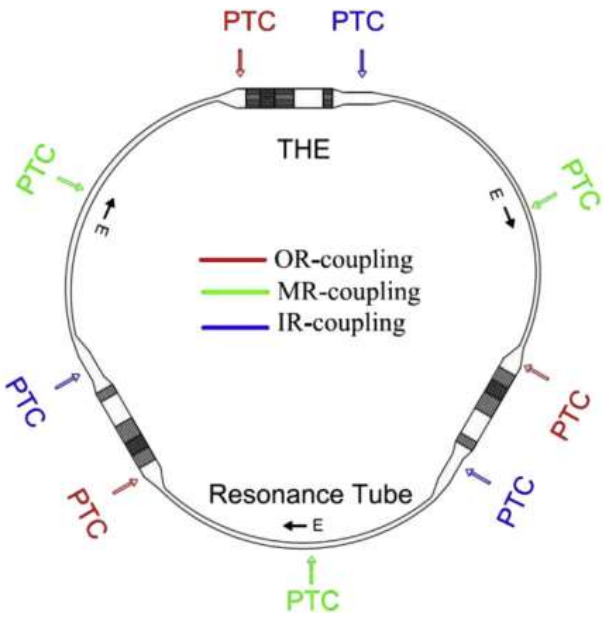

Figure 2.15: Schematic view of the acoustically resonant cooling system [49].

THE: Thermoacoustic Heat Engines, PTC: Pulse Tube Coolers, OR-coupling: the outlet of the resonance tube, MR-coupling: the middle of the resonance tube, IR-coupling: the inlet of the resonance tube.

For the same resonance tube length, the highest exergy efficiency of 16.3% is achieved for the outlet coupling position, whereas the middle and inlet coupling positions only achieved highest exergy efficiencies of 9% and 14.93%, respectively. There are two

reasons for the acceptable performance of OR-coupling. Firstly, a satisfying phase difference in the branch of the thermoacoustic heat engine at the inlet of the PTC was achieved. Secondly, increasing the cross-sectional area of the resonator pipe leading to reduced flow velocity, and ultimately decreasing the viscosity resistance losses.

One of the important applications of the thermoacoustic technology is liquefaction of natural gas, so the same above group investigated this application. In 2016, Xu et al. [50] studied numerically and experimentally an efficient looped multiple-stage thermoacoustically-driven cryocooler for liquefaction and recondensation of natural gas. This system operates in the temperature range of natural gas liquefaction. The experimental results showed good agreement with the simulation results. The experimental system reached a maximum total cooling capacity of 880 W and exergy efficiency of 7.8% at 110 K. The three-stage thermoacoustically-driven PTC system is schematically shown in Figure 2.16.

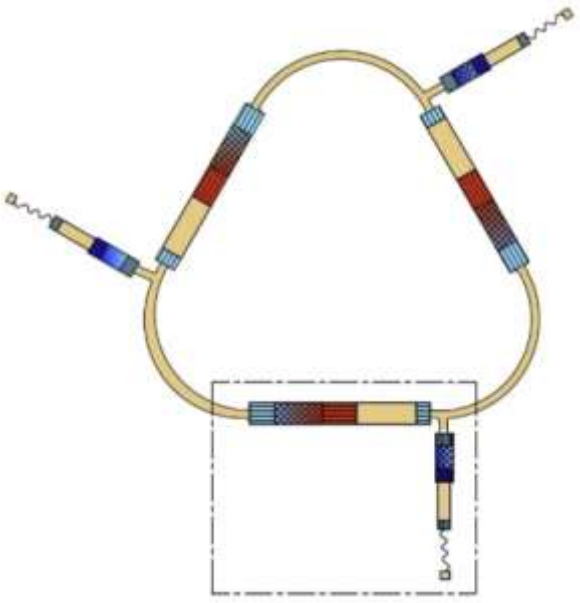

Figure 2.16: Schematic view of 3-stage looped thermoacoustically driven cooling system [50].

The analysis showed that flow-area ratio and the acoustic load impedance are one of the key factors determining thermoacoustic conversion and acoustic power transmission,

and ultimately determining system performance. The results from cooler/refrigerator papers are listed in Table 2.1

Table 2.1: Summary of results from cooler/refrigerator papers.

Author/Date	Topic	Mean pressure (bar)	Frequency (Hz)	Working fluid	COP%	Qc (W)
Hofler (1986)	Refrigerator	10.2	650	Helium	12	121
Hofler (1999)	Refrigerator	-	-	Helium-argon mixture	15	91
Adeff and Hofler (2000)	Refrigerator	6	-	Argon-helium mixture	-	2.5
Chen et al. (2001)	Cooler	5.5	159.5	Helium-argon mixture	~	5.7
Dai et al. (2006)	Refrigerator	30	57.7	Helium	-	250
Tijani et al. (2008)	Cooler	15	60	Argon	2.8	25
Yu et al. (2013)	Cooler	30	100	Helium	2.25	2600
Yu and Al-Kayiem (2014)	Cooler	30	100	Helium	2.01	4500
Xu et al. (2015)	Cryocooler	60	-	Helium	-	750
Xu et al. (2016)	Cryocooler	70	-	Helium	-	880

One of the most important applications of thermoacoustic technology is the generation of electric power using low-temperature energy sources. Energy sources include; solar energy, waste heat energy and cooking stoves. Thus the thermoacoustic generator would be the perfect solution for people living in rural areas, providing them with electricity by utilising the cooking stove energy. The original concept is employing the thermoacousticsystem to convert heat to sound wave and then to electricity using an alternator.

2.2.3 Themoacoustic generators

In the past decades, great efforts have been made to develop thermoacoustic generators with different configurations and transducers. This research have been distributed between several joints in terms of heat resources, the number of engine stages, working fluids, the type of study, whether numerical, experimental or both, as explained in next section.

In 2004, Backhaus et al. [51] demonstrated the ability of travelling-wave thermoacoustic heat engines to convert high-temperature heat to acoustic power with high efficiency. A small-scale travelling-wave thermoacoustic engine was optimised for use with an electrodynamic linear alternator. A travelling-wave thermoacoustic electric generator was created; a power conversion system suitable for demanding applications such as electricity generation aboard spacecraft. The engine efficiency, alternator efficiency, system efficiency (thermal-to-electric), driven ratio, electrical power output and frequency were 24%, 75%, 18%, 6.3%, 39 W and 120 Hz respectively. The electric power output increased from 39 W to 58 W when the driven ratio increases from 6.3% to 9.8%. High-cost alternator was used in this study, however, commercial loudspeakers as inexpensive electro-dynamic transducers used to convert the acoustic power to electricity can be used, as demonstrated by Yu et al. [54, 56]

In 2006, Telesz [18] built a thermoacoustic power converter consisting of a thermoacoustic-Stirling engine interfacing with a pair of linear alternators to produce 100 W of electricity. Helium at 31 bar was used as the working fluid. The operating frequency was 100 Hz. The heat to acoustic power conversion had an efficiency of 26.3% (40% of the Carnot efficiency), while the efficiency of conversion of heat to electricity was 16.8%.

In 2010, Yu et al. [52] described the construction and testing of a prototype thermoacoustic electricity generator to test the concept of a low-cost device for application in remote or rural areas of developing countries. A travelling-wave

thermoacoustic engine with the configuration of a looped-tube resonator was designed and constructed to convert heat to acoustic power. A commercially available loudspeaker was employed as an alternator to convert the acoustic power to electricity. The system was supplied with 800 W as a heat input and produced 5.17 W of electricity at an acoustic–electric conversion efficiency of 0.65 %. These results showed that the approach is possible in principle, to produce electric power levels in the order of 4–5 W, with overall heat-to-electric efficiencies in the order of 1%. The experimental set-up is shown schematically in Figure 2.17.

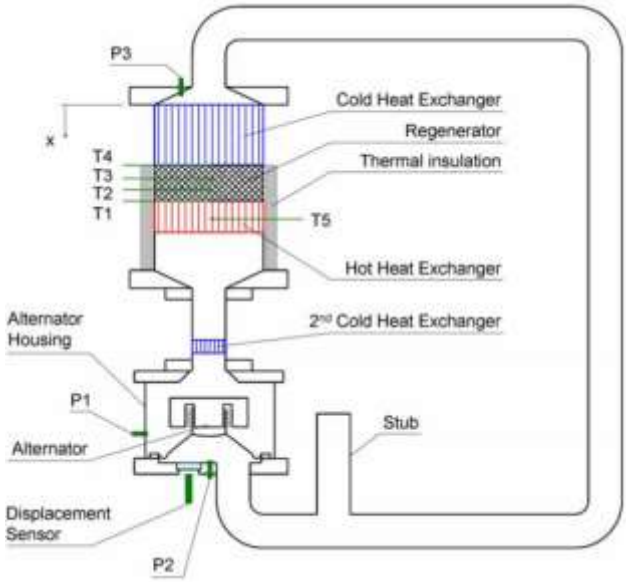

Figure 2.17: Schematic diagram of the test rig [52].

This group used a commercial loudspeaker as an inexpensive electro-dynamic transducer, which is considered in chapter 6 in this thesis.

In 2011, Wu et al. [53] introduced an experimental investigation of a travelling-wave thermoacoustic electricity generator, which consists of a travelling-wave thermoacoustic heat engine and a linear alternator driven by that engine. This system is based on the Stirling thermodynamic cycle and can convert heat into acoustic work (i.e. mechanical work) with a high intrinsic efficiency. 450.9 W of electrical power was obtained with a maximum thermal-to-electrical efficiency of 15.03% and the system produced 481 W

electric power with an efficiency of 12.65%. The experimental rig is schematically shown in Figure 2.18.

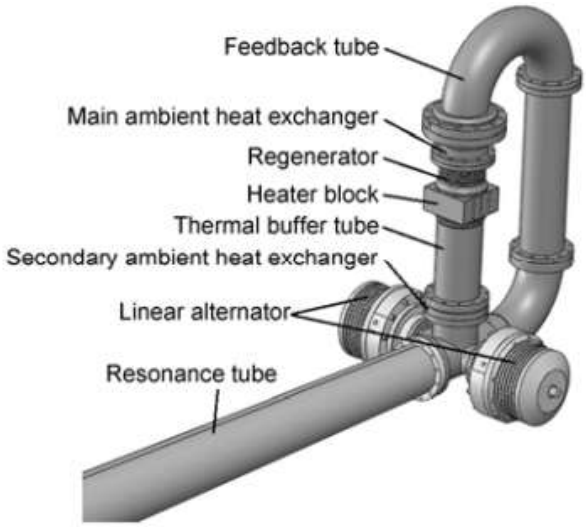

Figure 2.18: Schematic of the travelling-wave thermoacoustic electricity generator (TWTAEG) [53].

Figure 2.19 below shows the output electrical power for different load resistances as a function of heating temperature. It can be seen in general that the output electrical power increases as the heating temperature increases. With the note that there is a tradeoff between the heat input and the output electrical power.

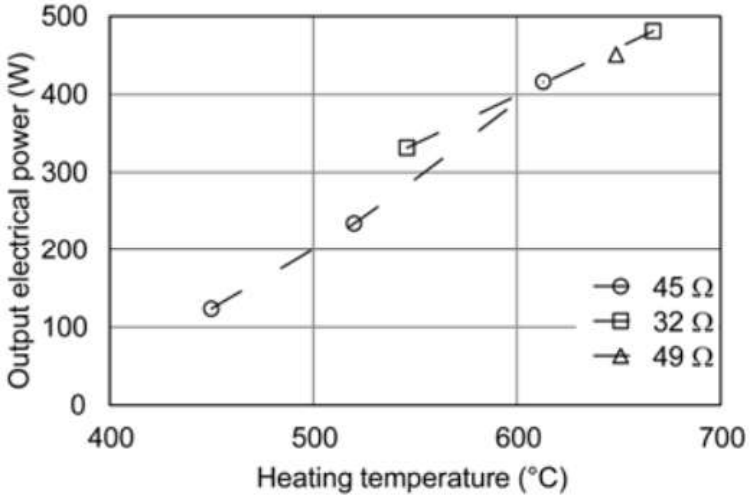

Figure 2.19: Output electrical power for different load resistances as a function of heating temperature [53].

In 2011, Yu et al. [54] studied the feasibility of using commercially available loudspeakers as low-cost linear alternators for thermoacoustic applications, to convert acoustic power to electricity. They presented a case study in which the characteristics of acoustic-to-electric energy conversion of a candidate loudspeaker (alternator) as well as parameters such as high force factor, low electrical resistance and low mechanical loss were measured. The experimental results showed that the selected candidate loudspeaker could reach acoustic–electric transduction efficiency of around 60%. The experimental results also showed that the displacement amplitude does not significantly affect the acoustic–electric transduction efficiency. Furthermore, this work also showed that the measurement methodology developed is useful and reliable for characterising acoustic–electric alternator efficiencies, and that the linear model is still quite useful to describe the behaviour of such alternators.

In 2012, Wu et al. [55] developed a solar-powered travelling-wave thermoacoustic electric generator. This system is a new device capable of converting heat, such as solar energy, into electric power. This system consists of a travelling-wave thermoacoustic electricity generator, a solar dish collector and a heat receiver. Electric cartridge heaters were used to simulate the solar energy, leading to a maximum electric power of 481 W and a maximum thermal-to-electric efficiency of 15.0% with 3.5 MPa pressurized helium and 74 Hz operating frequency. Thereafter, the system was integrated with the solar dish collector and the heat receiver. Experimentally, 200 W was achieved as a maximum electric power. It is notable that the electric power output decreased dramatically; this is mainly due to solar dish collector problems.

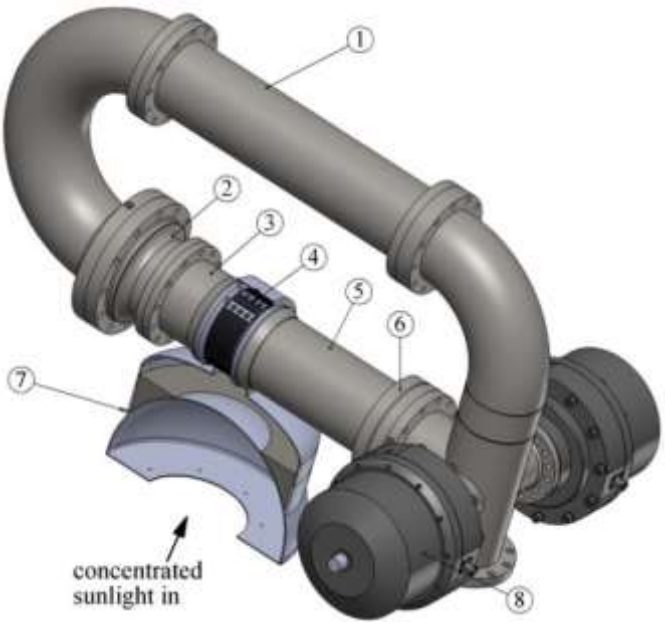

Figure 2.20: Schematic of the travelling-wave thermoacoustic electricity generator (TWTAEG) [55].

1: feedback tube, 2: main ambient HX, 3: regenerator, 4: heater block, 5: thermal buffer tube, 6: secondary ambient HX, 7: heat receiver, 8: linear alternator.

In 2012, Yu et al. [56] investigated the novel concept of a travelling-wave thermoacoustic electricity generator numerically and experimentally. They utilised a looped-tube travelling-wave thermoacoustic engine to convert thermal energy to acoustic power, then, an ultra-compliant alternator was coupled to the system to convert the acoustic power to electrical power. A stub was used for phase and impedance tuning. The cold heat exchanger was designed carefully to have a phase shifting inertancein order to improve its performance. The whole system was simulated numerically by using DeltaEC tool. Numerically, this system's performance can be improved further when using high pressure helium as the working gas and an improved alternator. A prototype was designed, constructed and tested. In conclusion, they found out that the small-scale inexpensive prototype generator produced 11.6 W of electrical power, indicating the potential to develop cheap thermoacoustic electricity generators for energy recovery from waste heat sources. The system which was studied is shown in Figure 2.21.

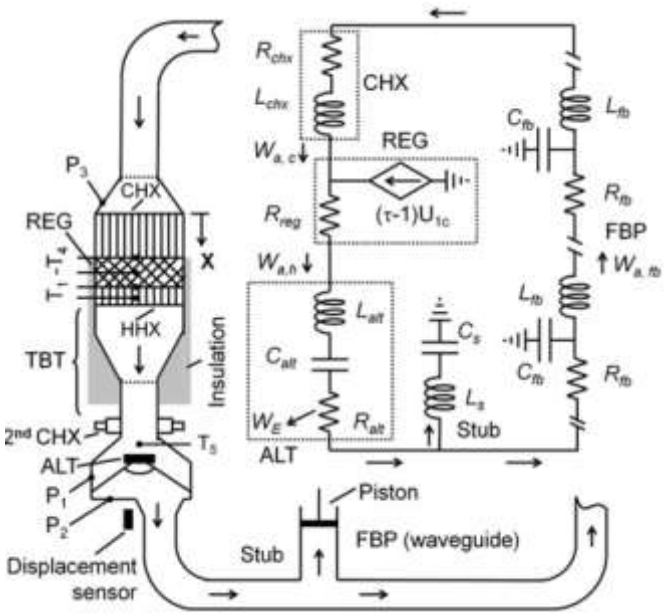

Figure 2.21: Schematic of the demonstrator unit and the lumped acoustic circuit [56].

In 2012, Chen et al. [57, 58] reviewed the development and assessment of two types of thermoacoustic engine powered by waste heat from cooking stoves, either using Propane gas or burning wood as cooking energy to produce an acceptable amount of electricity for the use of rural communities. The design, system architecture and power assessment of these two types of thermoacoustic engine were discussed. Regarding the Propane gas, stove efficiency was found to be 25.13%. The wood burning thermoacoustic engine was tested and found to generate about 57 W of acoustic power, which in turn was converted into 22.7 W of electricity by employing a commercially available loudspeaker as alternator; the studied system is shown in Figure 2.22.

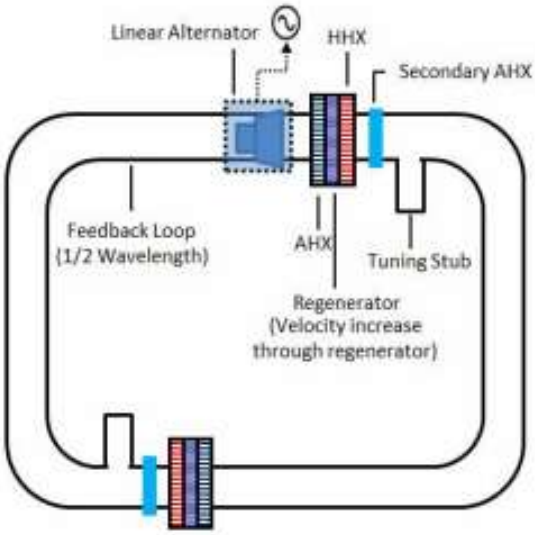

Figure 2.22: Schematic of thermoacoustic generator [58].

In 2013, Sun et al. [59] developed a travelling-wave thermoacoustic electric generator using helium at 3.0 MPa as the working gas, at around 65 Hz. They pointed out that the acoustic coupling of the linear alternators to the travelling-wave thermoacoustic engine is crucial to the performance of the system, and achieved a maximum electric power of 345.3 W with a thermal-to-electric efficiency of 9.3%. At the most efficient operating point, the system produced electric power of 321.8 W with a thermal-to-electric efficiency of 12.33%. The group pointed out that the system's performance can be improved by increasing the pressure amplitude and minimising the acoustic losses in the FBP. The schematic of the travelling-wave thermoacoustic electric generator is shown in Figure 2.23.

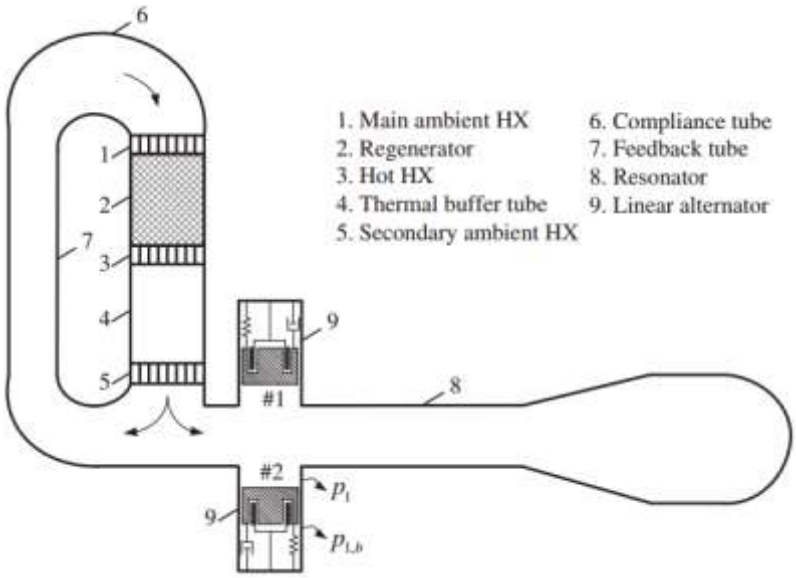

Figure 2.23: Schematic of the travelling-wave thermoacoustic electric generator [59].

In 2014, Wu et al. [60] investigated a 1-kW travelling-wave thermoacoustic electrical generator. A prototype of the 1 kW travelling-wave thermoacoustic electrical generator was designed and tested. In the first test, only 638 W electric power with 16.6% thermal-to-electrical efficiency was obtained. This is mainly due to the high clearance seal loss that was caused by the pistons of the alternator. After further comprehensive analysis, a maximum electric power of 1043 W with a thermal-to-electrical efficiency of 17.7% with a maximum thermal-to-electrical efficiency of 19.8% and an electric power of 970 W were successfully obtained. Operating conditions with a mean pressure of 4.0 MPa, a heating temperature of 650°C and a cooling temperature of 15°C (see Figure 2.24 below).

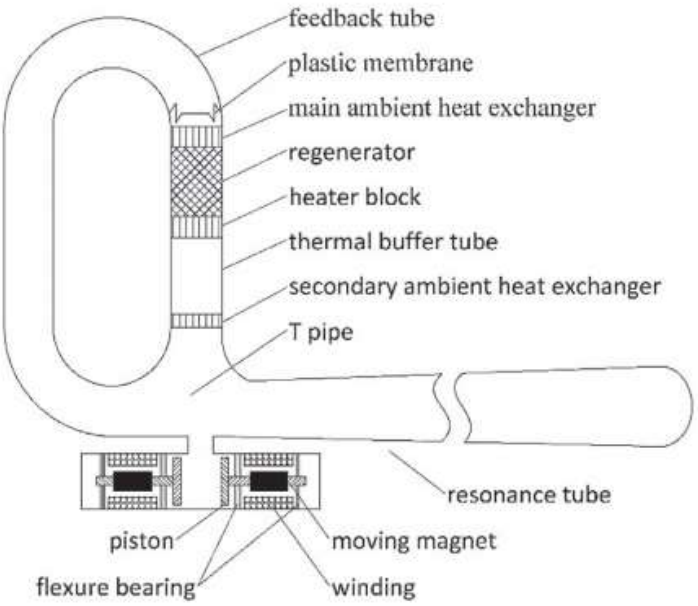

Figure 2.24: Diagram of the experimental system [60].

In 2014, Wu et al. [61] developed a double-acting thermoacoustic Stirling electric generator which had three thermoacoustic Stirling engine stages and three linear alternators, using 5 MPa pressurised helium as working gas and 86 Hz working frequency. The prototype achieved a maximum electric power of about 1.57 kW and a maximum thermal-to-electric conversion efficiency of 16.8%. The schematic of the double-acting thermoacoustic Stirling electric generator is shown in Figure 2.25.

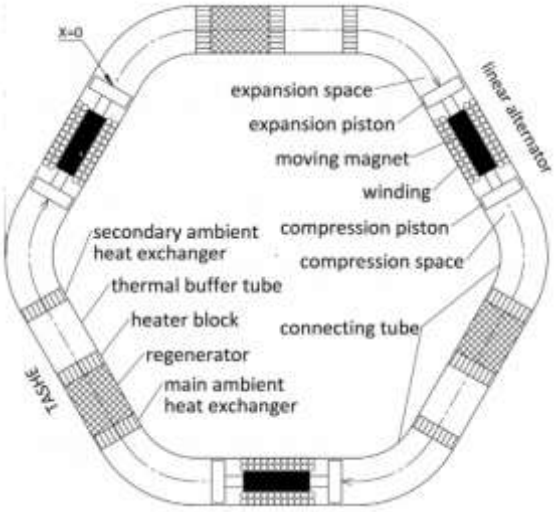

Figure 2.25: Schematic of the double-acting thermoacoustic Stirling electric generator [61].

In 2015, Wang et al. [62] studied numerically and experimentally a travelling-wave thermoacoustic electric generator capable of generating about 500 W electric power both. This study showed that the resonator causes most of the acoustic power losses, and that losses in the HHX, TBT, and FBP are also significant. They pointed out that the performance of the system can be improved by increasing the heating temperature and the mean pressure. Experimentally, this system achieved a maximum electric power of 473.6 W and a highest thermal-to-electric efficiency of 14.5%, when the mean pressure is 2.48 MPa and the heating temperature is 650°C. Numerically, results showed that the maximum electric power can be increased to 718 W and 1005 W when the mean pressures are kept at 2.48 MPa and 3.20 MPa. The experimental rig which was studied is shown in Figure 2.26.

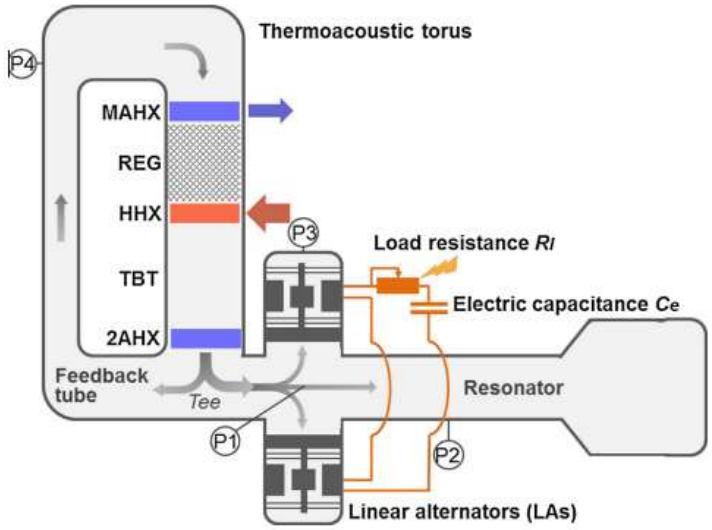

Figure 2.26: Schematic of travelling-wave thermoacoustic electric generator [62].

In 2015, Kang et al. [63] reported the design, construction and tests of a two-stage travelling wave thermoacoustic electric generator, using two audio loudspeakers as transducers. A two-stage travelling-wave thermoacoustic engine converted thermal energy to acoustic power. This study employed two linear alternators to extract and convert the engine's acoustic power to electricity. The working fluid was helium at 1.8 MPa, the operating frequency was 171 Hz. Based on the experimental results, a maximum electric power of 204 W was achieved ,when the hot end temperature of the

two regenerators reached 512°C and 452°C, respectively. A maximum thermal-to-electric efficiency of 3.43% was achieved when the hot end temperature of the two regenerators reached 597°C and 511°C, respectively. In conclusion, the results of this study demonstrated that multi-stage travelling-wave thermoacoustic electricity generators have great potential for developing inexpensive electric generators. The experimental rig is shown in Figure 2.27.

Figure 2.27: The photo of the thermoacoustic generator [63].

In 2016, Bi et al. [64] proposed a new travelling-wave thermoacoustic electric generator, consisting of a multi-stage travelling-wave thermoacoustic heat engine and linear alternators. In this system, as shown in Figure 2.28, the engines are connected by a slim resonance tubes to create a travelling wave in the regenerator, which is important in achieving a high efficiency. It can be seen that the alternator is connected as a bypass at the end of each resonance tube. From the experiment tests, the maximum electric power of 4.69 kW with thermal-to-electric efficiency of 15.6% and the maximum thermal-to-electric efficiency of 18.4% with electric power of 3.46 kW were achieved with 6 MPa pressurized helium, 650°C and 25°C heating and cooling temperatures.

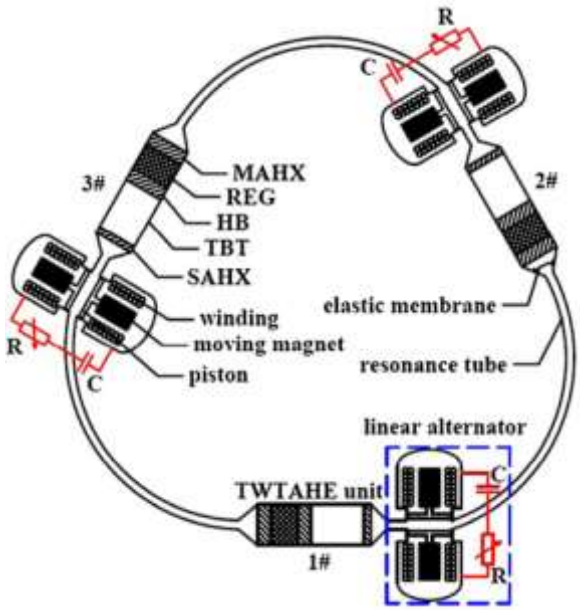

Figure 2.28: Schematic of the three-stage the travelling-wave thermoacoustic electricity generator (TWTAEG) [64].

In 2016, Wang et al. [65] further developed and tested a TWTEG (travelling-wave thermoacoustic electric generator). A maximum electric power output of 750.4 W and a highest thermal-to-electric efficiency of 16.3% were achieved, with helium of 3.16 MPa as the working gas. The experimental rig which was studied is shown in Figure 2.29.

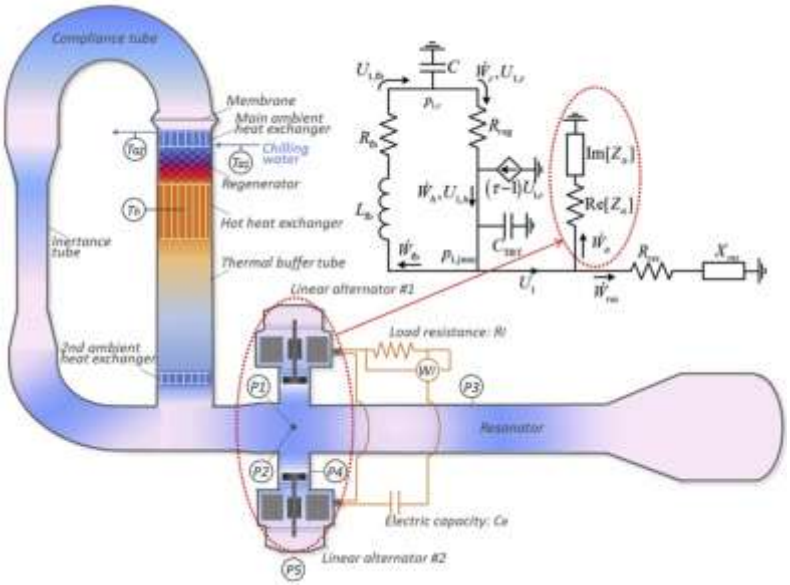

Figure 2.29: Schematic diagram of travelling-wave thermoacoustic electric generator and the equivalent electric circuit network [65].

P1 denotes the location of a piezoresistive pressure sensor, and P2-P5 denote that of piezoelectric pressure sensors. Heating temperature Th, temperatures of the inlet T_{a1} and outlet T_{a2} of chilling water were measured by K-type thermocouples. The coils of the linear alternators are connected in series with a variable electric R-C load to extract electric power. Electric power W_l was measured by a power meter.

According to the above research, the loudspeaker transducer is the best choice for an experimental study, as it efficient, cheap and widely available. In the current study, the loudspeaker transducer is coupled numerically to the travelling wave thermoacoustic system with a by-pass configuration, which is a novel concept compared to the previous studies in this field. The main goal of this study is to reveal whether the loudspeaker can work with a by-pass without violating the thermodynamic principles, and to what extent the loudspeaker affects the thermoacoustic system. These issues will be addressed in detail in chapter 6. The results from generator papers are listed in Table 2.2

Table 2.2: Summary of results from generator papers.

Author/ Date	Topic	Mean pressure (bar)	Frequency (Hz)	Working fluid	Generator efficiency%	Electrical power output(W)
Backhaus et al. (2004)	Generator	55	120	Helium	18	39
Telesz (2006)	Generator	31	100	Helium	16.8	100
Yu et al. (2010)	Generator	p_{atm}	75	Air	0.6	5.17
Wu et al. (2011)	Generator	35.4	74	Helium	15.03	450.9
Wu et al. (2012)	Generator	35	74	Helium	15	481
Yu et al. (2012)	Generator	p_{atm}	70	Air	2.4	11.6
Chen et al. (2012)	Generator	1.513	80	Air	25.13	22.7
Sun et al. (2013)	Generator	30	65	Helium	12.33	345.3
Wu et al. (2014)	Generator	40	74	Helium	17.7	1043
Wu et al. (2014)	Generator	50	86	Helium	16.8	1570
Wang et al. (2015)	Generator	24.8	65	Helium	14.5	473.6
Kang et al. (2015)	Generator	18	171	Helium	3.43	204
Bi et al. (2016)	Generator	60	70	Helium	15.6	4690
Wang et al. (2016)	Generator	31.6	65.5	Helium	16.3	750.4

2.3 Related work and justification of the current study

My current research covers a broad range of areas within traveling wave thermoacoustic engines with my work involving several aspects including by-pass configurations [39], inertance [66, 67, 68 and 69], multi-stage systems [12, 32, 40, 48 and 70], travelling wave thermoacoustic engine driven cooler [7, 12, 48 and 71] or alternator [51, 55 and 63], travelling wave thermoacoustic engine with Helmholtz resonator or RC-load [7, 38, 55 and 72] connected ,along with associated experimental works and measuring techniques[73]. Due to the broad range of applications and various branches covered by

my work the majority of traveling wave engine literature was relevant to my study. With regard to the by-pass configuration, the first relevant research I reviewed was by Kees [39] which studied and analysed the by-pass configuration to reduce acoustic losses. Therefore, I reviewed this research carefully to understand the mechanism's at work of this new configuration, and discovered that the researcher's focus was not on system efficiency and as a result chose heat exchangers (type SX) which are inefficient when compared to other alternatives. In addition, the author did not employ DeltaEC software to analyses his system. My focus was on trying to increase the efficiency of the system and changing the type of heat exchangers to type TX (shell and tube) as well as to employ DeltaEC software to analysing this new configuration to reveal whether DeltaEC can capture the essence of this system.

Therefore, based on what has been mentioned above about by-pass configuration, this work has been divided up in most of this thesis with:

- Chapter 4 dedicated to analysis and validation of the by-pass configuration using DeltaEC.

- Chapter 5, after the success of the validation in chapter 4, encouraged me to keep improving this configuration in terms of changing the type of heat exchangers to shell and tube kind, and then add an acoustic load to the system(i.e. cooler).

- Chapter 6, the success of Chapters 4 and 5 allowed me to broaden the application of my work and add an alternative acoustic load, namely alternator, to generate electricity.

- Chapter 7, in order to enhance this study and to overcome the problem of acoustic losses associated with the length of feedback pipe, a two engine system was investigated. This concept leads to sharing the feedback pipe between the two engines and thus reduces the acoustic losses.

Regarding to the Chapter 8, by reviewing the previous research which studied a looped tube travelling wave thermoacoustic engine experimentally and numerically, it can be observed that all of these studies used various techniques (for example a stub) to decrease the velocity and then reduce viscosity losses but did not employ these techniques to shift phase between the pressure and velocity oscillations.
Therefore, I decided to study such a system by using a side-branched Helmholtz resonator to force the phase angle between the pressure and velocity oscillations towards zero, which in turn leads to reduced acoustic losses and increases the system performance. This concept combines between the RC-load to consume the acoustic power and the Helmholtz resonator which can be varied manually to reveal their effects on the system performance.

2.4 Concluding remarks

This chapter has been dedicated to the review of the related research in the field of thermoacoustic technologies. This chapter focuses on the history of development to date, and the applications of this technology (i.e. engines, coolers, and generators).

These topics mainly focus on maximising acoustic power production, and minimising acoustic losses in the FBPs. The current research focuses on a looped-tube travelling-wave thermoacoustic engine in two respects. First, numerical investigation of a looped-tube travelling-wave thermoacoustic engine with a by-pass pipe and its applications (cooler and generator). Secondly, fundamental investigation of a side-branched volume to tune the acoustic field in a looped tube travelling-wave thermoacoustic engine, both with and without a RC-load. The first aspect has been investigated numerically using DeltaEC software to analyse and simulate this configuration. The second aspect has been studied experimentally and numerically, then a comparison has been carried out to validate the model.

Chapter 3 Theory of thermoacoustics

3.1 Introduction

The thermoacoustic effect can be defined as heat transfer between a fluid and solid metal in the presence of an acoustic wave. A sound wave consists of pressure, motion and temperature oscillations. When the sound travels in small channels, oscillating heat flows to and from the channel walls. The combination of all oscillations produces thermoacoustic effects.Thermoacoustics is based on a complex physical principle drawing on many scientific disciplines (acoustics, fluid mechanics, thermodynamics, heat transfer, dynamic systems, solid-state physics, and electronics) [74]. The effect of thermoacoustics is demonstrated by imposing a temperature gradient within the generator. Supplying heat energy leads to a spontaneous generation of an acoustic wave along the direction of the temperature gradient according to Rayleigh's criteria as mentioned before.The acoustic wave itself comes from molecular collisions and the random motion leads to expansion and compression, causing heat transfer to and from a solid surface.This chapter presents the thermodynamic cycle i.e. Stirling cycle, and the thermoacoustic power cycles i.e. travelling and standing wave cycle. Thereafter, it describes the key parameters for the thermoacoustic system i.e. wavelength, thermal penetration depth, viscous penetration depth, gas parcel displacement, relative pressure amplitude, working gas, mean pressure and frequency. Furthermore, this chapter explains the theory of thermoacoustic by deriving the thermoacoustics continuity, momentum, and energy flow equations.

3.2 Thermodynamics

In this section, the basic thermodynamic concepts on which the thermoacoustic phenomenon is based will be described. The prime mover receives heat (Q_H) from a high-temperature source at (T_H) and rejects heat (Q_C) to a low-temperature (T_C) to generate work (W).

3.2.1 Stirling cycle

The Stirling cycle is a thermodynamic cycle that describes the general class of Stirling's devices. This includes the original Stirling engine that was invented, developed and patented in 1816 by Reverend Dr Robert Stirling [8]. The Stirling cycle machine is a device which operates on a closed regenerative thermodynamic cycle, with cyclic compression and expansion of a working fluid between different temperature levels. The cycle consists of four processes; namely isothermal compression, isothermal expansion, isentropic heat addition and isentropic heat rejection, as shown in Figure 3.1.

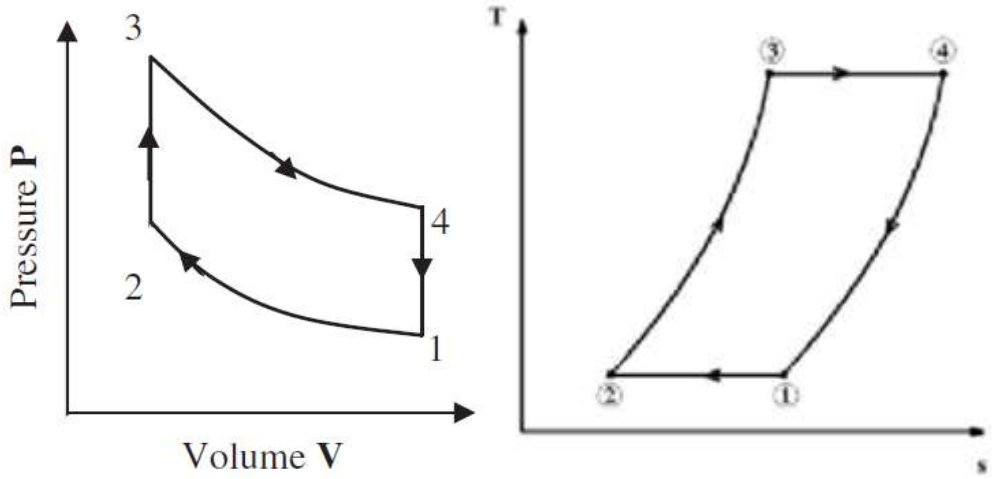

Figure 3.1: Stirling cycle: P-V digram [75], T-S digram [8].

Considering a piston acting upon a cylinder containing a working fluid. If heat can be added or removed from the cylinder, then the Stirling cycle can be described as follows.

Process 1–2 isothermal compression process: The piston moves inward, reducing the enclosed volume of the cylinder, compressing the gas and increasing its pressure from P_1 to P_2. Heat generated by the compression process is rejected from the cylinder so that the temperature of the working fluid is maintained. Work is done on the fluid equal to the heat rejected from the cycle. There is no change in internal energy and a decrease in entropy.

Process 2–3, constant volume heat addition process: The piston maintains a constant volume in the cylinder while heat is added to the system. The temperature of working

fluid increases from T_{min} to T_{max}, increasing the working fluid pressure. No work is done, and there is an increase in the entropy and internal energy of the working fluid.

Process 3– 4, isothermal expansion process: The piston now moves outward increasing the volume of the cylinder, expanding the gas and reducing its pressure from P_3 to P_4. The temperature of the working fluid is maintained with the addition of heat. Work is done by the working fluid on the piston, equal in magnitude to the heat supplied. There is no change in the internal energy, but an increase in the entropy of the working fluid.

Process 4–1, constant volume heat rejection process: The piston maintains a constant volume in the cylinder while heat is rejected from the system. The temperature of the working fluid decreases from T_{max} to T_{min}, reducing the working fluid pressure. No work is done; and there is a decrease in the internal energy and the entropy of the working fluid [75].

3.3 Thermoacoustic power cycles

There are two types of thermoacoustic device, depending on the type of acoustic wave which will be used: standing-wave and travelling-wave devices.

3.3.1 Standing-wave engine

The standing-wave is one version of a thermoacoustic engine; and is generated inside a tube with an open end, while the other is closed. The phase angle between the pressure and velocity oscillations is 90^{o}. In other words, the velocity at the closed end is zero (because it is a closed area and there is no movement of the gas molecules), the pressure is a maximum value (because, as it is well known physically, the pressure is inversely proportional to the velocity, so when the velocity is zero, the pressure is maximum) and the opposite is true at the open end, as shown in Figure 3.2.

Generally, in the standing wave engine, heat transfer is delayed due to the pressure and velocity not being in phase, meaning that the pressure and velocity amplitude are out of

phase by 90° (in a real standing-wave thermoacoustic device, the phase difference drops slightly below 90° to permit power flow to the acoustic load). The spacing in the stack of a standing-wave device should be greater than that for the regenerator in a travelling wave device, which provides imperfect heat transfer between the gas parcels and the solid surface of the stack, thus causing the necessary phase shift between the pressure and velocity waves. The large space between stack plates is wanted, resulting in a standing-wave which is needed for some applications.

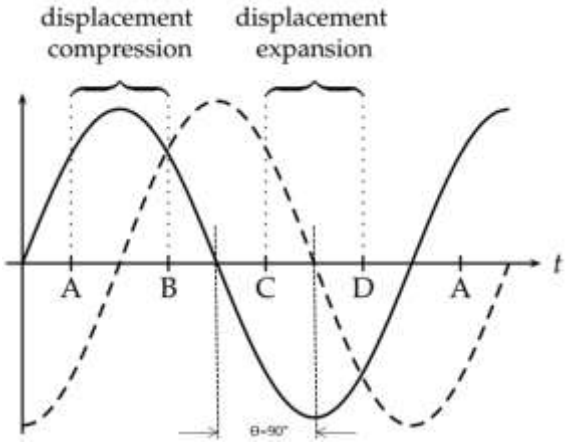

Figure 3.2: Velocity (-) and pressure (--) as a function of time in a gas supporting a standing wave [22].

A basic concept for generating acoustic power from heat energy was introduced by Ceperley [30] by using the singing pipe which produces sound when the closed tube's end is placed in a flame. The kind of wave which is generated is the standing-wave, this concept uses acoustic standing waves to force the gas inside the tube to undergo cyclic processes (compression, heating, expansion and cooling) similar to what happens in the conventional heat engine [30]. It should be mentioned here that the maximum thermoacoustic effect can be reached when the phase angle between pressure and velocity oscillations is zero, as it will be explained in the next section. To further understand the different processes and the phase angle between pressure and velocity one can refer to Figure 3.3 below.

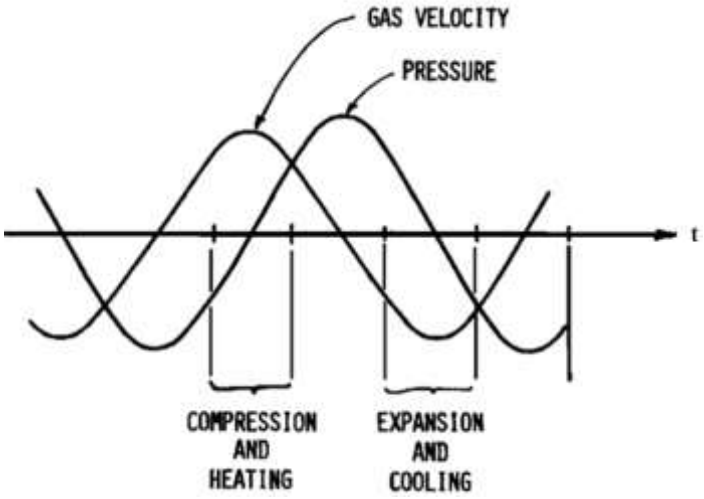

Figure 3.3: Pressure and velocity versus time in standing wave device, Phase difference of 90° between acoustic pressure and velocity [30].

3.3.2 Travelling-wave engine

The oscillating gas pressure and velocity are in phase, which means that the phase angle difference between pressure and velocity is zero. The travelling-wave engine can be referred to as the thermoacoustic-Stirling engine, because the gas in it follows a Stirling-like-thermodynamic cycle.

A travelling wave thermoacoustic engine usually consists of a pair of cold and hot heat exchangers, a regenerator, and the acoustic resonator. The regenerator of the travelling wave thermoacoustic engine is a section of porous material. Perfect thermal contact between the gas and solid material is maintained; therefore the gas has the same temperature as the local solid material within the regenerator. The hot heat exchanger extracts heat from the heat sources and transfers it to the working gas within the thermoacoustic engine, while the ambient heat exchanger removes the heat from the working gas and rejects it to the external heat sink. This pair of heat exchangers build up and maintain a steep temperature gradient along the axle of the regenerator where the thermodynamic cycle takes place and converts the thermal energy to acoustic power. As

shown in Figure 3.4, acoustical travelling waves propagating through the differentially heated regenerator from cold to hot are amplified [76].

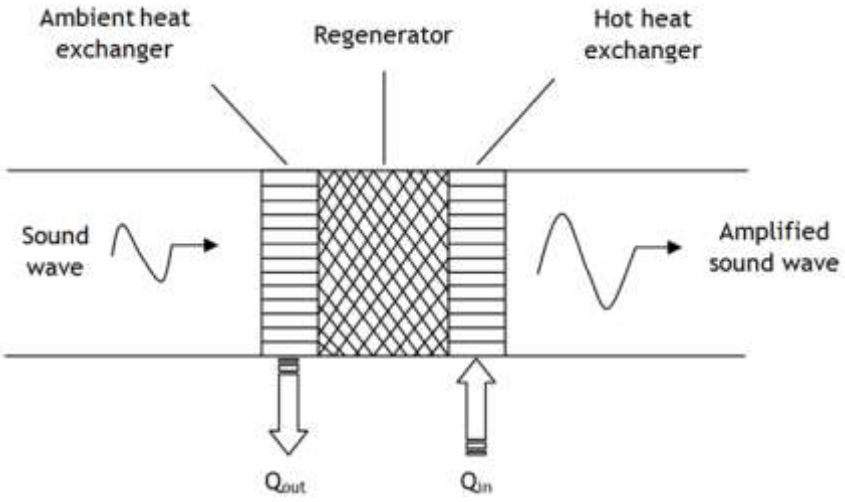

Figure 3.4: Practical regenerator in a travelling-wave thermoacoustic engine.

A continuous temperature gradient is set up along the length of the regenerator by external sources which heat one end and cool the other. When a wave forces a volume of gas to move towards the hot end, it is heated by the higher temperature regenerator and travels towards the colder end, where it is likewise cooled.

Figure 3.5 shows the travelling wave's pressure and velocity which is propagating through the regenerator as a function of time. A sound wave travelling from the cold to the hot end of a differentially heated regenerator would cause a build-up of pressure (compression), then a flow of gas towards the hot end (heating), followed by a drop in pressure (expansion), and finally a flow of gas towards the cool end (cooling). This is similar to the thermodynamic cycle a gas volume would undergo in a standard Stirling engine (compression, heating, expansion, and cooling). However, since the acoustical wave is responsible for the compression, expansion, and gas movement, the mechanical energy produced by the cycle in the travelling wave heat engine will amplify the sound wave [30].

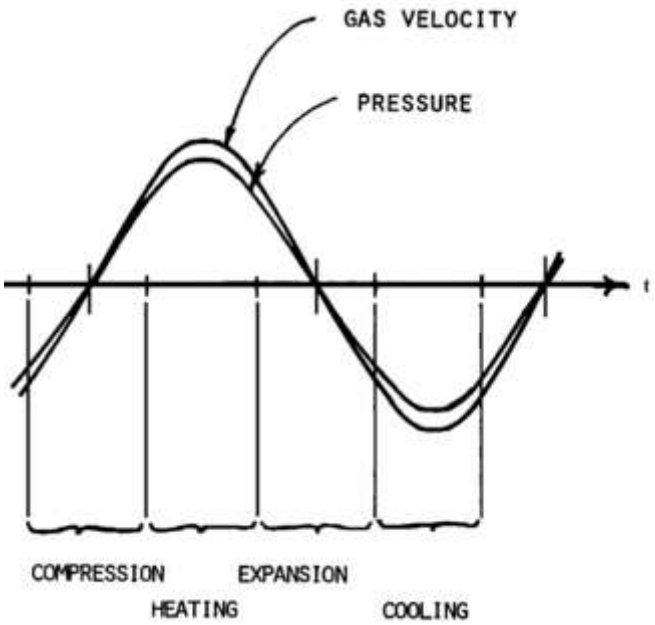

Figure 3.5: Pressure and velocity variation with time in a travelling-wave thermoacoustic device [30].

In Figure 3.6, there is a comparison between the Stirling cycle and travelling wave thermoacoustic cycle. It can be seen that the thermoacoustic Stirling cycle will be less efficient than the Stirling cycle [76].

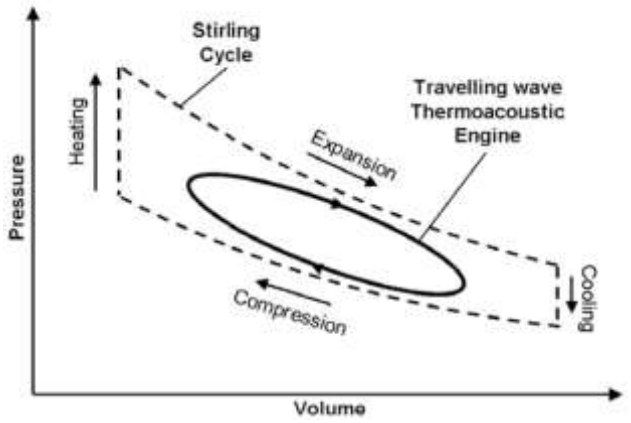

Figure 3.6: Schematic of the thermodynamic cycle that a ‘‘gas parcel” experiences in the regenerator [76].

3.3.3 Key parameters

There are several important length scales and parameters which are used to design and operate the thermoacoustic devices. They will be introduced and described in this section.

3.3.3.1 Wavelength

The wavelength of the sound wave can be calculated by equation (3.1) below. The wavelength has a strong effect on the length of the thermoacoustic device, and in turn the power density of the system. For example, if helium is used, the length of the thermoacoustic device will be much longer than a device which uses nitrogen as a working gas.

$$\lambda = a / f, \tag{3.1}$$

where, λ is the wavelength (m), a is the speed of sound (m/sec), and f is the oscillation frequency (rad/sec).

3.3.3.2 Thermal penetration depth

The thermal penetration depth is perpendicular to the direction of the wave propagation, and is important in thermoacoustics. The thermal penetration gives an idea about heat diffusion, according to the distance between the working gas and solid surface of the stack or regenerator. In other words, it is the thickness of the layer around the stack plate through which the heat diffuses. This length scale is important for understanding the performance of the thermodynamic cycle, since the diffusive heat transport between the gas and the solid boundary is only significant within this region [77]. It can be expressed as

$$\delta_k = \sqrt{\frac{2k}{\rho c_p \omega}}, \tag{3.2}$$

where k is the thermal conductivity of fluid, ρ is the density of fluid, C_p is the specific heat of fluid (heat capacity per unit mas), ω is the angular frequency of fluid.

3.3.3.3 Viscous penetration depth

The viscous penetration depth is the thickness of the layer around the stack plate where the viscous effects are significant. Viscous shear forces occur within this layer, which results in the dissipation of acoustic power. It can be expressed as

$$\delta_v = \sqrt{\frac{2\mu}{\rho\omega}}, \tag{3.3}$$

where μ is the dynamic viscosity (Pa s).

These two parameters are very important in thermoacoustic processes, which determine the required spacing within the stack or regenerator. Thereby, at a distance much greater than these penetration depths from the solid boundary (e.g. plates of stack) the gas feels no thermal or viscous contact with the solid boundaries [74]. In other words, the heat transfer between the gas parcel and the stack plate occurs only at the distance less than the thermal penetration depth (δ_k) from the stack plate. It should be noted here that there is a trade-off between the value of the thermal penetration depth and the viscous penetration depth. The Prandtl numb**e**r describes the ratio between the viscous and thermal penetration depth, which is written as

$$\sigma = \left[\frac{\delta_v}{\delta_k}\right]^2 = \frac{\mu c_p}{k}. \tag{3.4}$$

The Prandtl numb**e**r should be as small as possible in regenerators for travelling wave thermoacoustics engines [78].

3.3.3.4 Gas parcel displacement

Gas parcel displacement is an important length scale in the direction of motion of the gas. The displacement amplitude at a certain position along the wave-propagation direction is given as [78]

$$\zeta = \frac{u_a}{\omega}, \tag{3.5}$$

where; u_a is the gas velocity amplitude (m/sec), ω is the angular frequency (rad/sec) which can be calculated as $\omega = 2\pi f$.

Gas parcel displacement represents half of the total tour of the gas parcel during one acoustic cycle. It is interesting to note that the peak-to-peak displacement amplitude (2ζ) represents the maximum displacement of the gas parcel in the axial direction during each acoustic oscillation cycle [1]. In thermoacoustic engines and refrigerators, the gas displacement amplitudes are much larger than the penetration depths, but still much smaller than acoustic wavelengths [74],

$$\delta_v, \delta_k << \zeta << \lambda. \tag{3.6}$$

It should be noted that the perfect length of a heat exchanger, which will be used in a thermoacoustic model later, is equal to 2ζ . The gas displacement amplitude is a very small fraction; if compared to a standing-wave device with length of tube equal to half the wavelength, it can be seen that the amplitude is largest in the middle (velocity antinode) and smallest at the hard end (velocity node) [78], as shown in Figure 3.7 below.

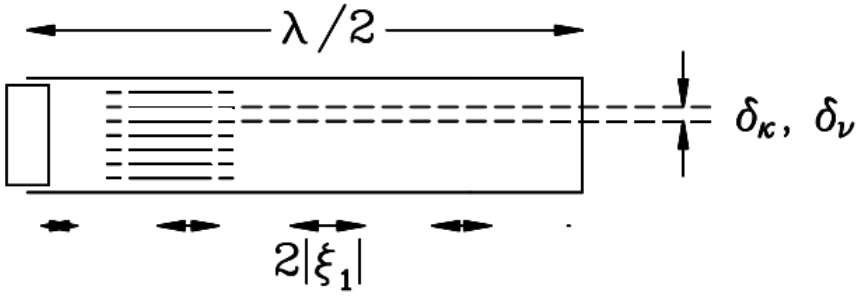

Figure 3.7: The gas displacement amplitude variation [79].

3.3.3.5 Relative pressure amplitude

Relative pressure amplitude (RPA) is the ratio of pressure amplitude $|p_1|$ to the mean pressure p_m which can be expressed as

$$RPA = \frac{|p_1|}{p_m} \times 100\%. \tag{3.7}$$

RPA is an important parameter for evaluating the strength of self-excited thermoacoustic oscillations [7].

3.3.3.6 Working gas

To choose a working gas for a thermoacoustic system there are several properties that should be considered: Prandtl number, sound speed, thermal conductivity and viscosity. As was mentioned before the best working gas for thermoacoustic devices should have a low Prandtl number, low viscosity to avoid large viscous dissipation, low sound speed, and high thermal conductivity [80].

3.3.3.7 Mean pressure

The power density in a thermoacoustic system is proportional to the mean pressure ($\dot{E} \propto P_m$) [30], high mean pressure results in high acoustic power. However, there is a limitation here, for P_m higher than atmospheric pressure the resonator needs to be designed and built as a conventional pressure vessel, which results in high material and manufacturing costs. It should be noted that the thermal penetration depth δ_k is inversely proportional to square root of P_m ($\delta_k \propto \frac{1}{\sqrt{p_m}}$), so a high pressure results in a small δ_k, which in turn results in a small flow channel size in the regenerator. This makes its construction difficult [80].

3.3.3.8 Frequency

The power density in the thermoacoustic devices is linearly proportional to frequency ($\dot{E} \propto f_m$) [48]. Thermal penetration depth δ_k is inversely proportional to the operating frequency ($\delta_k \propto \frac{1}{f_m}$). High frequency leads to small channel size for the regenerator, which will increase the cost of the regenerator material [15].

3.4 Linear thermoacoustic theory

The important concepts which govern the thermoacoustic phenomena are explained in this section. As shown in Figure 3.8 below, a half-wavelength resonator of length *L*, which contains a stack, sandwiched between two heat exchangers, generates an acoustic wave. The required assumptions are:

1. Steady state
2. The plates are rigid and stationary.
3. The acoustic pressure is *x* direction only.
4. Radiation is negligible.
5. Viscosity is independent of temperature.
6. The average fluid velocity is zero.
7. The length of the plates is small compared to the length of the resonator.

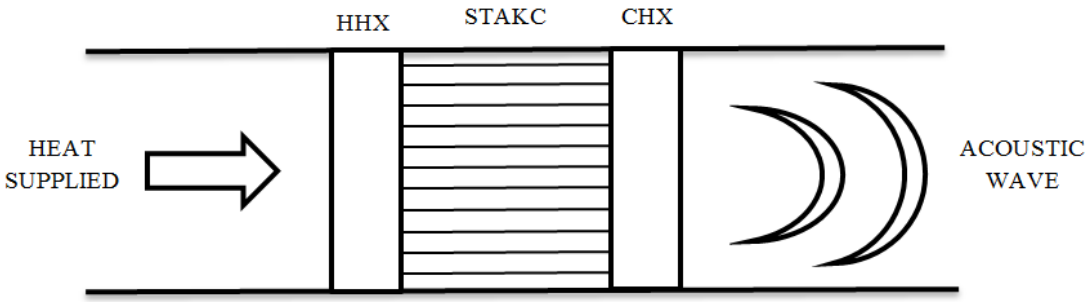

Figure 3.8: A simple short thermoacoustic engine model.

The derivations of the thermoacoustics governing equations (continuity, momentum and energy) are listed below

3.4.1 Thermoacoustics continuity equation

The continuity equation is based on a scientific principle that mass is conserved within any control volume of the fluid. The change in the amount of mass within a fixed control volume can only be caused by the difference between the amount of fluid flowing into the control volume and the amount flowing out [81]. This equation is expressed as follows [74]

$$\frac{\partial \rho}{\partial t} + \nabla \cdot (\rho V) = 0. \tag{3.4.1}$$

Equation (3.4.1) consists of the density and velocity of the fluid, so these two variables can be expressed in complex notation as mentioned before

$$\rho(x, y, z, t) = \rho_m(x) + \rho_1(x, y, z) e^{i\omega t} = \rho_m + \rho_1, \tag{3.4.2}$$

$$V(x, y, z, t) = V_1(x, y, z) e^{i\omega t} = V_1. \tag{3.4.3}$$

These two equations can be substituted into equation (3.4.1), resulting in

$$\frac{\partial}{\partial t}(\rho_m + \rho_1) + \nabla \cdot ([\rho_m + \rho_1] \mathrm{V}_1) = 0, \tag{3.4.4}$$

there is no temporal dependence for the mean density which leads to

$$\frac{\partial}{\partial t}[\rho_m(x)] = 0, \tag{3.4.5}$$

substituting equation (3.4.5) into equation (3.4.4) will give

$$\frac{\partial \rho_1}{\partial t} + \nabla \cdot ([\rho_m + \rho_1] \mathrm{V}_1) = 0. \tag{3.4.6}$$

In addition, assuming the oscillating parts of the variables are very small, then multiplying the density by the velocity leads to a very small value, and therefore can be neglected. Based on that, equation (3.4.6) becomes

$$\frac{\partial \rho_1}{\partial t} + \nabla \cdot (\rho_m \mathrm{V}_1) = 0. \tag{3.4.7}$$

Complex notation allows replacing the temporal part of the variables by $e^{i\omega t}$

$$i\omega\rho_1 + \nabla \cdot (\rho_m \mathrm{V}_1) = 0. \tag{3.4.8}$$

One knows that the velocity vector consists of three components; in the *x*, *y* and *z* direction, but the velocity in the *x* direction is greater than the velocities in *y* and *z* directions, which can be neglected so equation (3.4.8) will be as follows

$$i\omega\rho_1 + \frac{d}{dx}(\rho_m u_1) = 0. \tag{3.4.9}$$

By using the ideal gas law, the density can be written as a function of the pressure and the temperature

$$(p_m + p_1) = R(\rho_m + \rho_1)(T_m + T_1). \tag{3.4.10}$$

Expanding this equation and taking the second order term out ($\rho_1 T_1$) to get

$$(p_m + p_1) = R(\rho_m T_m + \rho_1 T_m + \rho_m T_1), \tag{3.4.11}$$

$$\rho_1 = \frac{p_1}{T_m R} - \frac{T_1 \rho_m}{T_m}. \tag{3.4.12}$$

Equation (3.4.12) can be substituted back into equation (3.4.9) to get

$$i\omega\left[\frac{p_1}{T_m R} - \frac{T_1 \rho_m}{T_m}\right] + \frac{d}{dx}\left[\rho_m u_1\right] = 0. \tag{3.4.13}$$

By applying the first law of thermodynamics to a control volume and rewriting it in temporal form

$$\frac{dQ}{dt} + \frac{dW}{dt} = \frac{dE}{dt}, \tag{3.4.14}$$

with;

$$\begin{aligned} &\frac{dQ}{dt} = kA\frac{dT}{dx}, \\ &\delta W = -p\delta V, \\ &E = \rho c_p T, \end{aligned} \tag{3.4.15}$$

where *Q*, *W*, and *E* are heat flux, work done on the control volume, and internal energy respectively.

Combining equation (3.4.15) and (3.4.14) gives

$$\rho c_p \frac{\partial T}{\partial t} + \rho c_p V \cdot \nabla T = \nabla \cdot k \nabla T + \frac{\partial p}{\partial t}. \tag{3.4.16}$$

Based on the last assumptions, the velocity in the *x* direction is much greater than the velocities in *y* and *z* direction

$$\rho c_p \frac{\partial T}{\partial t} + \rho c_p u_1 \cdot \nabla T = \nabla \cdot k \nabla T + \frac{\partial p}{\partial t}. \tag{3.4.17}$$

Also the temperature gradient in *x* direction is smaller than the temperature gradient in *y* and *z* directions

$$\rho c_p \frac{\partial T}{\partial t} + \rho c_p u_1 \frac{\partial T}{\partial x} = k \left[\frac{\partial^2 T}{\partial y^2} + \frac{\partial^2 T}{\partial z^2} \right] + \frac{\partial p}{\partial t}. \tag{3.4.18}$$

By replacing the temporal derivatives with $i\omega$ and rearranging we will get

$$\rho_m c_p \left[i\omega T_1 + u_1 \frac{dT_m}{dx} \right] - i\omega p_1 = k \left[\frac{\partial^2 T}{\partial y^2} + \frac{\partial^2 T}{\partial z^2} \right]. \tag{3.4.19}$$

When $dT_m / dx \neq 0$. Regarding this as a differential equation for the *y* and *z* dependences of T_1, and following the same procedure as before but now including *y* and *z* dependences of u_1 and allowing for arbitrary channel cross section, gives [74]

$$T_1 = \frac{1}{\rho_m c_p}\left(1-h_k\right) p_1 - \frac{1}{i\omega A}\frac{dT_m}{dx}\frac{\left(1-h_k\right)-\sigma\left(1-h_v\right)}{\left(1-f_v\right)\left(1-\sigma\right)}U_1, \tag{3.4.20}$$

where,

h_v function dependant on geometry and δ_v (thermoviscous function)

h_k function dependant on geometry and δ_k (thermoviscous function)

k subscript refers to the thermal penetration depth

v subscript refers to the viscous penetration depth

f_k spatial average of h_k

f_v spatial average of h_v

σ Prandtl number.

This is most easily verified by direct substitution into equation (3.4.19), using the general property that h_v and h_k satisfy $\partial^2 h/\partial y^2 + \partial^2 h/\partial z^2 = 2ih/\delta^2$.

The spatial average of equation (3.4.20) can be found by replacing all the *h* functions with their spatially averaged counterparts as follows

$$T_1 = \frac{1}{\rho_m c_p}\left(1-f_k\right) p_1 - \frac{1}{i\omega A}\frac{dT_m}{dx}\frac{\left(1-f_k\right)-\sigma\left(1-f_v\right)}{\left(1-f_v\right)\left(1-\sigma\right)}U_1. \tag{3.4.21}$$

By putting the constant pressure specific heat in terms of the ratio of specific heat gives

$$T_1 = \frac{\gamma-1}{\rho_m R\gamma}\left(1-f_k\right) p_1 - \frac{1}{i\omega A}\frac{dT_m}{dx}\frac{\left(1-f_k\right)-\sigma\left(1-f_v\right)}{\left(1-f_v\right)\left(1-\sigma\right)}U_1. \tag{3.4.22}$$

Equation (3.4.22) combined with equation (3.4.13) with algebraic arrangements results in the continuity equation of thermoacoustics phenomenon as follows

$$dU_1 = -\frac{i\omega A dx}{\lambda p_m}\left[1+(\gamma-1) f_k\right] p_1 + \frac{(f_k - f_v)}{(1-f_v)(1-\sigma)}\frac{dT_m}{T_m}U_1. \tag{3.4.23}$$

Equation (3.4.23) is the thermoacoustic version of continuity equation. This equation is a first order differential equation which describes how the volumetric flow changes as a function of pressure, volumetric flow, and the mean temperature gradient. This dependence on the mean temperature gradient is what causes the thermoacoustic effect to take place.

3.4.2 Thermoacoustics momentum equation

Starting from Navier Stokes equation

$$\rho\left[\frac{\partial V}{\partial t} + (V\cdot\nabla)V\right] = -\nabla p + \mu\nabla^2 V. \tag{3.4.24}$$

Based on the previous assumptions:

1. The second term on the left-hand side of equation (3.4.24) can be neglected as it is made up of the second order terms.
2. Many of the velocity components are removed since their values are negligible. Thereby, the final version of the equation (3.4.24) will be as follows

$$i\omega\rho_m u_1 = -\frac{dp_1}{dx} + \mu\left[\frac{\partial^2 u_1}{\partial y^2} + \frac{\partial^2 u_1}{\partial z^2}\right]. \tag{3.4.25}$$

Equation (3.4.25) is a differential equation for $u_1(y,z)$, with boundary condition $u_1 = 0$ at the solid surface.

By solving this second order differential equation for u_1

$$u_1 = \frac{i}{\omega \rho_m}\left[1 - h_v\right]\frac{dp_1}{dx}, \tag{3.4.26}$$

integration of this equation over the cross sectional area of the channel gives

$$dp_1 = -\frac{i\omega\rho_m dx / A}{1 - f_v}U_1. \tag{3.4.27}$$

Equation (3.4.27) is the thermoacoustic version of momentum equation. This equation is a first order differential equation describing how the pressure changes as a function of the volumetric flow and geometrical properties of the channel.

3.4.3 Thermoacoustics energy flow equation

Based on the first law of thermodynamics, the energy contained within a control volume of fluid is the internal plus kinetic energy

$$\left[\rho\varepsilon + \frac{1}{2}\rho|V|^2\right]dxdydz, \tag{3.4.28}$$

where, $\mathcal{E}$ is the internal energy. According to the first law of thermodynamics, the change in energy must be equal to the heat flow into the system plus the work done on the system and the energy gained or lost by mass flow into and out of the control volume. The energy equation for a fluid control volume is then described by

$$\frac{\partial}{\partial t}\left[\rho\varepsilon+\frac{1}{2}\rho|V|^2\right]=-\nabla\cdot\left[-k\nabla T+V\cdot\sigma'+\left(\rho h+\frac{1}{2}\rho|V|^2\right)V\right]. \tag{3.4.29}$$

The term on the left hand side in equation (3.4.29) is the time derivative of equation (3.4.28). There are three terms on the right hand side in equation (3.4.29). They are heat conduction into the control volume, work done on the control volume (where the stress tensor for the fluid is σ'), and the energy flow due to mass flux into the control volume. From the equation (3.4.29), the total power flux *H* is as follows

$$\dot{H}=-k\nabla T+V\cdot\sigma'+\left(\rho h+\frac{1}{2}\rho|V|^2\right)V. \tag{3.4.30}$$

The kinetic energy term on the right hand side of the equation (3.4.30) will be ignored because it is third order, and the equation will be as follows

$$\dot{H}=-k\nabla T+V\cdot\sigma'+(\rho h)V, \tag{3.4.31}$$

the *V* vector represents just the velocity in the *x* direction; the velocities in *y* and *z* direction are very small.

The velocity in the *x* direction is once again assumed to be much greater than the velocities in the transverse directions, so the velocity vector is simplified for the enthalpy flow term. Also, due to the sinusoidal nature of the time dependence of the variables, an average over one period is assumed, and denoted by the over bar in the equations below. The second order power flow across the cross sectional area of a duct can then be written as follows

$$\dot{H}_2 = \int \left[-k \frac{\overline{\nabla T}}{dx} + \overline{V \cdot \sigma'} + \overline{\rho h u} \right] dA. \tag{3.4.32}$$

Rott's acoustic approximation can now be used to simplify this equation. Because all the terms inside the integral are time averaged, the first order parts of all the variables are zero. Keeping this in mind and examining the first term which is due to thermal conduction, it is assumed that the second order part is much less than the first order part, allowing the following simplification

$$k \left[\frac{\overline{\nabla T}}{dx} \right] dA \approx \left(Ak + A_{solid} k_{solid} \right) \frac{dT_m}{dx}. \tag{3.4.33}$$

The second term in equation (3.4.32) is due to the stress tensor, and it is assumed that this term is of the same order of magnitude as the viscous penetration depth, while the last term in equation (3.4.32) is on the order of the acoustic wavelength. The third term is evaluated as follows [74, 81]

$$\int \left(\overline{\rho u h} \right)_2 dA = \int \left(\overline{\rho u} \right)_2 h_m dA + \int \overline{\left(\rho u \right)_1 h_1} dA. \tag{3.4.34}$$

For a standing wave refrigerator or engine

$$\int \left(\overline{\rho u} \right)_2 dA = \dot{m} = 0, \tag{3.4.35}$$

this means that equation (3.4.34) is simplified as follows

$$\int \left(\overline{\rho u h} \right)_2 dA = \frac{1}{2} \rho_m \int \mathrm{Re}\left[h_1 \tilde{u}_1 \right] dA. \tag{3.4.36}$$

Combining the above results means that

$$\dot{H}_2(x) = \frac{1}{2}\rho_m \int \mathrm{Re}\left[h_1 \tilde{u}_1\right] dA - \left(Ak + A_{solid}k_{solid}\right)\frac{dT_m}{dx}, \tag{3.4.37}$$

the enthalpy as a function of temperature and pressure is as follows

$$dh = c_p dT + \frac{\left(1 - T\beta\right)dp}{\rho}. \tag{3.4.38}$$

At first order, this becomes

$$h_1 = c_p T_1, \tag{3.4.39}$$

This result can be plugged back into (3.4.37) to obtain the following

$$\dot{H}_2(x) = \frac{1}{2}\rho_m c_p \int \mathrm{Re}\left[T_1 \tilde{u}_1\right] dA - \left(Ak + A_{solid}k_{solid}\right)\frac{dT_m}{dx}. \tag{3.4.40}$$

Expressions for *T1* and *u1* were found in equations (3.4.22) and (3.4.26) respectively. If these results are plugged into (3.4.40), and the integration is carried out results in the following equation

$$\begin{aligned}\dot{H}_2 = {} & \frac{1}{2}\mathrm{Re}\left[p_1 \tilde{U}_1 \left\{ 1 - \frac{f_k - \tilde{f}_v}{\left(1+\sigma\right)\left(1 - \tilde{f}_v\right)} \right\} \right] + \\ & \frac{\rho_m c_p \left|U_1\right|^2}{2A\omega\left(1-\sigma^2\right)\left|1 - f_v\right|^2} \mathrm{Im}\left(f_k + \sigma \tilde{f}_v \right)\frac{dT_m}{dx} - \left(Ak + A_{solid}k_{solid}\right)\frac{dT_m}{dx}.\end{aligned} \tag{3.4.41}$$

Equation (3.4.41) describes the energy flow through standing wave thermoacoustic devices only. The energy equation used in unison with the thermoacoustic continuity and momentum equations is the basis for most, if not all, models of thermoacoustic devices [81].

3.5 Regenerators

3.5.1 Regular geometries of regenerators

According to the linear thermoacoustic theory [34] and [74], the time-averaged acoustic power in a length of channel can be written in complex notation form as

$$\frac{d\dot{E}_2}{dx} = \frac{1}{2}\mathrm{Re}\left[\tilde{U}_1 \frac{dp_1}{dx} + \tilde{p}_1 \frac{dU_1}{dx}\right], \tag{3.5.1}$$

where, U_1 is the complex volumetric velocity and p_1 is the pressure. "~" indicates a complex conjugate. Subscript 2 indicates that it is a second order quantity. $\mathrm{Re}[\bullet]$ denotes the real part of a complex number.

For regular geometries: Parallel-plates, pin-array and circular-pores, equation (3.5.1) can be written as

$$\frac{d\dot{E}_2}{dx} = -\frac{r_v}{2}|U_1|^2 - \frac{1}{2r_k}|p_1|^2 + \frac{1}{2}\mathrm{Re}\left[g\tilde{p}_1 U_1\right], \tag{3.5.2}$$

where r_v is the viscous resistance per unit length of the channel, $1/r_k$ is the thermal-relaxation conductance per unit length of the channel, and g is the complex gain. They can be written as

$$r_v = \frac{\omega \rho_m}{A_g} \frac{\mathrm{Im}[-f_v]}{|1-f_v|^2}, \tag{3.5.3}$$

$$\frac{1}{r_k} = \frac{\gamma - 1}{\gamma} \frac{\omega A_g}{p_m} \mathrm{Im}[-f_k], \tag{3.5.4}$$

and

$$g = \frac{(f_k - f_v)}{(1-f_v)(1-\sigma)} \frac{1}{T_m} \frac{dT_m}{dx}, \tag{3.5.5}$$

where, γ, σ, ρ_m, p_m and T_m are the ratio of specific heat capacities, Prandtl number, mean density, mean pressure and mean temperature of the working gas, respectively. A_g is the cross sectional area of gas channels in the regenerator.

f_v and f_k have analytical formulae. For the parallel-plates it can be wrttien as follows

$$f_k = \frac{\tanh[(1+i) y_0 / \delta_k]}{(1+i) y_0 / \delta_k}, \tag{3.5.6}$$

$$f_v = \frac{\tanh[(1+i) y_0 / \delta_v]}{(1+i) y_0 / \delta_v}, \tag{3.5.7}$$

where y_0 is the half of the plate spacing (m), δ_k is the thermal penetration depth (m), δ_v is the viscous penetration depth (m).

Also, for the circular-pores f_v and f_k can be wrttien using complex Bessel functions as follows

$$f_k = \frac{2J_1\left[(i-1)r_0/\delta_k\right]}{(i-1)(r_0/\delta_k)J_0\left[(i-1)r_0/\delta_k\right]}, \tag{3.5.8}$$

$$f_v = \frac{2J_1\left[(i-1)r_0/\delta_v\right]}{(i-1)(r_0/\delta_v)J_0\left[(i-1)r_0/\delta_v\right]}, \tag{3.5.9}$$

the effective radius to be defined $r_0 = 2A/\Pi$ and J is the Bessel function.

It should be mentioned here that the first term on the right hand side of equation (3.5.2) demonstrates viscous dissipation, and the second term represents thermal-relaxation dissipation. Both of these consume acoustic power, leading to high losses. The third term denotes the acoustic power produced from heat energy.

3.5.2 Stacked-screen regenerators

A set of thermoacoustic equations for a stacked-screen (wire-meshes) regenerator with the method of simple harmonic analysis were proposed by Swift and Ward [79]. Thus, the analysis of the acoustic power dissipation and production in the stacked-screen regenerator can be further developed. Substituting their continuity and momentum equations into equation (3.5.2) leads

$$\frac{d\dot{E}_2}{dx} = \frac{1}{2}A_g \,\mathrm{Re}\left\{ i\omega\left[\beta_m \frac{T_m\beta_m}{\rho_m c_{p,m}} \frac{\varepsilon_s + \left(g_c + e^{2i\theta_p} g_v\right)\varepsilon_h}{1+\varepsilon_s + \left(g_c + e^{2i\theta_T} g_v\right)\varepsilon_h} - \frac{\gamma_m}{\rho_m a_m^2}\right]|p_1|^2 \right.$$
$$\left. -i\omega\rho_m |\langle u_1\rangle|^2 - \frac{\mu_m}{r_h^2}\left[\frac{c_1(\phi)}{8} + \frac{c_2(\phi)Re_1}{3\pi}\right]|\langle u_1\rangle|^2 + \beta_m \frac{dT_m}{dx}\left[1 - \frac{\varepsilon_s + (g_c - g_v)\varepsilon_h}{1+\varepsilon_s + \left(g_c + e^{2i\theta_T} g_v\right)\varepsilon_h}\right]\tilde{p}_1\langle u_1\rangle \right\}, \tag{3.5.10}$$

where, $\langle\rangle$ denotes a local spatial average. β_m, γ_m and μ_m are the mean thermal expansion coefficient, mean ratio of specific heats, and mean dynamic viscosity of the gas, respectively. $b(\phi)$, $c_1(\phi)$, $c_2(\phi)$, $g_c(Re_1)$, and $g_\nu(Re_1)$ are factors resulting from the fitting of data of Kays and London [82].

θ_p, θ_T, ε_s and ε_h are defined as

$$\theta_p = phase(\langle u_1 \rangle) - \text{phase}(p_1), \tag{3.5.11}$$

$$\theta_T = phase(\langle u_1 \rangle) - phase(\langle T \rangle_{u,1}), \tag{3.5.12}$$

$$\varepsilon_s = \phi \rho_m c_{p,m} / (1-\phi) \rho_{s,m} c_{s,m}, \tag{3.5.13}$$

$$\varepsilon_h = 8 i r_h^2 / b(\phi) \sigma^{1/3} \delta_k^2, \tag{3.5.14}$$

subscript s means solid.

ε_s is the correction factor for finite solid heat capacity, which gives the ratio of gas heat capacity to solid heat capacity. Typically, regenerators have $\varepsilon_s << 1$.

Reynolds number is a positive real number, and it can be written as

$$Re_1 = 4 |\langle u_1 \rangle| r_h \rho_m / \mu_m . \tag{3.5.15}$$

3.6 Heat exchangers

In DeltaEC software, heat exchangers are used to inject or remove heat. DeltaEC heat exchangers have surface area, so they experience both viscous and thermal dissipation of acoustic power.

In heat exchangers, wave propagation is calculated using the below equations which come from simplification of equations (3.4.23) and (3.4.27)

$$\frac{dp_1}{dx} = -\frac{i\omega\rho_m}{(1-f_v)A_{gas}}U_1, \tag{3.6.1}$$

$$\frac{dU_1}{dx} = -\frac{i\omega A_{gas}}{\rho_m a^2}\left(1+\frac{(\gamma-1)f_k}{1+\varepsilon_s}\right)p_1. \tag{3.6.2}$$

The following equations can be used to calculate f_k, f_v and ε_s for a heat exchanger using parallel plate geometry

$$f_k = \frac{\tanh\left[(1+i)y_0/\delta_k\right]}{(1+i)y_0/\delta_k}, \tag{3.6.3}$$

$$f_v = \frac{\tanh\left[(1+i)y_0/\delta_v\right]}{(1+i)y_0/\delta_v}, \tag{3.6.4}$$

$$\varepsilon_s = \left(\frac{k\rho_m c_p}{k_s\rho_s c_s}\right)^{1/2}. \tag{3.6.5}$$

Similarly, for heat exchangers with cylindrical geometry and if $r_0/\delta_k < 25$, f_k and f_v can be calculated using complex Bessel functions.

$$f_k = \frac{2J_1\left[(i-1)r_0/\delta_k\right]}{(i-1)(r_0/\delta_k)J_0\left[(i-1)r_0/\delta_k\right]}, \tag{3.6.6}$$

$$f_v = \frac{2J_1\left[(i-1)r_0/\delta_v\right]}{(i-1)(r_0/\delta_v)J_0\left[(i-1)r_0/\delta_v\right]}. \tag{3.6.7}$$

If r_0/δ_k > 30, the boundary-layer approximation is used

$$f_k = (1-i)\delta_k / r_0, \tag{3.6.8}$$

$$f_v = (1-i)\delta_v / r_0. \tag{3.6.9}$$

For intermediate values, linear interpolation is used to make a smooth match between the two regimes. In both cases, ε_s is calculated using equation (3.6.5).

3.7 Thermal buffer tubes

The thermal buffer tube provides a thermal buffer between the hot heat exchanger and room temperature, thus limiting heat losses. Usually, it is located behind the HHX to insulate it from the surroundings. There is a trade-off between the length of the TBT and heat losses to the surroundings. If it is short, the pipe cannot be insulated to prevent heat losses. In contrast, if the TBT is too long the viscous losses will be high, leading to low system performance. The TBT length should be longer than the peak-to-peak gas displacement amplitude $2|\zeta|$ [74].

In thermal buffer tubes, wave propagation is calculated using the below equations which come from simplification of equations (3.4.23) and (3.4.27)

$$\frac{dp_1}{dx} = -\frac{i\omega\rho_m}{(1-f_v)A_{gas}}U_1, \tag{3.7.1}$$

$$\frac{dU_1}{dx} = -\frac{i\omega A_{gas}}{\rho_m a^2}\left(1+\frac{(\gamma-1)f_k}{1+\varepsilon_s}\right)p_1 + \frac{\beta(f_k-f_v)}{(1-f_v)(1-\sigma)(1+\varepsilon_s)}\frac{dT_m}{dx}U_1. \tag{3.7.2}$$

Subject to the condition that the energy flow $\dot{H}_{2,k}$ is independent of *x*, which imposes the following condition on $T_m(x)$

$$\frac{dTm}{dx} = \frac{\dot{H}_{2,k} - \frac{1}{2}\mathrm{Re}\left[p_1\tilde{U}_1\left(1-\frac{T_m\beta(f_k-\tilde{f}_v)}{(1+\varepsilon_s)(1+\sigma)(1-\tilde{f}_v)}\right)\right]}{\frac{\rho_m c_p|U_1|^2}{2\omega A_{gas}(1-\sigma)|1-f_v|^2}\mathrm{Im}\left[\tilde{f}_v+\frac{(f_k-\tilde{f}_v)(1+\varepsilon_s f_v/f_k)}{(1+\varepsilon_s)(1+\sigma)}\right]-A_{gas}k-A_{solid}k_s}. \tag{3.7.3}$$

For the thermal buffer tube

$$f_k = (1-i)\Pi\delta_k/2A, \tag{3.7.4}$$

$$f_v = (1-i)\Pi\delta_v/2A, \tag{3.7.5}$$

$$\varepsilon_s = \left(\frac{k\rho_m c_p}{k_s\rho_s c_s}\right)^{1/2}\frac{1}{\tanh\left[(1+i)\ell/\delta_s\right]}, \tag{3.7.6}$$

where ℓ =wall cross-sectional area/ perimeter.

3.8 Feedback pipes

A FBP is necessary to contain the working fluid of the thermoacoustic system, sustain the transmission of the acoustic power through the system and close the looped waveguide. Based on the FBP length, the operating system frequency can be calculated.

In FBPs with no superimposed steady flow, p_1 and U_1 evolve according to

$$\frac{dp_1}{dx} = -\frac{i\omega\rho_m}{(1-f_v)A}U_1, \tag{3.8.1}$$

$$\frac{dU_1}{dx} = -\frac{i\omega A_{gas}}{\rho_m a^2}\left(1+\frac{(\gamma-1)}{1+\varepsilon_s}f_k\right)p_1, \tag{3.8.2}$$

which is equivalent to

$$\left(1+\frac{\gamma-1}{1+\varepsilon_s}f_k\right)p_1 + \frac{a^2}{\omega^2}(1-f_v)\frac{d^2p_1}{dx^2} = 0. \tag{3.8.3}$$

In narrow FBPs, for $r_0/\delta_k < 25$, f_k and f_v are calculated using complex Bessel functions [1], as expressed in equations (3.6.6) and (3.6.7).

If $r_0/\delta_k > 30$, the boundary-layer approximation is used

$$f_k = (1-i)\Pi\delta_k/2A, \tag{3.8.4}$$

$$f_v = (1-i)\Pi\delta_v / 2A. \tag{3.8.5}$$

In both cases, ε_s is calculated using equation (3.6.5).

3.9 DeltaEC software

DeltaEC "Design Environment for Low-amplitude ThermoAcoustic Energy Conversion" is a computer program that can calculate details of how thermoacoustic systems perform. The program was originally written by Dr Bill Ward and Dr Gregory Swift of Los Alamos National Laboratories.

DeltaEC numerically integrates the continuity, momentum, and energy equations for thermoacoustic devices. It is based on the linear thermoacoustic theory discussed in earlier sections. It uses a simplified one-dimensional approximation and assumes that the amplitude of oscillation is low and has sinusoidal time dependence. Models include a number of segments, which are combined together by the user. These segments reflect the physical properties of the thermoacoustic devices and assume the problem is one dimensional throughout the segment. The solver assumes that all oscillating variables have a time dependence of Re ($e^{i\omega t}$). This assumption on the time dependence transforms the temporal part of the governing equations from differential equations in time to algebraic equations of time. This leaves the governing equations as spatial differential equations, which are much easier to solve than the starting partial differential equations [81].

DeltaEC numerically integrates the one-dimensional wave equation to get a converged solution by employing an iterative shooting process. The shooting method starts with a guess value of the model parameters and integrates through the model. After each integration round DeltaEC compares the values of targets (outputs)

to the guess (inputs). If the targets do not match, the guess is adjusted and the integration is repeated. In other words, if the difference between guess and target $r(g)-t\approx 0$ is zero, leading to a converged solution, where *g* is the guess, *t* is the target and *r* is the calculated results. If any of the guesses are too far off from the ultimate solution, then the procedure will not converge on the targets [83].

Essentially, the users can build a thermoacoustic system by selecting required acoustic elements as needed. DeltaEC software gives a high flexibility to choose various thermoacoustic system's segments, such as compliance volumes, inertance ducts, heat exchangers and regenerators, etc. After having a complete system, DeltaEC starts to solve the appropriate 1-D wave equation through each of these segments. The program does this for the whole system of segments, by ensuring that the pressure and volumetric flow rates are matched at the boundaries of each segment [18]

In general, DeltaEC is a computer program that can calculate details of how thermoacoustic systems perform. It is based on the linear theory and assumes that the amplitude of oscillation is low and has sinusoidal time dependence. It should to be mentioned here that the linear theory means all variables oscillate at angular velocity *w*. Temporal parts are replaced by $e^{i\omega t}$ by using complex notation methods, where $e^{i\omega t}$ is known as the oscillatory part. At the beginning of the numerical solution, the shooting method starts with a guess value of the model parameters and integrates through the model. After each integration round DeltaEC compares the values of targets (outputs) to the guess (inputs). If the targets do not match, the guess is adjusted and the integration is repeated.

Chapter 4 Analysis of a looped-tube travelling-wave thermoacoustic engine with a by-pass configuration

4.1 Introduction

A new configuration of thermoacoustic system (a looped-tube with a by-pass pipe) was recently proposed for low temperature travelling wave thermoacoustic engines, and a prototype using atmospheric air, as the working gas achieved a minimum onset temperature difference of 65°C [39]. However, no further research has been reported about this new configuration to reveal its advantages and disadvantages. This chapter aims to analyse this type of engine through comprehensive numerical research. DeltaEC software has been employed to simulate and analyse this configuration. An engine of this type having dimensions similar to the reported prototype was firstly modelled. The calculated results were then qualitatively compared with the reported experimental data. The verified model was then used to further understand the working principle of this type of thermoacoustic engine.

4.2 Modelling and simulations of a by-pass engine

A travelling wave thermoacoustic engine with the by-pass configuration is schematically shown in Figure 4.1. It is denoted as a by-pass engine hereafter, and is modelled using DeltaEC software (Design Environment for Low-amplitude ThermoAcoustic Energy Conversion) [14, 74]. The purpose of this modelling is to qualitatively capture and demonstrate the working principle of this type of engine [39], rather than to accurately reproduce the prototype.

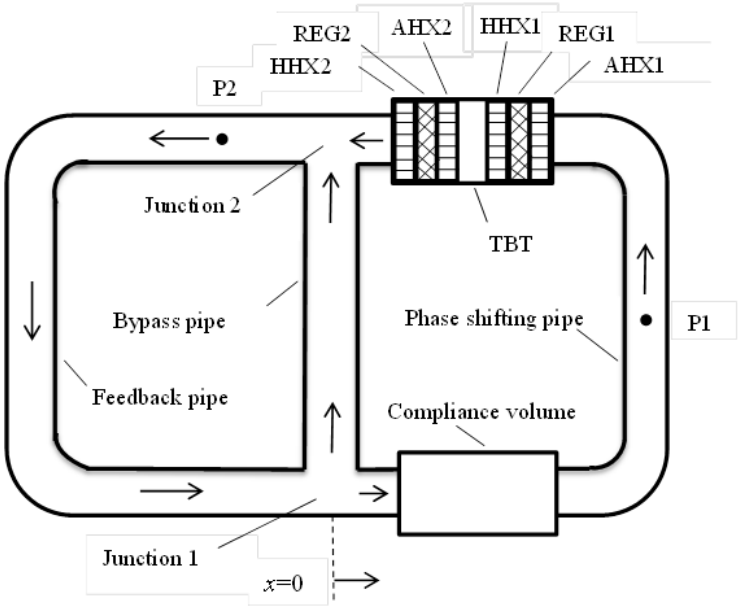

Figure 4.1: Schematic diagram of a travelling wave thermoacoustic engine with a by-pass configuration [39].

The arrows indicate the direction of the acoustic power flow according to the simulations presented later in this paper. HHX: hot heat exchanger, REG: regenerator, AHX: ambient heat exchanger, TBT: thermal buffer tube.

As shown in Figure 4.1, this engine has two stages, each stage having a hot heat exchanger (HHX), a regenerator (REG), and an ambient heat exchanger (AHX). The system also has a feedback pipe (FBP), a by-pass pipe, a compliance volume, and a "phase shifting pipe". It should be noted that the "phase shifting pipe" was denoted as an "inertance tube" in reference [39]. As explained later in this chapter, the inertance tube, widely used in pulse-tube coolers, usually has a very small cross-sectional area and long length to provide a significant phase shifting effect [66] Strictly speaking, the pipe that connects the compliance volume and the engine core in the reference [39] does not have the characteristics of an "inertance pipe", and therefore is denoted as a "phase shifting pipe" instead in this research.

It should be noted that, like other travelling wave thermoacoustic engines, there are torus paths within this by-pass configuration. As a result, Gedeon streaming, a second-order time-averaged mass flow, will be induced along the loop. In such a system, this

type of mass flow can take heat from the hot heat exchanger of the engine and dump it at the ambient heat exchanger, causing heat loss and reducing the thermal efficiency [10]. This is a well understood effect, which can be supressed using a jet-pump [10] or elastic membrane [74]. In this chapter, it is assumed that the Gedeon streaming has been supressed in order to simplify the analysis.

From reference [39], some dimensions and operating parameters of the prototype were reported in the paper and the associated conference presentation. The working gas was air at atmospheric pressure. The operating frequency was 119 Hz. The heat source temperature was 148 °C, and the heat sink temperature was 28 °C. The heat exchangers of the prototype were made by soldering several lays of copper mesh screen to copper water tubes. The regenerators were made of stainless steel mesh discs.

These reported dimensions and operating parameters are used as a basic framework to establish the present DeltaEC model. Screen-type heat exchangers (i.e., SX) and regenerators (i.e., STKSCREEN) have been used in the model. Some unreported parameters are then carefully tuned to force the model to closely approach the reported experimental data, including the pressure amplitude at location P2, and the acoustic power measured at locations P1 and P2 (see Figure 4.1). The final dimensions used in this model are summarised in Table 4.1.

Table 4.1: The dimensions used in the present model of a by-pass engine.

Part	Area (m^2)	Length(mm)	r_h (μm)	Porosity
AHX1	0.012*	0.56†	40	0.8*
REG1	0.012*	1.58†	150	0.73*
HHX1	0.012*	0.56†	120	0.8*
AHX2	0.012*	0.56†	120	0.8*
REG2	0.012*	1.58†	130	0.73*
HHX2	0.012*	0.56†	120	0.8*
	Diameter (mm)		Length (cm)	
By-pass pipe	75*		100	
Feedback pipe(FBP)	75*		175	
Phase shifting pipe	50*		120	
Compliance volume	110*		12.7	
Thermal buffer tube	100 mm× 120 mm*		3*	

***These dimensions were the same as those reported in the paper (*) and the associated conference presentation (†) [39].**

Based on the obtained model, the distribution of pressure amplitude, the acoustic power flow along the system, normalised specific acoustic impedance, and phase angle between the pressure and velocity oscillations are then calculated and presented in Figure 4.2-Figure 4.5. The coordinate *x* starts from (and also ends at) Junction 1 as shown in Figure 4.1.

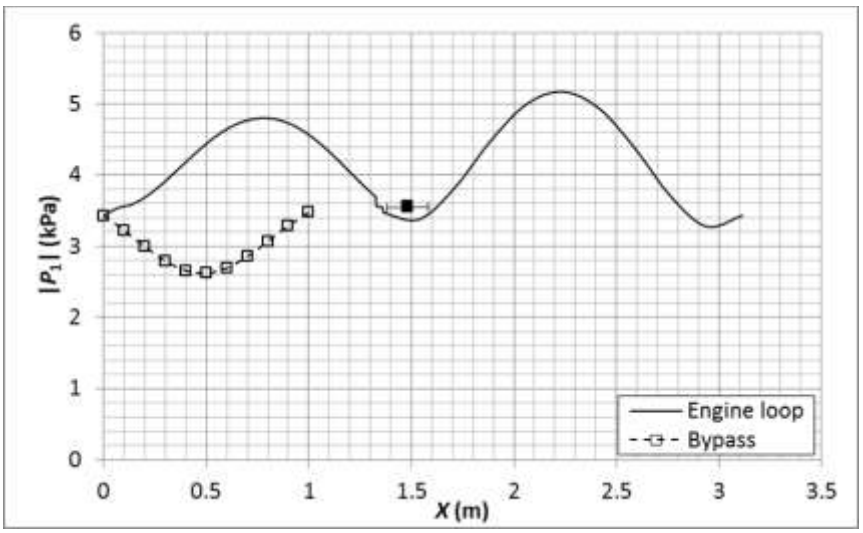

Figure 4.2: Distribution of the amplitude of acoustic pressure along the engine.

The solid squares represent the measured data in the paper [39].

As reported in reference [39], the pressure amplitude at location P2 in the resonator (see Figure 4.1) was measured as 3430 Pa. According to the estimation, the location P2 is about 15-25 cm away from Junction 2. For the convenience of comparison, the pressure amplitude is set to 3430 Pa at the location P2 in the present model. Figure 4.2 shows the calculated pressure amplitude along the main loop (solid line) and by-pass pipe (dashed line with symbols). The measured pressure amplitude at location P2 (see Figure 4.1) in reference [39] is also represented by a solid square in Figure 4.2. The horizontal error bar shows the uncertainty of the location of P2 due to the estimation.

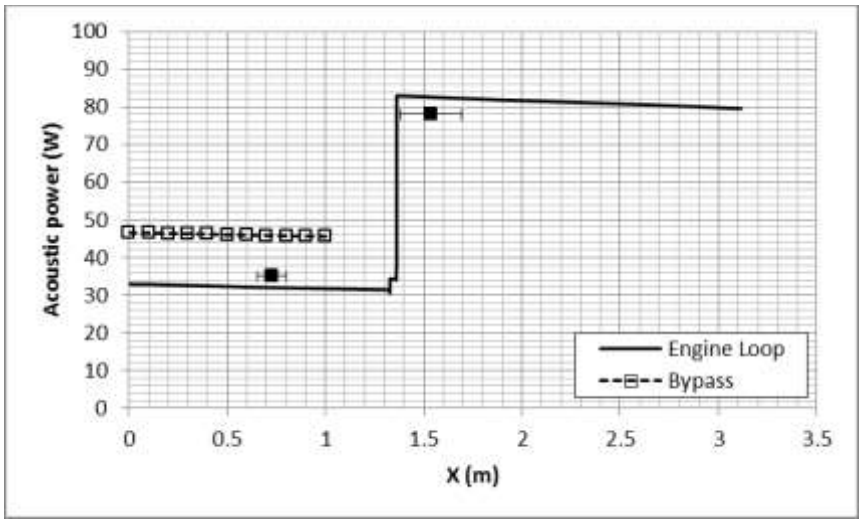

Figure 4.3: Distribution of acoustic power along the engine.

The solid squares represent the measured data in the paper [39].

Figure 4.3 shows the acoustic power flow along the system according to the present model. The simulation starts from the Junction 1 where x=0. The total acoustic power is around 80 W, and it splits into two parts. One part (about 47 W) flows into the by-pass pipe, and the other part (about 33 W) flows into the compliance volume. The compliance volume and phase shifting pipe dissipate about 2 W, and the remaining 31 W power flows into the first engine stage. The two engine stages slightly amplify the acoustic power to 37 W, which then joins with the acoustic power (45 W) exiting from the by-pass pipe. The total power of about 82 W flows into the FBP. About 2 W of acoustic power has been dissipated in the FBP, and the remaining 80 W flows back to starting point (x=0).

In Figure 4.2 and Figure 4.3, only two points have been selected to carry out the validation of the current simulation model. This is in line with the procedures used by Kees [39] who used only these two locations to measure the pressure amplitude and acoustic power.

In reference [39] acoustic power was measured at two locations, P1 and P2, as schematically shown in Figure 4.1. Location P1 lies in the centre of the phase shifting pipe, and location P2 is located about 15-25 cm away from Junction 2. The measured

acoustic power was about 35 W at location P1 and about 78 W at location P2. As shown in Figure 4.3, in the present model, the calculated acoustic power is 32 W and 79 W at locations P1 and P2 respectively, showing a reasonably good agreement.

As reported in reference [39], the design principle of the prototype was so that the specific acoustic impedance at the end of the FBP (x=0 or 3.1 m) should be tuned to the characteristic impedance $\rho_m a$ for air at atmospheric pressure, so that the acoustic reflection within the FBP can be minimised. As such, the acoustic power can be transmitted through the FBP with the least losses [39]. Here, the specific acoustic impedance is defined as the ratio of acoustic pressure $p_1$over acoustic velocity u_1, $z=p_1/u_1$ [74].

To check this principle in the present model, normalised specific acoustic impedance $|z|/\rho_m a$ has been calculated and presented in Figure 4.4. It has been found that $|z|/\rho_m a$ at the end of the FBP (x=3.1 m) is about 0.7. The value of $|z|/\rho_m a$ increases along the compliance volume from 2.45 to 4, and then sharply drops to 0.7 at the start of the phase shifting pipe, due to a sudden change of the cross sectional area, which is in the range 4.6-5.4 around the two regenerators of the prototype (see Figure 4.4). According to reference [39], it was estimated to be in the range of 4.1-6.1 around the two regenerators, but no measurement was reported. Furthermore, $|z|/\rho_m a$ is in the range 0.6-1.4 within the FBP, which is very close to the ideal value of 1 as proposed in the reference [39]. As expected, $|z|/\rho_m a$ is close to 1 throughout the by-pass pipe.

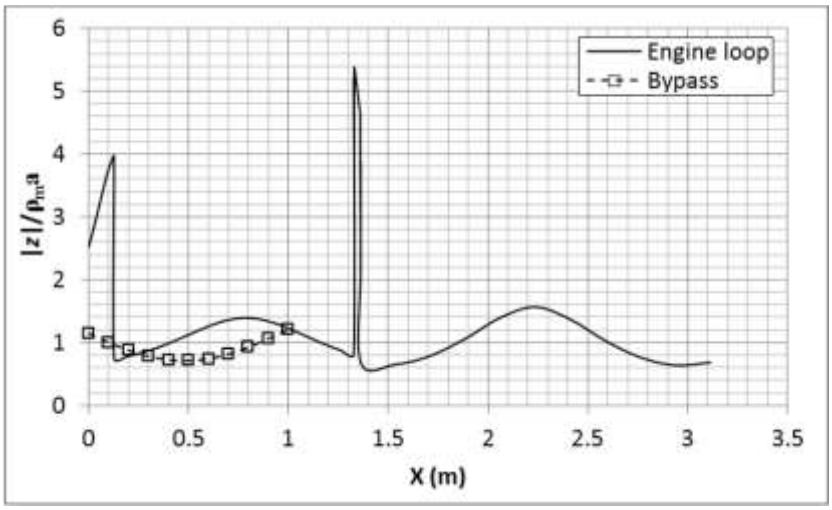

Figure 4.4: Distribution of the normalized specific acoustic impedance along the engine.

To further check the working principle of this by-pass engine, the phase difference between the pressure and velocity oscillations has been calculated and shown in Figure 4.5. The compliance volume section shifts the phase significantly from -56° to about -8°. However, the phase shifting pipe (the so-called "inertance tube" in reference [39]) works like a section of FBP. The phase shifting effect is insignificant. This is not a surprise, because its diameter is 50 mm, which is comparable to the diameter of the FBP (i.e., 75 mm). For this reason, it does not have the characteristics of a typical inertance tube, and therefore it is denoted as phase shifting pipe in this study.

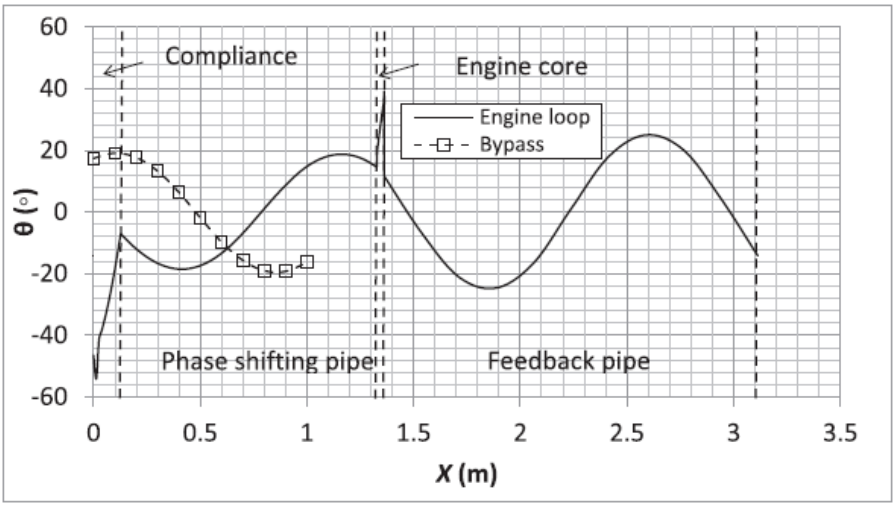

Figure 4.5: Phase angle θ between pressure and velocity oscillations along the engine.

Since the regenerator and the heat exchangers have a high porosity, and a much larger cross-sectional area than the phase shifting pipe, their large volumes introduce a strong compliance effect. As a result, the phase angle has been sharply shifted from 18° to 39° within the engine core section, as shown in Figure 4.5. This is similar to a typical looped-tube travelling wave thermoacoustic engine [12]. The phase angle is then shifted back to around 12° where the by-pass pipe re-joins with the engine branch at Junction 2. Thereafter, the phase angle changes gradually along the FBP as expected.

4.3 Discussion the by-pass configuration

According to Figure 4.3, the directions of the acoustic power flow are then schematically shown in Figure 4.1. Air is the working gas and the speed of sound is around 343 m/s at room temperature. As the operating frequency is 119 Hz, the wavelength is 288 cm. According to Table 1, the lengths of by-pass pipe and FBP are 100 and 175 cm, respectively. Hence the total length of the loop formed by these two components is about 275 cm, which is very close to the sound wavelength under these conditions. Furthermore, according to Figure 4.5, both the by-pass (dashed line with symbols) and the FBP have a phase angle in the range $-22° < \Theta < 22°$, and therefore a near travelling wave field has been achieved in these two components. From the acoustic viewpoint, these two components seem to form a near-travelling wave acoustic resonator for the engine.

Following the above analysis, the engine branch (including compliance, the phase shifting pipe, and the engine core) extracts a part (i.e., <50%) of the acoustic work from the resonator, slightly amplifies it within the engine core, and then injects it back to the resonator. The compliance volume and the phase shifting pipe both provide the required phase shifting for the engine core to operate in a right phase condition. As the travelling wave resonator has low losses, it requires little acoustic power to sustain acoustic resonance, leading to low onset temperature difference.

The short regenerator length (<2 mm) is another special design of the prototype. According to the linear thermoacoustic theory [14, 74, 79], the time-averaged acoustic power $d\dot{E}_2$ produced in length dx of a stack-screen regenerator, can be approximately written as [79, 76]

$$\frac{d\dot{E}_2}{dx}=\frac{1}{2}A_g\,\mathrm{Re}\left\{i\omega\left[\beta_m\frac{T_m\beta_m}{\rho_m c_{p,m}}\frac{\varepsilon_s+\left(g_c+e^{2i\theta_p}g_v\right)\varepsilon_h}{1+\varepsilon_s+\left(g_c+e^{2i\theta_T}g_v\right)\varepsilon_h}-\frac{\gamma_m}{\rho_m a_m^2}\right]|p_1|^2\right.$$
$$\left.-i\omega\rho_m\left|\langle u_1\rangle\right|^2-\frac{\mu_m}{r_h^2}\left[\frac{c_1(\phi)}{8}+\frac{c_2(\phi)Re_1}{3\pi}\right]\left|\langle u_1\rangle\right|^2+\beta_m\frac{dT_m}{dx}\left[1-\frac{\varepsilon_s+\left(g_c-g_v\right)\varepsilon_h}{1+\varepsilon_s+\left(g_c+e^{2i\theta_T}g_v\right)\varepsilon_h}\right]\tilde{p}_1\langle u_1\rangle\right\} \tag{4.1}$$

In equation (4.1), A_g is the cross-sectional occupied by working gas, Re {} denotes the real part of a complex variable, and ⟨⟩ denotes a local spatial average. β_m, γ_m and μ_m are the mean thermal expansion coefficient, mean ratio of specific heats, and mean dynamic viscosity of the gas, respectively. $b(\phi)$, $c_1(\phi)$, $c_2(\phi)$, $g_c(Re_1)$, and $g_v(Re_1)$ are factors resulting from the fitting of data of Kays and London [82].

θ_p, θ_T ε_s and ε_h are defined as

$$\theta_p=\theta\left(p_1,\langle u_1\rangle\right), \tag{4.2}$$

$$\theta_T=\theta\left(\langle u_1\rangle,\langle T\rangle_{u,1}\right), \tag{4.3}$$

$$\varepsilon_s=\phi\rho_m c_{p,m}/\left(1-\phi\right)\rho_{s,m}c_{s,m}, \tag{4.4}$$

subscript s means solid.

$$\varepsilon_h = 8ir_h^2 / b(\phi)\sigma^{1/3}\delta_k^2. \tag{4.5}$$

Reynolds number is a positive real number and it can be written as [84],

$$Re_1 = 4\left|\langle u_1\rangle\right| r_h\rho_m / \mu_m . \tag{4.6}$$

In the curly brackets at the right hand side of equation (4.1), the first term represents the acoustic power dissipation due to thermal relaxation effects, the second and third terms together represent the acoustic power dissipation due to flow resistance in the regenerator, and the fourth term is the acoustic power generation from thermal energy through the thermoacoustic effect. Integrating the right hand side of equation (4.1) over the length of the regenerator L leads to the total net acoustic power generation by the regenerator as

$$\Delta\dot{E} = \frac{1}{2}\int_0^L A_g \mathrm{Re}\left\{\begin{array}{l} i\omega\left[\beta_m\frac{T_m\beta_m}{\rho_m C_{p,m}}\frac{\varepsilon_s+\left(g_c+e^{2i\theta_p}g_v\right)\varepsilon_h}{1+\varepsilon_s+\left(g_c+e^{2i\theta_p}g_v\right)\varepsilon_h}-\frac{\gamma_m}{\rho_m a_m^2}\right]\left|p_1\right|^2 - i\omega\rho_m\left|\langle u_1\rangle\right|^2 \\ -\frac{\mu_m}{r_h^2}\left[\frac{c_1(\phi)}{8}+\frac{c_2(\phi)R_{e_1}}{3\pi}\right]\left|\langle u_1\rangle\right|^2 \\ +\beta_m\frac{dT_m}{dx}\left[1-\frac{\varepsilon_s+\left(g_c-g_v\right)\varepsilon_h}{1+\varepsilon_s+\left(g_c+e^{2i\theta_T}g_v\right)\varepsilon_h}\right]\tilde{p}_1\langle u_1\rangle \end{array}\right\} dx \tag{4.7}$$

In order to further demonstrate the effect of the length of a regenerator on the power production within it, neglecting the dissipations due to thermal relaxation and viscosity in equation (4.7) leads to

$$\Delta\dot{E} \cong \frac{1}{2} A_g \beta_m \int_0^L \mathrm{R_e} \left\{ \left[1 - \frac{\varepsilon_s + \left(g_c - g_v\right)\varepsilon_h}{1 + \varepsilon_s + \left(g_c + e^{2i\theta_T} g_v\right)\varepsilon_h} \right] \tilde{p}_1 u_1 \frac{dT_m}{dx} \right\} dx \tag{4.8}$$

According to equation (4.8), one can see that acoustic power production from the regenerator strongly depends on the length of the regenerator L, the temperature gradient $\frac{dT_m}{dx}$, and the term $\tilde{p}_1\langle u_1\rangle$ that is related to the acoustic power flowing into the regenerator. Qualitatively speaking, in order to increase the acoustic power production from a regenerator, we should increase the regenerator length, the temperature gradient, or the acoustic power flowing into the cold end of the regenerator. However, these parameters are strongly dependent on one another. For instance, the average temperature gradient along the regenerator depends on the length of the regenerator, and can be defined as:

$$\frac{dT_m}{dx} \approx \frac{T_H - T_L}{L}, \tag{4.9}$$

where T_H and T_L are the temperatures at the hot and cold end of the regenerator, respectively. According to equation (4.9), for a given temperature difference, the temperature gradient decreases as the regenerator length increases. Therefore, in a practical design, a trade-off is needed to obtain an optimal regenerator length when the temperature difference is given. The derivation of these equations has been explained in details in chapter 3.

Looking back to the prototype [39], for the very low temperature heat sources, the temperature differential between the two ends of the regenerator is very small.

Therefore, the regenerator length has to be very short to achieve a sufficient temperature gradient for a positive net power production, according to equation (4.7). The net power generation of one engine stage may be still too low, since the regenerator length is so short. In order to generate enough acoustic power to maintain the acoustic oscillation, the prototype was designed with two engine stages [39].

As analysed above, both the travelling wave resonator and short regenerators are likely to be the factors behind the extremely low onset temperature difference achieved by the by-pass engine prototype. Overall, it is a very successful design strategy to reduce the engine's onset temperature difference. However, as a power generator, two important performance parameters are power density and thermal efficiency. The researcher will continue to analyse whether there are any drawbacks due to this by-pass engine configuration.

Firstly, as shown in Figure 4.3, the net power production by the two engine stages is only 6 Watts, while the acoustic power flow within the resonator is about 80 Watts, leading to a low power density. This problem will get even worse if gas with high speed of sound (e.g., helium) is used as working fluid, because the total length of the loop is around one wave-length.

Secondly, in the prototype [39], the regenerator is around 1.58 mm in length, while the calculated temperature difference between the two ends of the regenerators is over 100°C. As a result, the axial temperature gradient along the regenerator is over 60,000°C/m, which is extremely high. For reference, in Backhaus and Swift's travelling wave Stirling engine, the temperature difference is about 600-700°C and the regenerator length is 8.89 cm [10], so the temperature gradient along the regenerator is in the range 6750-7874°C/m. The temperature gradient along the regenerators of the prototype is 10 times higher than that in Backhaus and Swift's engine. Apparently, such an extremely short regenerator will potentially cause severe heat conduction losses from the hot heat exchanger to the ambient heat exchanger through the regenerator. Such heat loss will increase dramatically if one increases the temperature difference to increase power

production. To reduce such heat conduction loss, the regenerator length has to be increased to ensure the temperature gradient is in a reasonable range.

The heat power input to the prototype, its net acoustic power production, and its thermal efficiency were not reported in reference [39]. It is therefore unknown how efficient the prototype was. This, however, is a very interesting and important question. In the present model, the temperatures of the hot heat exchanger and cold heat exchanger are kept the same as those in the experiments. Under these conditions, the calculated heat input to each hot heat exchanger is around 600 W, and thus the total heat energy input is 1200 W as the system consists of two engine units. As shown in Figure 4.3, the total net acoustic power generation is about 6 W. If one roughly assumes this net power production as the engine's power output, the thermal efficiency of the modelled engine is estimated at around 0.5%.

It should be noted that the researcher has used idealised Screen-type heat exchangers in this model, which are assumed to have perfect heat transfer between the working gas and the metal surface of the heat exchanger. The actual heat exchangers in the prototype were made by soldering a few lays of copper mesh to copper tubes [39]. The heat transfer to the working gas would be much lower than the prediction based on the idealised Screen-type heat exchangers in our simulation. Therefore, the actual efficiency of the prototype, which was not reported, should be higher than our predictions here.

Nevertheless, in order to make this type of engine technically attractive, both its power density and thermal efficiency need to be better than, or at least as good as other travelling wave thermoacoustic engines. A few operations can be performed to achieve this, such as increasing the charging pressure. For instance, Backhaus and Swift's thermoacoustic Stirling engine used helium at 30 bar as working fluid [10]. Luo's thermoacoustic generators used helium at 50 or 60 bar as the working gas [61, 64]. Secondly, the temperature of the heat source can be increased, and the regenerator length needs to be increased accordingly.

Alternatively, if the heat source temperature is low, the number of engine stages can be increased. This, however, will increase the number of heat exchangers, which are expensive and bulky. Hence, increasing the regenerator length and mean pressure seem to be more feasible. It is unclear however whether such modifications would violate the working principle as discussed above. In the next chapter, these problems will be investigated.

4.4 Conclusions

This chapter presents a comprehensive numerical research of a travelling wave thermoacoustic engine with a by-pass configuration. Based on the reported dimensions and operating parameters, an engine of this type was modelled to qualitatively represent this prototype. The working principle was then demonstrated and analysed.

According to the results, this type of engine essentially operates on the same thermodynamic principle as other travelling wave thermoacoustic engines, differing only in the design of the acoustic resonator. The novelty of such a by-pass configuration [39] is that the by-pass and FBPs actually created a pure travelling wave resonator. The engine unit extracts small amount of acoustic work from the resonator, and amplifies and sends it back to it. As the pure travelling wave resonator has very low losses, it requires very little acoustic power to sustain an acoustic resonance. This is quite similar to the phenomenon of children playing on swings, where a small push could sustain the swing for a long time. Both the travelling wave resonator and two stages of engines with very short regenerators are effective measures to significantly reduce the engine's onset temperature difference.

The acoustic power fed back to the engine branch is low, because the by-pass pipe shunts more than half of the power flow away. As a result, the net acoustic power production from the engine core is relatively low. The short regenerator is useful for utilising low temperature heat sources, but it also limits the power generation capacity

and potentially causes severe heat conduction losses. Both of these features could lead to a low power density and low thermal efficiency.

Chapter 5 Application of a looped-tube travelling-wave thermoacoustic engine with a by-pass configuration to cooler

5.1 Introduction

In the previous chaper, the working principle of the by-pass type thermoacoustic engine has been formulated and analysed. The agreement between the simulations and the experimental results demonstrate that the model has captured the essence of working principle of this type of thermoacoustic engine. It was also indicated that the protype has several drawbacks, such as low power density. In this chapter, a thermoacoustic cooler is coupled to the engine to utilise its acoustic power, allowing the evaluation of thermal efficiency. The research will then focus on how to improve the power density and thermal efficiency of this by-pass type engine without violating the working principles of thermodynamics.

5.2 The concept

The by-pass configuration will now be applied to design a thermally driven thermoacoustic refrigerator with a cooling temperature at about -20°C. The targeted waste heat source is the exhaust gas of vehicle engines, which has a temperature in the range of 200-300°C. The ambient temperature is set to 28°C. The whole system has the same configuration as that shown in Figure 4.1 in the last chapter. However, the second engine unit is replaced by a cooler stage as shown in Figure 5.1, and the regenerator of the engine stage has been increased from 1.58 to 10 mm to utilise such a heat source. The working gas is nitrogen at 10 bar. The operating frequency is reduced to about 76.5 Hz.

The dimensions of the main components are summarised in Table 5.1. The regenerators are made of stainless steel mesh screen. All of the heat exchangers have a tube-and-shell configuration, which is simpler for manufacturing than the idealised Screen-type heat

exchanger. In Table 5.1, AHX1, REG1 and HHX1 form the engine unit, while AHX2, REG2 and CHX2 form the cooler unit. In de Blok's prototype, the gap between the two engine stages is only about 3 cm, to act as a TBT, due to the low temperature of the heat source. In this system, the temperature difference between HHX1 and AHX2 is about 230°C, and therefore, its length is increased to 19 cm, to reduce the heat losses from the hot heat exchanger of the engine stage to the ambient heat exchanger of the cooler stage.

Table 5.1: The dimensions of the components of the thermally driven thermoacoustic cooler.

Part	Diameter (cm)	Length (mm)	r_h (um)	Porosity
REG1	13.8	10	30	0.77
REG2	13.8	10	30	0.77
AHX1	13.8	21	700	0.5
AHX2	13.8	21	800	0.5
HHX1	13.8	20	800	0.51
CHX2	13.8	21	800	0.5

Part	Diameter (mm)	Length (cm)
By-pass pipe	55.2	120
Feedback pipe(FBP)	71.3	308
Phase shifting pipe	42.2	120
Compliance volume	100.9	13.6
Thermal buffer tube (TBT)	44.0	19

5.3 Effect of important design parameters

In this section, the effect of the important parameters is investigated. The effect of each parameter is carried out individually, to reveal how the parameter affects the thermoacoustic engine-driven cooler performance. The lengths of the regenerator, by-pass pipe, phase shifting pipe, compliance volume and TBT are important design parameters, and therefore are selected and varied to determine the ideal design parameters, as shown in Figure 5.2-Figure 5.6.

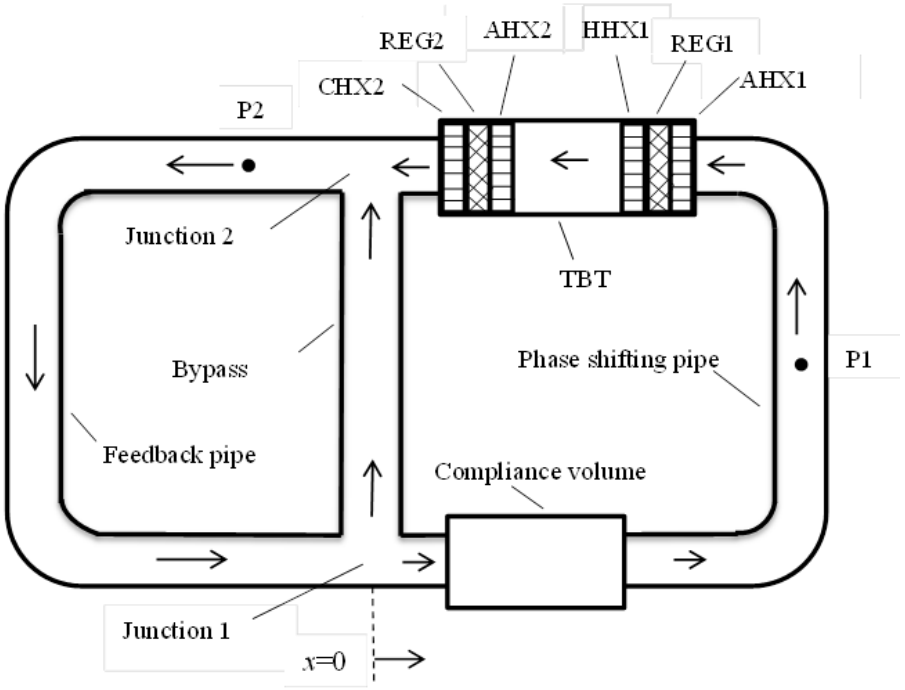

Figure 5.1: Schematic diagram of the thermoacoustic engine driven cooler with a by-pass configuration.

HHX: hot heat exchanger, REG: regenerator, CHX: cold heat exchanger, AHX: ambient heat exchanger, TBT: thermal buffer tube.

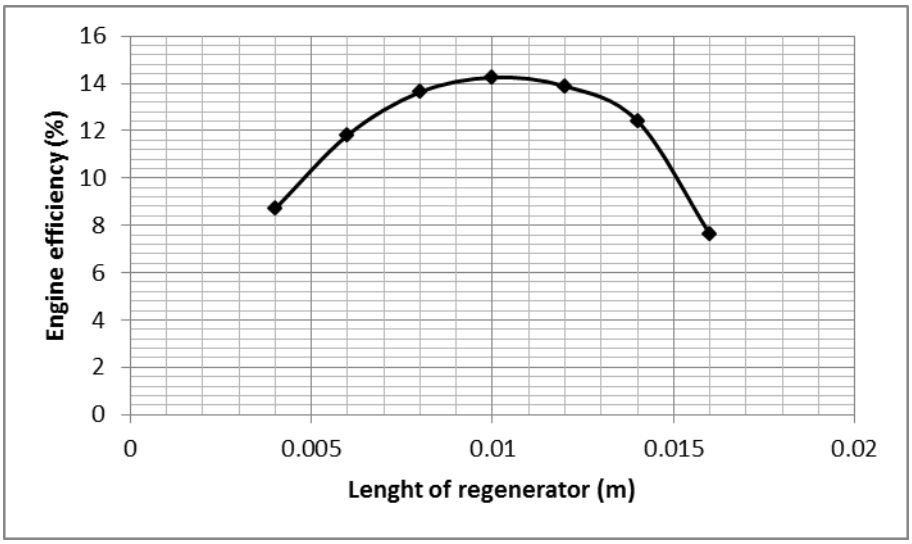

Figure 5.2: Engine efficiency changes as the length of the regenerator varies.

Figure 5.2 shows the effect of the regenerator length of the engine stage on efficiency. Here, the engine efficiency is defined as the ratio of acoustic power consumption of the

cooler over the heat input to the engine. It can be found that there is an ideal regenerator length of about 10 mm, and it is selected for the final design as summarised in Table 5.1. The regenerator length is crucial, as on one hand, its flow resistance increases when the length increases, leading to high acoustic losses. On the other hand, according to equation (4.7) in the previous chapter, the acoustic power production is approximately propotional to the temperature gradient. For a given temperature difference, the longer the length, the smaller the temperature gradient. Furthermore, the shorter the length, the higher the conductive heat loss through the regenerator. Also its flow resistance increases when the length increases, leading to high acoustic losses.Therefore, a very careful trade-off is required.

Figure 5.3 shows the relationship between the engine efficiency and length of the by-pass pipe. The ideal length is about 120 cm, and it is selected for the final design. Similarly, Figure 5.4 shows the relationship between the length of the phase shifting pipe and engine efficiency. The ideal length is about 120 cm, and it is selected for the final design. Figure 5.5 shows the effect of the length of the compliance volume on the engine efficiency. Compared with other parameters, it has a relatively weak effect on the engine efficiency. In the final optimised model, the length of the compliance volume is selected to be 13.6 cm. The by-pass pipe, compliance volume and phase shifting pipe are all the phase control components. Their dimensions are important for achieving the right phase and impedance within the engine and cooler units, as well as in the FBP.

Figure 5.6 shows engine efficiency as a function of the length of the TBT. It can be found from this figure that its length slightly affects the engine efficiency. It is selected as 19 cm in the final model. In practice, it provides a thermal buffer between the hot heat exchanger and room temperature. Its length should be much greater than the local gas displacement. In the present model, the local gas displacement amplitude is around 3 cm in this system. The length of the TBT is about 6 times this displacement, which is in line with the arrangement of Backhaus and Swift's thermoacoustic Stirling engine [10].

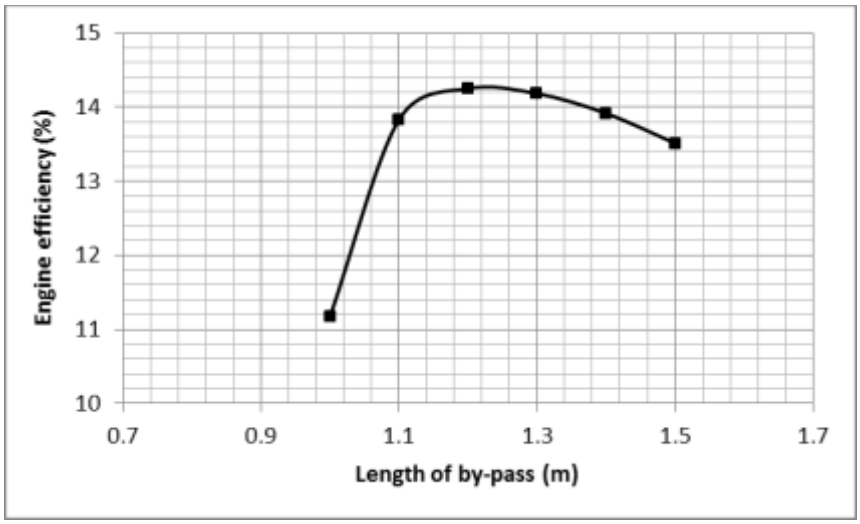

Figure 5.3: Engine efficiency changes as the length of the by-pass pipe varies.

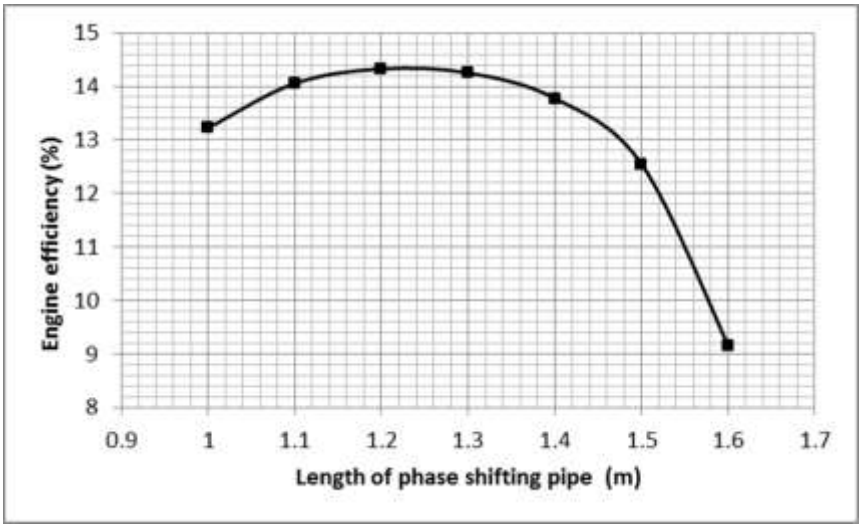

Figure 5.4: Engine efficiency changes as the length of the phase shifting pipe varies.

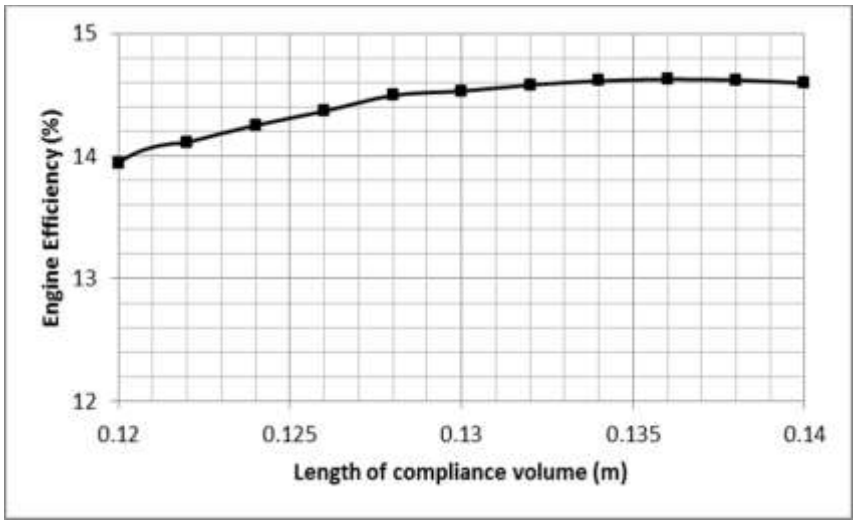

Figure 5.5: Engine efficiency changes as the length of the compliance volume varies.

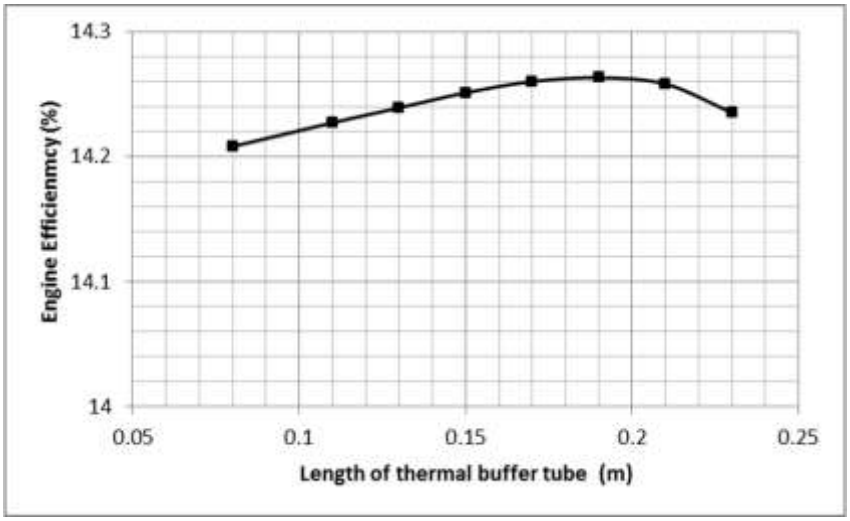

Figure 5.6: Engine efficiency changes as the length of the thermal buffer tube varies.

5.4 The final design model

In the final design model, the maximum pressure amplitude is about 54 kPa, and therefore the relative pressure amplitude to the mean pressure is about 5.4%, which meets the low amplitude criteria to use the DeltaEC software. The whole system is schematically shown in Figure 5.1. The simulation results of the optimised model are

summarised in Table 5.2. The heat source temperature (i.e. the solid temperature at HHX1) is set as 260°C, and the heat sink temperature (i.e., the solid temperature of AHX1 and AHX2) is 28°C. The net acoustic power production from the engine unit (i.e., the difference between its inlet and outlet acoustic power) is about 195.8 W. The acoustic power consumed by the cooler is 159.5 W. The heat input to the engine's hot heat exchanger is 1100.7 W. The thermal efficiency η_e, defined as the ratio of the acoustic power consumed by the cooler over the heat input to the engine, is 14.5%. This is equivalent to 33.4% of the Carnot efficiency for the same heat source and sink temperatures. The cooler removes 232.4 W heat at -19.1°C, and rejects it at 28°C. The cooler's coefficient of performance (COP) is defined as the ratio of the heat absorbed at CHX2 over the acoustic power it consumes. The calculated COP is about 1.46, equivalent to 27% of the Carnot COP at this temperature range. The performances predicted by this model are comparable to multi-stage travelling wave thermoacoustic systems under similar conditions. [12, 70].

Table 5.2: Summary of the simulation results of the thermoacoustic engine driven cooler.

Symbol	Definition	Unit	Engine	Cooler
T_h	Solid temperature of HHX	°C	260	N/A
T_a	Solid temperature of AHX	°C	28	28
T_c	Solid temperature of CHX	°C	N/A	-19.1
$\dot{E}_{2,\,in}$	Acoustic power inlet	W	417.6	612.0
$\dot{E}_{2,\,out}$	Acoustic power outlet	W	613.0	452.5
$\dot{E}_{2,\,net}$	Net acoustic power production (engine) or consumption (cooler)	W	195.8	-159.5
$\dot{Q}_{in}$	Heat input to HHX (engine) or CHX (cooler)	W	1100.7	232.4
η_e	Engine efficiency	%	14.5	
COP	Coefficient of performance (COP)		1.46	
η_{Carnot}	Carnot efficiency: $(T_h\text{-}T_a)/T_h$	%	43.5	
COP_C	Carnot COP: $T_c/(T_a\text{-}T_c)$		5.4	
η_r	Percentage of Carnot efficiency	%	33.4	
COP_R	Percentage of Carnot COP	%	27	

The details of the acoustic field within the system have been calculated and shown in Figure 5.7-Figure 5.11 to further investigate the final design. In the figures, the solid line represents the results for the engine loop (i.e., engine branch and FBP), and the dashed line with symbols represents the results of the by-pass pipe.

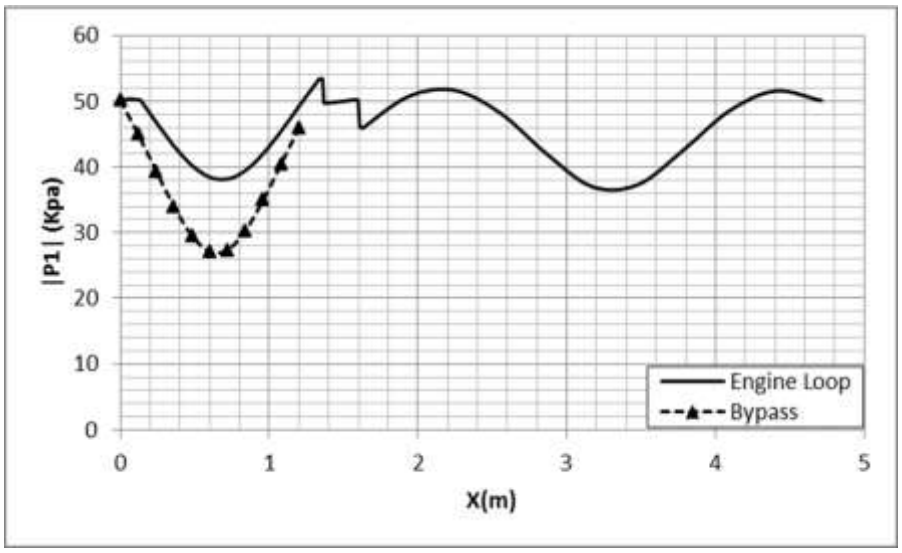

Figure 5.7: Distribution of the amplitude of acoustic pressure along the thermoacoustic engine driven cooler

Figure 5.7 shows the distribution of the acoustic pressure amplitude along the system. The maximum pressure amplitude is 54 kPa at the engine core and the minimum pressure amplitude is 27 kPa at the middle of the by-pass pipe, so the maximum-to-minimum ratio is about 2 in the whole system, which is slightly higher than 1.2 in de Blok's prototype. This is mainly due to the regenerator length having been increased to 10 mm, and therefore the flow resistance at the engine core is higher, and thus the acoustic reflection is higher. In the FBP, the maximum pressure amplitude is about 52 kPa, and the minimum amplitude about 36 kPa, so the maximum-to-minimum ratio is about 1.4, which is very close to 1 in the ideal travelling wave condition.

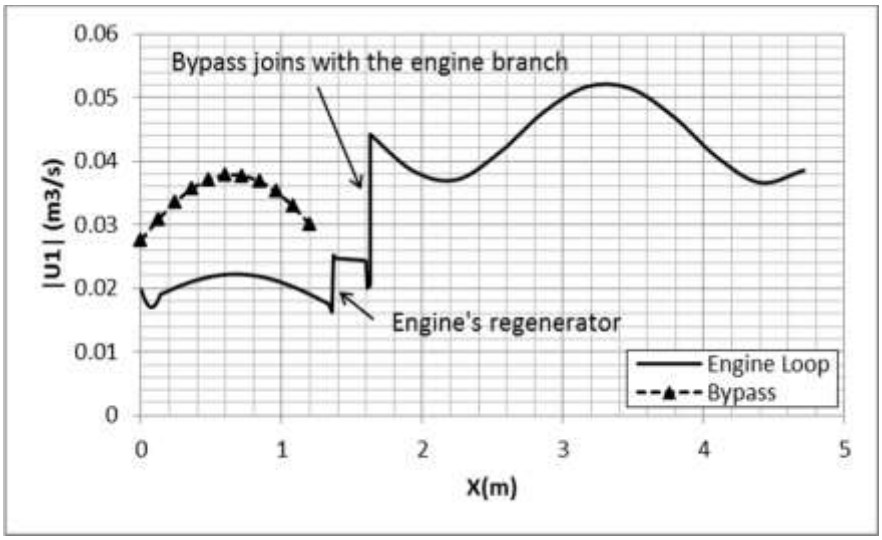

Figure 5.8: Distribution of the amplitude of volumetric velocity along the thermoacoustic engine driven cooler.

Figure 5.8 shows the distribution of the amplitude of volumetric velocity along the system. It can be seen that the by-pass pipe shunts away more than half of the volumetric velocity at the location x=0. As a result, more than half of the acoustic power (i.e., 512 W) flows to the by-pass, and only 428 W acoustic flows into the engine branch. There is a sharp increase of volumetric velocity at the regenerator of engine stage, due to the steep temperature gradient along the regenerator. The other sharp increase is due to the by-pass pipe joining after the end of the cooler.

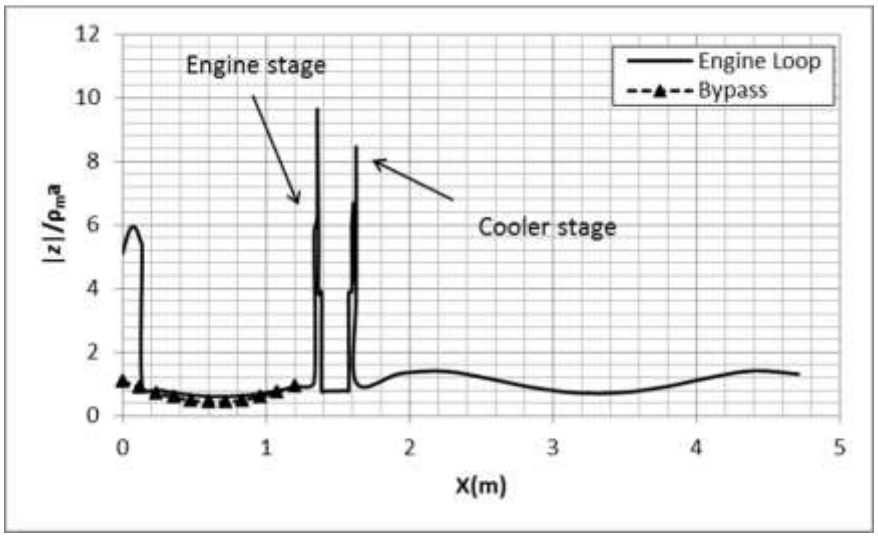

Figure 5.9: Distribution of the normalized specific acoustic impedance along the thermoacoustic engine driven cooler.

Figure 5.9 shows the normalised specific acoustic impedance along the system. To reduce the acoustic losses with in the regenerator, the specific acoustic impedance $|z|$ should be designed in the range of 15-30 times of $\rho_m a$ [10]. In the present model, it can be seen that the value of $|z|/\rho_m a$ in most parts of the system is around 1, except for the engine and cooler sections, where it is 9.6 and 8.4 respectively. It should be noted that, in order to achieve a very low onset temperature difference, de Blok's prototype has low impedance within the regenerators due to the short regenerators. In this design, the researcher substantially increased the regenerator length to use a heat source with a higher temperature. Therefore, the resultant system has relatively higher impedance in the regenerator.

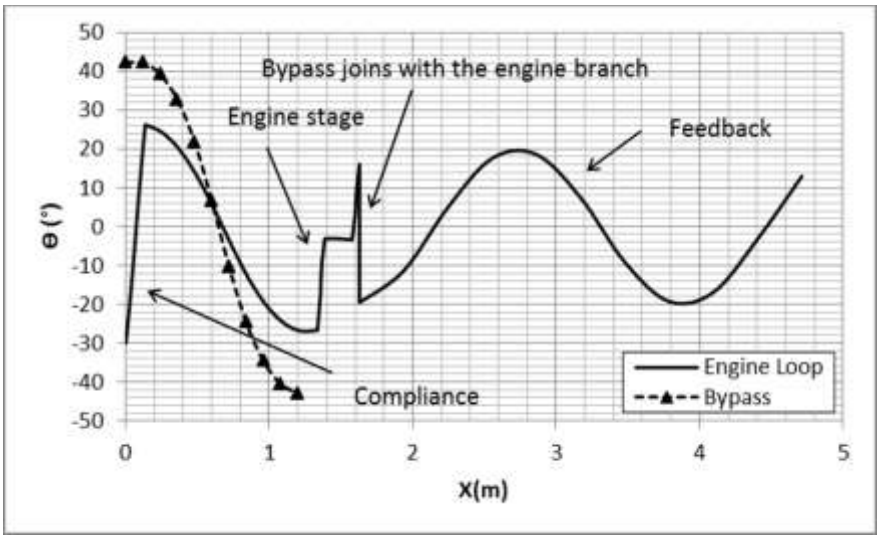

Figure 5.10: Phase angle θ between pressure and velocity oscillations along the thermoacoustic engine driven cooler.

Figure 5.10 shows the phase difference between pressure and velocity oscillations along the loop. It can be found that the phase angle is in the range -20°<Θ<20° in the FBP, engine unit, and cooler, as expected. The rest of the system also has a phase angle in the range -40°<Θ<40°. Therefore, the whole system works in near travelling wave conditions as expected.

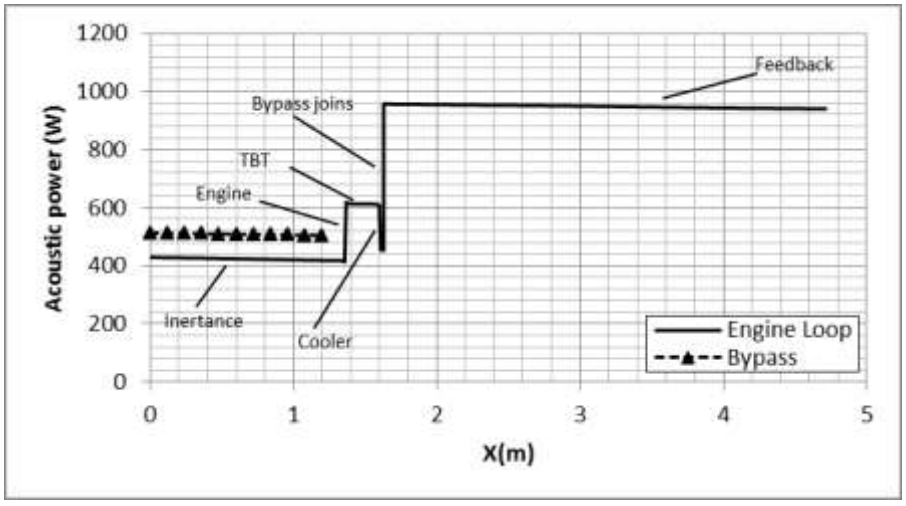

Figure 5.11: Distribution of acoustic power along the thermoacoustic engine driven cooler.

Figure 5.11 shows the acoustic power flow along the system. The simulation starts from Junction 1 (x=0). At this point, the 940 W of acoustic power is divided into two parts, one part (~512 W) flows into the by-pass and the other part (~428 W) flows into the compliance volume section. About 420 W of acoustic power is fed into the engine core, which is then amplified to around 613 W. There is a small amount of acoustic loss (around 1.35 W) along the TBT. The cooler unit consumes around 159.5 W. Around 452 W of acoustic power exits the cooler and joins with the acoustic power flow from the by-pass pipe (~504 W) at Junction 2. In total, about 956 W of acoustic power then flows into the FBP. The FBP transmits the acoustic power back to the starting point (x=0) after about 10 W of acoustic power is dissipated. The ratio of power flows to the by-pass and engine branch is quite similar to that in de Blok's prototype.

The results presented in this chapter suggest that the working principle of de Blok's by-pass engine can be achieved after the regenerator length and mean pressure are substantially increased. As such, the system's power density and thermal efficiency can be improved. The modelled thermoacoustic engine driven cooler predicted a performance similar to systems having other configurations.

5.5 Conclusions

This chapter presents comprehensive numerical research of a travelling wave thermoacoustic engine with a by-pass configuration and its application to thermoacoustic engine driven coolers. The validated model which has been used in chapter 4 was then applied to design a thermally driven travelling wave thermoacoustic cooler with such a by-pass configuration.

To improve power density and thermal efficiency, the regenerator length and mean pressure can be increased. The model was then applied to design a thermoacoustic engine driven thermoacoustic cooler with a much longer regenerator and higher mean pressure. The design principle contained in the by-pass type engine was successfully implemented in the design.

Nitrogen at 10 bar was used as the working gas, and the engine had an operating frequency around 76.5 Hz. When the engine was loaded with a thermoacoustic cooler, the simulation results show that the whole system could achieve a thermal efficiency of 14.5%, which is equivalent to 33.4% of the Carnot efficiency at the tested temperature range. The cooler consumes 159.5 W acoustic power to remove 232.4 W heat at about -19°C and rejects it at 28°C, which leads to a COP of about 1.46 that is equivalent to 27% of Carnot COP under these operating conditions.

It is inferred that a longer regenerator length is possible for this by-pass engine configuration. The model of the thermoacoustic engine driven cooler predicts similar performance with those systems having other configurations [10, 61, and 64].

Chapter 6 Looped-tube travelling-wave thermoacoustic generator with a by-pass pipe

6.1 Introduction

In the previous chapter, the by-pass configuration with cooler was thoroughly investigated. In the current chapter, the research will focus on how engines using a by-pass configuration can be coupled with an alternator to develop inexpensive electric generators.

This chapter proposes and numerically demonstrates a looped-tube travelling wave thermoacoustic electric generator using this configuration. It essentially employs a one wave-length travelling-wave acoustic resonator which has low acoustic losses. The engine branch consists of compliance, an inertance tube, an engine core, and an alternator. An ultra-compliant alternator (i.e., a sub-woofer) is installed in the acoustic compliance section where the local acoustic impedance is relatively low, but the cross sectional area is large. The numerical simulations demonstrate the working principle, and show that it can achieve comparable performance to other types of travelling wave thermoacoustic electric generators.

6.2 The concept

A linear alternator is coupled to the engine to develop an electric generator, as schematically shown in Figure 6.1. This system has a very similar configuration to that shown in chapter 5, but the cooler unit is now replaced by an alternator to utilise the acoustic power. The compliance volume has relatively low acoustic impedance and a larger cross sectional area, which is ideal for installing the alternator. As such, the alternator housing can work as a compliance volume at the same time. The regenerator of the engine stage has been further increased from 10 to 19.7 mm to utilise a high-temperature heat source.

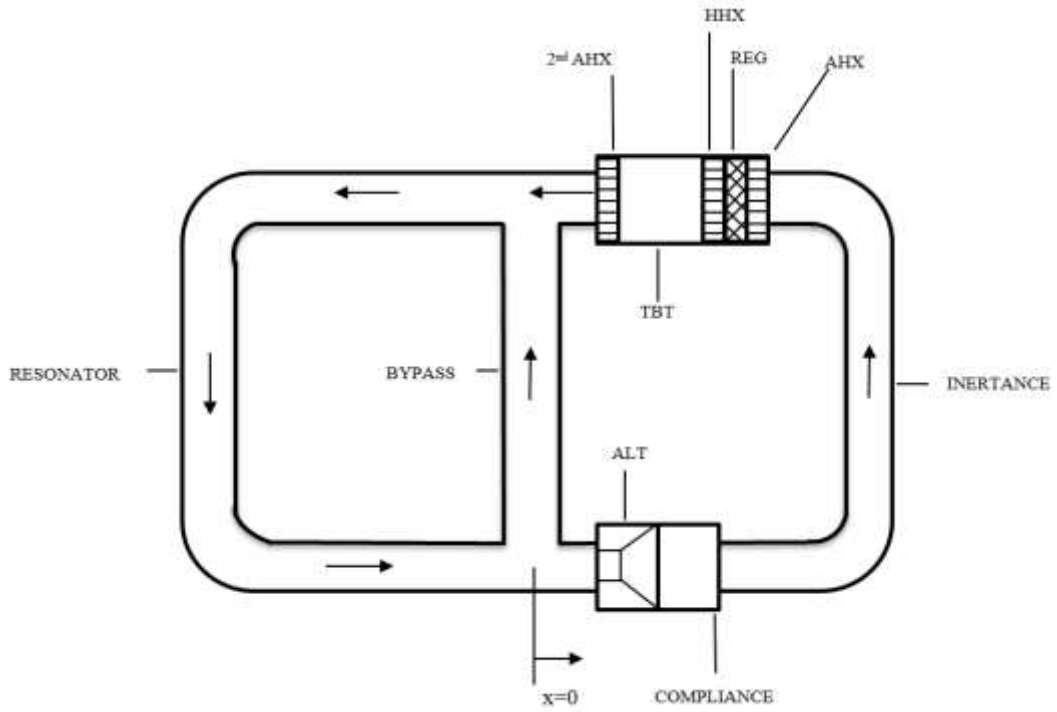

Figure 6.1: Schematic diagram of the thermoacoustic electric generator with a by-pass configuration.

The dimensions of the main components are summarised in Table 6.1.

Table 6.1: The dimensions of the system's components.

Part	Diameter (m)	Length (mm)	r_h (μm)	Porosity
REG	0.138	19.7	30	0.77
AHX	0.138	21	700	0.5
HHX	0.138	20	800	0.5
SAHX	0.138	21	700	0.5

Part	Diameter (mm)	Length (cm)
By-pass	55.2	100
Resonator	71.3	244
Inertance	40.68	165
Compliance	107	28
TBT	138	5

6.3 Loudspeaker selection

To convert acoustic energy to electrical power, there are some commercially available devices, such as linear alternators, piezoelectric generators and audio loudspeakers. Due to their cost and efficiency, the linear alternators and piezoelectric generators are not suitable for the thermoacoustic applications. Audio loudspeakers might be treated as low impedance alternators (because they usually have relatively small moving mass and stiffness) with audio loudspeakers being cheaper than comparable linear alternators. However, this cost gap may be reduced in the future, if audio loudspeaker manufacturing techniques and technologies are utilised in linear alternator manufacturing.

To achieve high transduction efficiency, based on the linear theory of alternators, an alternator should have a high force factor Bl, low mechanical resistance R_m, and low electric resistance R_e [80].

It should be mentioned here that the loudspeakers were originally manufactured for high audio quality, and not to convert acoustic power to electric power. This might cause some matching problems because they are not fitted to the requirements of a thermoacoustic generator [56]. The loudspeaker which was used in simulation procedures to convert acoustic energy to electricity is schematically shown in Figure 6.2. The loudspeaker has two sections, one section for the mechanical part (with subscript (m)), and the other for the electrical part with subscript (e)) [54]. All the components in Figure 6.2 are described below

S: Effective area
M_m: total mass of the diaphragm and the coil or called moving mass.
K_m: mechanical stiffness.
R_m: mechanical resistance
L_e: electric inductance.
R_e: electric resistance.

R_l: load resistor.

Bl: force factor.

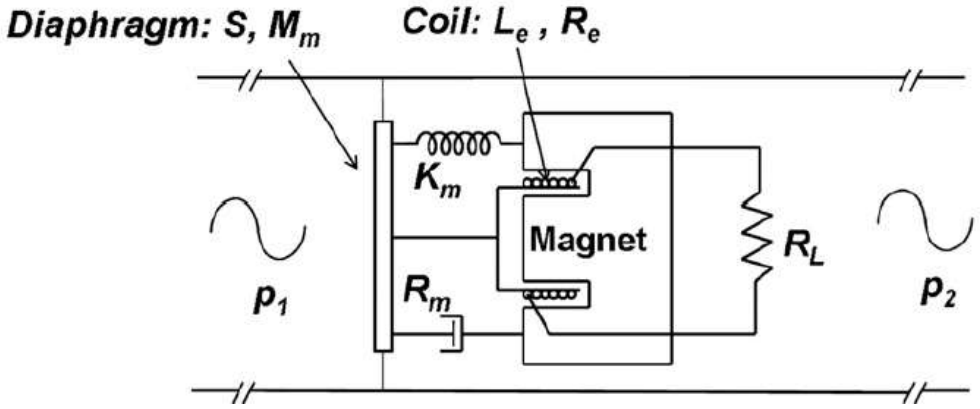

Figure 6.2: Schematic of the alternator's physical model [80].

The parameters of the alternator are listed in Table 6.2, which are properties based on an actual subwoofer (B&C 8NW51 [84]) with slight changes to match acoustic characteristics of the engine. The parameters are believed to be achievable using audio loudspeaker manufacture technologies, as subwoofers with similar parameters are widely available in the market [63].

Table 6.2: Parameters of the linear alternator used in the research [84] B&C Speakers.

Data sheet of 6PS38. http://www.bcspeakers.com.

Parameter	Symbol	Unit	Value
Resonance frequency	F_s	Hz	74
Force factor	*Bl*	N/A	30
Electric inductance	L_e	mH	0.6
Electric resistance	R_e	Ω	4.2
Moving mass	M_m	g	30
Stiffness	k_m	mm/N	7500
Mechanical resistance	R_m	kg/s	0.8
Maximum excursion	X_{max}	mm	5.7
Effective area	*S*	cm^2	150

6.4 Effect of important design parameters

To further demonstrate the design procedure of this system, the effect of the important parameters is investigated. The effect of each parameter is carried out individually, to reveal how the parameter affects the thermoacoustic engine-driven generator performance. This proceddure aims to gain in-depth understanding and ultimately facilitate further development of this type of thermoacoustic system. The ideal lengths of the by-pass pipe, inertance tube, the compliance, the thermal buffer tube and operating frequency have been determined when the generated electric power from the alternator (which is calculated by DeltaEC model) is used as a performance indictor. The obtained results are shown in Figure 6.3-Figure 6.7.

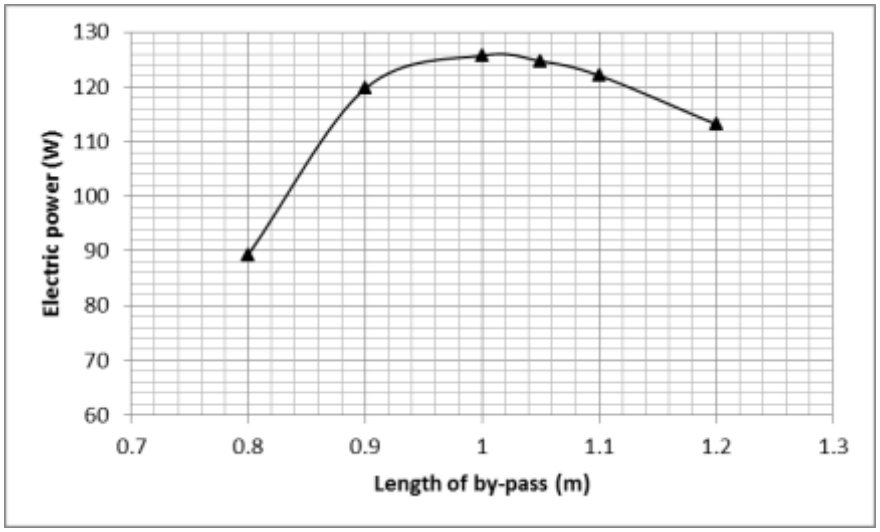

Figure 6.3: Electric power output as function of the length of the by-pass pipe.

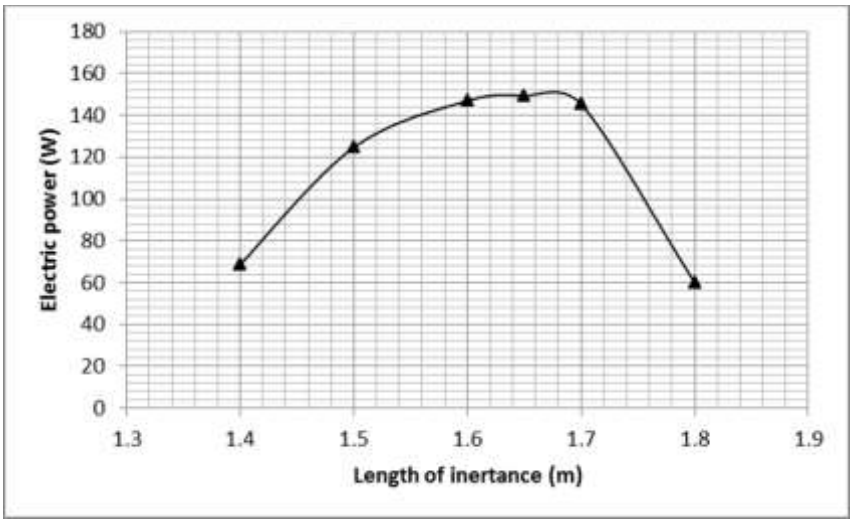

Figure 6.4: Electric power output as function of the length of the inertance tube.

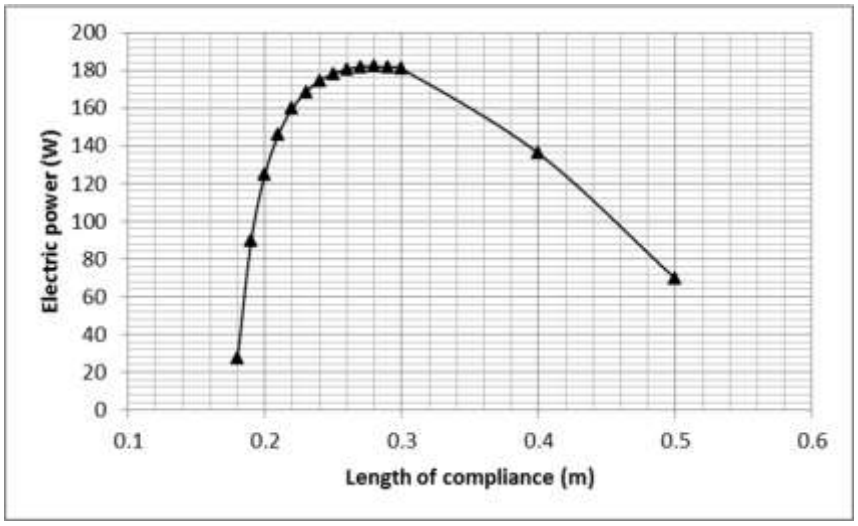

Figure 6.5: Electric power output as function of the length of the compliance.

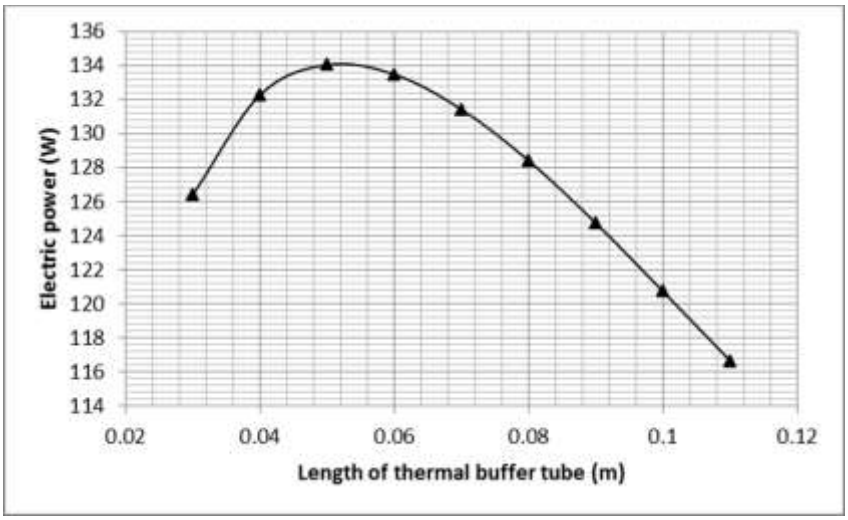

Figure 6.6: Electric power output as function of the TBT.

Figure 6.3 shows the effect of the length of the by-pass pipe on the electric power output. The ideal length is about 1 m and it is selected for the final design. It can be noticed that the generated electric power increases dramatically until the curve reaches a maximum value of 126 W when the optimal by-pass length is 1 m, and then decreases gradually when the by-pass length increases further. Similarly, Figure 6.4 shows the relationship between length of the inertance tube and electric power output. The results lead to an ideal length about 1.65 m. The by-pass and inertance tube are the components affecting the phase angle between the pressure and velocity oscillations in such a system. Their dimensions are very sensitive for achieving the correct phase and impedance within the engine and the FBP. According to their cross-sectional area they act the role of forcing the phase angle between the pressure and velocity oscillations towards zero (right phase) which leads to getting a travelling wave system, leading to decreasing the acoustic losses and increasing the performance of the system.

Furthermore, Figure 6.5 shows the relationship between length of the compliance and electrical power output. The ideal length is about 0.281 m and it is selected for the final design. In the same way, Figure 6.6 shows the relationship between length of the TBT and electrical power output. The results lead to an ideal length about 0.05 m.

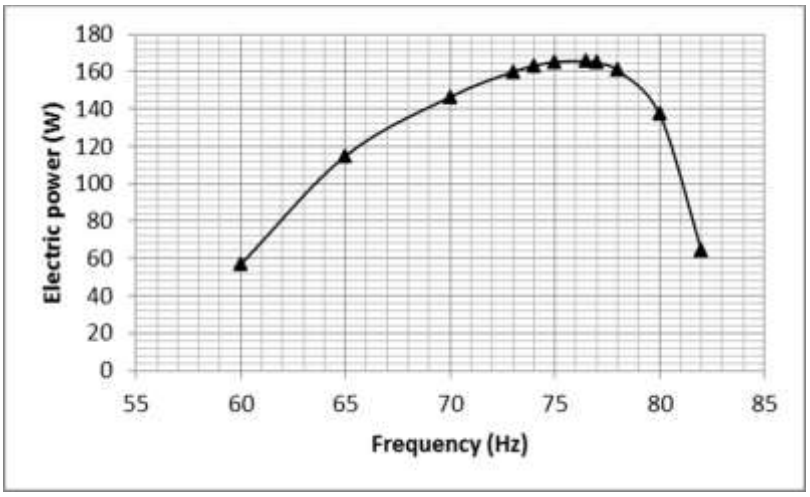

Figure 6.7: Electric power output as function of the operating frequency.

Figure 6.7 shows the relationship between the electrical power output and the operating frequency of the system. The FBP length has been varied to change the operating frequency of the system. It can be seen from Figure 6.7 that the electrical power output increases rapidly with the frequency. It reaches a maximum value 162 W when the optimal frequency is about 76.5 Hz, and then decreases sharply when frequency increases further. Referring to Table 6.2, one can find that the ideal operating frequency is very close to the resonance frequency of the alternator. This phenomenon agrees with the experimental observations in previous research work [52].

6.5 The final design model

After a series of optimisation procedures, the final simulation results of the final design model are summarised in

Table 6.3. The heat source temperature (i.e. the solid temperature at HHX) is now set as about 624°C, and heat sink temperature (i.e., the solid temperature of AHX and 2nd AHX) is set as 28°C. The working gas is still nitrogen at a pressure of 10 bar, and the operating frequency is kept as 76.5 Hz. The heat input to the hot heat exchanger is 1100.7 W.

Table 6.3: Summary of simulation results of the thermoacoustic electric generator.

Symbol	Definition	Unit	Engine	Alternator
T_h	Solid temperature at HHX	°C	624	N/A
T_a	Solid temperature at AHX	°C	28	N/A
$W_{a,\,in}$	Acoustic power inlet	W	217	467
$W_{a,\,out}$	Acoustic power outlet	W	505	230
$W_{a,\,net}$	Net acoustic power production (engine) or consumption (alternator)	W	288	237
$Q_{in,i}$	Heat input to HHX (engine) or (alternator)	W	1100.7	N/A
η_e	Engine efficiency	%	21.5	
$\eta_{a\text{-}e}$	Alternator efficiency	%	70	
η_{Carnot}	Carnot efficiency: $(T_h\text{-}T_a)/T_h$	%	66.4	
η_r	Percentage of Carnot efficiency	%	32.37	

The details of the acoustic field within the system have been calculated and shown in Figure 6.8-Figure 6.12 to further investigate the final design.

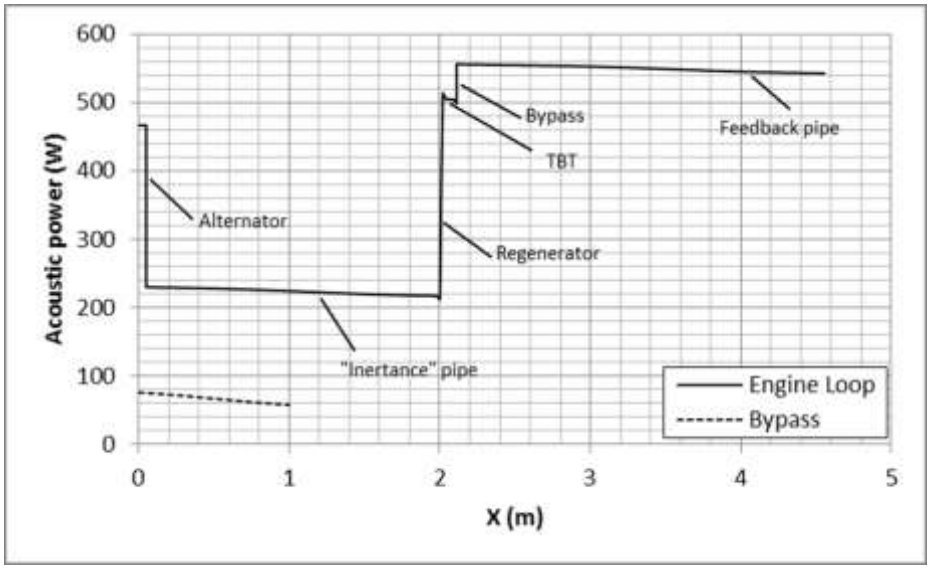

Figure 6.8: Distribution of acoustic power along the system.

Figure 6.8 demonstrates the acoustic power flow along the loop. About 465 W of acoustic power enters the alternator housing and dissipates around 13 W. The alternator extracts about 237 W of acoustic power and produces 166 W of electricity, with an

acoustic to electricity efficiency $\eta_{a\text{-}e}$=70%. The remaining 227 W acoustic power feeds into the cold heat exchanger and dissipates about 6 W. About 210 W acoustic power flows into the regenerator where it is amplified to around 514W. On the other hand, about 75.7 W of the acoustic power is shunted to the by-pass. After some dissipation, about 60 W acoustic power exits and joins with the acoustic power that leaves the secondary ambient heat exchanger. Finally, around 556 W of acoustic power goes to the FBP. The net acoustic power production from the engine unit is about 288 W. This ultimately leads to the engine efficiency of 21.5%, which is about 32.37% of the Carnot efficiency for these heat sources and sink temperatures. As a result, the thermal to electrical efficiency $\eta_{h\text{-}e}$=15%.

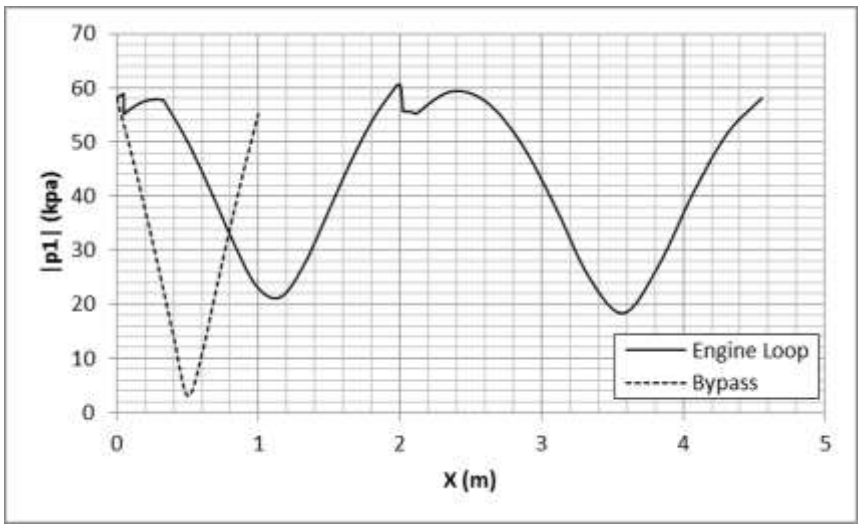

Figure 6.9: Distribution of the amplitude of acoustic pressure along the system.

Figure 6.9 presents the acoustic pressure distribution along the system. The maximum value of pressure is 61 kPa at the engine core, and the minimum value is 3 kPa at the middle of the by-pass pipe; the resulting standing wave ratio can be estimated by the ratio of these two pressure amplitudes as 2.3. This means that the acoustic reflection within the resonator is still relatively high.

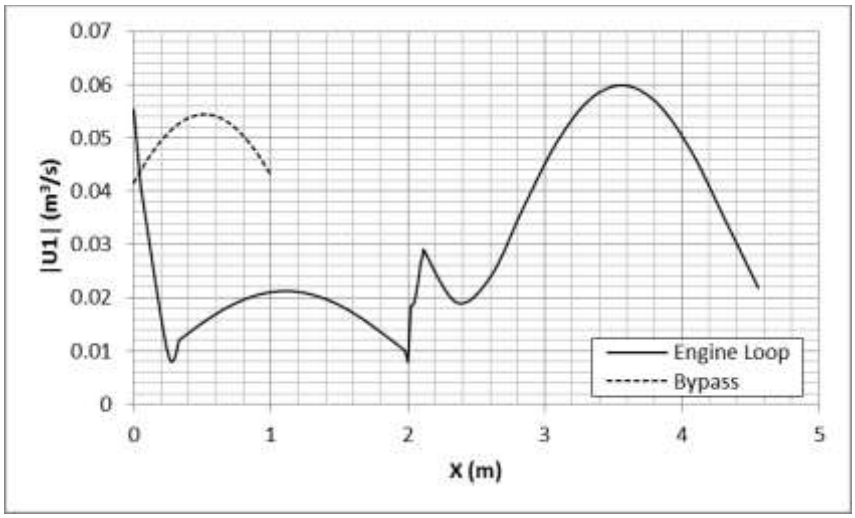

Figure 6.10: Distribution of the amplitude of volumetric velocity along the system.

Figure 6.10 shows the distribution of the amplitude of volumetric velocity along the system. It can be seen that the by-pass pipe shunts a large amount of volumetric velocity as explained in previous chapters. In contrast, a small part of the acoustic power (i.e., 75.7 W) flows to the by-pass and the rest (i.e., 466.8 W) flows into the alternator branch, enabling the alternator to utilise most of the acoustic power to convert it to electricity.

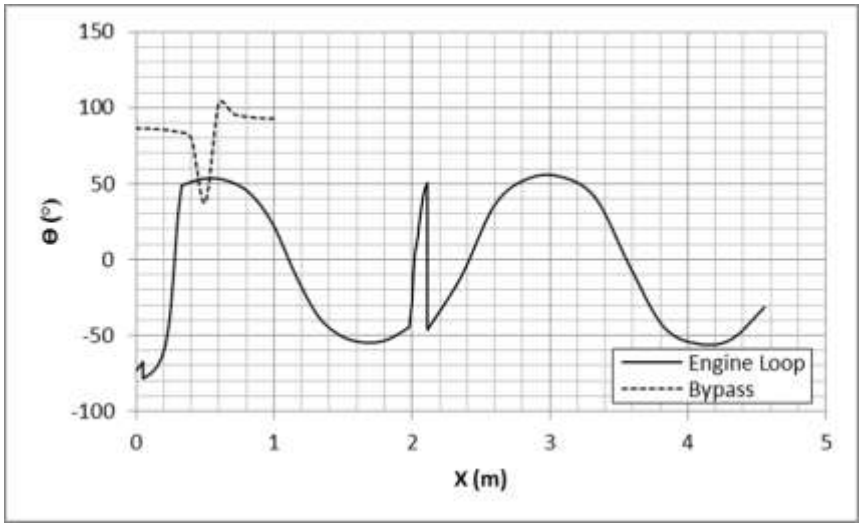

Figure 6.11: Phase angle θ between the pressure and velocity oscillations along the system.

Figure 6.11 shows the phase difference between the pressure and velocity oscillations along the system. It can be noticed that phase angle is in the range -55°<Θ<55° along the FBP, -45°<Θ<50° within the engine branch, and between 38°<Θ<105° along the by-pass pipe. It can be found that the phase angles in this thermoacoustic generator system are far away from the travelling wave conditions, which indicates that the alternator has strongly altered the acoustic field along the system. This can be attributed to the fact that the alternator causes a large pressure drop but has the same volumetric velocity at its two sides [56], and thus strong acoustic reflections are induced. Further investigation is required to understand how the altered acoustic field can be corrected in the future.

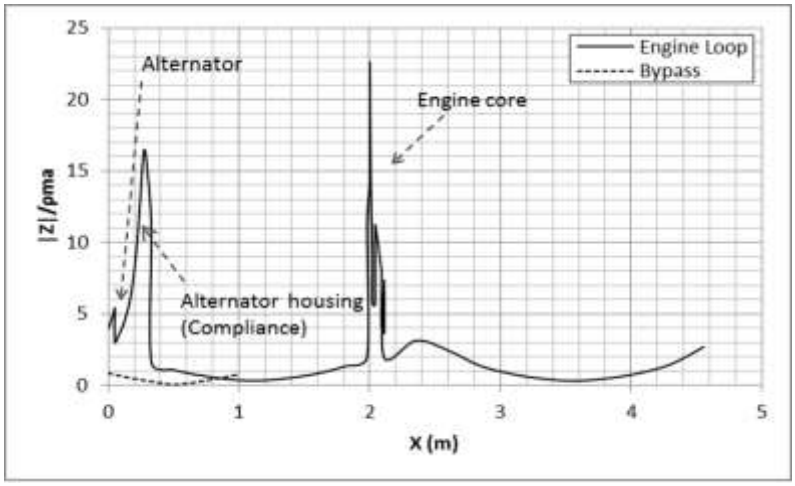

Figure 6.12: Distribution of the normalized acoustic impedance along the system.

Figure 6.12 shows the normalised acoustic impedance along the system. There are two high acoustic impedance regions along the system. One is around the engine core with $\rho_m a$ = 23, and the other is within the alternator housing with $\rho_m a$ = 16, which is in line with the results shown in Figure 6.10-Figure 6.12. It can also be seen that the alternator causes a sharp drop in the acoustic impedance as expected. As proposed by Backhaus [10], to reduce the acoustic losses within the regenerator, the acoustic impedance should be in the range of 15-30 times of $\rho_m a$. Hence, the engine core is in the suitable region, according to Figure 6.12. From Figure 6.13, it can be clearly seen that the electric power is linearly proportional to the heat input.

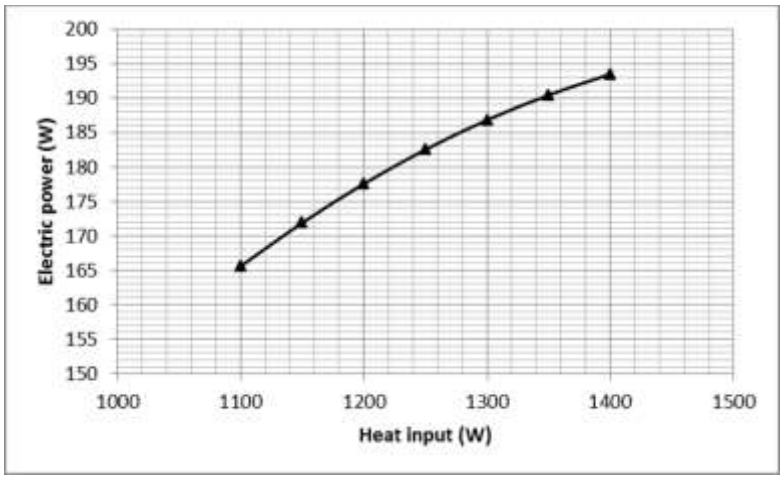

Figure 6.13: Electric power output as function of the heat input of the system.

6.6 Conclusions

This chapter presents a comprehensive numerical analysis of the travelling wave thermoacoustic engine with a by-pass configuration, and its application to develop a thermoacoustic engine driven electric generator. The final design model in chapter 4 and 5 was applied to design a thermally driven travelling wave thermoacoustic electric generator with such a by-pass configuration. The design principle contained in the by-pass configuration was successfully implemented in this design, although the design objectives were changed to achieve higher efficiency. It was found that the design strategy for high efficiency engine as suggested by Backhaus [10] can also be incorporated in this design.

When the engine was loaded with a linear alternator to generate electricity, the whole system achieved a thermal efficiency (engine efficiency η_{h-a}) of 21.5% which is equivalent to 32.4% of the Carnot efficiency under the operating conditions. The alternator extracted 237 W acoustic power from the engine and generated 166 W electricity, which ultimately led to an alternator efficiency (acoustic to electricity efficiency η_{a-e}) of about 70%. The overall thermal-to-electrical efficiency (generator efficiency η_{h-e}) was about 15%, which is comparable to the experimental results of other

types of travelling wave thermoacoustic generators [56, 63, 85, 53, 59, 61, and 62]. It can be expected that a better performance could be achieved were pressurised helium to be used as a working medium, like other prototypes.

Chapter 7 Two-stage travelling-wave thermoacoustic engine with a by-pass configuration

7.1 Introduction

In the two previous chapters, the by-pass engine configuration was applied to a thermoacoustic engine-driven cooler and electric generator, respectively. Comprehensive analysis has shown that this type of engine can potentially achieve a performance similar to other types of travelling wave thermoacoustic engines. As discussed in previous chapters, one drawback of this by-pass configuration is the long resonator, which has approximately the same length as one sound wave-length under the test condition. This becomes a particular challenge when helium is used as the working gas, because the speed of sound in helium is much higher than in air, leading to a very long resonator, and consequently a low power density. As in multi-stage looped-tube travelling wave thermoacoustic engines, it may be possible to install more than one engine stage to a by-pass type of travelling wave thermoacoustic engine, so that they can share the long resonator to improve the system's power density. This chapter investigates this possibility. Another engine stage will be added to a single stage by-pass engine as described in the previous chapters. The working principle and performance of the two-stage by-pass type engine will then be analysed.

7.2 Two-stage travelling-wave thermoacoustic engine with a by-pass configuration without acoustic load

7.2.1 The concept

The design philosophy of the current thermoacoustic system is to reveal whether the by-pass configuration with two-stage engine can be employed to increase the system's power density, and improve the performance of such a system, as shown schematically in Figure 7.1. This section investigates a two-stage travelling-wave thermoacoustic engine with a by-pass configuration. By-pass travelling-wave thermoacoustic

engines essentially employ a near pure-travelling wave acoustic resonator to provide acoustic resonance to the engine unit as shown schematically in Figure 7.1. The physical principles behind the design were explored in detail from previous chapters. This chapter will continue to explore the advantages of a nearly pure travelling wave acoustic resonator.

Two-stages of engine units have been installed to share an acoustic resonator. Each engine stage consists of an ambient heat exchanger (AHX), regenerator (REG), and hot heat exchanger (HHX).

The new system consists of a pair of engines, compliances, inertances, FBPs, and by-passes. The aim is to reduce the length of the resonator and to share it between the two engines. This leads to a shared resonator between two engines, which is called the Travelling Wave Resonator (TWR). The TWR consists of two by-passes and two FBPs. Decreasing the length of the resonator leads to a reduction in the acoustic losses, and ultimately improves the system performance. The working gas is nitrogen, which leads to short thermoacoustic system based on its speed of sound and the mean pressure is 10 bar, which increases the acoustic production. The operating frequency of the system is 75 Hz, which is proportional inversely to the length of the FBP of the system.

To describe how the acoustic power flows through the system, the start point should be x=0 (see Figure 7.1). At this point, part of the acoustic power feeds to the first engine unit, with most of the acoustic power going to by-pass 1. These two parts of acoustic power gather at the end of by-pass 1 and flow through FBP1. This scenario will repeat itself again at engine-stage 2. It can be clearly seen that the by-pass affects the acoustic power distribution through the whole system, and is explained in detail later in this chapter.

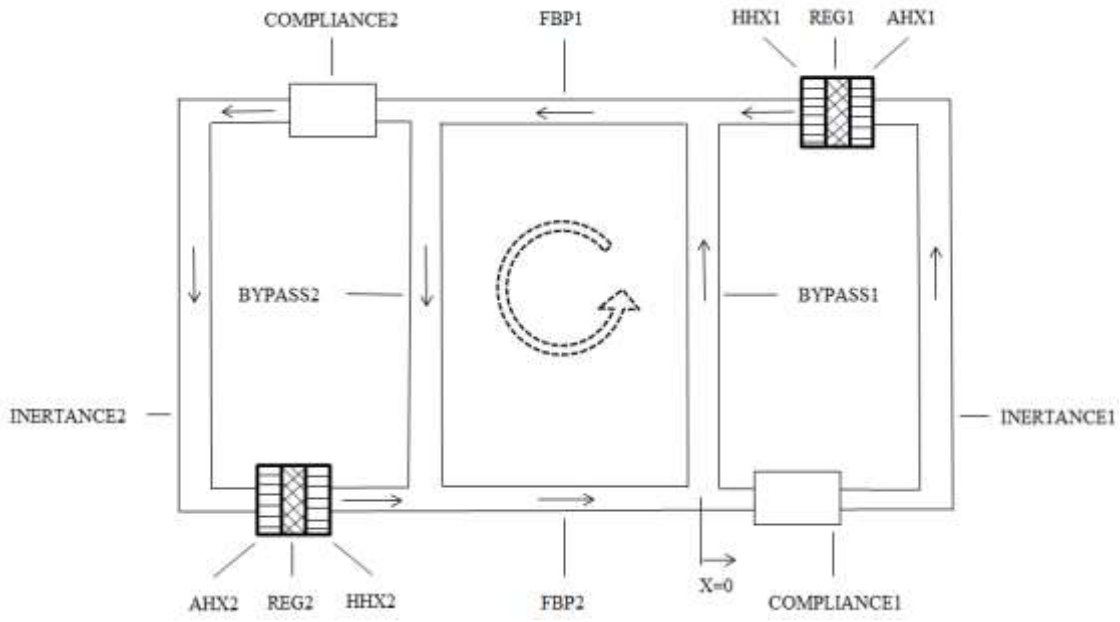

Figure 7.1: Schematic diagram of the two engines by-pass configuration system.

The final dimensions used in this model are summarised in Table 7.1.

Table 7.1: The dimensions of the system.

	Part	Diameter (m)	Length (mm)	r_h(μm)	Porosity
Engine1	HHX1	0.138	20	30	0.5
	REG1	0.138	10	40	0.78
	AHX1	0.138	20	30	0.5
Engine2	HHX2	0.138	20	30	0.5
	REG2	0.138	10	40	0.78
	AHX2	0.138	20	20	0.5

7.2.2 Effect of important design parameters

To further understand the design principle of this complicated system, as shown in Figure 7.1, the effect of the important parameters is presented here, including the areas and lengths of the inertance tube, the by-pass pipe, and compliance. It should be noted that only the FBP area has been determined, because its length has already been determined by the operating frequency. The phase angle and impedance within the

engine unit and the FBP are very sensitive to these dimensions. The obtained results are shown in Figure 7.2-Figure 7.8. All the ideal results are selected in the final design.

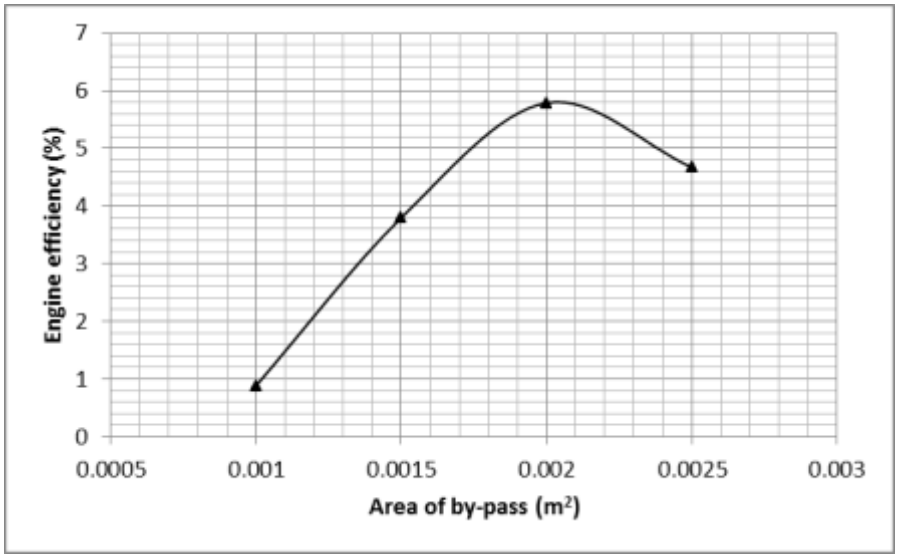

Figure 7.2: Engine efficiency as function of the area of the by-pass.

Figure 7.2 shows the engine efficiency as a function of the area of the by-pass. From experience, the dimensions of the by-pass are very sensitive and crucial, particularly the length. The engine efficiency increases dramatically with the increase of the by-pass area, reaching the maximum efficiency at the ideal by-pass area of 0.002 m^2. This value has been selected in the final design model.

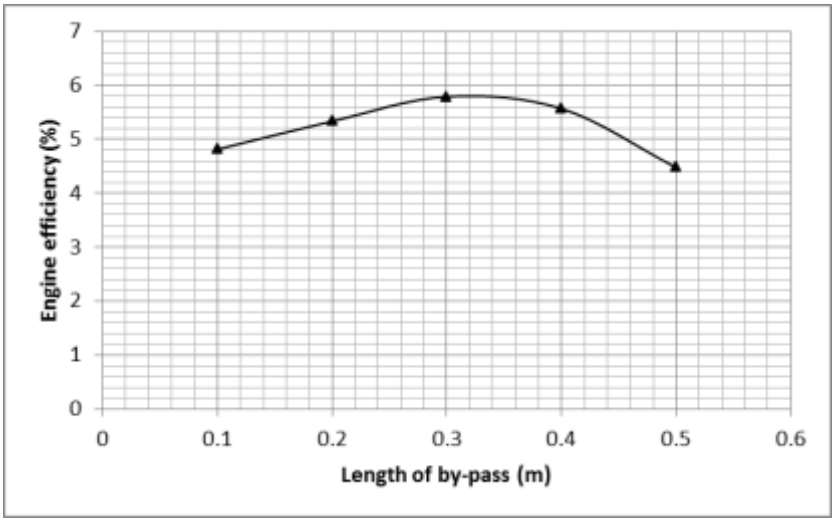

Figure 7.3: Engine efficiency as function of the length of the by-pass.

Figure 7.3 shows the engine efficiency as a function of the length of the by-pass. The engine efficiency increases gradually by increasing the by-pass length, reaching the maximum efficiency at the ideal length of 0.3 m. This value has therefore been selected in the final design model.

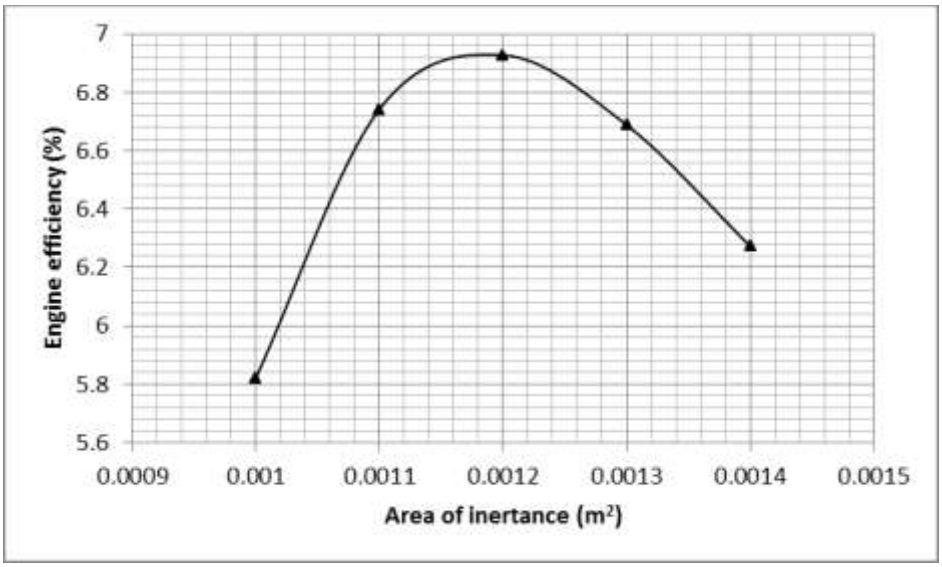

Figure 7.4: Engine efficiency as function of the area of the inertance.

Figure 7.4 presents the engine efficiency as a function of the area of the inertance. The engine efficiency rises rapidly with increasing inertance area, reaching the maximum efficiency at the ideal area of 0.0012 m^2. It is well known that the role of the inertance is to shift the phase angle between pressure and volumetric velocity amplitude to the right phase. This can be done if the inertance has a small area and long length. The ideal value of the inertance area is 0.0012 m^2, and is selected in the final design model.

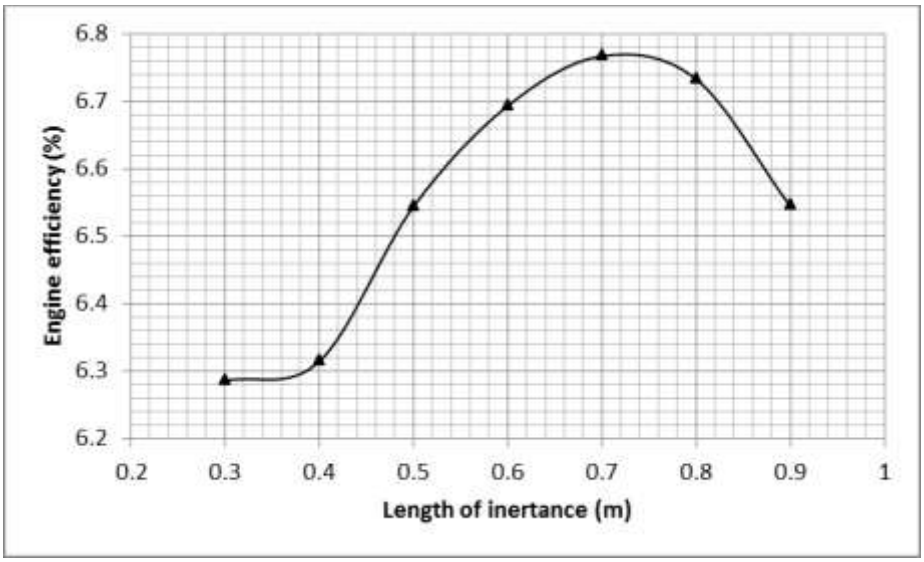

Figure 7.5: Engine efficiency as function of the length of the inertance.

Figure 7.5 shows the engine efficiency as a function of the length of the inertance. It can be clearly seen that the first two points of the curve change slightly, and then significantly increase to the maximum efficiency. After reaching the ideal value of the inertance length, the curve declines suddenly. The ideal value of the inertance length is 0.7 m and is selected in the final design model.

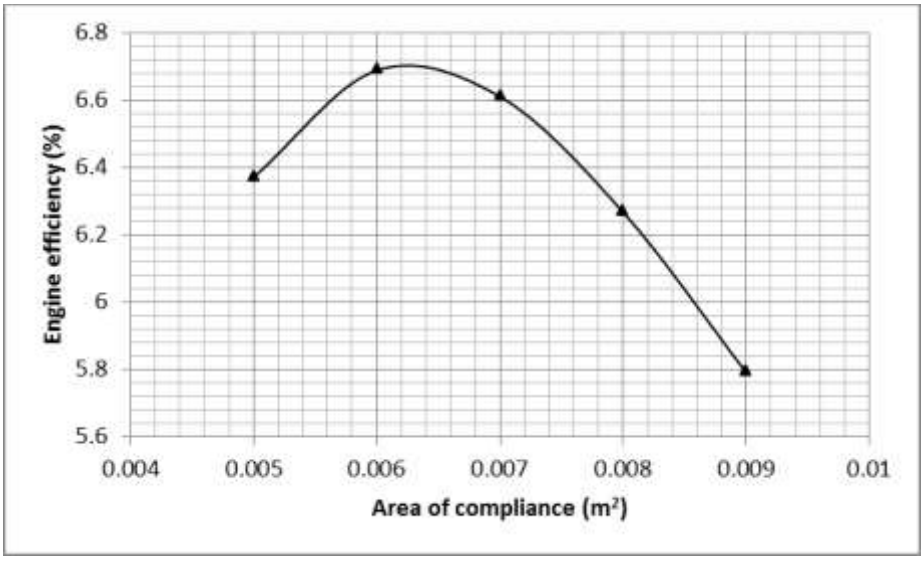

Figure 7.6: Engine efficiency as function of the area of the compliance.

Figure 7.6 explains the engine efficiency as a function of the area of the compliance. The compliance contributes in adjusting the phase between pressure and velocity. There is a significant increase in the engine efficiency associated with an increase in the compliance area. After the maximum efficiency, at the ideal compliance area, there is a steep fall in the efficiency curve. The ideal value of the compliance area is 0.006 m^2 and isselected in the final design model.

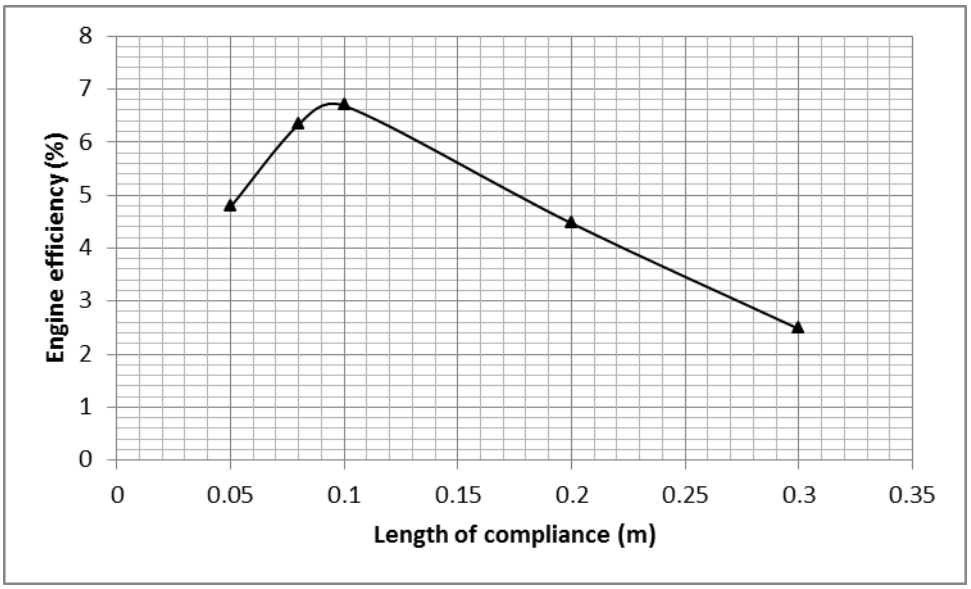

Figure 7.7: Engine efficiency as function of the length of the compliance.

Figure 7.7 addresses the engine efficiency as a function of the length of the compliance. This figure shows a rapid climb of the engine efficiency with increase in the compliance length, leading to the optimised values of the efficiency and compliance length. After the peak point a steady decrease occurs in the efficiency curve. The ideal value of the compliance length is 0.1 m and is selected in the final design model.

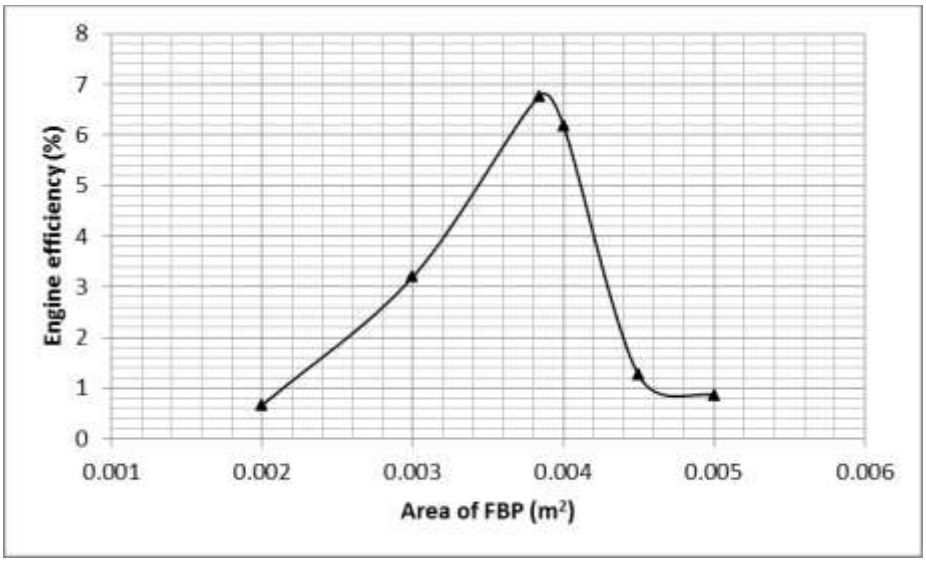

Figure 7.8: Engine efficiency as function of the area of the FBP.

Figure 7.8 gives an indication of the engine efficiency as a function of the area of the FBP. It is important to determine the FBP area, which is related to the velocity of the working fluid in the FBP. A large area of FBP leads to low velocity, resulting in a reduction of acoustic losses and vice versa. Before and after the maximum point of the efficiency there is a sudden increase and decrease in the efficiency curve. The ideal value of the FBP area is 0.004 m^2 and is selected in the final design. It is worth mentioning here that the length of FBP is left as an estimate in the DeltaEC code, leading to a calculated length of the FBP, according to the operating frequency of the system. In order to design a thermoacoustic system, it is important to calculate the operating frequency and the length of the FBP. Both of these parameters strongly depend on each other. Based on the DeltaEC software, to calculate these parameters either choose the frequency as a guess and choose a value of the FBP length (this value is selected based on the working fluid which is used) or choose the FBP length as a guess and select a value of the frequency. In both cases, the guess parameter will be calculated according to the selected parameter. Following the above figures, the ideal dimensions are listed in Table 7.2 below, and implemented in the final design.

Table 7.2: Ideal dimensions of the important parameters.

Parameters	Optimized value	Unit
Area of by-pass	0.002	m^2
Length of by-pass	0.3	m
Area of compliance	0.006	m^2
Length of compliance	0.1	m
Area of inertance1,2	0.0012	m^2
Length of inertance1,2	0.7	m
Area of FBP1,2	0.004	m^2
Length of FBP1,2	2.142 (from the model)	m

7.2.3 The final design model

Compared with a one-stage engine (efficiency is 0.5%), the current system has significantly reduced the acoustic losses, leading to an overall efficiency of around 6.8%. For more accuracy, all the obtained optimised dimensions have been used in the final design model. The simulation results of the optimised model are summarised and presented in Figure 7.9-Figure 7.13. For convenience of presentation, the by-pass curves have been removed from these figures.

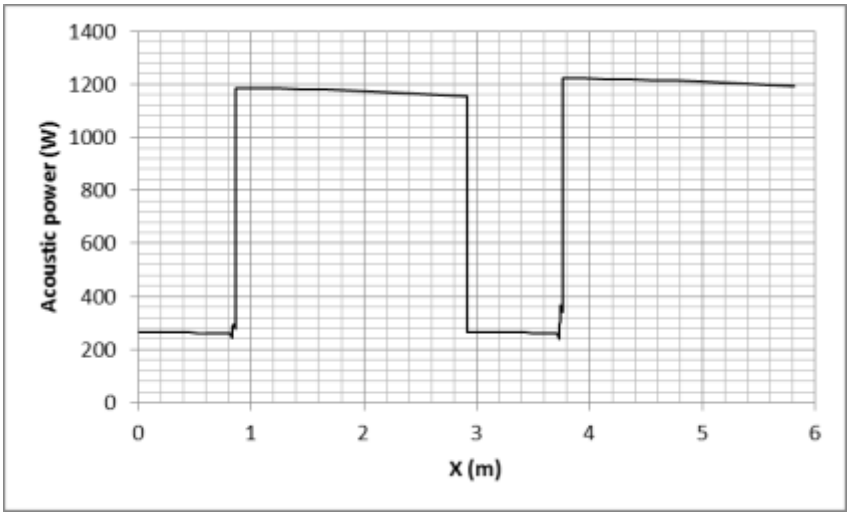

Figure 7.9: Distribution of acoustic power along the engine.

Figure 7.9 shows acoustic power distribution along the system. Around 267 W of acoustic power is fed into the AHX1, which dissipates around 21 W. The rest of the acoustic power 246 W is fed into the cold end of REG1, where the acoustic power will be amplified to around 295 W. 276 W of the acoustic power leaves engine unit 1. 276 W merges with the 910 W acoustic power that comes from by-pass1 to get 1186 W at Junction 1.

The acoustic loss in FBP1 is 33 W, similar to the above description, around 262 W of acoustic power is fed into the AHX2, which dissipates around 21 W. Therefore, 241 W is fed into the cold end of REG2, so the acoustic power will be amplified to around 366 W at the hot end of REG2. 343 W of acoustic power comes out from engine unit 2, and then is merged with the 880 W acoustic power coming from by-pass 2. These two parts of acoustic power are gathered at Junction 2 to get 1223 W. FBP2 dissipates around 31 W from the generated acoustic power.

It is noticeable that the by-pass configuration performs its function as expected, in terms of shunting more than half of the volumetric velocity, leading to a reduction in acoustic power transmission losses, which ultimately leads to an increase in the performance of such a system. As discussed in previous chapters, the key challenge is to increase acoustic power production within the engine unit, while minimising acoustic losses within the FBP. For this reason, the by-pass configuration has been employed to reduce the acoustic power calculation of losses transmission.

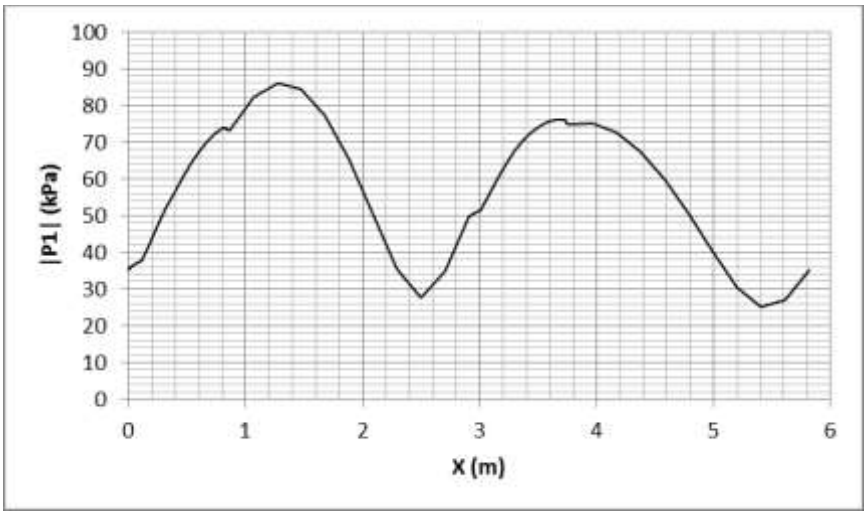

Figure 7.10: Distribution of the amplitude of acoustic pressure along the engine.

Figure 7.10 shows the pressure amplitude distribution along the system. It can be clearly seen that there are two maxima of pressure amplitude along the loop. Firstly, at the beginning of FBP1 close to engine unit 1, and secondly, exactly at engine unit 1, whose values are 86 and 77 kPa respectively. In addition, there are two minimum pressure amplitudes along the loop, both at the ends of the FBPs, which have pressures of 27 and 25 kPa receptively. The ratio between the maximum and minimum pressures for each FBP is known as the standing wave ratio (SWR), which gives an indication about the acoustic reflection along the system.

The current system has two FBPs, as schematically shown in Figure 7.1, leading to a SWR of 2. FBP1 has a SWR equal to 3.1 and FBP2 has a SWR of 3. Consequently, the value of SWR along this system is far from the ideal condition, i.e., SWR for the ideal travelling wave condition should be close to 1). There are many reasons behind that; firstly streaming losses are neglected, and secondly the complex configuration in terms of containing pairs of by-passes, FBPs, inertances, and compliances.

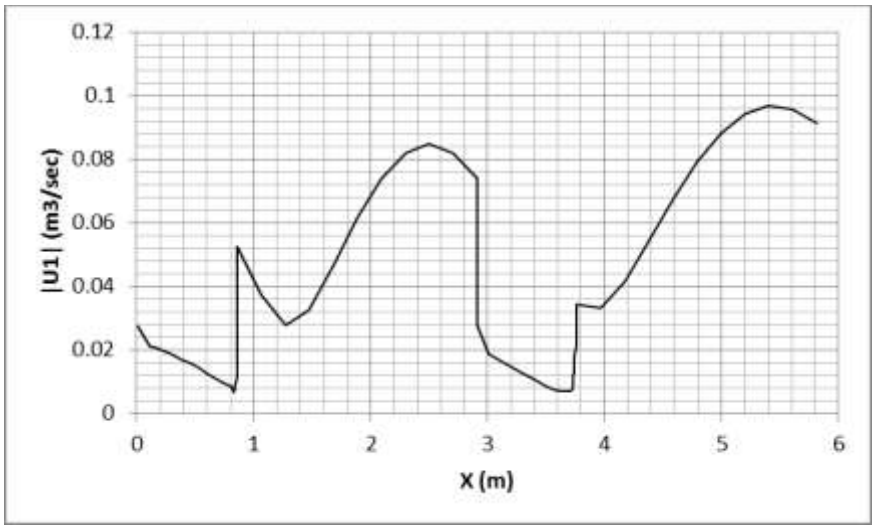

Figure 7.11: Distribution of the amplitude of volumetric velocity along the engine.

Figure 7.11 presents the distribution of volumetric velocity along the system. There are two peaks and two troughs along the loop. The two troughs are exactly located at the end of inertance 1 and 2. In other words, the troughs lie at the beginning of the engine units. The two peaks are located nearly at the end of the FBPs. It should be mentioned here that the small volumetric velocity within the core engine is required to avoid viscous dissipation. The volumetric velocity is the volume of working fluid which passes per unit time. High volumetric velocity leads to high acoustic losses and low efficiency. In the current chapter, the volumetric velocity is reduced in the core engine by using the by-pass configuration. Also, due to the sharp temperature gradient along the regenerator, the volumetric velocity increases significantly.

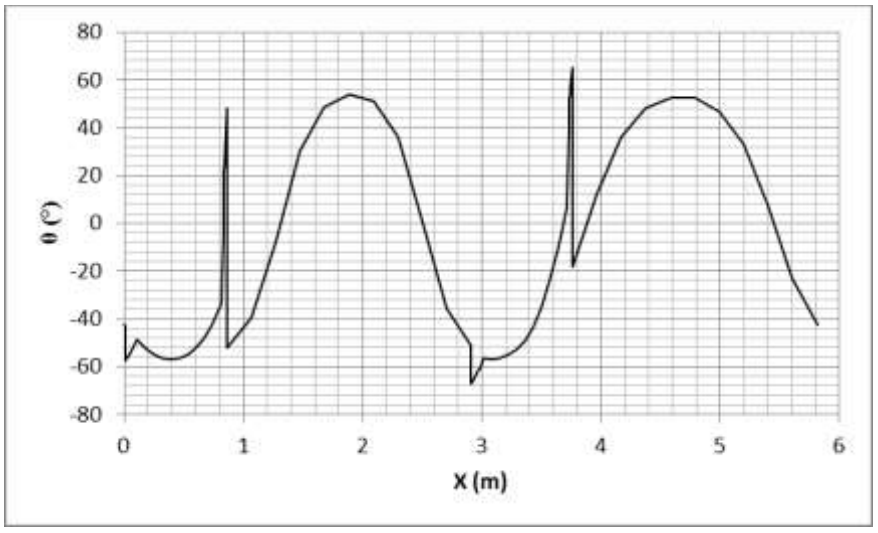

Figure 7.12: Phase angle θ between pressure and velocity oscillations along the engine.

Figure 7.12 shows the phase difference between pressure and velocity oscillation along the loop. Most of the system works in the phase region-52°<Θ<48°, indicating that such a new configuration works far from the ideal condition. It can be seen that compliance and inertance play the role of shifting the phase angle significantly, attempting to force it to the ideal range, i.e., around 0°. There are two spikes (unexpected changes) at the engine units; which is mainly due to the sudden change of area from a small inertance area to a large engine section.

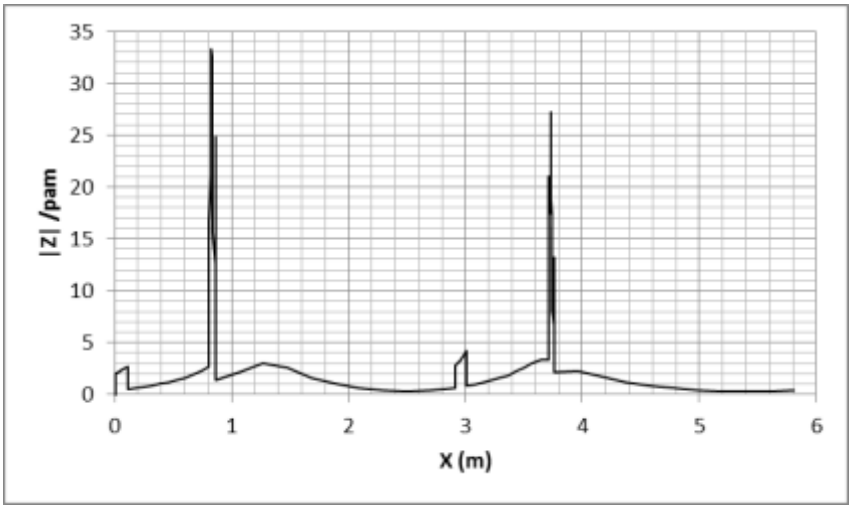

Figure 7.13: Distribution of the normalized specific acoustic impedance along the engine.

Figure 7.13 presents the normalised acoustic impedance along the system. It can be seen that the two engines are located at the high impedance region, with values of $|z|/\rho_m a$ about 33 and 27 respectively. Usually, the amplitude of acoustic impedance should be designed in the range of 15-30 times that of $\rho_m a$ to reduce acoustic losses [10]. It is noteable that the second engine unit works within the optimised normalised acoustic impedance range, but that the first engine unit exceeded this range to 33. This is possibly due to the current complex acoustic system with the multiple by-passes, resonators and inertances. Following the above analysis, it could be inferred that the new configuration has achieved the expected goal, without violating the working principle.

The simulation results of the optimised model are summarised in Table 7.3 below. The heat source temperature (i.e. the solid temperature at HHX1 and HHX2) are set as 129℃ and 265℃ respectively, and the heat sink temperature (i.e., the solid temperature of AHX1 and AHX2) are 30°C and 29.6°C respectively. The net acoustic power production from the engine units (i.e., the difference between its inlet and outlet acoustic power) is about 15 W and 81 W respectively. The heat input to the engine's hot heat exchangers is 407 W and 801 W respectively. The thermal efficiency η_e, defined as the ratio of the acoustic power generated by the engines over the heat input to the engines, is 3.68% and 10.11% respectively. The average engines efficiency is 6.8%.

Table 7.3: Summary of simulation results.

Symbol	Definition	Unit	Engine1	Engine2
T_h	Solid temperature at HHX	°C	129	265
T_a	Solid temperature at AHX	°C	30	29.6
$W_{a,\,in}$	Acoustic power inlet	W	261	262
$W_{a,\,out}$	Acoustic power outlet	W	276	343
$W_{a,\,net}$	Net acoustic power production	W	15	81
$Q_{in,i}$	Heat input to HHX	W	407	801
η_i	Efficiency for each engine	%	3.68	10.11
η_m	Average engine efficiency	%	6.8	

7.3 Two-stage travelling-wave thermoacoustic engine with a by-pass configuration driving two coolers

7.3.1 The concept

The system studied and presented above does not have any acoustic loads. The key challenge for an acoustic system is to verify the extent to which this system can be loaded by an acoustic load, such as an alternator or a cooler. For this reason, a two-stage engine with a by-pass configuration driving two coolers is investigated in this section. Two thermoacoustic heat pumps have been employed to utilise the acoustic power to upgrade heat. This section investigates this new concept based on a series of comprehensive numerical simulations.

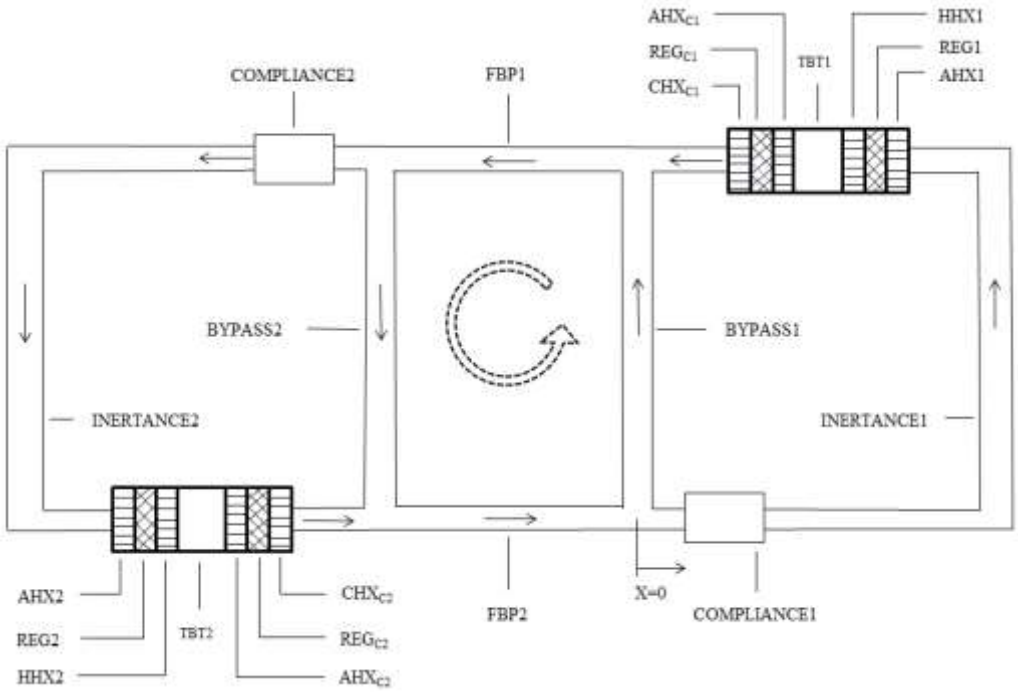

Figure 7.14: Schematic diagram of the two engines, two coolers by-pass configuration system.

The design principles contained in the new by-pass configuration have been successfully implemented in the current design to achieve higher efficiency. As shown schematically in Figure 7.14, there are four stages in this thermoacoustic system, two engines to produce acoustic power and two coolers to consume the generated acoustic power. Each engine stage consists of an ambient heat exchanger (AHX), regenerator

(REG), and hot heat exchanger (HHX). The coolers are designed to consume the acoustic power which is generated in the engine units. Each cooler stage consists of an ambient heat exchanger (AHX), regenerator (REG), and cold heat exchanger (CHX). Furthermore, the system has two by-pass pipes, two inertances, two compliances, two TBTs, and two FBPs.

To simplify the analysis, all the system dimensions have been selected to be easy to design and manufacture. For example, a shell-and-tube heat exchanger has been selected for practical designs. The working gas is nitrogen. The frequency and mean pressure are 50 Hz and 10 bar respectively .All the parameters dimensions are listed in Table 7.4 below

Table 7.4: The dimensions of the system.

	Part	Diameter (m)	Length (mm)	r_h(μm)	Porosity
Engine1	HHX1	0.138	20	30	0.5
	REG1	0.138	10	40	0.78
	AHX1	0.138	20	30	0.5
Engine2	HHX2	0.138	20	30	0.5
	REG2	0.138	10	40	0.78
	AHX2	0.138	20	30	0.5
Cooler1	AHX_{C1}	0.138	20	30	0.5
	REG_{C1}	0.138	8	20	0.78
	CHX_{C1}	0.138	20	30	0.5
Cooler2	AHX_{C2}	0.138	20	30	0.5
	REG_{C2}	0.138	8	50	0.78
	CHX_{C2}	0.138	20	30	0.5

7.3.2 Effect of important design parameters

To find the design parameter of the whole system, there are several important parameters which have an influence on the efficiency of the system, such as length of the by-pass, inertance and compliance, as listed in Table 7.5. These values are selected for the final design.

Table 7.5: Ideal dimensions of the important parameters.

Part	Diameter (m)	Length (m)
By-pass1,2	0.05	1
Compliance1,2	0.0797	0.01
Inertance1,2	0.0422	0.3
FBP1,2	0.071	3.062

The obtained results are shown in the figures below. Figure 7.15 demonstrates engine efficiency as a function of the length of the by-pass pipe. The engine efficiency increases steadily with the increase of the by-pass length to reach maximum efficiency at the ideal by-pass length, then the curve goes down moderately. The ideal value of the length of the by-pass is 1 m.

Figure 7.16 shows engine efficiency as a function of the length of inertance. The engine efficiency curve goes up steadily when the inertance length increases. The maximum efficiency and ideal inertance length are 16.8% and 0.3 m respectively. After that, the curve falls substantially.

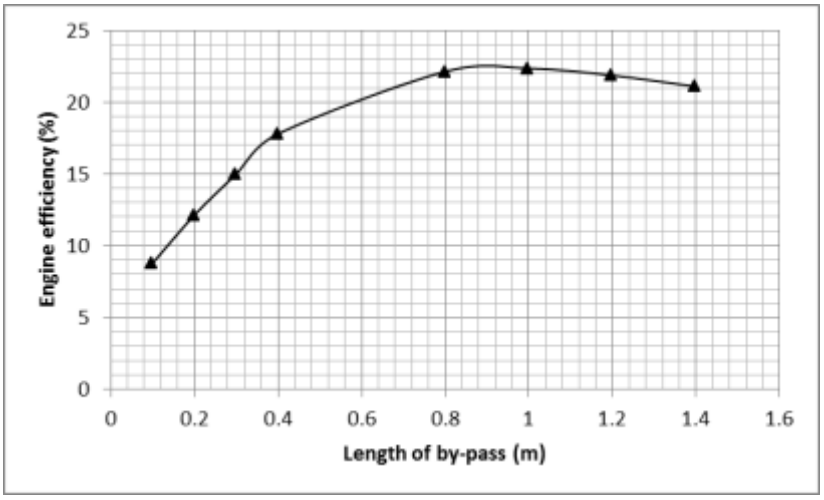

Figure 7.15: Engine efficiency as a function of the length of the by-pass pipe.

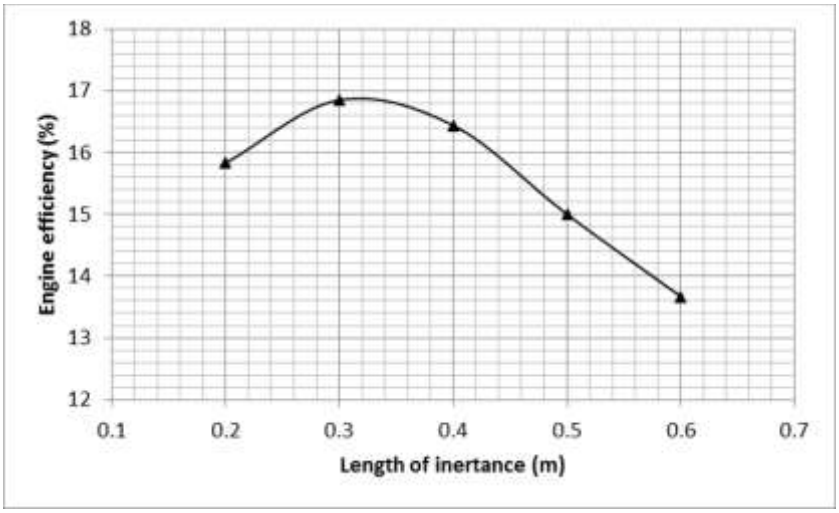

Figure 7.16: Engine efficiency as a function of the length of inertance.

7.3.3 The final design model

The design philosophy of the current thermoacoustic system is to find out two important points. Firstly, how the by-pass configuration with two-stage engines driving two coolers can be used to reduce acoustic losses. Secondly, the extent to which this system is able to drive an acoustic load, i.e., cooler-stage. After a series of comprehensive numerical analyses, the acoustic losses have significantly decreased. Compared with the last section (efficiency is 6.8%), the current system has significantly reduced acoustic losses, leading to overall efficiency of around 20.3%. To further understand the final design, the acoustic wave propagation along the loop needs to be closely analysed. The distribution of acoustic power, pressure amplitude, volumetric velocity, phase angle and acoustic impedance are analysed, as shown in Figure 7.17-Figure 7.21.

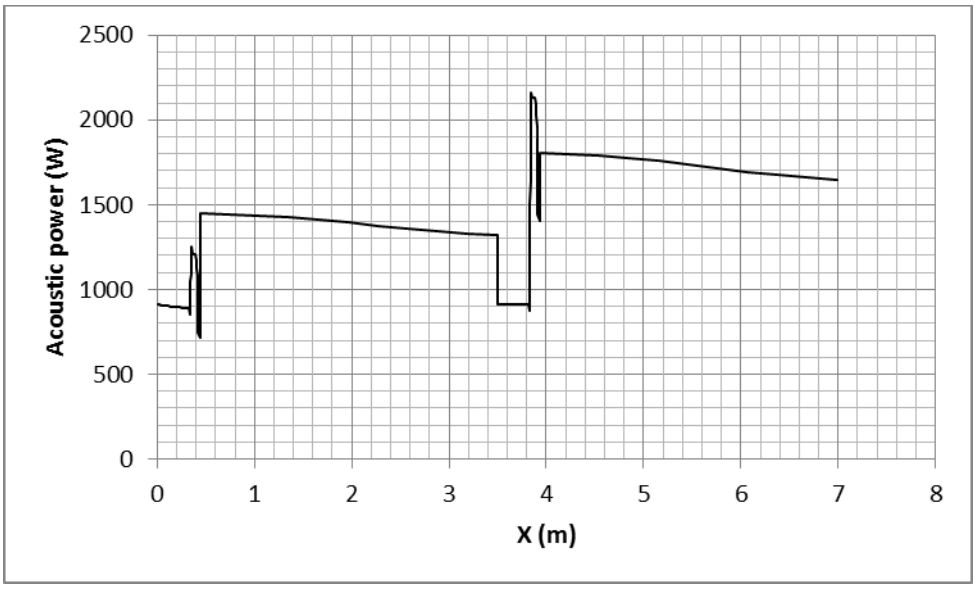

Figure 7.17: Distribution of acoustic power along the engine.

Figure 7.17 shows the distribution of acoustic power along the system. The thermoacoustic engine units generate acoustic power, which is fed into the cooler stages. Around 890 W is fed into engine core 1, and it is amplified to about 1208 W within the regenerator. The amplified acoustic power of 1208 W will be utilised to drive cooler 1, and consumes around 708 W. Exiting the first cooler stage, it merges with the acoustic power coming from by-pass pipe 1, thus the acoustic power increases sharply from 719 W to around 1450 W at Junction 1. Around 35 W of acoustic power was dissipated in FBP1. Around 909 W of acoustic power is fed into engine core 2 and it is amplified to 2131 W. Around 2129 W of acoustic power flows into cooler stage 2 and around 1406 W of acoustic power exits it. This cooler consumes around 723 W. Similarly, the acoustic power leaving cooler 2 merges with the power coming from by-pass 2, and, therefore, the acoustic power flow rises from 1406 W to 1800 W at Junction 2. Around 50 W of acoustic power is dissipated in FBP2. Finally, the remaining acoustic power is then fed back to engine core 1, to start the thermodynamics cycle once again.

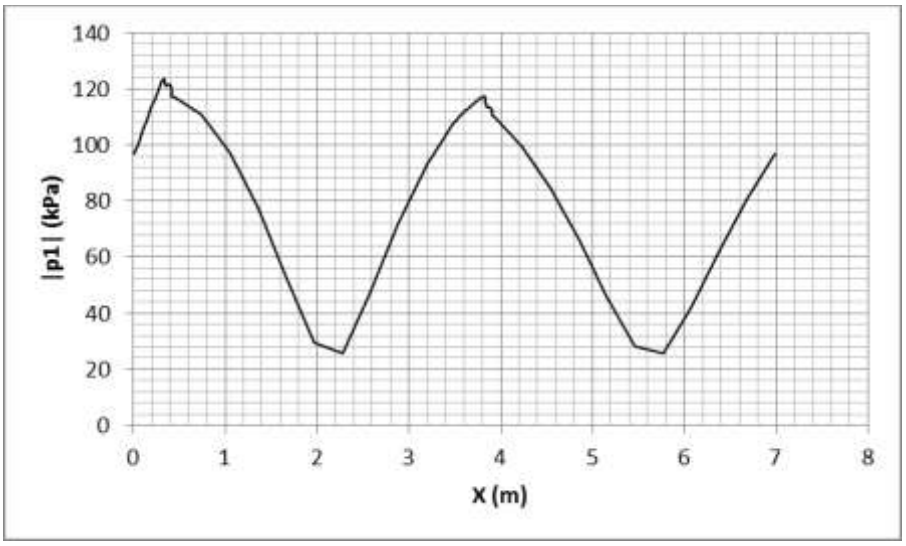

Figure 7.18: Distribution of the amplitude of acoustic pressure along the engine.

Figure 7.18 shows the pressure amplitude distribution along the system. It can be clearly seen that there are two maxima and two minima pressure amplitudes along the loop. The two maximum values are 124 and 118 kPa respectively, located at the two engine cores, and the two minimum values are 24 kPa, located in the middle of the FBPs. The SWR is 5.1 for FBP1, and is 4.9 for FBP2. Although they are far from the ideal value they are close to each other, which reflect the fact that the new configuration does not violate the working principle.

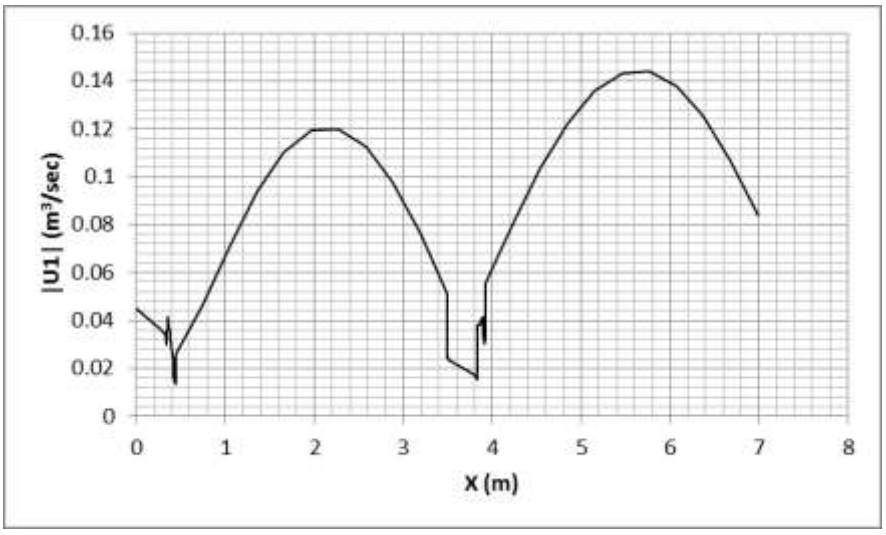

Figure 7.19: Distribution of the amplitude of volumetric velocity along the engine

Figure 7.19 presents the distribution of volumetric velocity along the system. There are two peaks and two troughs along the loop. The two troughs are located exactly at the end of the inertance tubes, in other words at the beginning of the two engine units. The two peaks are located nearly in the middle of the two FBPs. It should be mentioned here that the small volumetric velocity within the engine core is required to avoid viscous dissipation. High volumetric velocity leads to high acoustic losses and low efficiency. Due to the sharp temperature gradient along the regenerator, the volumetric velocity increases significantly.

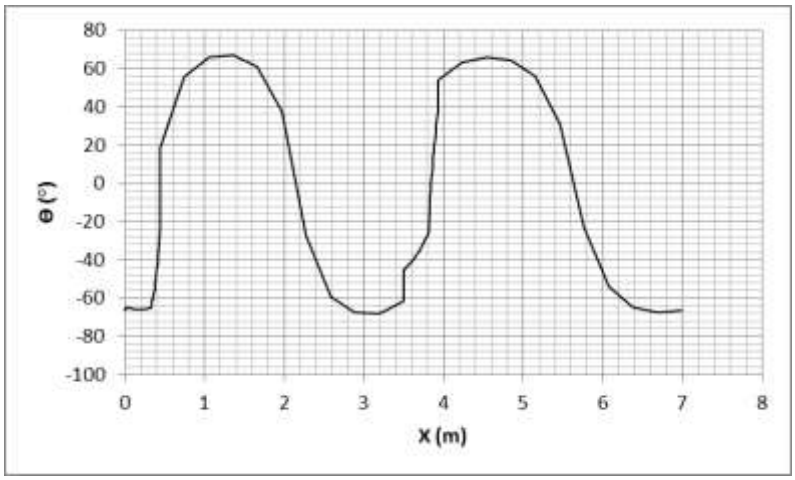

Figure 7.20: Phase angle θ between pressure and velocity oscillations along the engine.

Figure 7.20 shows the phase difference between pressure and velocity oscillations along the loop. It can be found that the system as a whole works in the region of $-68° < \Theta < 68°$. The large phase differences between oscillation pressure and velocity are possibly due to the complexity of the design and the resultant reflections.

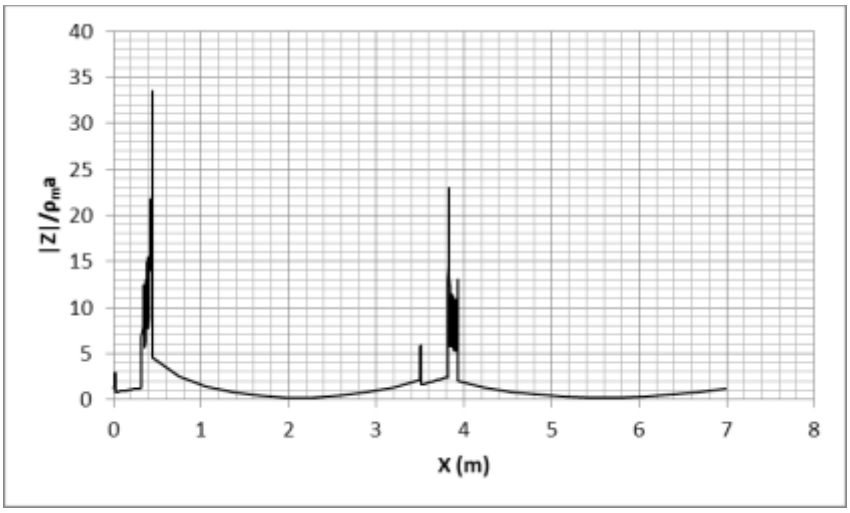

Figure 7.21: Distribution of the normalized specific acoustic impedance along the engine.

Figure 7.21 presents the normalised acoustic impedance along the system. It can be seen that the two engines are located at the high impedance region, with values of $|z|/\rho_m a$ around 33 and 23 respectively. As discussed above in Figure 7.18 and Figure 7.19, the engine units have the highest pressure oscillation and lowest volumetric velocity, which in turn leads to a high amplitude of acoustic impedance. Usually, the amplitude of acoustic impedance should be designed in the range of 15-30 times of $\rho_m a$ to reduce the acoustic losses [10]. It is noteable that the second engine unit works within the optimised normalised acoustic impedance range, but that the first engine unit exceeded this range to 33. This is possibly due to the current complex acoustic system with the multiple by-passes, resonators and inertances.

Finally, the simulation results are summarised in Table 7.6. For the engine stages, the heat source temperatures (i.e. the solid temperature at HHX1 and HHX2) are set as 223°C and 535°C respectively, and the heat sink temperatures (i.e., the solid temperature of AHX1 and AHX2) are 30°C and 21.5°C respectively. The net acoustic power production from the engine units (i.e., the difference between its inlet and outlet acoustic power) are about 318 W and 1222 W respectively. The heat input to the engine's hot heat exchangers is 2240 W and 3851 W respectively. The thermal efficiency η_e is defined as the ratio of the acoustic power generated by the engines over the heat input to the engines, are 21.8% and 18.77% respectively. The average engine

efficiency is 20.29%, which is equivalent to 40% of the Carnot efficiency at the tested temperature range.

As for the cooler stages, cooler 1 removes 708 W of thermal energy at -36°C, and rejects it at 64°C. Also cooler 2 removes 1200.5 W of heat energy at 188°C, and rejects it at 372°C. The cooler's coefficient of performance (COP) is defined as the ratio of the heat absorbed at CHX_C over the acoustic power it consumes. The calculated COP1 is about 1.44, and the calculated COP2 is about 1.66, resulting in the average cooler coefficient of performance (COP) of 1.55, which is equivalent to 64% of the Carnot COP at this temperature range.

Table 7.6: Summary of simulation results.

Symbol	Definition	Unit	Engine1	Engine2	Cooler1	Cooler2
T_h	Solid temperature at HHX	°C	223	535	-	-
T_a	Solid temperature at AHX	°C	30	21.5	64	372
T_c	Solid temperature at CHX_C	°C	-	-	-36	188
$W_{a,\,in}$	Acoustic power inlet	W	890	909	1207	2129
$W_{a,\,out}$	Acoustic power outlet	W	1208	2131	719	1406
$W_{a,\,net}$	Net acoustic power production (engine) or consumption (cooler)	W	318	1222	488	723
$Q_{in,i}$	Heat input to HHX (engine) or AHX_C (cooler)	W	2240	3851	708	1200.5
η_i	Efficiency for each engine	%	21.82	18.77		
η_m	Average engine efficiency	%	20.29			
COP	Coefficient of performance for each cooler				1.44	1.66
COP_m	Average Coefficient of performance				1.55	
η_{Carnot}	Carnot efficiency: (Th-Ta)/Th for each Engine	%	39	64		
$\eta_{Carnot\ m}$	Average Carnot efficiency	%	51			
COPC	Carnot COP: Tc/(Ta-Tc) for each cooler				2.39	2.49
$COPC_m$	Average Carnot COP				2.44	
η_r	Percentage of Carnot efficiency	%	40			
COPR	Percentage of Carnot COP	%			64	

This research shows that this new configuration has the potential for developing a low cost thermally driven heat pump system, which can achieve high efficiency. Because of

the presence of a two-stage engine, the system needs to employ two bypasses. This ultimately leads to the creation of a rectangular resonator feedback at the centre of the system, which is called a Travelling Wave Resonator (TWR). The flow direction of the generated acoustic power inside the TWR is counterclockwise,

7.4 Conclusions

This chapter presents a series of comprehensive numerical analyses of two-stage engines by-pass type travelling-wave thermoacoustic engines. This study has two parts; with coolers and without coolers. Nitrogen at 10 bar is used as a working gas, and the engine has an operating frequency around 75 Hz. The average engine efficiency of the system without acoustic load is 6.8%. When the engine is loaded with a thermoacoustic cooler, the simulation results show that the whole system can achieve a thermal efficiency of 20.3%, which is equivalent to 40% of the Carnot efficiency at the tested temperature range. Cooler 1 consumes 488 W of acoustic power to remove 708 W of thermal energy at about -36°C, and rejects it at 64°C. Cooler 2 consumes 723 W of acoustic power to remove 1200.5 W of heat energy at about 188°C, and rejects it at 372°C, which leads to a COP of about 1.55; that is, equivalent to 64% of the Carnot COP under these operating conditions.

The novelty of such a by-pass configuration is that the by-pass and FBPs actually create a pure travelling wave resonator. The engine unit extracts small amounts of acoustic work from the resonator, amplifies it and sends it back to it. As the pure travelling wave resonator has very low losses, it requires very little acoustic power to maintain an acoustic resonance.

According to the results shown in this section, it can be found that the design strategies proposed by de Blok and Backhaus can be implemented in the current travelling wave thermoacoustic engine driven cooler system. It was found that there is a trade-off between engine efficiency and cooler COP. This research demonstrates that this new configuration has the potential to develop a low cost thermally driven heat pump system.

Chapter 8 Investigation of side-branched Helmholtz resonator to tune phase in looped-tube travelling wave thermoacoustic engine

8.1 Introduction

The studies throughout the previous chapters have been performed numerically. These chapters were focused on the numerical investigation of looped-tube travelling wave thermoacoustic engines with a by-pass configuration, and obtained some interesting results. The by-pass configuration was studied in different cases throughout the preceding chapter, to find out how this system works without violating the thermodynamics principles. Despite the different cases studied, the results were encouraging. Based on this, it is important to understand looped-tube travelling wave thermoacoustic engine experimentally. Thus, it is very useful scientifically to conduct some practical studies that strengthen and support the theoretical studies in previous chapters. This leads to the convenience of comparison between the numerical and experimental works.

The travelling-wave thermoacoustic engine utilises a compact acoustic network to obtain the correct time-phasing between the acoustic velocity and pressure oscillations within the regenerator, to force gas parcels to execute a Stirling-like thermodynamic cycle, so that thermal energy can be converted to mechanical work (i.e., high-intensity pressure waves). It is therefore crucial to tune and control time-phasing (i.e. the phase angle between pressure and velocity oscillations) carefully to improve the performance of thermoacoustic engines. This chapter reports a new phase tuning method, i.e., using a side-branched volume to tune the time-phasing within a looped-tube travelling wave thermoacoustic engine.

One of the key challenges in developing a high efficiency travelling wave thermoacoustic engine is to accurately control and tune the phase angle between the acoustic pressure and velocity to near in-phase (i.e., travelling-wave condition). Various techniques have been proposed and investigated in recent decades, such as the inertance

tube [67, 68 and 69], side branched stub [52, 56], side branched loudspeakers [63], etc. This study presents a new phase tuning technique, i.e., a side-branched Helmholtz resonator, to tune the phase angle between the acoustic velocity and pressure oscillations in a looped-tube travelling wave thermoacoustic engine. The function of such a tuning mechanism is firstly modelled and demonstrated through a series of comprehensive numerical simulations based on DeltaEC software (Design Environment for Low-amplitude ThermoAcoustic Energy Conversion). An experimental rig is then designed and constructed. The obtained experimental results have verified the numerical model. The performance of the engine is significantly improved after the installation of the side-branched Helmholtz resonator, and then the proposed phase tuning technique has been demonstrated experimentally.

8.2 Experimental setup

This section of the current chapter focuses on the instrumentation and experimental procedure applied in this research, and the experimental apparatus including the details of the engine and the RC-load is described. The experimental parts which are used in this thesis have been designed by using SolidWorks software (as shown in appendix two) and then manufactured in the workshop at the University of Glasgow.

8.2.1 Key components

The thermoacoustic engine core consists of three vital parts: AHX, HHX, and REG, where the thermoacoustic processes take place. They are described in the next section in detail. The method of design of such heat exchangers is different from one researcher to another, depending on how much heat the system needs to be supplied, and how much heat needs to be rejected from the system.

8.2.1.1 Ambient Heat Exchanger (AHX)

The heat exchangers are one of the main components of any thermoacoustic device; they keep a temperature gradient along the stack or regenerator. AHX transfers heat

energy from the working fluid to an external sink of heat such as ambient-temperature water. It worth to saying that a secondary ambient heat exchanger (SAHX, which is exactly the same design of AHX) is used in the thermoacoustic system to cool the TBT, which is usually located behind the HHX.

The ambient heat exchanger is made of a copper block which is 65 mm in diameter and 27 mm long. Gas passages are made of 204 holes (I/D 3 mm) drilled in parallel to the heat exchanger's centreline. Two holes with the diameter of 6 mm are drilled perpendicular to the heat exchanger to pass the cooling water. The porosity of the heat exchanger is 28%. As shown in Figure 8.1 below:

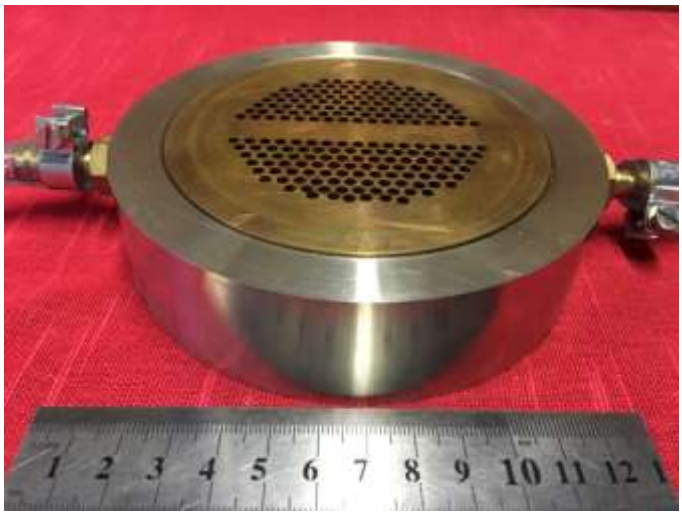

Figure 8.1: Photograph of the ambient heat exchanger.

8.2.1.2 Hot Heat Exchanger (HHX)

The hot heat exchanger transfers heat from an external source of heat to the working gas in thermoacoustic system. The HHX has been made from Nickel-Chromium resistance wire (NIC-80-020-125), which was inserted inside ceramic tubes to prevent any electrical contact with the metal surface. This resistance wire is formed as a coil with 3.2 mm diameter, and the wire diameter is 0.51 mm, as shown in Figure 8.2 (a). The ceramic tubes (with resistance wire) should line up inside a cylindrical metal container, as shown in Figure 8.3.

The diameter and length of HHX are 65 and 30 mm, respectively. The porosity of the hot heat exchanger is around 50%. The length of the ceramic tube is 25 mm, and the outside and inside diameters are 6.4 and 4 mm, respectively, as shown in Figure 8.2 (b). The total resistance of this heater is about 5 Ohms. Electrical power is supplied to the heater at a maximum voltage of 50 V (which can be varied in the range of 0-50 V) and a maximum current of 10 A from an AC power supply by using a feed-through to maintain a good pressure seal. Accordingly, the heat energy is supplied to the system in the range between 0 and 500 Watt.

Figure 8.2: Photograph of a: the wire resistance and b: ceramic tubes.

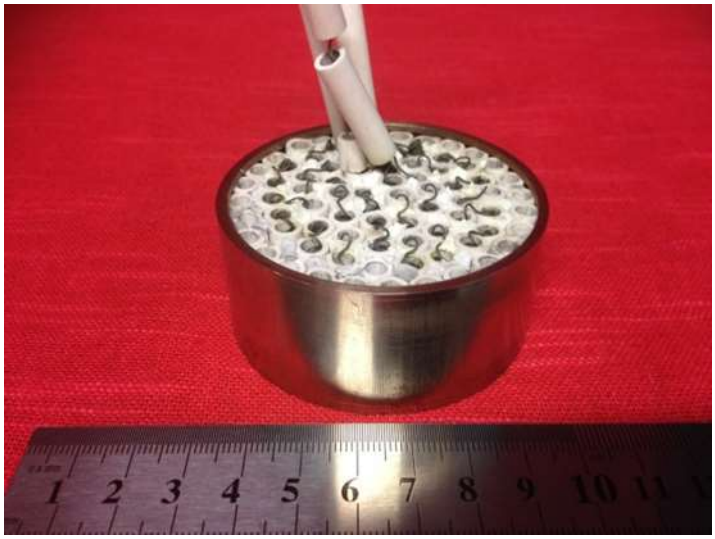

Figure 8.3: Photograph of the hot heat exchanger (HHX).

8.2.1.3 Regenerator (REG)

The regenerator is made of stainless steel mesh screen wire discs with a mesh number of 50, as shown in Figure 8.4. The disk diameter is 65 mm. The diameter of the wire and the aperture width are 0.14 mm and 0.375 mm, respectively. In total, 60 mesh discs are placed inside 20 mm long stainless steel casing (1 mm in thickness). The calculated porosity and hydraulic radius are 78.4% and 126.77 μm, respectively, as demonstrated later in this chapter.

Figure 8.4: Photograph of the case of the regenerator and mesh screen.

To further clarify the mesh screen, the dimensions and properties are highlighted in the schematic figure shown in Figure 8.5.

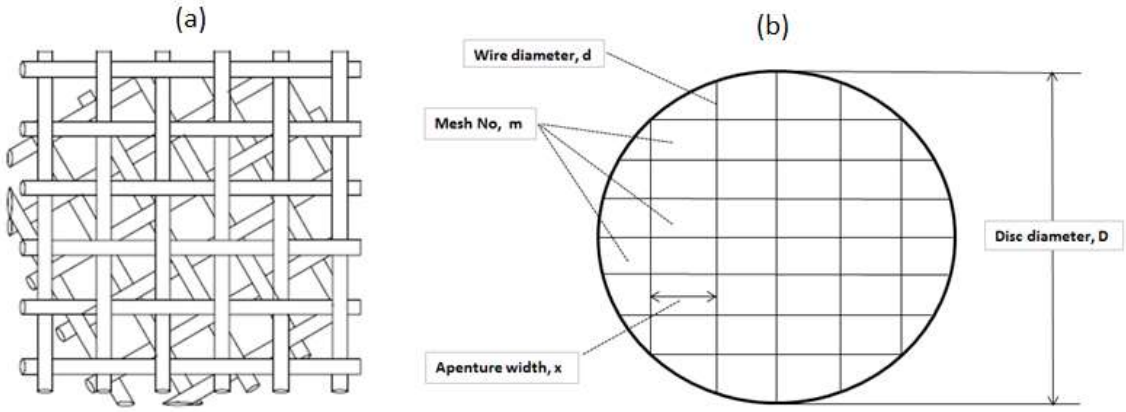

Figure 8.5: A tortuous porous medium (mesh screen), a: a screen bed [79], b: schematic of the mesh screen.

where *D* is the disc diameter, *d* is the wire diameter, *m* is the mesh number, and *x* is the aperture width. All these dimensions are in mm. The companies providing these mesh screen give information regarding *D*, *d*, and *m* only. The hydraulic radius and porosity of the mesh screen are calculated using

$$m = \frac{25.4}{x+d}, \tag{8.1}$$

$$r_h = \frac{\gamma_{pf}\left(x+d\right) - \frac{\pi d}{2}}{2\pi}, \tag{8.2}$$

where γ_{pf} the effective thickness, which is defined as the screen packing density. So γ_{pf} =2 corresponds with the non-shifted situation. The normal value of γ_{pf} is expected to be around 2,

$$\varnothing = 1 - \frac{\pi d}{2\gamma_{pf}\left(x+d\right)}. \tag{8.3}$$

The hydraulic radius r_h of the regenerator is defined as the ratio of the total gas volume to gas-solid interface surface area. The porosity $\varnothing$ of the regenerator is the ratio of gas volume to the total regenerator volume [74].

With respect to the mesh screens which have been used during the experimental work, the above equations are dedicated to calculating the *x*, r_h, and ∅ respectively. The wire diameter is 0.14 mm and the mesh number is 50, leading to the aperture width 0.368 mm, r_h=1.267x10^{-4} m, and ∅=78.4%, respectively.

8.2.2 Electric and water supply

8.2.2.1 Electric power supply

To avoid potentially dangerous electrical contact between the HHX wire resistance and the metal surface of the engine house during the experimental processes, the normal voltage 250 V has been decreased to 50 V using a transformer (2 Output Toroidal Transformer, 1kVA, 50V, AC). This transformer provides the system with 500 Watt (50 Vx10 Am) for each output. Electrical power is supplied to the heater at a maximum voltage of 50 V (which can be varied in the range of 0-50 V) and a maximum current of 10 A from an AC power supply, by using a feed-through to maintain a good pressure seal.

8.2.2.2 Water cooling system

In order to remove the heat energy from the system, an ambient heat exchanger has been employed. Water with ambient temperature is used to cool the system which is fed to the ambient heat exchanger using a water pump (40 l/min, 65Watt). The circulation water used the AHX is supplied from a 1000 Litre IBC Carboid Water Tank through PVC transparent tube (6mm ID, 12mm OD), as shown in Figure 8.6 below.

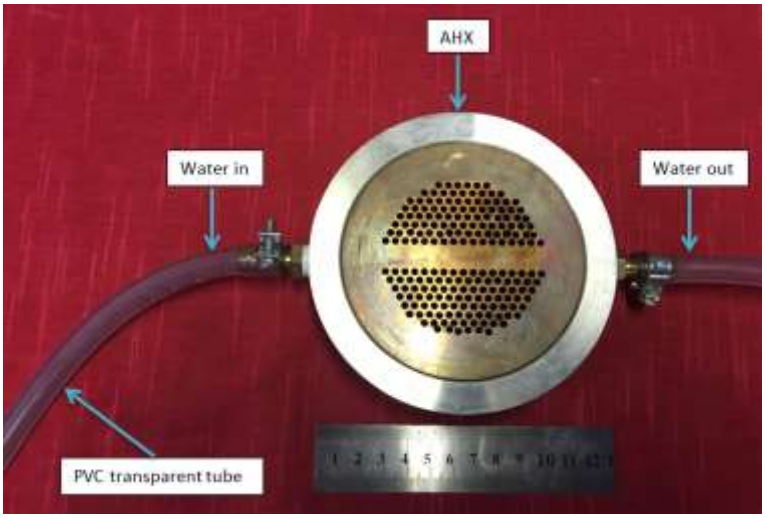

Figure 8.6: Photograph of the water cooling system for the AHX.

There are two additional components which have been used in the experimental testing. Firstly, the RC-load, which is coupled to the thermoacoustic system in order to consume the acoustic power and provide a means to determine the system efficiency accurately. Secondly, the side-branched volume, which is also connected to the thermoacoustic system in order to tune the phase angle between pressure and velocity towards zero, as demonstrated in detail in next two sections.

As for the RC-load; it is well known that generated acoustic power in an acoustic system will be dissipated in the FBP if there is no acoustic load connected to this system. Quantitative experimental measurements require the addition of an acoustic load to the system to consume any generated acoustic power, leading to the possibility of calculating the system performance accurately. The RC-load consists of a needle valve (mountiring hydraulic flow control valve 201012) and compliance which are connected in series, as shown in Figure 8.7-Figure 8.8. The volume of the compliance is 1512.8 cm^3.

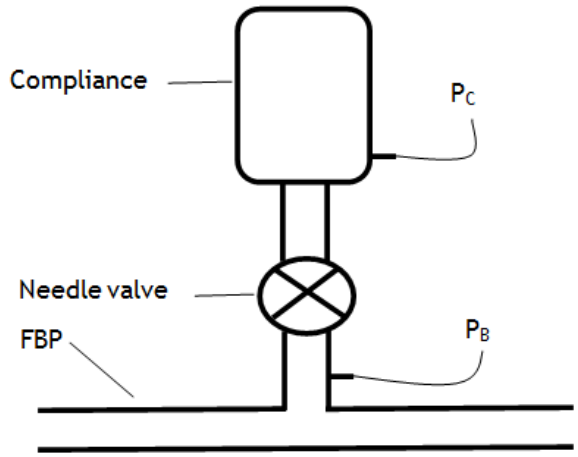

Figure 8.7: Schematic of the RC-load.

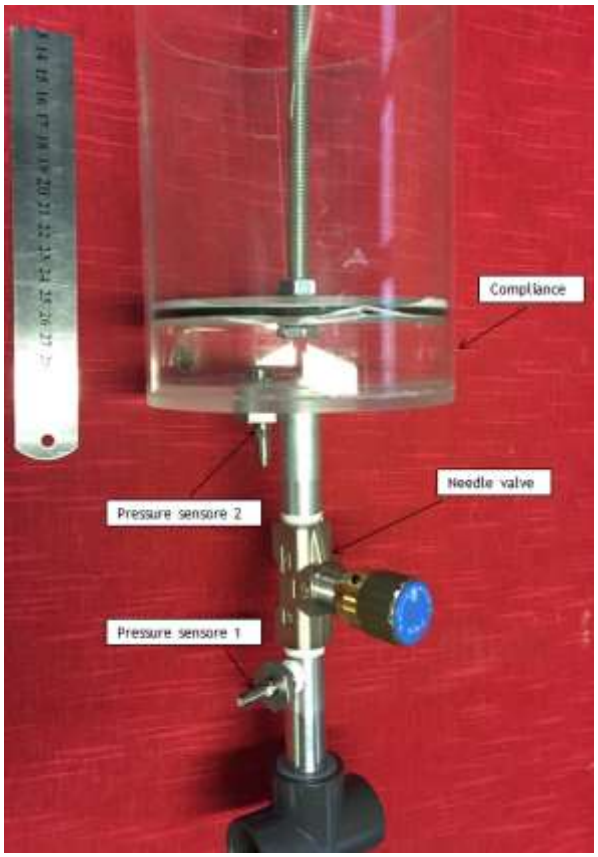

Figure 8.8: Photograph of the RC-load.

Helmholtz resonator; a side-branched Helmholtz resonator has been used to tune the phase angle between the acoustic velocity and pressure oscillations in a looped-tube travelling wave thermoacoustic engine. The Helmholtz resonator has been made of a clear plastic cylinder within which a piston works manually up and down. The outer diameter of this piston is equal to the inner diameter of the cylinder. It should be mentioned here that to maintain a good pressure seal between the working gas and the ambient, the contacting surface area between the cylinder surface and the piston need to be sealed. This has been done by employing an o-ring around the outer circumference of the piston. Obviously, the Helmholtz resonator was closed at one end and open to the system at the other, as shown in Figure 8.9.

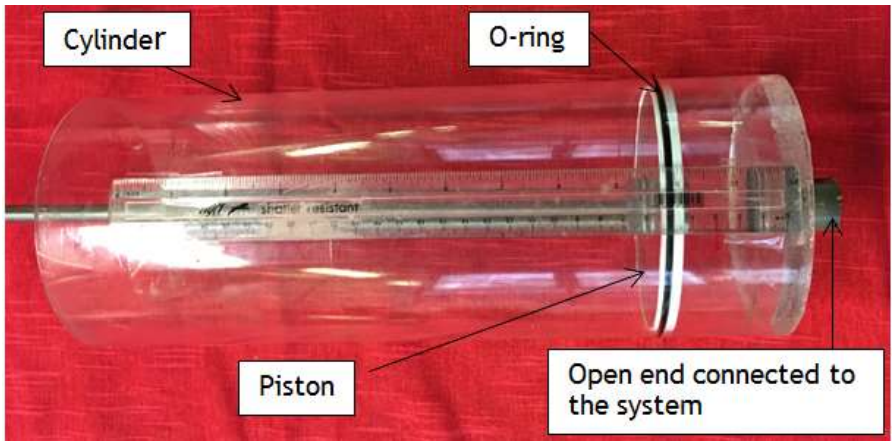

Figure 8.9: Photograph of Helmholtz resonator.

8.2.3 Data acquisition system

The required data from the current thermoacoustic experimental system is temperature, pressure, and phase angles between the pressure signals. A thermocouple is employed to measure the temperature, which is connected to the selected location, with the signal being passed through a data acquisition card (DAQ), and the data displayed and saved on the computer. As for the pressure, a pressure sensor is connected to the selected location, then to the DAQ and thereafter to the computer, to show and save the pressure signals. It should be mentioned here that the pressure signals unit is mV which is converted into Pa using a scaling factor for each pressure sensor. Phase angles between the pressures signals can be measured using a lock-in amplifier. The measurements equipment is described briefly below.

- A data acquisition card (OMEGA OMB-Daq Temp 16-bit/200-kHz Data Acquisition Module) has been used to record the signals from the thermocouples and pressure sensors.

- The phase angles between the pressure signals and the frequency for the system are measured by a SR830 DSP lock-in amplifier with an accuracy of 0.01°.

- The signal is also visualised and saved using the oscilloscope. Programming code is then used to calculate the wave frequency and analyse the wave into its different modes, to obtain the acoustic power.

To measure the pressure amplitudes and the phase angle between them, three pressure sensors (PCB PIEZOTRONICS model 113B27) are installed at three different positions. These pressure sensors were calibrated by the manufacturer, as shown in appendix five. The voltage which is provided to the system is measured by multimeter (1705 TRUE RMS PROGRAMMABLE MULT TIMETER). Also, the voltage which is generated by alternator is measured by a small multimeter (ISO-TECH IDM 73). Type-K thermocouples are installed to measure the temperatures at both ends of the regenerator and within the heater. The thermocouples were certified by the manufacturer to conform to K-Type calibration, which gives an accuracy of ±2 degrees. It should be mentioned here that to reduce heat loss from the high temperature section of the thermoacoustic engine core to the ambient air, the TBT is wrapped with a Ceramic Fibre Insulation Blanket (Ceramic Fibre Blanket 25mm For Kiln Furnace Forge – VITCAS, 128 Kg/m^3 density).

8.2.4 Acoustic power measurements in TA systems

To calculate the acoustic power, the pressure amplitude and volumetric velocity and the phase angle between them are required. The pressure amplitude can be measured directly by using a pressure sensor. However, it is much more challenging to measure the volumetric velocity compared to measuring the pressure amplitude. To overcome this problem there are two methods to measure the volumetric velocity, direct and indirect.

In the indirect method, the volumetric velocity is estimated by reading the signals from the pressure sensors across for example the FBP, acoustic load, compliance [7].

In the direct method, the volumetric velocity has to be measured by using a hot wire anemometer or a laser-based velocimetry technique (Laser Doppler Velocimetry-

LDV or Particle Image Velocimetry-PIV). The laser method has some practical drawbacks; it is expensive, complex, sensitive to gas density, leading to the inability to use it to measure the acoustic power in complex thermoacoustic configurations and in high-pressure systems. While the hot wire techniques are sensitive to gas density and provide the square of the velocity amplitude, this is problematic for phase measurements, and makes them less suitable for high power thermoacoustic measurements [86].

Because of the disadvantages and limitations of the direct method, the indirect methods are used. There are two common ways for the indirect method to be used the two-microphone method and RC-load method, as described in detail in the next section.

8.2.4.1 Two-microphone method

This technique is based on using two pressure sensors across a duct (with a short distance) in the thermoacoustic system, as schematically shown in Figure 8.10. By measuring the pressure amplitude at A and B, along with the phase angle between the two readings, this can be used to estimate acoustic power transferred through the mid-point location between locations A and B [1].

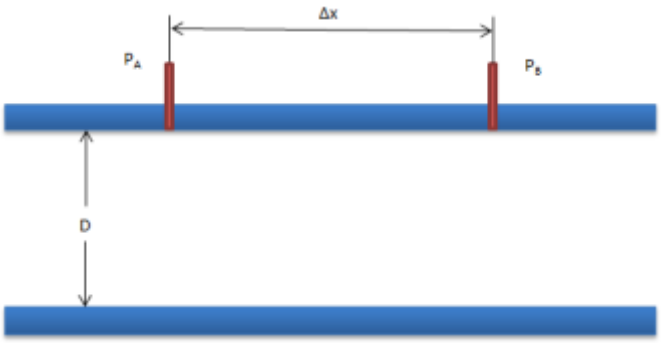

Figure 8.10: Schematic diagram of two-microphone method.

The following expression is used to calculate the output acoustic power

$$\dot{E} = \frac{A}{2\omega\rho_m \Delta x} |\, p_A \,||\, p_B \,| \sin\theta_{AB}, \tag{8.4}$$

where:

A is the area of the resonator (m^2)

ω is the angular frequency (rad/sec)

ρ_m is the mean density (kg/m^3)

Δx is the distance between A and B

p_A is the amplitude pressure at the location A (Pa)

p_B is the amplitude pressure at the location B (Pa)

θ_{AB} is the phase angle difference between two pressure signals (°).

This method uses the complex signals of two pressure sensors to estimate the acoustic power. However, this method has some practical drawbacks.

- a large distance between both sensors is required (» 0.6 m)
- needs a constant diameter section between both sensors
- requires lock-in amplifiers with an accuracy of 0.01° to get sufficient accuracy for the phase measurements
- a correction term is needed to compensate for loss between both sensors [86].

8.2.4.2 RC-acoustic load method

The schematic of this method is shown in Figure 8.7. This method utilises the presence of an acoustic load to consume acoustic power. Similar to the previous method, there are two pressures sensors locations; however, in the current method, these locations have been selected before and after the acoustic load. It is worth noting here that the RC-acoustic load method is more accurate than the two-microphone method, which is why it is used in this study to calculate the generated acoustic power.

$$\dot{E} = \frac{\omega V}{2\gamma p_m} | p_B || p_C | \sin\theta_{BC}, \tag{8.5}$$

where:

ω is the angular frequency (rad/sec)

V is the volume of the compliance (m^3)

γ is the ratio of specific heat capacity

p_m is the mean pressure (Pa)

p_B is the amplitude pressure before the Needle valve (Pa)

p_C is the amplitude pressure after the Needle valve at the compliance (Pa)

θ_{AB} is the phase angle difference between two pressure signals (°).

Equation (8.5) describes the acoustic power calculation corresponding to the Rc-load method, which depends dramatically on the values of pressure amplitude at the two locations P_B and P_C.

In conclusion, the two-microphone method may cause an error in the measurement of the phase difference of the two sensors, leading to an error in acoustic power measurement. Accordingly, the effect of phase angle measurement error should be minimised by separating the sensors by velocity antinode distance [74]. In addition there is a large distance (0.6 m) between the sensors so the measuring device should have sufficient accuracy (better than 0.01°) for the phase measurement [87].

The RC-load method gives a straightforward and reasonably accurate result for evaluating the acoustic power [74]. It has been broadly used in thermoacoustic devices [47, 88, 89 and 90].

For these reasons the RC-load method is more accurate than the two-microphone method, so it is used in this study to calculate the generated acoustic power.

8.2.5 Integrated system

Figure 8.11 and Figure 8.12 show the integrated engine core when all the engine's components are put together. It should be mentioned here that the sound wave is passing firstly through the AHX and then to the REG, and finally to the HHX.

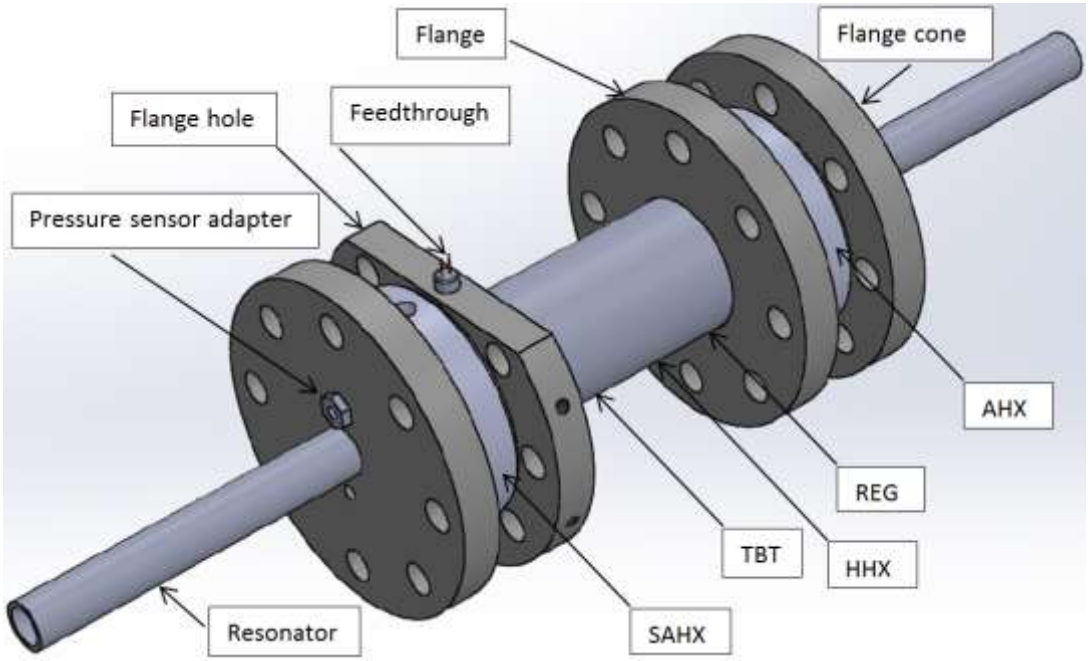

Figure 8.11: Thermocoustic engine unit as a whole by SolidWork.

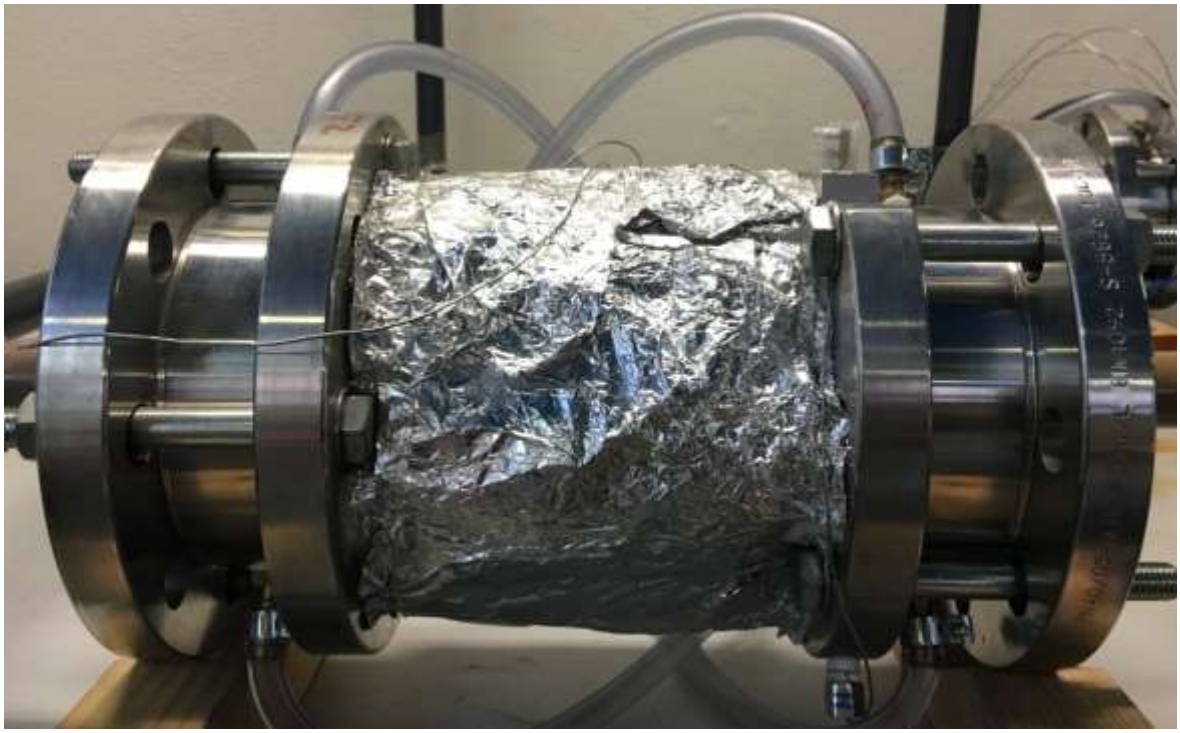

Figure 8.12: Photograph of the thermoacoustic engine unit.

The experimental thermoacoustic system as a whole and all the measurement equipment are shown in Figure 8.13 and Figure 8.14.

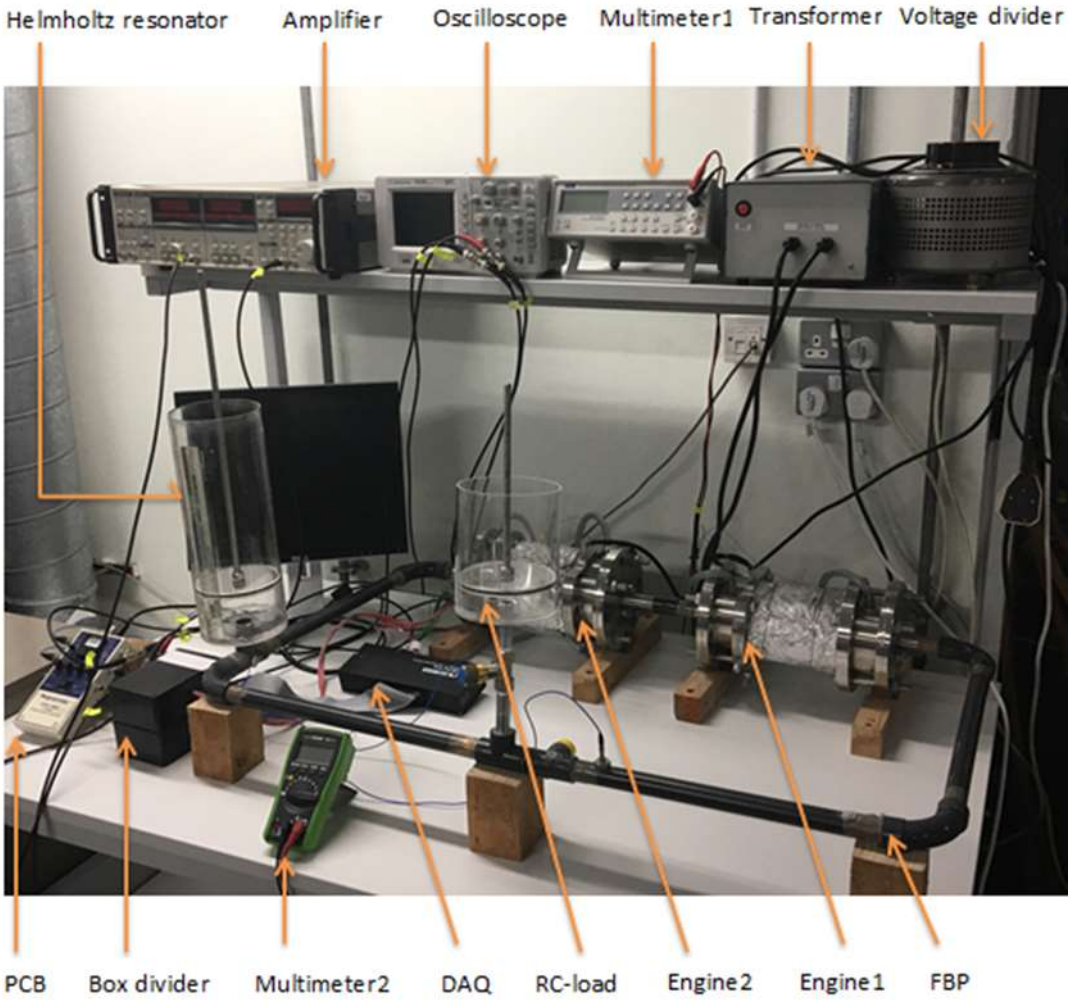

Figure 8.13: Photograph of the experiment system as a whole and all the measurement equipment.

8.2.6 Experimental procedures

Figure 8.14 shows a flow chart of steps in the experimental system, and the measurement tools. The cycle starts with providing power to the system using a transformer, and a voltage divider to govern the supplied power. Electrical power is supplied to the heater at a maximum voltage of 50 V, which can be varied in the range of 0-50 V, and a maximum current of 10 A from an AC power supply by using a feed-through to maintain a good pressure seal.

The main objective of thermoacoustic research is to enable utilisation of low grade waste heat commonly released into the environment by many industrial processes. However, to meet laboratory requirements and create a comfortable working environment, the heat source has been replaced by an electrical source. The power supply is fed to the hot heat exchangers, which in turn transfers it to the regenerator. The heat generated by the hot heat exchanger heats up the first side of the regenerator (the hot side of the regenerator). Part of this heat reaches the other side of the regenerator (the cold side of the regenerator) by conduction.

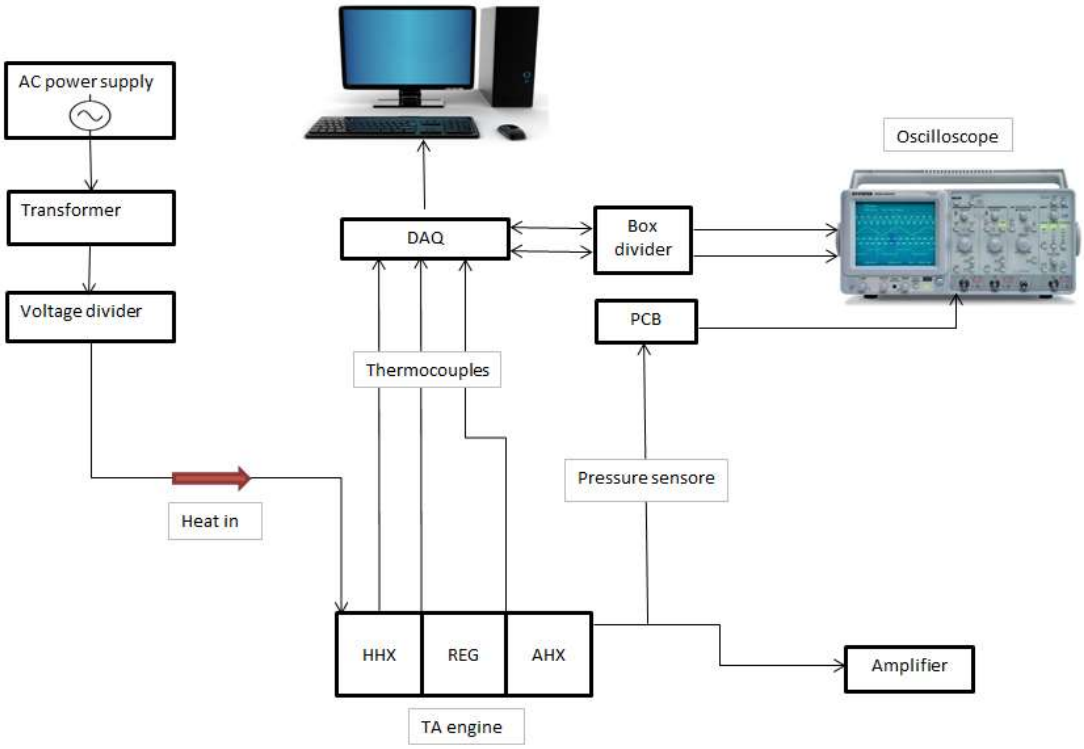

Figure 8.14 : Schematic of the thermoacoustic engine system and measurement instrumentation.

The temperature of both HHX and the hot side of REG increases dramatically, resulting in the system reaching the onset temperature (the temperature difference between the two ends of REG). Therefore the system starts to spontaneously acoustically oscillate. At this point, the working gas waves begin to transfer the heat energy from HHX to the hot side of REG faster, leading to a sharp decrease in the temperature of the HHX and a

dramatic increase in the temperature of the hot end of the REG. Thereafter, both the temperature of HHX and REG reach the steady state, with the continuation of the spontaneous acoustic oscillations, producing acoustic power accordingly.

To measure and monitor the temperature along the system, three K-type thermocouples are located at three locations, the centre of the HHX, hot side of the REG, and cold side of the REG. These thermocouples are then connected to the data acquisition card (DAQ) which is in turn connected to the computer.

The pressure sensors are connected to the data acquisition card (DAQ) to measure and log the pressure values, and to the PCB device display signals using the oscilloscope. It should be mentioned that the DAQ reads the pressure in volts, so to convert it to Pascals it is multiplied by a conversion factor supplied with the pressure sensors.

After obtaining the values of pressure, temperature, and the phase angle between pressure signals, the thermoacoustic system can be analysed and evaluated. The DAQ data enables plotting of temperature distribution curves in real time, which in turn helps to monitor the temperature level at the HHX, and the two sides of the REG. The curve clearly demonstrates the onset temperature where the system starts spontaneously oscillating and produces acoustic power. The DAQ also allows plotting of the pressure distribution curve over time, which helps to visualise the pressure distribution.

Finally, according to the values of pressure at two selected locations and the phase angle between them, the acoustic power can be estimated. As mentioned before, either the two-microphone method or RC-acoustic load can be used, based on the experiment system utilised.

8.3 Analysis of the system without RC-load

8.3.1 Simulations results and discussion

As schematically shown in Figure 8.15, this engine consists of an ambient heat exchanger (AHX), regenerator (REG), hot heat exchanger (HHX), thermal buffer tube (TBT) and secondary ambient heat exchanger (SAHX). A side-branched Helmholtz resonator whose volume can be varied by changing the position of a piston connects to the looped-tube engine about 70 cm away from the secondary ambient heat exchanger. The Helmholtz resonator is connected to the loop through a connection pipe that is only 3 cm in length. The design procedure consists of numerical modelling of the system using DeltaEC tools; this is followed by the construction of a practical engine system. The preliminary testing results are obtained and compared with the simulations in detail. The total length of the looped tube engine system is about 4.5 m. The operating frequency of the system is 60.5 Hz. The diameters of the engine core and acoustic resonator are 65 mm and 20 mm, respectively. As the main interest of this research is to demonstrate the function of the proposed phase tuning technique rather than the high efficiency or power output, atmospheric air is used as working fluid. PVC pipe rather than metal pipe is used as a FBP to minimise the cost.

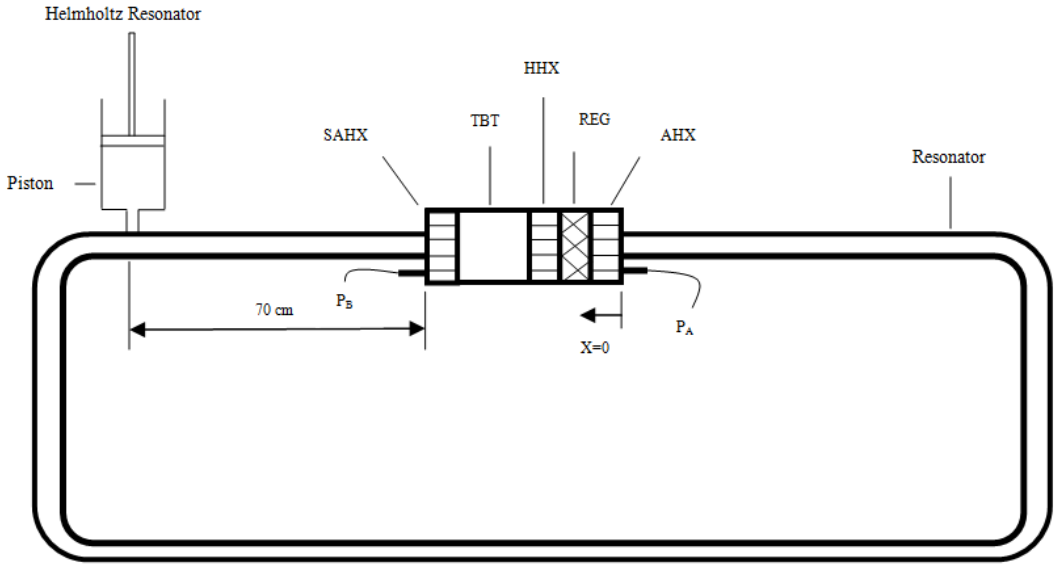

Figure 8.15: Schematic of the experimental system without RC-load.

Previous research showed that the acoustic velocity tends to be very high in the looped-tube thermoacoustic engine, due to the sudden change of the cross-sectional area. Side-branched stubs were introduced to correct the acoustic field within the looped tube engine [56]. The physical principle behind the function of the side-branched stub lies in the fact that it can shunt part of volumetric velocity away from the engine's FBP, and then reduce the acoustic losses, due to higher acoustic velocity along the loop. It is understood that the compliance of the side branched stub plays the main role in improving the performance of the engine, while the acoustic inertance and resistance of the stub do not contribute significantly to the phase tuning effect. For this reason, a side-branched acoustic compliance is introduced to the looped engine instead in this research. From the acoustical point of view, such a side-branched acoustic compliance is a Helmholtz resonator, as shown in Figure 8.15. Its acoustic compliance C_s which is defined as

$$C_s = \frac{V}{\rho_M a^2} = \frac{V}{\gamma P_M}, \tag{8.6}$$

where V, a, ρ_M, P_M and γ are the volume of the Helmholtz resonator, sound speed, mean density, mean pressure and ratio of specific heat capacity, respectively [74]. The compliance is varied by changing the volume of the resonator in both experiments and simulation.

DeltaEC code has been employed to model and simulate the present thermoacoustic system. The design process involves a series of comprehensive simulations. The experimental rig shown in Figure 8.15 was constructed based on an optimised model. Some typical simulation results are presented in this section to demonstrate the working principle of the rig, as well as the function and effectiveness of the new phase tuning device, i.e., the side-branched Helmholtz resonator.

The Helmholtz resonator's volume is varied to achieve the maximum acoustic power generated in the engine. To allow the analysis of engine's performance, engine efficiency η is defined as

$$\eta = \frac{\dot{E}}{\dot{Q}_{in}}, \tag{8.7}$$

where $\dot{E}$ is the net production acoustic power generated by the thermoacoustic engine core, and $\dot{Q}_{in}$ is the heat power input to the system. The simulations results are summarised and presented in Figure 8.16-Figure 8.20.

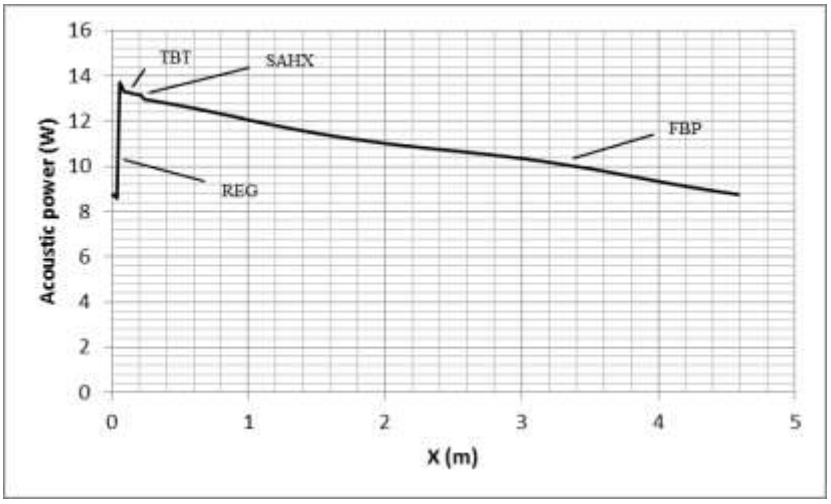

Figure 8.16: Distribution of acoustic power along the loop.

The frequency of the engine is 60.5 Hz. The heating power is fixed as 150 W in the simulations. The distribution of the acoustic power flow along the engine is shown in Figure 8.16. About 8.7 W acoustic power is fed to the ambient end of the REG, and is then amplified to about 13.8 W within the REG. The HHX, TBT and the SAHX dissipate at about 0.7 W. As no acoustic load is installed to the engine at this stage, the FBP dissipated around 4.6 W acoustic power, and the remaining acoustic power is then fed back to the thermoacoustic engine core for the next cycle.

Figure 8.17 and Figure 8.18 show the effect of the side branched Helmholtz resonator on the efficiency of the engine and pressure amplitude, respectively. It can be seen that the acoustic compliance of the Helmholtz resonator has strong effects on the performance and pressure amplitude of the engine. Both the efficiency and pressure amplitude firstly increase, and then decrease with the increase of C_s. There is an optimal value about C_s=2.9x10^{-9} m^3/Pa.

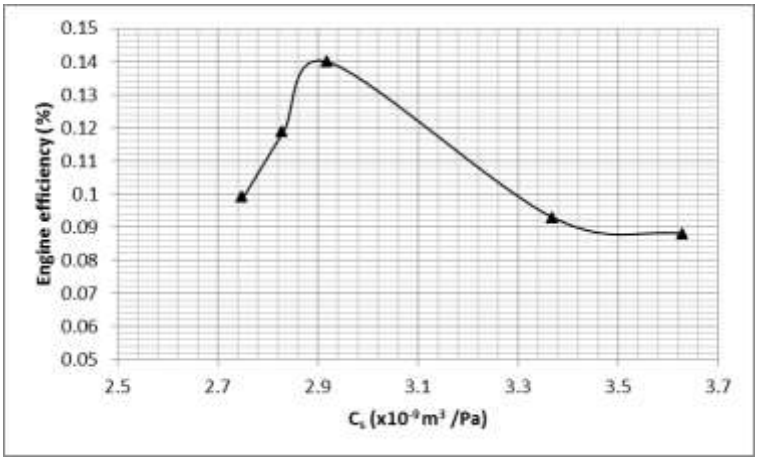

Figure 8.17: Optimisation of acoustic compliance C_s for efficiency of the engine.

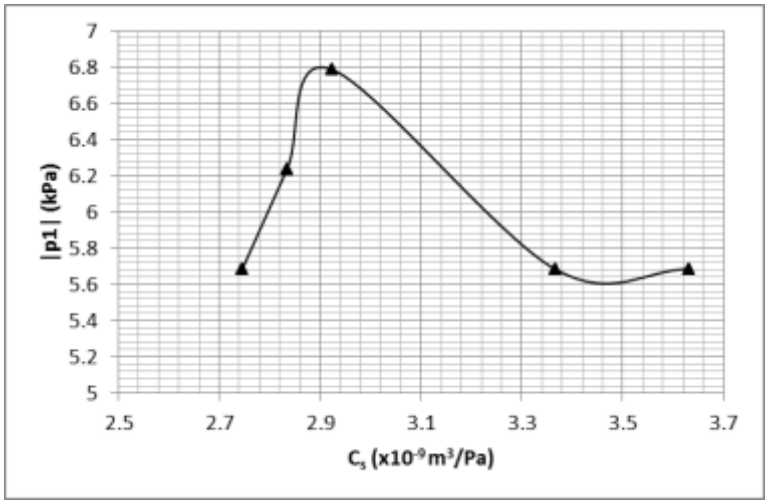

Figure 8.18: The relationship between pressure amplitude of the engine Cs.

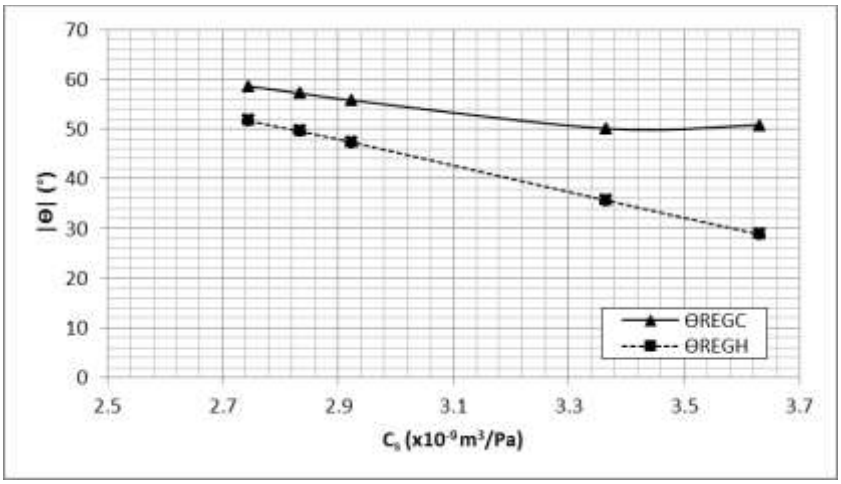

Figure 8.19: Phase angle at the two ends of the regenerator (Θ_{REGC}&Θ_{REGH}) versus C_s.

Figure 8.19 shows the effects of the Helmholtz resonator on the phase angle between the velocity and pressure amplitude at two ends of the regenerator. It can be seen that the phase angles decrease significantly when the acoustic compliance of the Helmholtz resonator (C_s) increases. The side-branched Helmholtz resonator works as expected in terms of tuning the phase angle between the velocity and pressure amplitude in the looped-tube travelling wave thermoacoustic engine.

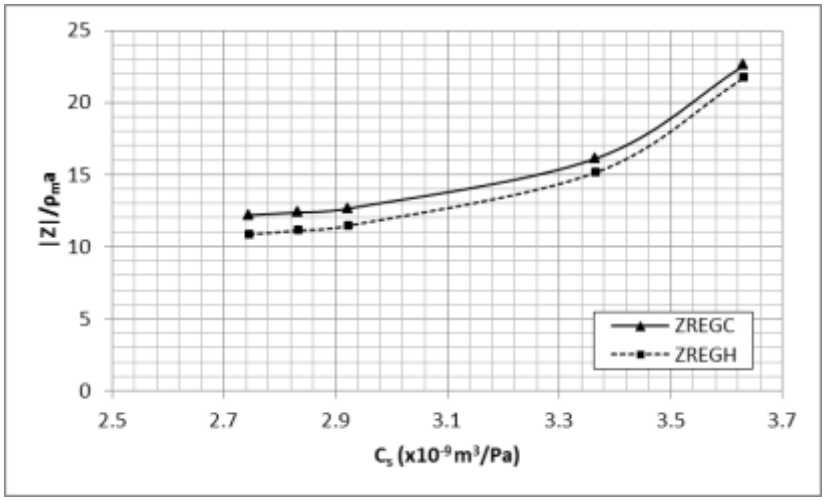

Figure 8.20: Normalised acoustic impedance at the two ends of the regenerator (Z_{REGC} and Z_{REGH}) versus C_s.

Figure 8.20 shows the Helmholtz resonator's effect on the normalised acoustic impedance at two ends of the regenerator. It can be clearly seen that C_s of Helmholtz resonator has strong effects on the normalised acoustic impedance, and increases as C_s increases.

These results numerically demonstrate that the acoustic field within the tested thermoacoustic engine can be controlled by adjusting the volume of the side-branched Helmholtz resonator.

8.3.2 Experimental results and discussion

The electrical power of the heater is supplied by the AC power supply, which is up to 450 W (45 V and 10 Amp). Acoustic oscillations start spontaneously in the system when the temperature difference between the cold and hot end of the regenerator exceeds the onset temperature gradient.

It should be mentioned here that there is a difference between the measured and calculated heat input to the system, and this difference is estimated as the heat losses to the ambient air. The operating frequency of this system is 60.5 Hz. The working gas is air at atmospheric pressure.

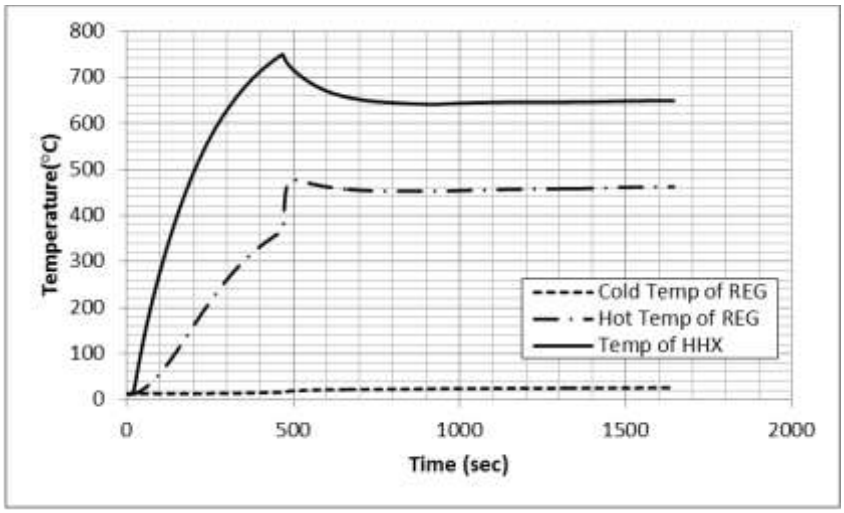

Figure 8.21: The measured temperature at the two ends of the regenerator, and within the hot heat exchanger.

Figure 8.21 shows the temperature changes with time for three important locations: centre of hot heat exchanger (i.e. heater), the hot and cold side of the regenerator. It can be clearly seen that the air temperatures at the centre of HHX and hot end of the REG increase rapidly after the electrical power is turned on to power the HHX. The working gas at the cold side of the REG remains at almost ambient temperature during this start up process.

It takes about 466 seconds to start the oscillation when the temperatures reach 750°C within the hot heat exchanger and 367°C at the hot end of the regenerator. During this period, both temperatures increase sharply. The temperature within HHX decreases rapidly after the oscillations start, reaching a steady state value of 649°C when the oscillation reaches steady state. However, the temperature at the hot end of the REG increases sharply from 367 to 477°C, and then smoothly decreases to around 450°C during this period. The difference between the evolutions of these two temperatures is mainly due to the fact that the spontaneous acoustic oscillation changes the mechanism of heat transfer from natural convection to an acoustically forced convection within the heat and regenerator. The acoustic oscillation enhances the heat transfer from the HHX to the hot side of REG, therefore the temperature of HHX decreases, but the

temperature at the hot end of the regenerator increases. The experimental results for the pressure amplitude against time are shown in Figure 8.22.

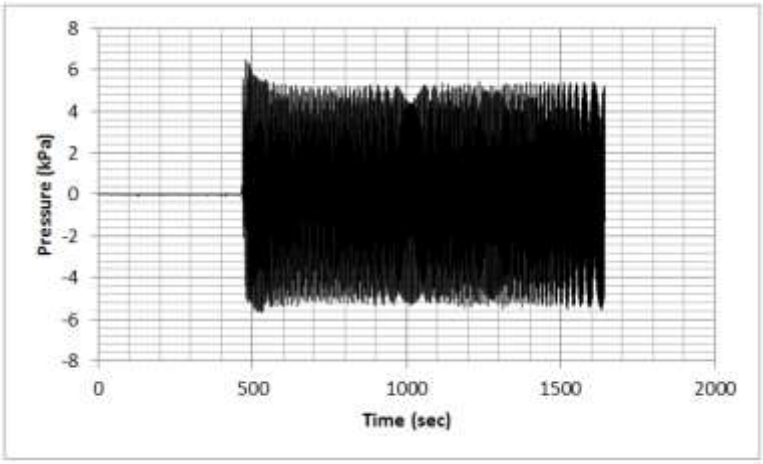

Figure 8.22: Pressure distribution along the loop.

As mentioned earlier, the engine starts the oscillation with growth of pressure amplitude at around 466 sec. The pressure amplitude then gradually grows with time to the peak value, which is around 6.45 kPa at 478 sec. Thereafter, the pressure amplitude drops to about 4.65 kPa and reaches steady.

The effects of the side-branched Helmholtz resonator on the performance of the engine have been investigated experimentally. The pressure amplitudes at locations P_A and P_B have been measured when the volume of the side-branched Helmholtz resonator varies. The heating power is fixed at 450 W in the experiments, while only 150 W is required in the simulations. The difference is estimated as the heat loss, and future measures are needed to reduce such heat loss if efficiency becomes a main research concern.

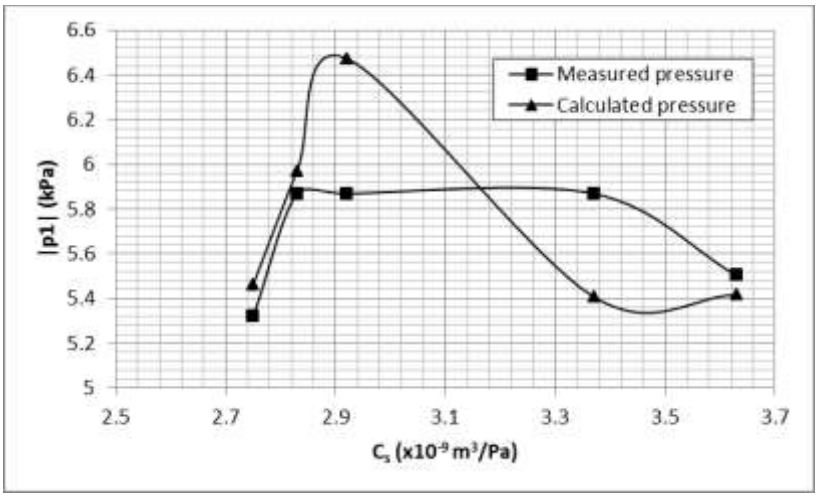

Figure 8.23: Measured and calculated pressure at P_B.

Typically, the uncertainty in |*p1*| is ±1%. The error bars are smaller than the symbols.

Figure 8.23 shows the measured and calculated pressures at location P_B when the volume of the resonator varies. It can be seen that, there is a strong dependence of pressure amplitude and acoustic power on the Helmholtz resonator volume (acoustic compliance), when all the other conditions are kept unchanged. This trend agrees with the simulation, while a large discrepancy is observed at high value of C_s. This contradiction between the experimental and simulation results comes from the lack of isolation of the system, resulting in significant thermal loss between the system and the surroundings. Also the use of PVC pipes will likely cause acoustic losses because of the imperfect seal between them. In addition, the DeltaEC code assumes many assumptions in order to converge on an acceptable numerical solution of the thermoacoustic issue in contrast to the experimental process which deals with the thermoacoustic issue as it is without any assumptions. The error percentage of the measured and calculated pressure values are listed in Table 8.1

Table 8.1: The data of measured and simulated pressure amplitudes

C_s(x$10^{-9}$$m^3$/Pa)	Measured pressure (kPa)	Calculated pressure (kPa)	Error (%)
2.75	5.318	5.461	2.618
2.83	5.868	5.971	1.816
2.92	5.868	6.474	9.36
3.37	5.868	5.407	8.525
3.63	5.501	5.416	1.569
		Average	4.777

8.4 Analysis of the system with RC-load

8.4.1 Simulation results and discussion

The thermoacoustic system in this section is the same as the previous section except the addition of an RC-load. Figure 8.24 shows the schematic of the experimental rig that is investigated in this research, and Figure 8.25 shows a photo of the obtained experimental rig. The aim of this study is to introduce a new phase tuning method (i.e., a side-branched acoustic volume) to tune the time-phasing within a looped-tube travelling wave thermoacoustic engine. The proposed concept has been investigated both numerically and experimentally in this research. An experimental rig was simulated and designed using DeltaEC software. It was then constructed according to the obtained theoretical model. The operating frequency of this system is 60.5 Hz. The working gas is air at atmospheric pressure.

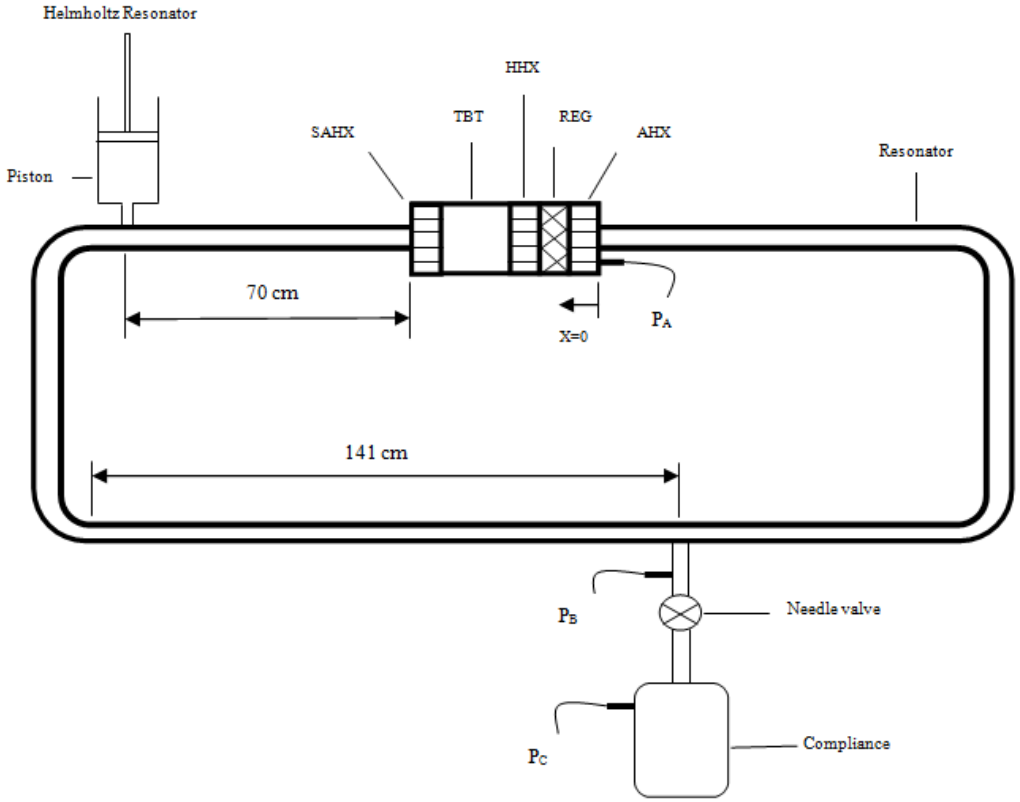

Figure 8.24: Schematic of the experimental system with RC-load.

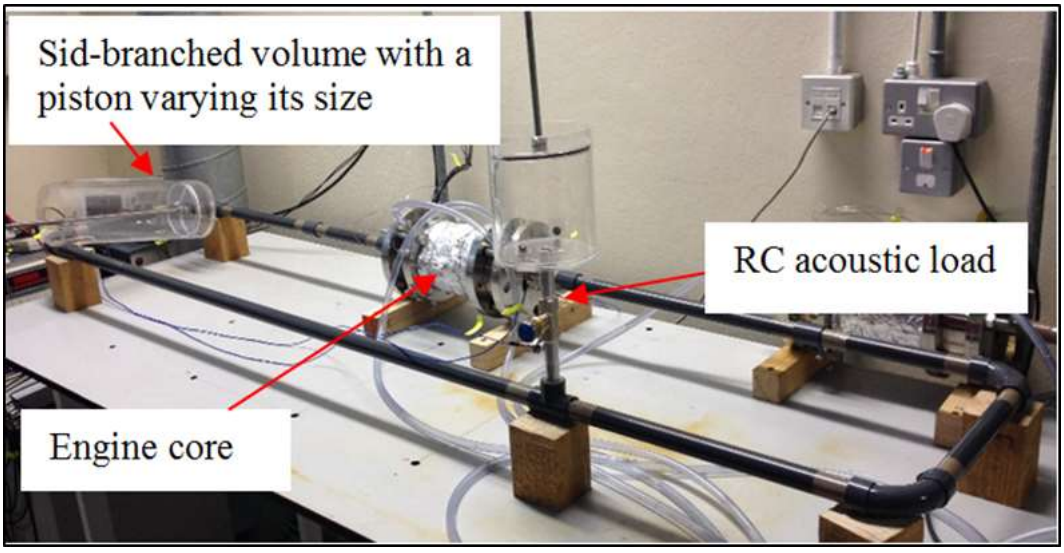

Figure 8.25: The photo of the experimental rig.

A block diagram of the segments in DeltaEC simulation is shown in Figure 8.26 below;

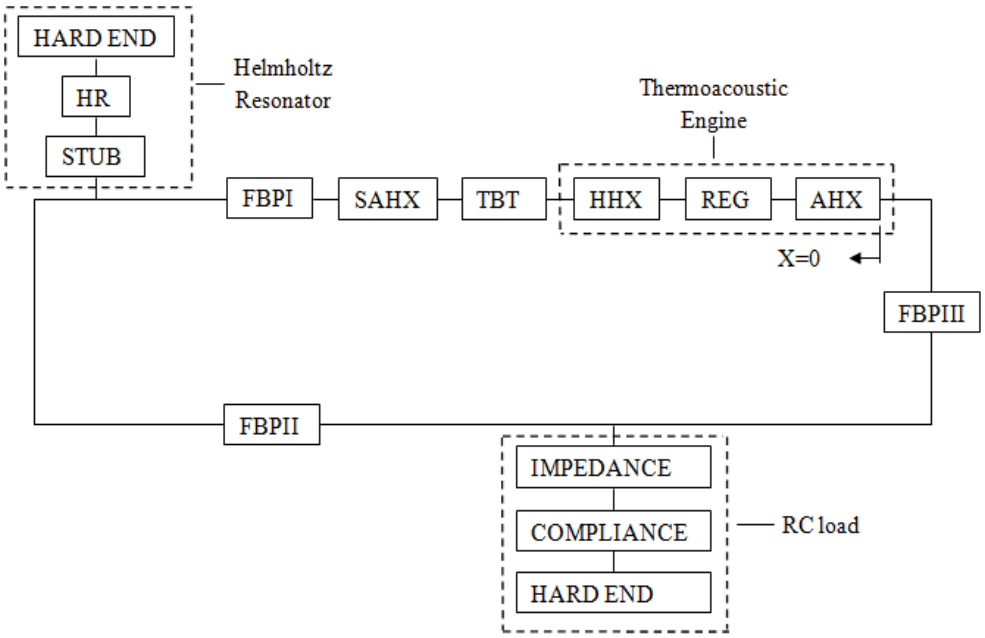

Figure 8.26: The block diagram of the segments in DeltaEC simulation.

The design process involves a series of comprehensive simulations. The experimental rig shown in Figure 8.24 was constructed based on an optimised model. Some typical simulations results are presented in this section to demonstrate the working principle of the rig as well as the function and effectiveness of the new phase tuning device, i.e., the side-branched Helmholtz resonator. The Helmholtz resonator's volume is varied to achieve the maximum acoustic power generated by the engine.

The simulation results are summarised and presented in this section. It should be mentioned here that, impedance acts as a resistance of the valve which can be utilised to get the optimiased turns of the valve. Numerically, RC-load should be put in a high pressure point in the system, this point is found at 2 m away from the Helmholtz resonator, as clearly shown in Figure 8.27-Figure 8.31.

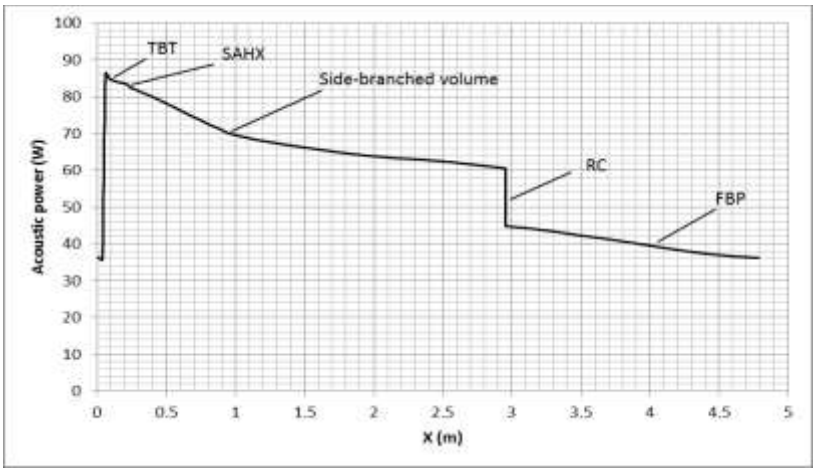

Figure 8.27: Distribution of acoustic power along the engine.

Figure 8.27 shows the distribution of the acoustic power flow along the engine. Around 36 W of acoustic power flows into the ambient heat exchanger of the engine core and is amplified inside the regenerator to around 87 W. The HHX, TBT, and a section of FBP dissipate around 27 W of acoustic power. The acoustic power dissipated by the side-branched Helmholtz resonator is unnoticeable as expected. There is a sharp drop of acoustic power at the location where the RC-acoustic load is connected. The RC-load extracts around 16 W of acoustic power. The section of FBP between the RC-load and the engine core further dissipates around 8 W of acoustic power, and the remaining 36 W acoustic power is fed back to the engine core. The heating power is around 260 W, so the calculated energy efficiency is around 6.1%.

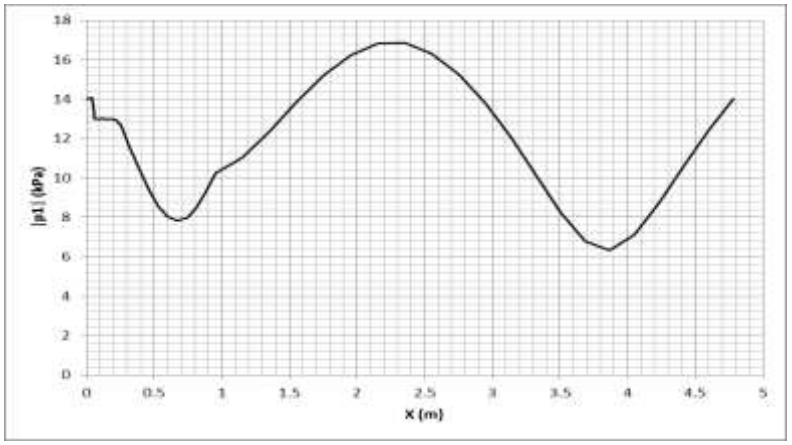

Figure 8.28: Distribution of the amplitude of acoustic pressure along the engine.

Figure 8.28 shows the pressure amplitude distribution along the system. It can be clearly seen that there are two peaks and two troughs of pressure amplitude along the engine loop. One peak appears at the engine core section (i.e., the regenerator and the hot and cold heat exchangers), indicating a high acoustic impedance at this location. The RC-load is located close to the other pressure amplitude peak, and the resultant high acoustic impedance could minimise the RC-load's effect on the acoustic field within the engine. The maximum and minimum pressure amplitude are around 16.8 and 6.0 kPa respectively along the engine. The ratio between them is about 2.8. In an ideal travelling wave condition, this ratio should be close to 1. Therefore, it can be inferred that the acoustic field has some standing wave components due to acoustic reflection.

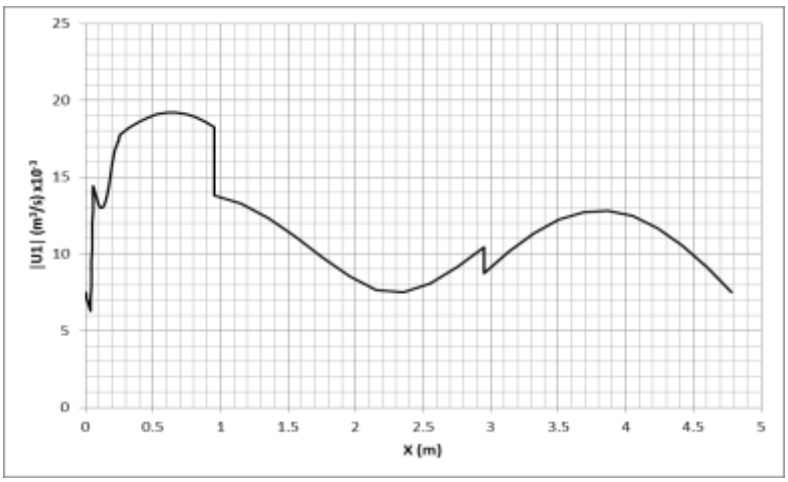

Figure 8.29: Distribution of the amplitude of volumetric velocity along the engine.

Figure 8.29 shows the distribution of volumetric velocity along the system. There are two peaks and two troughs along the engine loop. Low volumetric velocity within the engine core is achieved to avoid viscous dissipation within the regenerator and heat exchangers where the flow resistances are high. It can also be seen that the volumetric velocity increases significantly due to the sharp temperature gradient along the regenerator. It should be highlighted that the volumetric velocity decreases sharply at the locations where the side-branched volume (i.e., a Helmholtz resonator) and the RC-load are installed, which is mainly due to the shunt of volumetric flow rate to these two components.

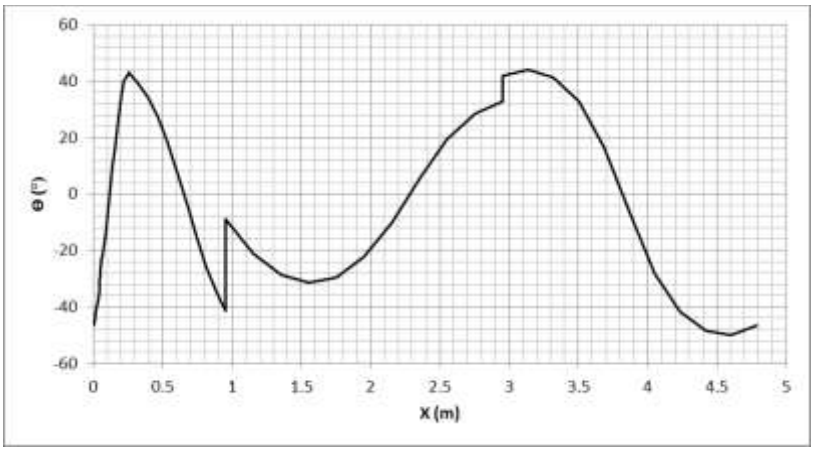

Figure 8.30: Phase angle Θ between pressure and velocity oscillations along the engine.

Figure 8.30 shows the phase difference between pressure and velocity oscillations along the engine loop. It clearly shows that the side branched volume significantly changes the phase angle between the pressure and velocity from -40° to about -8°, bringing it towards the ideal travelling wave condition, i.e., 0°. The RC-load changes the phase angle slightly by around 4°, moving it away from the ideal travelling wave conditions. This figure clearly demonstrates that the side-branched volume can effectively adjust the phase angle in the engine.

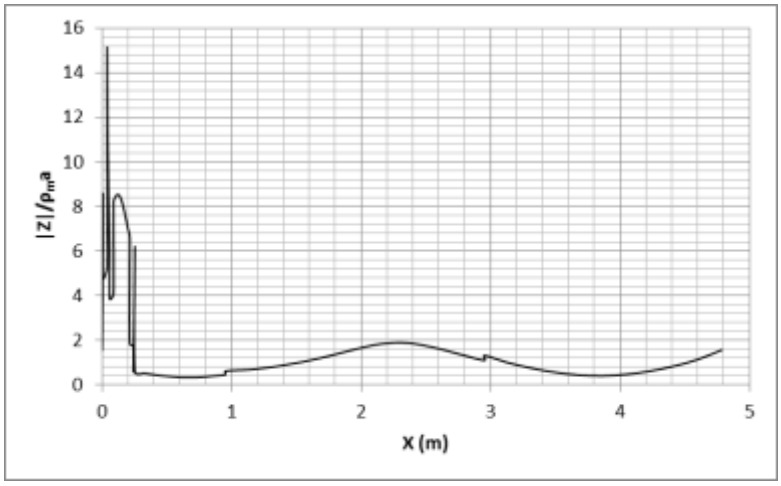

Figure 8.31: Distribution of the normalized specific acoustic impedance along the engine.

Figure 8.31 presents the normalised acoustic impedance along the system. In this model, it can be seen that the normalised acoustic impedance in most parts of the system is

around 1 as expected, and around 15 at the engine core section. Usually, the acoustic impedance within the engine core should be in the range 15-30 times that of $\rho_m a$ to reduce the acoustic losses [10]. Therefore, this model has met this requirement.

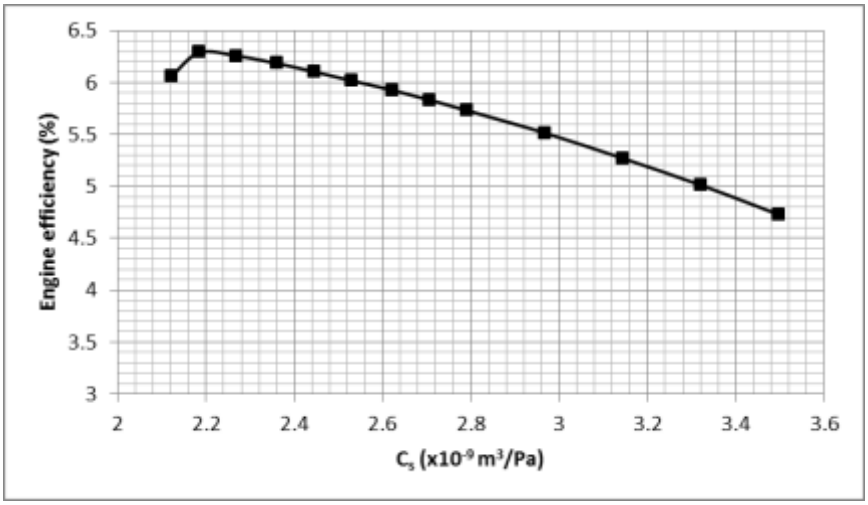

Figure 8.32: Optimisation of acoustic compliance C_s for efficiency of the engine.

Figure 8.32 shows the effect of the side-branched volume on the efficiency of the engine. It can be seen that the acoustic compliance of the side-branched volume has strong effects on the performance of the engine. The efficiency firstly increases, and then decreases with the increase of C_s. There is an optimal value about C_s=2.185x10^{-9} m^3/Pa. It should be noted that C_s=2.185x10^{-9} m^3/Pa was chosen for the optimised model, of which the results are shown in Figure 8.27-Figure 8.31.

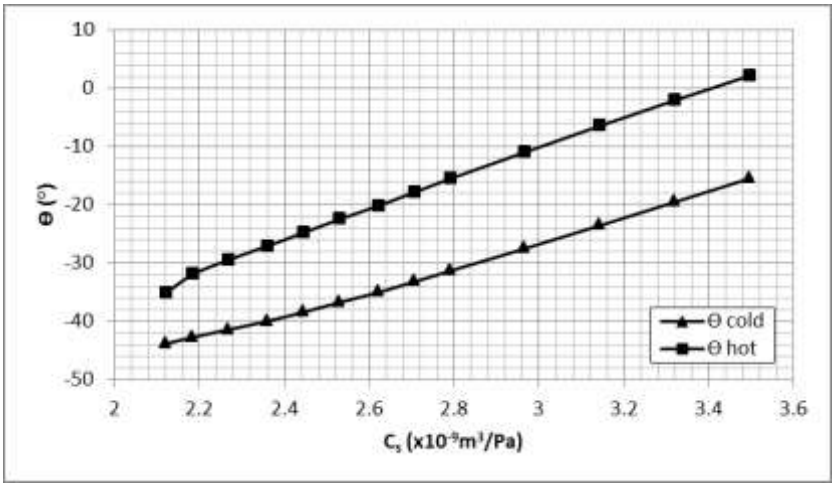

Figure 8.33: Phase angle at the two ends of the regenerator ($\Theta_{\text{cold end of REG}}$&$\Theta_{\text{hot end of REG}}$) versus C_s.

Figure 8.33 shows the effects of the Helmholtz resonator on the phase angle between the velocity and pressure amplitude at two ends of the regenerator. It can be seen that the phase angle increases significantly when the acoustic compliance of the Helmholtz resonator (C_s) increases. The side-branched Helmholtz resonator works as expected in terms of tuning the phase angle between the velocity and pressure amplitude in a looped-tube travelling wave thermoacoustic engine. This indicates that the varying volume of the Helmholtz resonator has a largely positive effect on the performance of the thermoacoustic system. The presence of the Helmholtz resonator improves the system under travelling wave thermoacoustic conditions by decreasing the phase angle, which in turn leads to a decrease in acoustic losses and increase in engine efficiency.

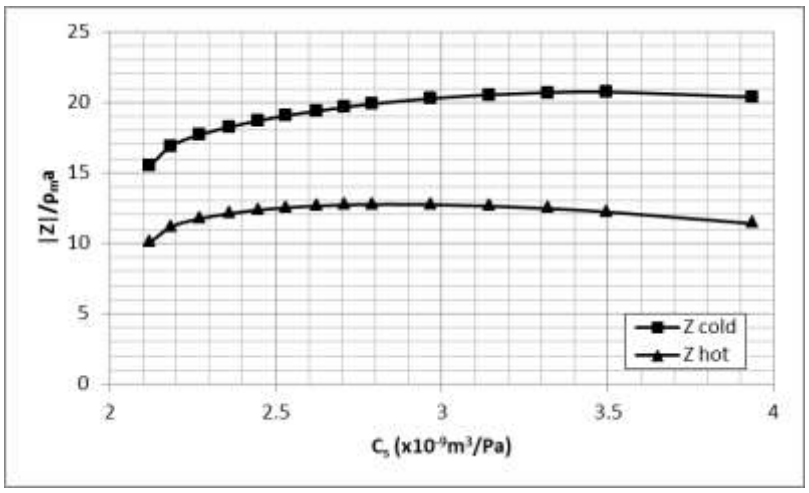

Figure 8.34: Normalised acoustic impedance at the two ends of the regenerator ($Z_{\text{cold end of REG}}$&$Z_{\text{hot end of REG}}$) versus C_s.

Figure 8.34 shows the Helmholtz resonator's effect on the normalised acoustic impedance at two ends of the regenerator. It can be clearly seen that the C_s of Helmholtz resonator has strong effects on the normalised acoustic impedance, and increases as C_s increases. These results above numerically demonstrate that the acoustic field within the tested thermoacoustic engine can be controlled by adjusting the volume of the side-branched Helmholtz resonator. It can be seen that there is a maximum value of normalised acoustic impedance at the cold end equal to 20.735, which is located at C_s =

3.496×10^{-9} m^3/Pa, and the normalised acoustic impedance at the hot end is equal to 12.753 which is located at $C_s = 2.791 \times 10^{-9}$ m^3/Pa.

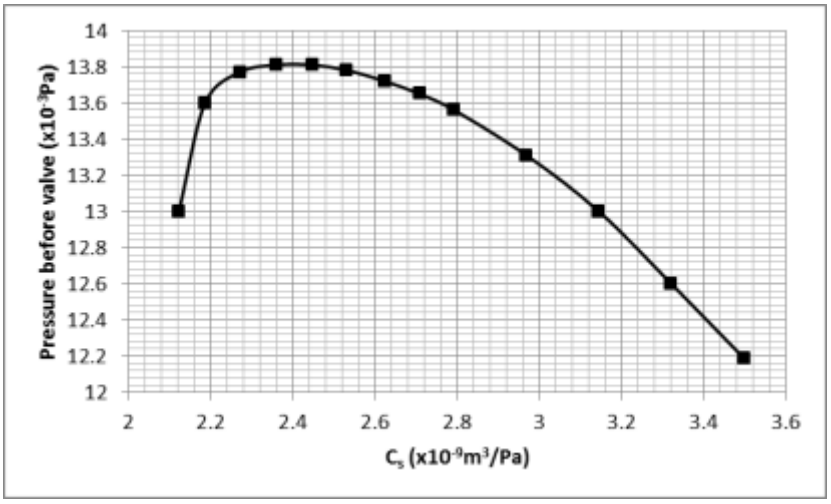

Figure 8.35: Pressure amplitudes before the valve of the RC-load versus C_s.

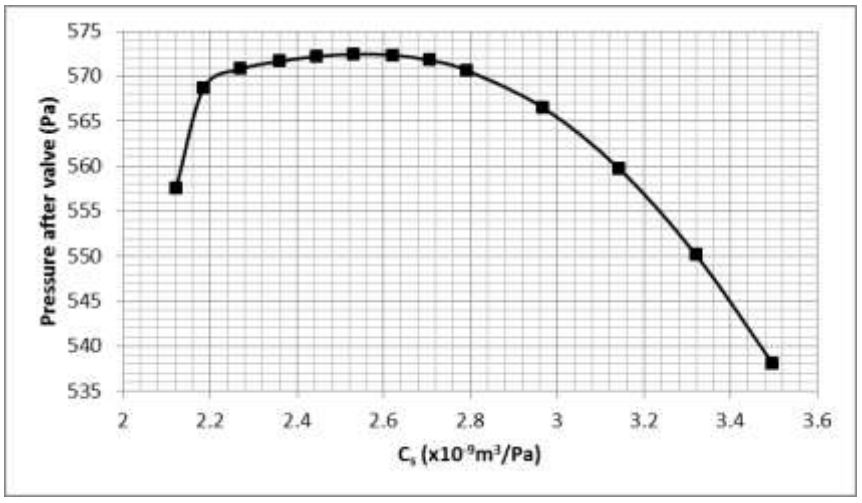

Figure 8.36: Pressure amplitudes after the valve of the RC-load versus C_s.

Figure 8.35 and Figure 8.36 present the pressure amplitude before and after the valve of the RC-load. In general, the pressure values before the valve are higher than the pressure values after the valve; this is mainly due to the presence of the needle valve. If the value is closed there is no pressure, but as the value is opened gradually, the pressure after the valve starts to rise. It should be mentioned here is that the maximum

values of the pressure before and after the needle valve are 13800 and 572 Pa respectively. Both are found at the $C_s = 2.531x10^{-9}$ m^3/Pa.

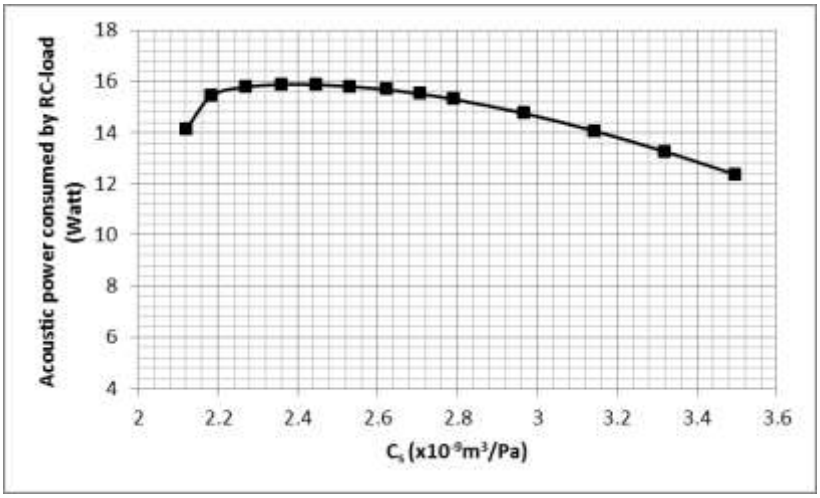

Figure 8.37: Acoustic power consumed by the RC-load versus C_s.

The acoustic power consumed by the RC-load is presented in Figure 8.37. It can be seen that the RC-load consumes around 16 Watt when the $C_s = 2.361x10^{-9}$ m^3/Pa.

8.4.2 Experimental results and discussion

As mentioned in the previous section, the electrical power of the heater is supplied by the AC power supply, which is up to 450 W (45 V and 10 A). The acoustic oscillations start spontaneously in the system when the temperature difference between the cold and hot end of the regenerator exceeds the onset temperature gradient. The operating frequency of this system is 60.5 Hz. The working gas is air at atmospheric pressure.

In order to evaluate a thermoacoustic engine's performance it is necessary to calculate the acoustic power which is generated. Some times for research reasons there is no acoustic load in the system, so acoustic power will be dissipated inside the FBP [54]. To estimate the acoustic power during any thermoacoustic system there are two methods; the two microphones method and RC-acoustic load method, as mentioned in the experimental setup section. The second is more accurate than the first, so it is used in

this study to calculate the generated acoustic power. Based on the RC-acoustic load technique above, acoustic power can be measured by using the equation (8.5).

This method benefits from the pressure amplitude difference on both sides of the needle valve. This difference depends on the number of turns of the valve; if the number of turns is zero there is no pressure difference, and when the number of turns is increased the acoustic power dissipates, which in turn leads to a pressure difference. This method gives a clear indication of how acoustic power dissipates, rather than the two microphones method which is influenced greatly by the distance between the two pressure sensors.

In the next section, two optimisation experiments are investigated. Firstly, the acoustic complaince C_s is fixed at 2.9 $x10^{-9}$ m^3/Pa (which was found from the last section), and the valve opening is adjusted by varying the turns of the valve. This leads to the optimised number of turns of the needle valve, which allows passing of the highest acoustic power. Secondly, having found the optimised number of turns of the valve, this value will be fixed and the volume of the Helmholtz resonator varied to determine how it affects the performance of the system as a whole.

- Varying valve opening in turns, C_s=2.9 $x10^{-9}$ m^3/Pa

The goal of this section is to find an optimised number of turns of the valve which allows passing of the highest acoustic power through the RC-load. This is achieved by maintaining the optimised acoustic compliance of the Helmholtz resonator which has been found to be 2.9 $x10^{-9}$ m^3/Pa for the current configuration without RC-load [91].

From the experimental work it can be mentioned here how the pressure amplitude at the three pressure sensor locations are affected by changing the number of turns of the needle valve; pressure amplitude at the locations P_A and P_B decrease, but increase at the location P_C. It can be seen that the lowest value of the pressure amplitude is at location

P_C because this location has the highest velocity amplitude, as shown in Figure 8.38-Figure 8.40 below;

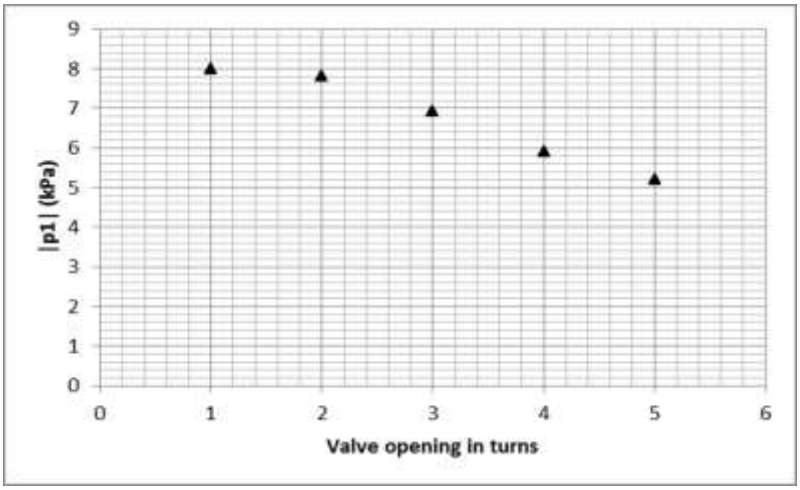

Figure 8.38 : Pressure distribution at location P_B versus valve opening in turns, C_s=2.9x10^{-9} m^3/Pa.

Typically, the uncertainty in |*p1*| is ±1%. The error bars are smaller than the symbols.

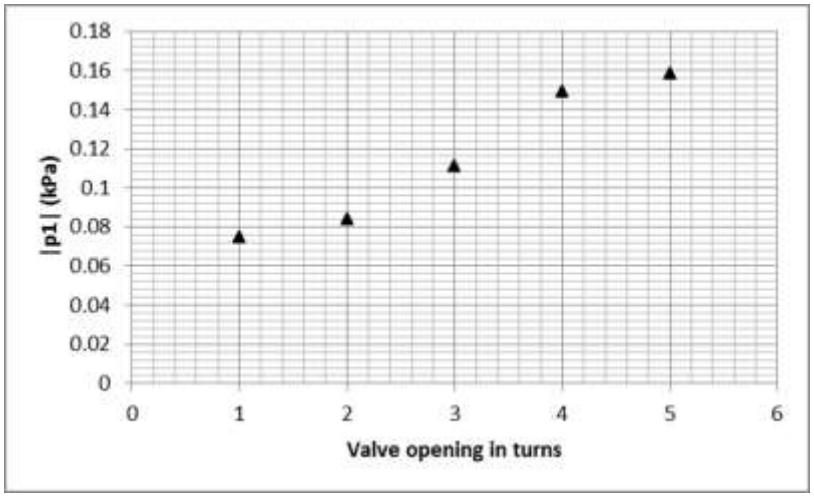

Figure 8.39: Pressure distribution at location P_C versus valve opening in turns, C_s=2.9x10^{-9} m^3/Pa.

Typically, the uncertainty in |*p1*| is ±1%. The error bars are smaller than the symbols.

Figure 8.38 and Figure 8.39 show pressure amplitude distribution as per changing of turns of valve. As aforementioned, the pressure at location P_B decreases and at location P_C increases.

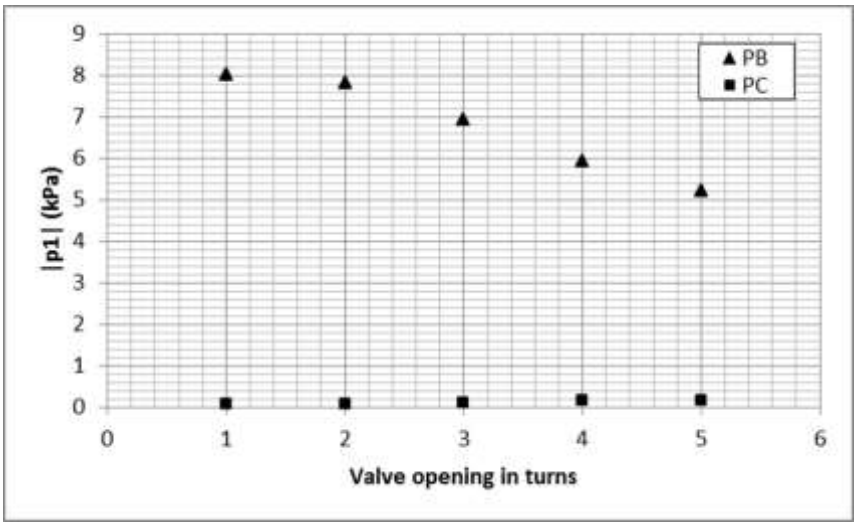

Figure 8.40 : Pressure distribution at locations P_B and P_C versus valve opening in turns, C_s =2.9x10^{-9} m^3/Pa.

Typically, the uncertainty in |*p1*| is ±1%. The error bars are smaller than the symbols.

Figure 8.40 shows a comparison between pressure distribution at locations P_B and P_C. It can be seen that the range of change in pressure at P_B is between 8 and 5 kPa, but the range of change in pressure at P_C is between 0.1 and 0.2 kPa. It can be noted that, there is a higher pressure at Pc at number of turns equal to 5 in Figure 8.39, however, there is a trade-off between pressure at P_B and P_C. This means that if the pressure at P_C increases, the pressure at P_B will decrease and vice versa, so an experimentally optimised value is required between these two values. Therefore 4 has been chosen as the number of valve turns.

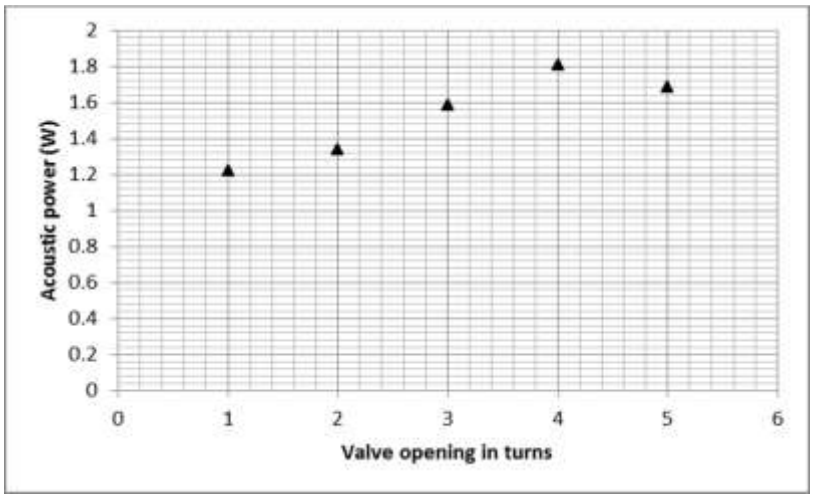

Figure 8.41 : Acoustic power versus valve opening in turns, C_s=2.9x10^{-9} m^3/Pa.

Figure 8.41 presents the highest output acoustic power (1.8 Watt) of the thermoacoustic system at turn 4 of the needle valve.

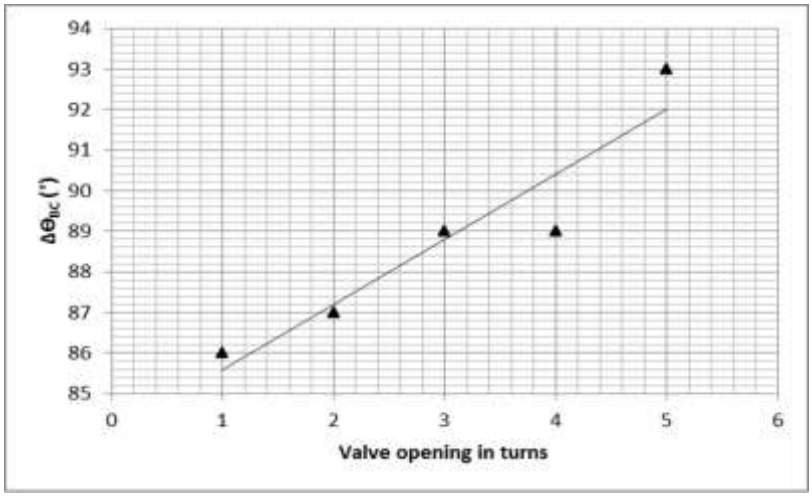

Figure 8.42: Phase angle difference between P_B & P_C locations versus valve opening in turns, C_s=2.9x10^{-9} m^3/Pa.

Lock-in amplifier with an accuracy of 0.01°.

Figure 8.42 shows the phase angle difference between P_B and P_C locations, which increases significantly by increasing the valve opening.

- Varying C_s at turn=4

In the last section, the optimised valve opening was determined to be equivalent to four valve turns of the needle valve. In this section the number of turns is fixed and the acoustic compliance of the Helmholtz resonator is varied to see how the Helmholtz resonator's volume affects the performance of the system. As was seen earlier, the same distribution of the pressure amplitude occurs here, but in a different range. In general, the pressure amplitude at locations P_A and P_B decreases and at location P_C increases for the same reason as mentioned abov, shown in Figure 8.43-Figure 8.45.

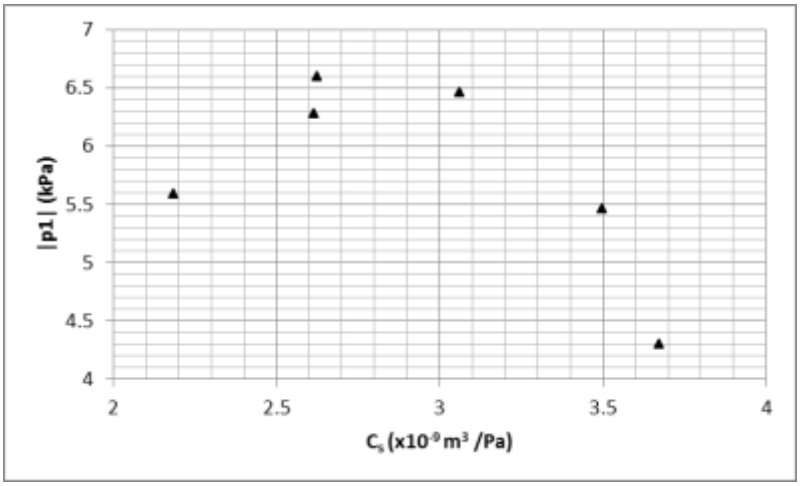

Figure 8.43: Pressure amplitude at location P_B changes as C_s varies when the heating power is constant. **Typically, the uncertainty in |*p*1| is ±1%. The error bars are smaller than the symbols.**

Figure 8.43 and Figure 8.44 show the effect of the acoustic compliance of the side-branched volume on the pressure amplitude at location P_B and P_C. As C_s increases the pressure amplitude firstly increases, and then decreases. The optimal value of C_s is measured as 2.62×10^{-9} m^3/Pa, which is close to the optimal value $C_s=2.185\times10^{-9}$ m^3/Pa as predicted in the simulations.

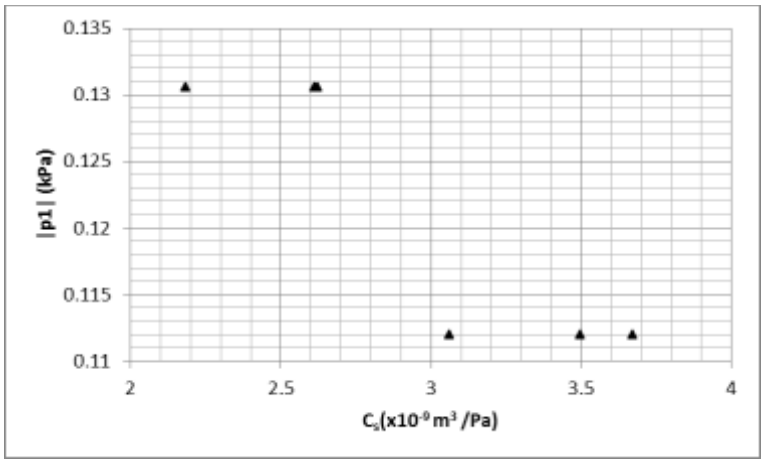

Figure 8.44: Pressure amplitude at P_C location versus C_s.

Typically, the uncertainty in |p1| is ±1%. The error bars are smaller than the symbols.

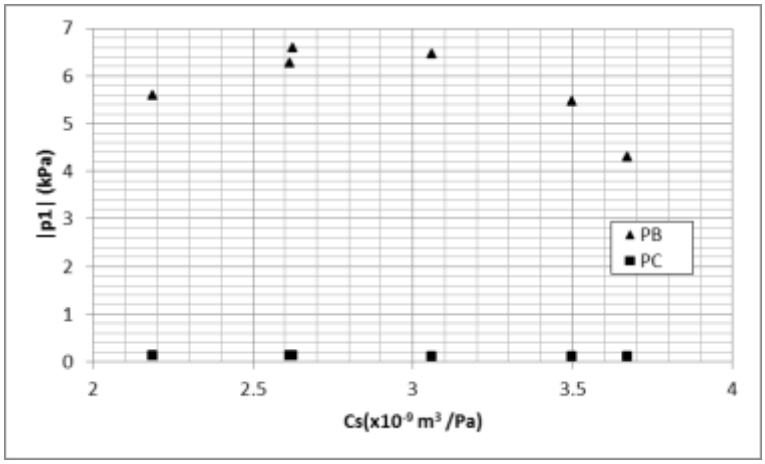

Figure 8.45: Pressure distribution at locations P_B and P_C locations versus C_s, turns=4.

Typically, the uncertainty in |*p1*| is ±1%. The error bars are smaller than the symbols.

Figure 8.45 shows how the volume of the Helmholtz resonator affects the pressure amplitude at two important locations, P_B and P_C. This presents a wide range of change of pressure amplitude at location P_B compared to location P_C. It can be seen from this figure that there is a highest pressure value (around 6.6 kPa) at the optimised C_s (2.62 $x10^{-9}$ m^3/Pa).

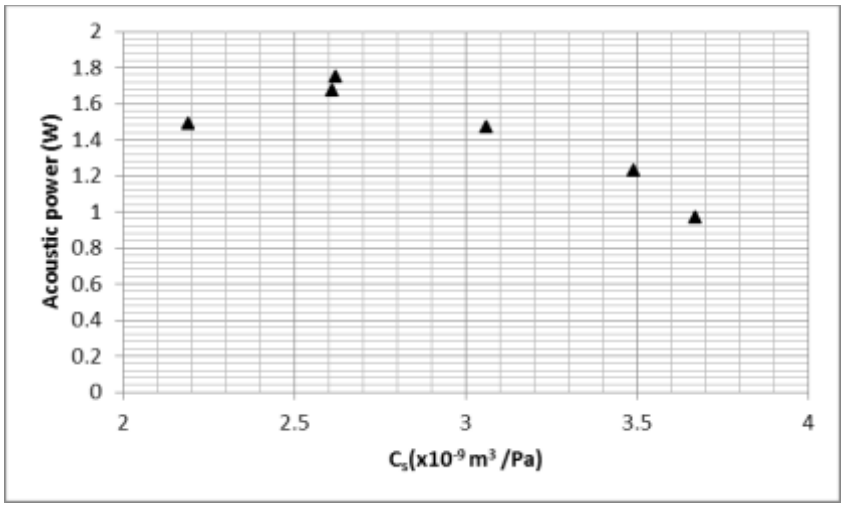

Figure 8.46: Acoustic power changes as C_s varies when the heating power is kept as constant, turns=4

The side-branched volume has been varied to find out the optimal value of C_s corresponding to the highest acoustic power output and energy efficiency. Figure 8.46 shows the relationship between acoustic compliance C_s against acoustic power extracted by the RC-load. The measured optimal compliance of the side-branched volume is C_s=2.62x10^{-9} m^3/Pa, which again is close to the predicted value as shown in Figure 8.32.

The experimental results shown in Figure 8.43 and Figure 8.46 demonstrate that the side-branched volume can strongly affect the performance of the engine. The measured optimal value of the acoustic compliance of the side-branched volume is close to the predicted optimal value, as shown in Figure 8.32.

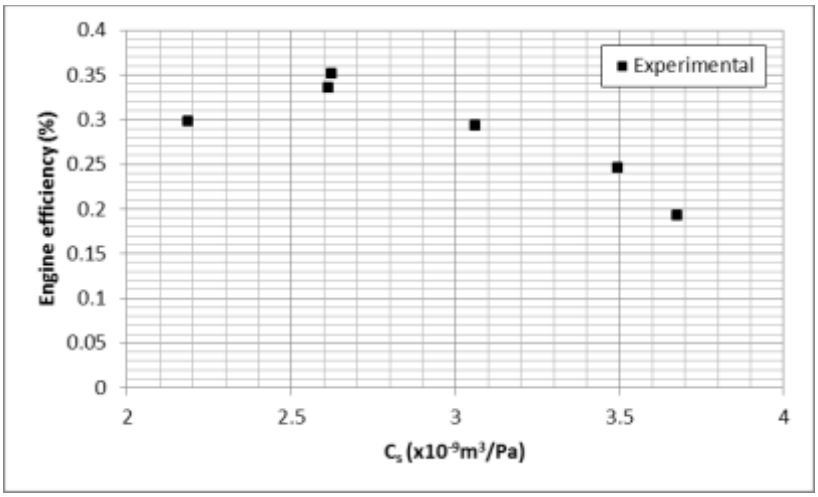

Figure 8.47: Engine's energy efficiency changes as C_s varies when the heating power is kept as constant. turns=4

Figure 8.46 and Figure 8.47 show the relationship between acoustic compliance of the Helmholtz resonator (C_s) against acoustic power and engine efficiency respectively. Having fixed the number of turns to four 4, the Helmholtz resonator volume has been varied to find the optimised volume which gives highest output power and efficiency. Based on these parameters, the optimised acoustic compliance of the Helmholtz resonator (C_s) has been found to be 2.62×10^{-9} m^3/Pa.

As the heat input power was kept as 450 W in the experiments, the energy efficiency of the experimental rig can then be deduced, as shown in Figure 8.47. The measured energy efficiency is much lower than the predictions, as described in the numerical section. Nevertheless, the results in Figure 8.47 show a qualitative agreement with the simulations as shown in Figure 8.32. Such a qualitative agreement demonstrates that the side-branched volume can effectively influence the performance of the tested engine.

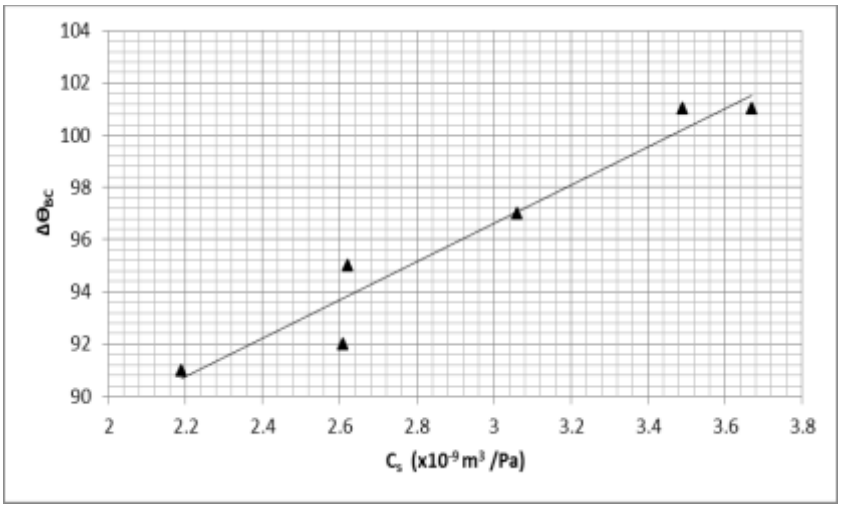

Figure 8.48: Phase angle difference between P_B & P_C locations versus C_s, turns=4.

Lock-in amplifier with an accuracy of 0.01°.

From Figure 8.48 can be observed a proportional relation between phase angle difference between P_B & P_C locations and C_s.

Usually, strong acoustic reflection can be induced due to the inconsistent cross-sectional area along looped-tube travelling wave thermoacoustic engines. This can result in relatively higher standing ratio in the acoustic field, and consequently higher acoustic velocity at locations close to the nodes of the acoustic field. High acoustic velocity normally causes high acoustic power losses, due to friction between the working gas and the inner wall of the FBP. Therefore, a logical approach is to reduce the local acoustic velocity without limiting the acoustic pressure.

The numerical simulations have clearly demonstrated the working principle of the proposed phase-tuning method. As described in the numerical section, the side-branched volume is essentially a Helmholtz resonator. As shown in Figure 8.29, it is connected to the engine at the location where the volumetric acoustic velocity is close to its maximum. It shunts away part of the volumetric velocity from the FBP, and significantly reduces the local volumetric velocity within the FBP (see Figure 8.29), but does not affect the local acoustic pressure (see Figure 8.28). As a result, the local phase

angle between acoustic pressure and velocity has been significantly improved towards the ideal travelling wave condition, i.e., $\theta=0$ (see Figure 8.30). Since a Helmholtz resonator is essentially an acoustic energy storage device, it does not consume acoustic energy (see Figure 8.27). The effectiveness of the proposed phase tuning method has been further demonstrated in Figure 8.32. The acoustic compliance has a strong effect on the engine's performance, and the simulations predict an optimal acoustic compliance $C_s=2.185\text{x}10^{-9}$ m^3/Pa, corresponding to the optimal energy efficiency of the engine.

The measured efficiency (0.35%) of the actual engine is much lower than the prediction of 6.1% by the simulations, as shown in the numerical section. The onset temperature of this system is about 247°C, which is also much higher than that of the systems tested (around 100°C) in the Ref [56]. There are several possible reasons behind this poor performance. One is the significant heat losses due to insufficient thermal insulation around the HHX and TBT and acoustic streaming, and the other is the acoustic losses due to the sudden change of the cross-sectional areas along the engine. The PVC pipe and the poor air tightness could also reduce their efficiency, due to the leakage of sound waves.

Nevertheless, the main objective of this research is to demonstrate the function of the side-branched volume rather than achieving high energy efficiency. The experimental results shown in Figure 8.45-Figure 8.47 demonstrate that the side-branched volume has a strong effect on the performance of the tested engine. It has also been proven that there exists an optimal acoustic compliance $C_s=2.62\text{x}10^{-9}$ m^3/Pa leading to an optimal energy efficiency (see Figure 8.47), which is close to the predicted value as shown in Figure 8.32. This qualitatively agrees with the numerical simulations.

8.5 Conclusions

This chapter proposes a new method to control and tune the acoustic field within a looped-tube travelling wave thermoacoustic engine using a side-branched volume. From the acoustic point of view, such a side-branched volume is essentially a Helmholtz resonator, and thus does not consume acoustic power. By changing its volume (acoustically speaking, its compliance), the researcher can change the acoustic impedance at the opening of this Helmholtz resonator, and thus adjust the acoustic field within the loop-tubed engine as demonstrated in Figure 8.24. It can essentially shunt away part of the volumetric velocity at the low impedance region of the engine, so that the acoustic loss can be reduced within the engine.

Based on the simulations, a simple experimental rig using inexpensive components and atmospheric air as a working fluid was constructed and tested. Although the measured energy efficiency of the actual experimental rig is much lower than the predictions, due to significant heat and acoustic power losses in experiments, there is a qualitative agreement between the simulations and the measurements in terms of the effect of the acoustic compliance of the side-branched volume on the engine's performance. Both the simulations and the experimental results have demonstrated that the proposed side-branched volume can effectively adjust the acoustic field within the looped-tube engine and affect its performance. There is an optimal acoustic compliance corresponding to the best performance in terms of acoustic power output and energy efficiency when the heating power input is fixed.

Chapter 9 Summary and future work

The findings of the work undertaken in this thesis are summarised in section 9.1, and some suggestions for future research are considered in section 9.2.

9.1 Summary

In chapter 4, a numerical analysis of a travelling wave thermoacoustic engine with a by-pass configuration was carried out. The interest in such a by-pass configuration is that the by-pass and FBPs actually created a pure travelling wave resonator. The engine unit extracts a small amount of acoustic work from the resonator, amplifies it and sends it back. As the pure travelling wave resonator has very low losses, it requires very little acoustic power to sustain an acoustic resonance. This new configuration can achieve comparable performance to other types of travelling wave thermoacoustic engines which have been intensively researched. Furthermore, from the fundamental acoustic research point of view, the travelling wave acoustic resonator can create a travelling wave acoustic field on a relatively large scale, which has not been reported before, according to the authors' knowledge. Such a concept for a travelling wave acoustic field has wide applications for acoustic research, such as testing microphones.

In chapter 5, numerical analysis of a travelling wave thermoacoustic engine with a by-pass configuration and its application to thermoacoustic engine driven coolers was investigated. Nitrogen at 10 bar was used as the working gas, and the engine had an operating frequency around 76.5 Hz. When the engine was loaded with a thermoacoustic cooler, the simulation results show that the whole system could achieve a thermal efficiency of 14.5%, which is equivalent to 33.4% of the Carnot efficiency at the tested temperature range. The cooler consumes 159.5 W acoustic power to remove 232.4 W heat at about -19°C and rejects it at 28°C, which leads to a COP of about 1.46, which is equivalent to 27% of Carnot COP under these operating conditions.

In chapter 6, numerical analysis of the travelling wave thermoacoustic engine with a by-pass configuration and its application to develop thermoacoustic engine driven electric generator was presented. The validated model in chapter 4 and 5 was applied to design a thermally driven travelling wave thermoacoustic electric generator with such a by-pass configuration. The design principle contained in the by-pass configuration was implemented successfully in the design, although the design objectives were changed to achieve higher efficiency. It was found that the design strategy for high efficiency engines as suggested by Backhaus, can also be incorporated in the design. When the engine was loaded with a linear alternator to generate electricity, the whole system achieved a thermal efficiency of 21.5% which is equivalent to 32.4% of the Carnot efficiency under the operating conditions. The alternator extracted 237 W acoustic power from the engine and generated 166 W electricity, which ultimately led to an alternator efficiency of about 70%. The overall thermal-to-electric efficiency was about 15%, which is comparable to the experimental results of other types of travelling wave thermoacoustic generator.

In chapter 7, numerical analysis of two-stage engines by-pass configuration travelling-wave thermoacoustic engines was presented. This study has two parts; with and without coolers. This research showed that this new configuration has the potential for developing a low cost thermally driven heat pump system. Nitrogen at 10 bar is used as a working gas, and the engine has an operating frequency of around 50 Hz. When the engine is loaded with a thermoacoustic cooler, the simulation results show that the whole system can achieve a thermal efficiency of 20.3%, which is equivalent to 40% of the Carnot efficiency at the tested temperature range. Cooler 1 consumes 488 W acoustic power to remove 708 W of heat energy at about -36°C, and rejects it at 64°C. Cooler 2 consumes 723W acoustic power to remove 1200.5 W of heat energy at about 188°C, and rejects it at 372°C, which leads to a COP of about 1.55; that is equivalent to 64% of Carnot COP under these operating conditions. The novelty of such a by-pass configuration is that the by-pass and FBPs actually create a pure travelling wave resonator. The engine unit extracts small amounts of acoustic work from the

resonator, amplifies it and sends it back to it. As the pure travelling wave resonator has very low losses, it requires very little acoustic power to maintain an acoustic resonance.

In chapter 8, the experimental components which were used in this thesis have been designed using SolidWorks software (as shown in appendix two) and then manufactured in the workshop at the University of Glasgow, for example the ambient heat exchanger, hot heat exchanger, regenerator case, and others. In addition, all the measurement tools are described here to reveal how the different parameters are measured.

In addition, a new method to control and tune the acoustic field within a looped-tube travelling wave thermoacoustic engine using a side-branched volume was introduced in this chapter. It can essentially shunt away part of the volumetric velocity at the low impedance region of the engine, so that the acoustic loss can be reduced within the engine. Based on these simulations, a simple experimental rig using inexpensive components and atmospheric air as a working fluid was constructed and tested. Although the measured energy efficiency of the actual experimental rig is much lower than the predictions, due to significant heat and acoustic power losses in actual experiments, there is a qualitative agreement between the simulations and the measurements, in terms of the effect of the acoustic compliance of the side-branched volume on the engine's performance. There is an optimal acoustic compliance corresponding to the best performance in terms of acoustic power output and energy efficiency when the heating power input is fixed.

The contribution of this thesis to new knowledge can be summarised in the section below:

Proves that the by-pass configuration operates on the same thermodynamic principle as other travelling wave thermoacoustic engines.

Utilise the by-pass configuration to design a thermally driven travelling wave thermoacoustic cooler, allowing for evaluation of thermal efficiency.

The by-pass configuration was applied to design a thermally driven travelling wave thermoacoustic system coupled with an electric generator. This new idea was implemented successfully in the design, indicating that the design strategy for a high efficiency engine, as suggested by Backhaus [10], can also be incorporated in the design.

Successful addition of a second stage engine to utilising the by-pass configuration. This idea was carried out with and without acoustic loads. Both of them contributed to increasing the system's performance. This research demonstrates that this new configuration has the potential for developing a low cost thermally driven heat pump system.

Presented a new method to control and tune the acoustic field within a looped-tube travelling wave thermoacoustic engine, using a side-branched volume. Both the simulations and the experimental results have demonstrated that the proposed side-branched volume can effectively adjust the acoustic field within the looped-tube engine and affect its performance.

9.2 Future work

The present study has investigated looped-tube travelling-wave thermoacoustic engines with a by-pass pipe and the effects of a side branched Helmholtz resonator to tune the phase in looped-tube travelling wave thermoacoustic engines. Therefore, future work should explore the following:

- To further demonstrate and validate the by-pass configuration, future work should be focused on the experimental prototypes as designed in this study.

- After successfully coupling the cooler to the by-pass configuration numerically, it would be very interesting to find out how this system works experimentally.

- Similarly, according to the simulation results from coupling the alternator to the by-pass system, future work should be focused on the experimental prototypes designed in this study. In addition, it can be expected that a better performance could be achieved if the pressurised helium is used as working medium like other prototypes.

- In Chapter 7, Numerical investigation of a two-stage travelling-wave thermoacoustic engine with a by-pass configuration has been numerically investigated. This study aims to reduce acoustic losses within the resonator. The simulation results in this study were reasonable, which makes it an attractive prospect to carry on with the experimental work. Such an experimental investigation will enable validation between the experimental and numerical results.

- Regarding the phase tuning study, future work should focus on building a high efficiency experimental rig using pressurised helium as a working fluid to further understand the fundamental mechanism of this type of phase tuning, method, and demonstrate and improve its effectiveness.

Appendices

Appendix One: DeltaEC Simulations

In this appendix, some of the DeltaEC codes which are already used in this thesis are presented.

A1.1: Simulation code of a looped-tube travelling-wave thermoacoustic engine with a by-pass configuration

```
TITLE
!--------------------------------  0
BEGIN
!Start to adjust the phase
 9.8000E+04 a Mean P Pa
  117.00    b Freq   Hz
  311.34    c TBeg   K        G
 3430.0     d |p|    Pa
-3.9632E-10 e Ph(p)  deg
 4.7837E-02 f |U|    m^3/s    G
   14.176   g Ph(U)  deg      G
air           Gas type
!--------------------------------  1 -------------------------
-------
DUCT       Dummy Duct
 5.4094E-03 a Area   m^2      G          3430.0     A |p|    Pa
    0.18845 b Perim  m                 -1.1600E-03 B Ph(p)  deg
 1.0000E-05 c Length m                  4.7837E-02 C |U|
m^3/s
 5.0000E-04 d Srough                      14.175   D Ph(U)  deg
                                          79.542   E Htot   W
 sameas  10   Solid type                  79.542   F Edot   W
!--------------------------------  2 -------------------------
-------
RPN        ChangeMe
    1.0000  a G or T          =2A       1.0000
A ChngeMe
p1 U1 / rho / a / 1a * mag
!--------------------------------  3 -------------------------
-------
TBRANCH    Change Me
 1.1498E+05 a Re(Zb) Pa-s/m^3 G          3430.0     A |p|    Pa
 3.6035E+04 b Im(Zb) Pa-s/m^3 G         -1.1600E-03 B Ph(p)  deg
                                         2.8465E-02 C |U|
m^3/s
                                           -17.402   D Ph(U)  deg
```

```
                                          46.584   E HtotBr W
                                          46.584   F EdotBr W
                                          32.958   G EdotTr W
!--------------------------------  4 --------------------------
-------
RPN        Phase1
     0.0000 a G or T                   17.401
A ChngeMe
3B 3D -
!--------------------------------  5 --------------------------
-------
DUCT       by pass
 3.7000E-03 a Area   m^2      Mstr       3476.4     A |p|    Pa
    0.21561 b Perim  m        5a         -135.12    B Ph(p)  deg
    1.0000  c Length m                   2.7328E-02 C |U|
m^3/s
 5.0000E-04 d Srough                     -118.77    D Ph(U)  deg
                                          46.584   E Htot   W
ideal           Solid type               45.581   F Edot   W
!--------------------------------  6 --------------------------
-------
RPN        Phase2
     0.0000 a G or T                   -16.35
A ChngeMe
5B 5D -
!--------------------------------  7 --------------------------
-------
SOFTEND    Change Me
     0.0000 a Re(z)                      3476.4     A |p|    Pa
     0.0000 b Im(z)                      -135.12    B Ph(p)  deg
     0.0000 c Htot   W                   2.7328E-02 C |U|
m^3/s
                                         -118.77    D Ph(U)  deg
                                           46.584   E Htot   W
                                           45.581   F Edot   W
                                            1.1644  G Re(z)
                                         -0.34161   H Im(z)
                                          311.34    I T      K
!--------------------------------  8 --------------------------
-------
DUCT       compliance
 8.0000E-03 a Area   m^2      Mstr       3574.8     A |p|    Pa
    0.31705 b Perim  m        8a           -3.922   B Ph(p)  deg
    0.1270  c Length m                   1.8535E-02 C |U|
m^3/s
 5.0000E-04 d Srough                      3.1982  D Ph(U)  deg
                                          32.958   E Htot   W
ideal           Solid type               32.874   F Edot   W
!--------------------------------  9 --------------------------
-------
RPN        Phase3
```

```
     0.0000 a G or T                    -7.1202
A ChngeMe
8B 8D -
!---------------------------------- 10 --------------------------
-------
DUCT       inertance1
 1.5000E-03 a Area   m^2                4789.7     A |p|    Pa
    0.18845 b Perim  m                  -74.062    B Ph(p)  deg
    0.6000  c Length m                 1.3412E-02 C |U|
m^3/s
 5.0000E-04 d Srough                    -69.242    D Ph(U)  deg
                                         32.958    E Htot   W
ideal           Solid type              32.006    F Edot   W
!---------------------------------- 11 --------------------------
-------
DUCT       Interance2
sameas  10a a Area   m^2      Mstr       3691.0     A |p|    Pa
    0.13729 b Perim  m        11a        -135.91    B Ph(p)  deg
    0.6000  c Length m                   1.7591E-02 C |U|
m^3/s
 5.0000E-04 d Srough                    -150.51    D Ph(U)  deg
                                         32.958    E Htot   W
ideal           Solid type              31.415    F Edot   W
!---------------------------------- 12 --------------------------
-------
RPN        Phase4
     0.0000 a G or T                    -4.8199
A ChngeMe
10B 10D -
!---------------------------------- 13 --------------------------
-------
RPN        ChangeMe
  302.31    a G or T                    302.31
A ChngeMe
13a =Tm
!---------------------------------- 14 --------------------------
-------
INSULATE   Change Me
!---------------------------------- 15 --------------------------
-------
SX         AHX1
sameas  19a a Area   m^2                3599.0     A |p|    Pa
    0.8000  b VolPor                    -135.53    B Ph(p)  deg
 5.6000E-04 c Length m                  1.7626E-02 C |U|
m^3/s
 4.0000E-05 d rh     m                  -150.98    D Ph(U)  deg
 -589.08    e HeatIn W        G         -556.12    E Htot   W
  301.00    f SolidT K        =15H        30.573   F Edot   W
                                        302.31    G GasT   K
ideal           Solid type              301.00    H SolidT K
```

```
!-------------------------------- 16 -------------------------
-------
RPN        Phase5
     0.0000 a G or T                    15.446
A ChngeMe
15B 15D -
!-------------------------------- 17 -------------------------
-------
RPN        Phase at cold end of Regenerator
     0.0000 a G or T                    15.446
A ChngeMe
p1 U1 / arg
!-------------------------------- 18 -------------------------
-------
RPN        ChangeMe
   30.033   a G or T                    6.2248
A ChngeMe
p1 U1 / rho / a / 19a * mag
!-------------------------------- 19 -------------------------
-------
STKSCREEN  REG1
 1.2000E-02 a Area   m^2                3576.9     A |p|    Pa
    0.7400  b VolPor                    -135.47    B Ph(p)  deg
 1.5800E-03 c Length m                  2.0409E-02 C |U|
m^3/s
 1.5000E-04 d rh     m                  -154.84    D Ph(U)  deg
    0.1500  e ksFrac                    -556.12    E Htot   W
                                          34.433   F Edot   W
                                         302.31    G TBeg   K
stainless           Solid type          360.46    H TEnd   K
!-------------------------------- 20 -------------------------
-------
RPN        ChangeMe
     0.0000 a G or T                    1.9783
A ChngeMe
dk 19d /
!-------------------------------- 21 -------------------------
-------
RPN        Phase6
     0.0000 a G or T                    19.374
A ChngeMe
19B 19D -
!-------------------------------- 22 -------------------------
-------
RPN        ChangeMe
     0.0000 a G or T                    1.9783
A ChngeMe
dk 19d /
!-------------------------------- 23 -------------------------
-------
RPN        ChangeMe
```

```
     0.0000 a G or T                    4.3174
A ChngeMe
p1 U1 / mag 19a * 19b * rho / a /
!---------------------------------- 24 -------------------------
-------
RPN        Phase at Hot end of Regenerator
     0.0000 a G or T                    19.374
A ChngeMe
p1 U1 / arg
!---------------------------------- 25 -------------------------
-------
RPN        ChangeMe
  414.76    a G or T                    414.76
A ChngeMe
25a =Tm
!---------------------------------- 26 -------------------------
-------
SX         HHX1
sameas  19a a Area   m^2                3561.3     A |p|    Pa
    0.8000  b VolPor                    -135.39    B Ph(p)  deg
sameas  15c c Length m                  2.0446E-02 C |U|
m^3/s
 1.2000E-04 d rh     m                  -155.22    D Ph(U)  deg
  600.10    e HeatIn W        G           43.979   E Htot   W
  421.04    f SolidT K        =26H        34.248   F Edot   W
                                         414.76    G GasT   K
ideal           Solid type              421.04    H SolidT K
!---------------------------------- 27 -------------------------
-------
RPN        Phase7
     0.0000 a G or T                    19.832
A ChngeMe
26B 26D -
!---------------------------------- 28 -------------------------
-------
DUCT       Section 2
sameas  19a a Area   m^2      Mstr       3545.5     A |p|    Pa
    0.38833 b Perim  m        28a        -135.86    B Ph(p)  deg
 3.0000E-02 c Length m                  2.3641E-02 C |U|
m^3/s
 5.0000E-04 d Srough                    -171.12    D Ph(U)  deg
                                           43.979   E Htot   W
ideal           Solid type                34.219   F Edot   W
!---------------------------------- 29 -------------------------
-------
RPN        ChangeMe
  306.49    a G or T                    306.49
A ChngeMe
29a =Tm
!---------------------------------- 30 -------------------------
-------
```

```
SX         AHX2
sameas  19a a Area   m^2                3531.2     A |p|    Pa
sameas  15b b VolPor                    -135.72    B Ph(p)  deg
sameas  15c c Length m                  2.3711E-02 C |U|
m^3/s
 1.2000E-04 d rh     m                  -171.41    D Ph(U)  deg
 -589.39    e HeatIn W        G         -545.41    E Htot   W
  301.00    f SolidT K        =30H        34.001   F Edot   W
                                         306.49    G GasT   K
ideal           Solid type              301.00    H SolidT K
!--------------------------------- 31 --------------------------
-------
STKSCREEN  REG2
sameas  19a a Area   m^2                3495.0     A |p|    Pa
    0.7400  b VolPor                    -135.34    B Ph(p)  deg
 1.5800E-03 c Length m                  2.7675E-02 C |U|
m^3/s
 1.3000E-04 d rh     m                  -174.05    D Ph(U)  deg
    0.1000  e ksFrac                    -545.41    E Htot   W
                                          37.742   F Edot   W
                                         306.49    G TBeg   K
stainless          Solid type           360.77    H TEnd   K
!--------------------------------- 32 --------------------------
-------
RPN        ChangeMe
     0.0000 a G or T                  2.9698E-04
A ChngeMe
dk
!--------------------------------- 33 --------------------------
-------
RPN        ChangeMe
     0.0000 a G or T                  2.2845
A ChngeMe
dk 31d /
!--------------------------------- 34 --------------------------
-------
RPN        ChangeMe
  415.71    a G or T                  415.71
A ChngeMe
34a =Tm
!--------------------------------- 35 --------------------------
-------
SX         HHX2
sameas  19a a Area   m^2                3476.4     A |p|    Pa
sameas  15b b VolPor                    -135.12    B Ph(p)  deg
sameas  15c c Length m                  2.7755E-02 C |U|
m^3/s
 1.2000E-04 d rh     m                  -174.28    D Ph(U)  deg
  600.13    e HeatIn W        G           54.723   E Htot   W
  421.01    f SolidT K        =35H        37.410   F Edot   W
                                         415.71    G GasT   K
```

```
ideal           Solid type                421.01    H SolidT K
!---------------------------------- 36 --------------------------
-------
UNION      Change Me
  7         a SegNum                     3476.4     A |p|    Pa
sameas   7A b |p|Sft Pa       =36A       -135.12    B Ph(p)  deg
sameas   7B c Ph(p)S deg      =36B       4.8747E-02 C |U|
m^3/s
sameas   7I d TSoft  K                   -146.76    D Ph(U)  deg
                                          101.31    E Htot   W
                                           82.990   F Edot   W
                                          415.71    G T      K
!---------------------------------- 37 --------------------------
-------
RPN        Phase8
     0.0000 a G or T                  11.638
A ChngeMe
36B 36D -
!---------------------------------- 38 --------------------------
-------
RPN        ChangeMe
sameas   0c a G or T                  311.34
A ChngeMe
38a =Tm
!---------------------------------- 39 --------------------------
-------
RPN        ChangeMe
     0.0000 a G or T                  11.638
A ChngeMe
p1 U1 / arg
!---------------------------------- 40 --------------------------
-------
DUCT       Change Me
 3.7000E-03 a Area   m^2               3430.0     A |p|    Pa
    0.23554 b Perim  m                -3.9606E-10 B Ph(p)  deg
    1.7508  c Length m        G        4.7837E-02 C |U|
m^3/s
 5.0000E-04 d Srough                    14.176    D Ph(U)  deg
                                       101.31     E Htot   W
ideal           Solid type              79.542    F Edot   W
!---------------------------------- 41 --------------------------
-------
RPN        Phase9
     0.0000 a G or T                  -14.176
A ChngeMe
40B 40D -
!---------------------------------- 42 --------------------------
-------
RPN        ChangeMe
     0.0000 a G or T                  0.71106
A ChngeMe
```

```
p1 U1 / mag 0.0038465 * rho / a /
!---------------------------------- 43 --------------------------
-------
RPN        ChangeMe
     0.0000 a G or T                    -14.176
A ChngeMe
p1 U1 / arg
!---------------------------------- 44 --------------------------
-------
RPN        P1
sameas   0d a G or T          =44A      3430.0
A ChngeMe
p1 mag
!---------------------------------- 45 --------------------------
-------
RPN        U1
sameas   0f a G or T          =45A      4.7837E-02
A ChngeMe
U1 mag
!---------------------------------- 46 --------------------------
-------
RPN        Ph(p1)
     0.0000 a G or T          =46A      2.6343E-13
A ChngeMe
p1 arg 0e -
!---------------------------------- 47 --------------------------
-------
RPN        Ph(U1)
     0.0000 a G or T          =47A      -3.5527E-15
A ChngeMe
U1 arg 0g -
!---------------------------------- 48 --------------------------
-------
RPN        Dr
     0.0000 a G or T                    3.5000
A %
0d 0a / 100 *
!---------------------------------- 49 --------------------------
-------
RPN        ChangeMe
     0.0000 a G or T                    32.006
A E inter
                                        79.542
B E reson
40F 10F
!---------------------------------- 50 --------------------------
-------
RPN        Phase checking
     0.0000 a G or T                    17.401
A ChngeMe
```

```
                                        -16.35
B ChngeMe
                                        -7.1202
C ChngeMe
                                        -4.8199
D ChngeMe
                                        15.446
E ChngeMe
                                        19.374
F ChngeMe
                                        19.832
G ChngeMe
                                        11.638
H ChngeMe
                                        -14.176
I ChngeMe
41A 37A 27A 21A 16A 12A 9A 6A 4A
!---------------------------------- 51 --------------------------
-------
RPN        Net acoustic power production (Einertance2-EHHX2)
     0.0000 a G or T                    5.9946
A Watt
35F 11F -
!---------------------------------- 52 --------------------------
-------
RPN        Overall Efficincy
     0.0000 a G or T                    0.49945
A %
51A 26e 35e + / 100 *
!---------------------------------- 53 --------------------------
-------
RPN        Carnt Efficiency
     0.0000 a G or T                    28.505
A %
35H 30H - 35H / 100 *
!---------------------------------- 54 --------------------------
-------
RPN        Relative Efficiency
     0.0000 a G or T                    1.7521
A %
52A 53A / 100 *
!---------------------------------- 55 --------------------------
-------
RPN        Thot & Tcold
     0.0000 a G or T                    301.00
A Tc1
                                        421.04
B Th1
                                        301.00
C Tc2
```

```
                                        421.01
D Th2
35H 30H 26H 15H
!--------------------------------- 56 -------------------------
-------
RPN        Th1-Tc1
     0.0000 a G or T                    120.04
A ChngeMe
26H 15H -
!--------------------------------- 57 -------------------------
-------
RPN        Th2-Tc2
     0.0000 a G or T                    120.01
A ChngeMe
35H 30H -
! The restart information below was generated by a previous run
! and will be used by DeltaEC the next time it opens this file.
guessz   0c   0f   0g   1a   3a   3b  15e  26e  30e  35e  40c
xprecn -2.0352E-03 -2.4186E-07  4.2227E-04  4.8487E-08
4.6918      0.21097 -1.1773E-03  2.7597E-03 -1.2069E-04
3.6168E-03  3.3285E-05
targs    2a  15f  26f  30f  35f  36b  36c  44a  45a  46a  47a
hilite 0c 5a 5c 8a 8c 10a 10c 11F 17A 19F 19c 24A 28c 40B 40D
40F 40a 47A 49A 49B 50G 51A
mstr-slave 4 5 -2 8 -2 11 -2 28 -2
! Plot start, end, and step values.  May be edited if you wish.
! Outer Loop:                       | Inner Loop .
```

A1.2: Simulation code of a side-branched Helmholtz resonator to tune phase in looped-tube travelling wave thermoacoustic engine (without RC-load)

```
TITLE
!--------------------------------  0
BEGIN      Change Me
 1.0133E+05 a Mean P Pa
   60.500   b Freq   Hz
  310.00    c TBeg   K
 6763.3     d |p|    Pa       G
     0.0000 e Ph(p)  deg
 5.1979E-03 f |U|    m^3/s    G
   60.137   g Ph(U)  deg      G
   68.227   h Htot   W        G
air           Gas type
!--------------------------------  1 -------------------------
-------
RPN        ChangeMe
```

```
 6785.7     a G or T          =1A       6785.7
A ChngeMe
2A
!--------------------------------  2 -------------------------
-------
CONE       Change Me
sameas  19a a AreaI  m^2      Mstr       6785.7     A |p|    Pa
 6.4027E-02 b PerimI m        2a           -0.1149  B Ph(p)  deg
 1.2000E-02 c Length m                   4.9023E-03 C |U|
m^3/s
sameas   6a d AreaF  m^2      Mstr         58.169   D Ph(U)  deg
    0.2042  e PerimF m        2d           68.227   E Htot   W
 5.0000E-04 f Srough                       8.7440  F Edot   W
ideal           Solid type
!--------------------------------  3 -------------------------
-------
DUCT       stage 1
sameas   6a a Area   m^2      Mstr       6785.7     A |p|    Pa
    0.2042  b Perim  m        3a           -0.1149  B Ph(p)  deg
 1.0000E-13 c Length m                   4.9023E-03 C |U|
m^3/s
 5.0000E-04 d Srough                       58.169   D Ph(U)  deg
                                           68.227   E Htot   W
ideal           Solid type                 8.7440  F Edot   W
!--------------------------------  4 -------------------------
-------
RPN        Dia of Engine
     0.0000 a G or T                  65.000
A mm
3a pi / 0.5 ^ 1000 * 2 *
!--------------------------------  5 -------------------------
-------
RPN        Dia of Resonator
     0.0000 a G or T                  20.380
A mm
19a pi / 0.5 ^ 1000 * 2 *
!--------------------------------  6 -------------------------
-------
TX         AHX1
 3.3183E-03 a Area   m^2               6836.0     A |p|    Pa
    0.2800  b GasA/A                  -0.54391    B Ph(p)  deg
 2.7000E-02 c Length m                 4.4612E-03 C |U|
m^3/s
 1.5000E-03 d radius m                   55.220   D Ph(U)  deg
 -100.0     e HeatIn W                  -31.773   E Htot   W
  293.98    f SolidT K                    8.5790  F Edot   W
                                         310.00    G GasT   K
ideal           Solid type              270.27    H SolidT K
!--------------------------------  7 -------------------------
-------
STKSCREEN  Regenetaor
```

```
sameas   6a a Area   m^2                6552.1     A |p|    Pa
    0.7840  b VolPor                     -3.6867  B Ph(p)  deg
 2.0000E-02 c Length m                  6.1726E-03 C |U|
m^3/s
 1.2677E-04 d rh     m                    43.652   D Ph(U)  deg
    0.1500  e ksFrac                     -31.773   E Htot   W
                                          13.703   F Edot   W
                                          310.00    G TBeg   K
stainless           Solid type            529.55    H TEnd   K
!--------------------------------  8 --------------------------
-------
RPN        ChangeMe
     0.0000 a G or T                   5.7630E-04
A ChngeMe
dk
!--------------------------------  9 --------------------------
-------
RPN        ChangeMe
     0.0000 a G or T                   4.5460
A ChngeMe
dk 7d /
!-------------------------------- 10 --------------------------
-------
RPN        phase checking
     0.0000 a G or T                   -47.339
A ChngeMe
7B 7D -
!-------------------------------- 11 --------------------------
-------
TX         HHX1
sameas   6a a Area   m^2                6566.5     A |p|    Pa
    0.5000  b GasA/A                     -3.9748  B Ph(p)  deg
 3.0000E-02 c Length m                  5.3867E-03 C |U|
m^3/s
 1.5000E-03 d radius m                    37.225   D Ph(U)  deg
  150.00    e HeatIn W                   118.23    E Htot   W
 1168.5     f SolidT K                    13.307   F Edot   W
                                          529.55    G GasT   K
ideal           Solid type               579.98    H SolidT K
!-------------------------------- 12 --------------------------
-------
DUCT       Change Me
sameas   6a a Area   m^2      Mstr       6564.8     A |p|    Pa
    0.2042  b Perim  m        12a          -4.3143  B Ph(p)  deg
    0.1250  c Length m                  5.5074E-03 C |U|
m^3/s
 5.0000E-04 d Srough                     -47.711   D Ph(U)  deg
                                          118.23    E Htot   W
ideal           Solid type                13.135   F Edot   W
!-------------------------------- 13 --------------------------
-------
```

Appendix One: DeltaEC simulation codes

```
RPN        ChangeMe
  350.00    a G or T                   350.00
A ChngeMe
13a =Tm
!---------------------------------- 14 --------------------------
-------
TX         SAHX
sameas   6a a Area   m^2                6497.4     A |p|    Pa
    0.2800  b GasA/A                     -4.6674  B Ph(p)  deg
 2.7000E-02 c Length m                  5.8233E-03 C |U|
m^3/s
 1.5000E-03 d radius m                   -51.464   D Ph(U)  deg
  -41.612   e HeatIn W        G           76.615   E Htot   W
  991.49    f SolidT K                    12.951   F Edot   W
                                         350.00    G GasT   K
ideal           Solid type              333.64    H SolidT K
!---------------------------------- 15 --------------------------
-------
RPN        EB
     0.0000 a G or T          =15A      -3.5527E-15
A ChngeMe
14e 11e 6e + + 14F 11F 3F - - -
!---------------------------------- 16 --------------------------
-------
RPN        ChangeMe
  300.00    a G or T                   300.00
A ChngeMe
16a =Tm
!---------------------------------- 17 --------------------------
-------
ANCHOR     Change Me
!---------------------------------- 18 --------------------------
-------
CONE       Change Me
sameas  19a a AreaI  m^2      Mstr       6474.4     A |p|    Pa
 6.4027E-02 b PerimI m        18a          -4.8489  B Ph(p)  deg
 1.2000E-02 c Length m                  6.0641E-03 C |U|
m^3/s
sameas   6a d AreaF  m^2      Mstr        -53.60    D Ph(U)  deg
    0.2042  e PerimF m        18d          12.943   E Htot   W
 5.0000E-04 f Srough                     12.943   F Edot   W
ideal           Solid type
!---------------------------------- 19 --------------------------
-------
DUCT       resonator
 3.2622E-04 a Area   m^2      Mstr       3400.5     A |p|    Pa
 6.4027E-02 b Perim  m        19a         -87.092   B Ph(p)  deg
    0.7000  c Length m                  7.3831E-03 C |U|
m^3/s
 5.0000E-04 d Srough                     -72.069   D Ph(U)  deg
                                          12.124   E Htot   W
```

```
ideal           Solid type                  12.124   F Edot   W
!---------------------------------- 20 --------------------------
-------
RPN        ChangeMe
     0.0000 a G or T                   -15.023
A ChngeMe
19B 19D -
!---------------------------------- 21 --------------------------
-------
TBRANCH    Change Me
 2305.9     a Re(Zb) Pa-s/m^3 G          3400.5     A |p|    Pa
-8.9473E+05 b Im(Zb) Pa-s/m^3 G           -87.092   B Ph(p)  deg
                                       3.8005E-03 C |U|
m^3/s
                                          2.7603  D Ph(U)  deg
                                       1.6653E-02 E HtotBr W
                                       1.6653E-02 F EdotBr W
                                         12.107   G EdotTr W
!---------------------------------- 22 --------------------------
-------
DUCT       stub
sameas  19a a Area   m^2      Mstr       3437.8     A |p|    Pa
 6.4027E-02 b Perim  m        22a         -87.112   B Ph(p)  deg
 6.9849E-03 c Length m                  3.7794E-03 C |U|
m^3/s
 5.0000E-04 d Srough                       2.7637  D Ph(U)  deg
                                       1.4123E-02 E Htot   W
ideal           Solid type             1.4123E-02 F Edot   W
!---------------------------------- 23 --------------------------
-------
DUCT       Volume
 1.2400E-02 a Area   m^2      Mstr       3440.0     A |p|    Pa
    0.39474 b Perim  m        23a         -87.112   B Ph(p)  deg
 3.3000E-02 c Length m                  1.0332E-18 C |U|
m^3/s
 5.0000E-04 d Srough                       175.49    D Ph(U)  deg
                                      -2.2895E-16 E Htot   W
ideal           Solid type            -2.2895E-16 F Edot   W
!---------------------------------- 24 --------------------------
-------
RPN        ChangeMe
     0.0000 a G or T                   -262.6
A ChngeMe
23B 23D -
!---------------------------------- 25 --------------------------
-------
HARDEND    Change Me
     0.0000 a R(1/z)          =25G       3440.0     A |p|    Pa
     0.0000 b I(1/z)          =25H        -87.112   B Ph(p)  deg
                                       1.0332E-18 C |U|
m^3/s
```

```
                                          175.49    D Ph(U)  deg
                                      -2.2895E-16 E Htot   W
                                      -2.2895E-16 F Edot   W
                                      -1.2749E-18 G R(1/z)
                                      -9.8134E-18 H I(1/z)
!---------------------------------- 26 --------------------------
-------
DUCT       Change Me
sameas  19a a Area   m^2      Mstr       6763.3     A |p|    Pa
 6.4027E-02 b Perim  m        26a        7.7048E-15 B Ph(p)  deg
    3.6312  c Length m        G          5.1979E-03 C |U|
m^3/s
 5.0000E-04 d Srough                       60.137   D Ph(U)  deg
                                            8.7523  E Htot   W
ideal           Solid type                 8.7523  F Edot   W
!---------------------------------- 27 --------------------------
-------
RPN        set p1 mag
sameas   0d a G or T          =27A      6763.3
A ChngeMe
p1 mag
!---------------------------------- 28 --------------------------
-------
RPN        set p1 phase
     0.0000 a G or T          =28A      7.7048E-15
A ChngeMe
p1 arg 0e -
!---------------------------------- 29 --------------------------
-------
RPN        set mag u1
sameas   0f a G or T          =29A      5.1979E-03
A ChngeMe
U1 mag
!---------------------------------- 30 --------------------------
-------
RPN        set u1 phase
     0.0000 a G or T          =30A      -2.1316E-14
A ChngeMe
U1 arg 0g -
!---------------------------------- 31 --------------------------
-------
RPN        Dr
     0.0000 a G or T                    6.6745
A ChngeMe
0d 0a / 100 *
!---------------------------------- 32 --------------------------
-------
RPN        Carnot Eff
     0.0000 a G or T                    53.400
A %
11H 6H - 11H / 100 *
```

```
!-------------------------------- 33 -------------------------
-------
RPN        acoustic production
     0.0000 a G or T                    4.7281
A ChngeMe
11F 6F -
!-------------------------------- 34 -------------------------
-------
RPN        overall efficiency
     0.0000 a G or T                    3.1521
A ChngeMe
33A 11e / 100 *
! The restart information below was generated by a previous run
! and will be used by DeltaEC the next time it opens this file.
guessz   0d   0f   0g   0h  14e  21a  21b  26c
xprecn  1.5443E-02 -3.8147E-08 -1.2862E-04 -2.0375E-04  6.7438E-
05 -2.5253E-02    -4.7206  -2.9233E-05
targs    1a  15a  25a  25b  27a  28a  29a  30a
hilite 0b 0c 19c 34A
mstr-slave 8 2 -9 3 -2 12 -2 18 -9 19 -2 22 -2 23 -2 26 -2
! Plot start, end, and step values.  May be edited if you wish.
! Outer Loop:                       | Inner Loop.
```

Appendix Tow: Additional details of the experimental rigs

A2.1: Hot heat exchanger case

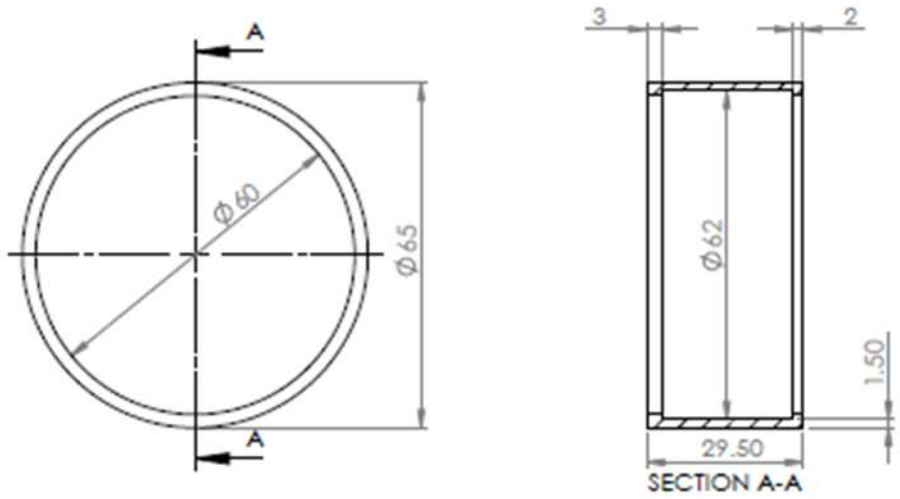

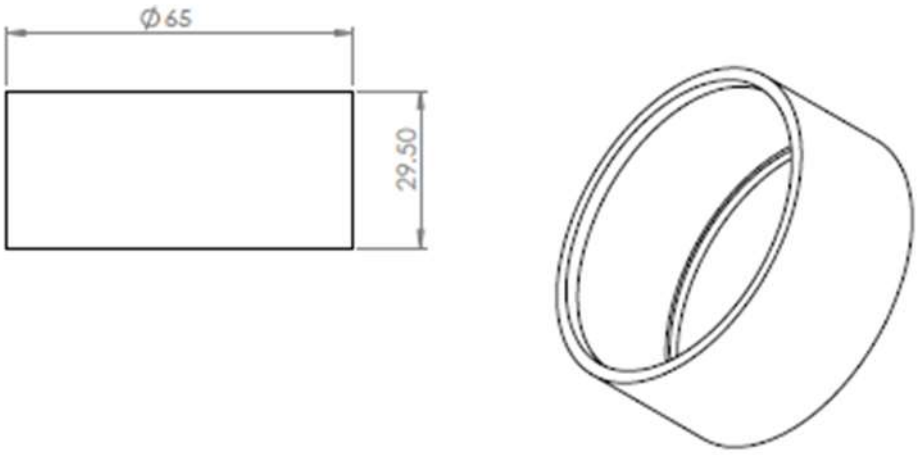

A2.2: Cold heat exchanger case

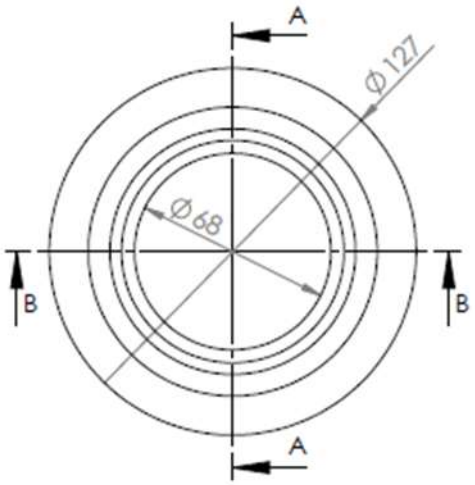

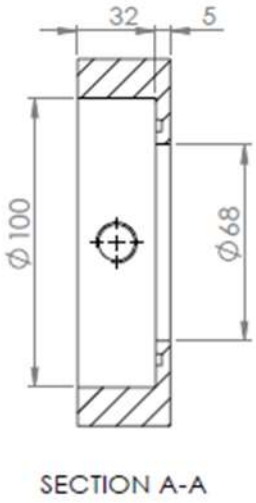

SECTION A-A

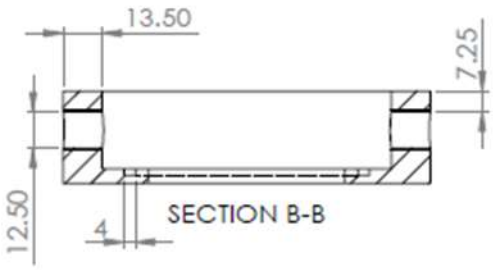

SECTION B-B

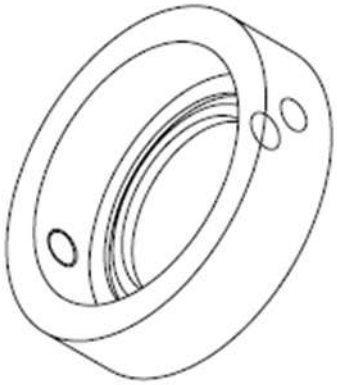

A2.3: Copper of cold heat exchanger

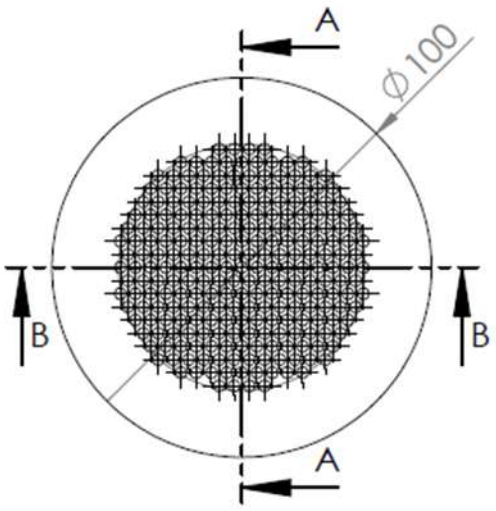

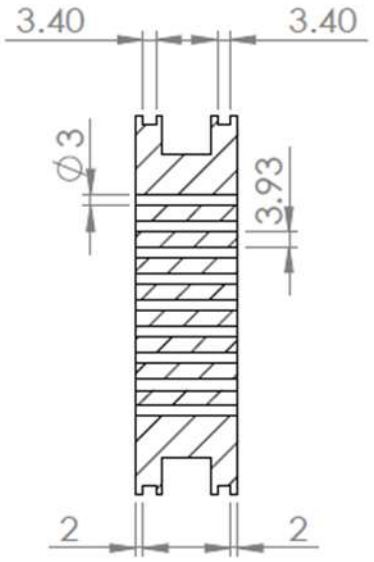

SECTION A-A

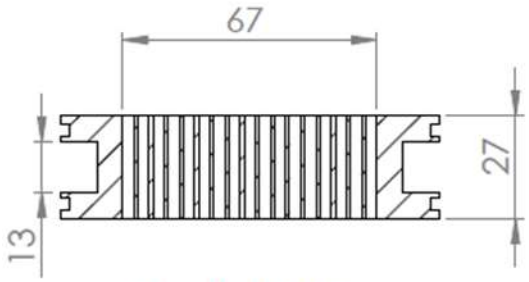

SECTION B-B

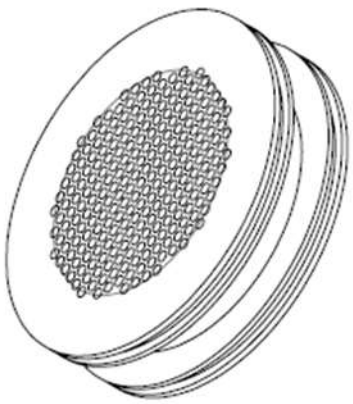

A2.4: Case of regenerator

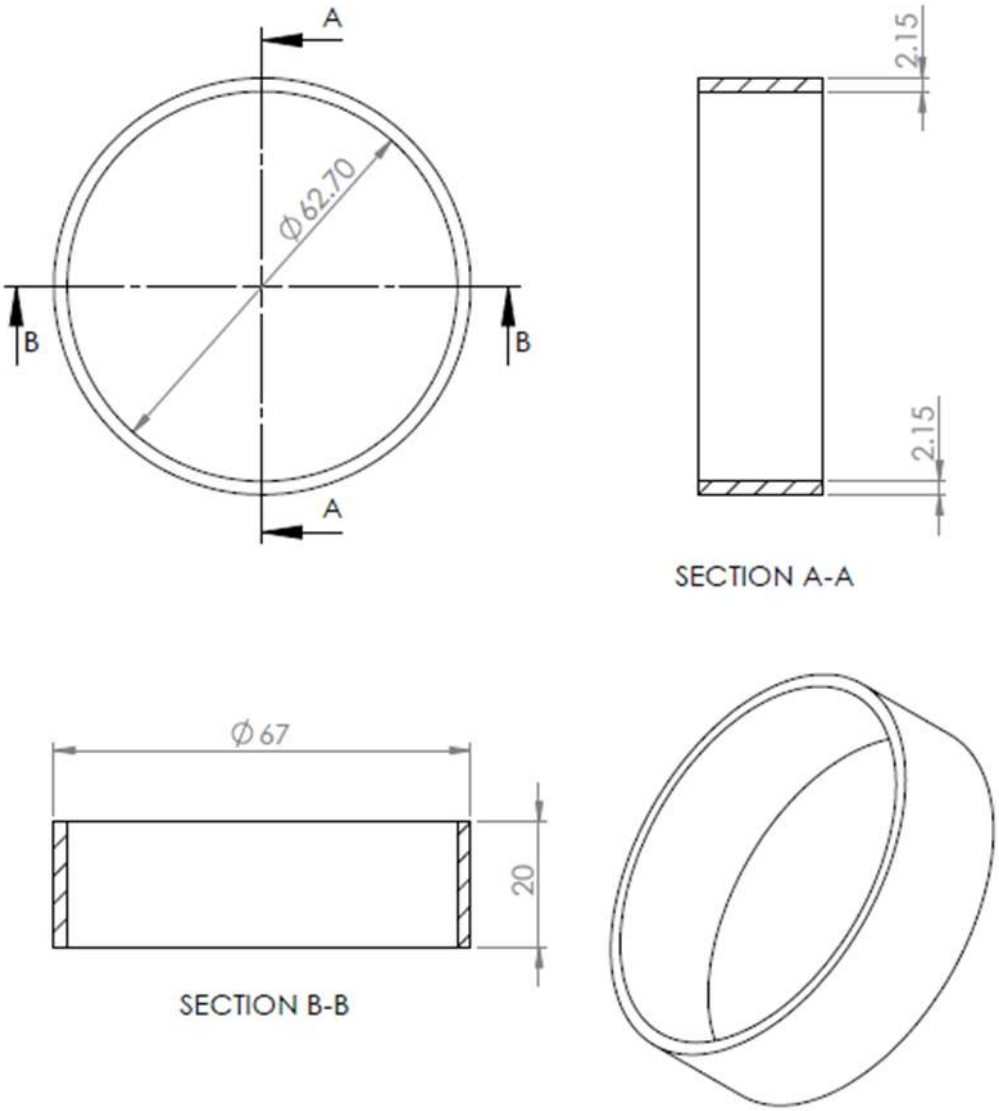

A2.5: Flange

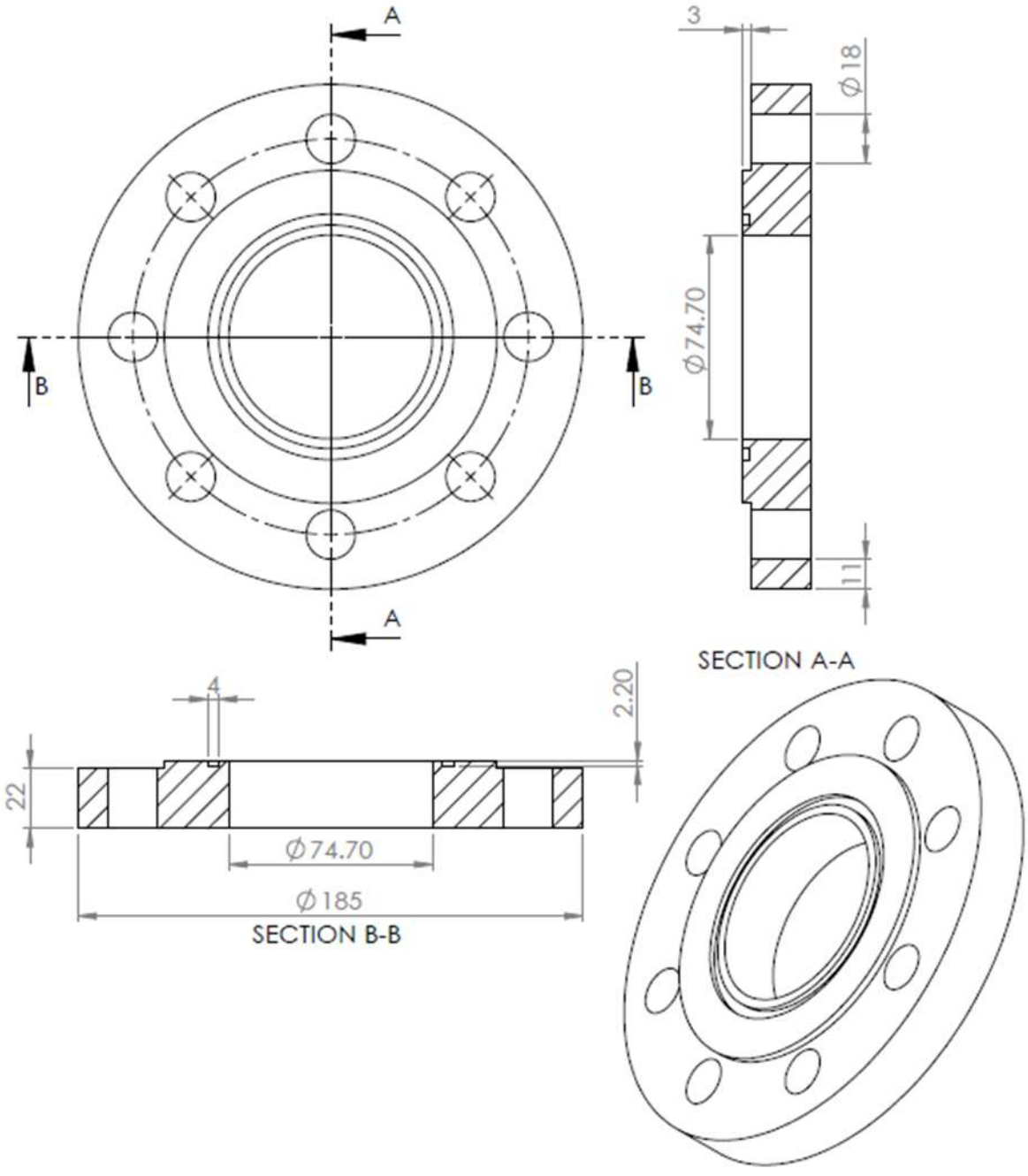

A2.6: Flange hole

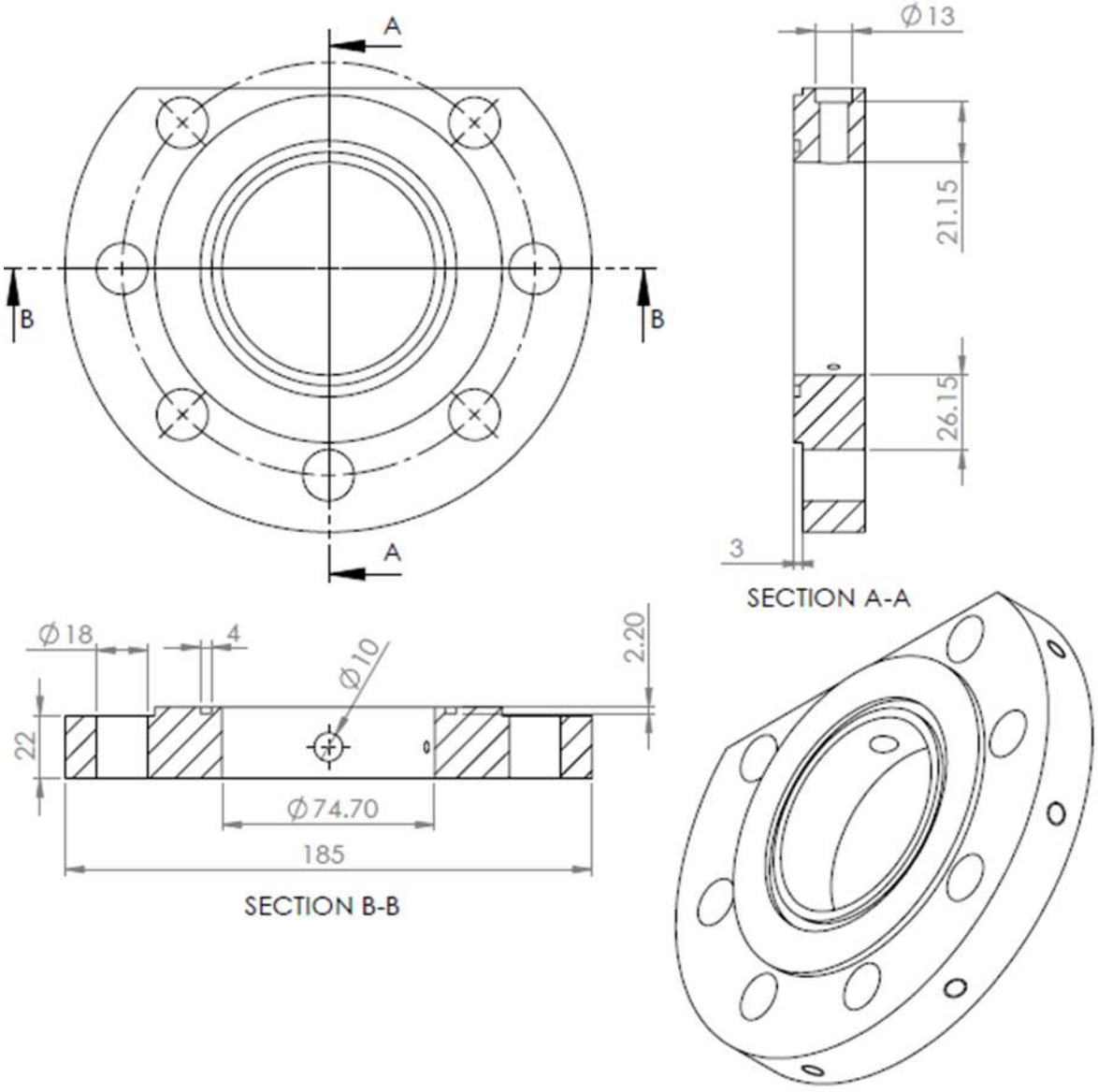

A2.7: Flange cone

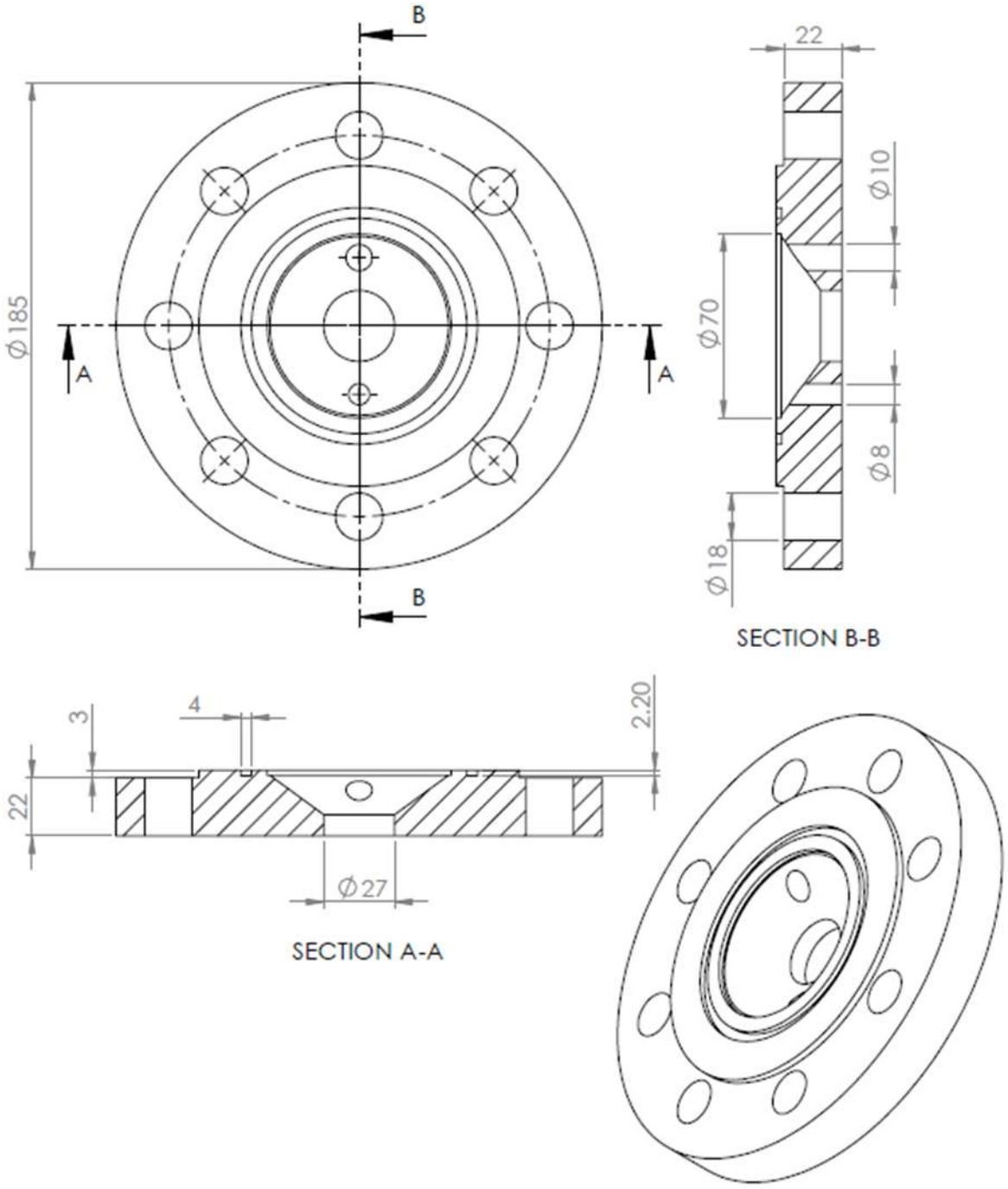

A2.8: Pressure sensor adapter

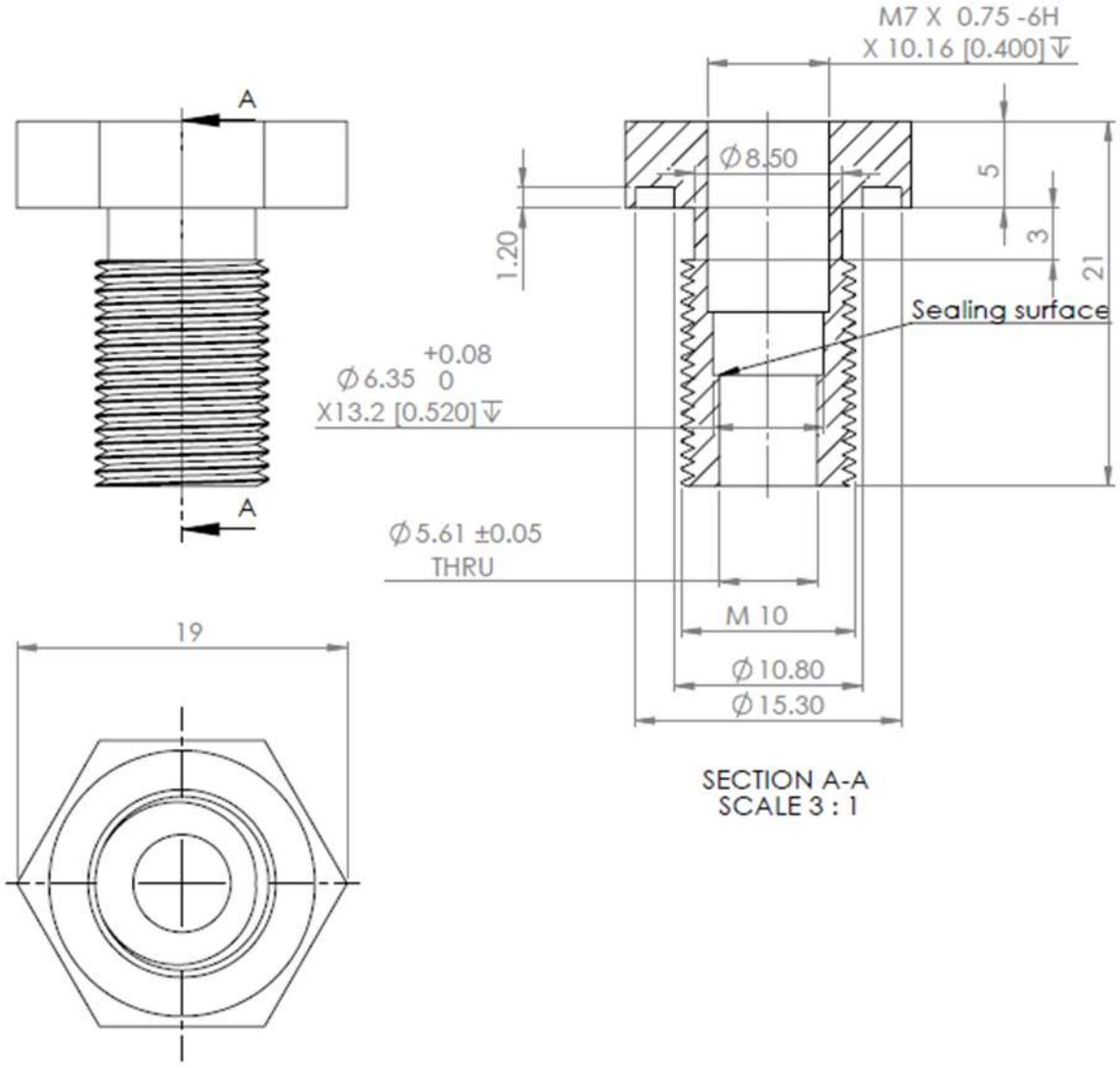

Appendix Three: Publications

A3.1: Journal publications:

1. **Al-Kayiem, A.**, Yu, Z., Using a side-branched volume to tune the acoustic field in a looped-tube travelling wave thermoacoustic engine with a RC load. Energy Conversion and Management 2017; 150: 814-821.

2. **Al-Kayiem, A.**, Yu, Z., Numerical investigation of a looped-tube travelling-wave thermoacoustic engine with a by-pass pipe. Energy 2016; 112: 111-120.

3. Yu, Z. and **Al-Kayiem, A.**, Numerical Analysis of a Thermally Driven Thermoacoustic Heat Pump for Low-Grade Heat Recovery. Computational Thermal Sciences 2014; 6(4): 317-327.

A3.2: Conference contributions:

1. **Al-Kayiem A.**, Yu, Z., Design of a traveling wave thermoacoustic engine driven cooler with hybrid configuration, proceeding of the World congress on engineering 2014 Vol II,WCE 2014, 2^{nd} – 4^{th} July , 2014, London, U.K

2. **Al-Kayiem A.**, Yu Z., Using side-branched Helmholtz resonator to tune phase in looped-tube travelling wave thermoacoustic engine, The ASME-ATI-UIT 2015 Conference on Thermal Energy Systems: Production, Storage, Utilization and the Environment". 17^{th} -20^{th} May, 2015, Napoli, Italy.

3. **Al-Kayiem A.**, Numercial investigation of a two-stage travelling-wave thermoacoustic engine driven heat pump with a hybrid configuration, UK Heat Transfer Conference 2015, 7^{th} -8^{th} September, Edinburgh, UK.

4. **Al-Kayiem A.**, Yu Z., Numerical investigation of the effects of a side-branched Helmholtz resonator on a looped-tube travelling wave thermoacoustic engine,

The 4th Sustainable Thermal Energy Management International Conference (SusTEM 2017), 28th – 30th June, Netherlands.

5. **Al-Kayiem A.**, Yu Z.,Numerical investigation of a looped-tube traveling-wave thermoacoustic generator with a by-pass pipe, Cardiff to Host 9th International Conference on Applied Energy (ICAE-2017), 21st - 24th August, Cardiff, UK.

Appendix Four: Awards and achievements

1. I won the James Watt PG award for an outstanding 2nd year Engineering Research student 2015 in Glasgow University (£5000). This award is for a PGR Engineering student. There are 205 students registered for this award, and I have been selected to win among these number of PhD students across the world.

2. I won an award - "Certificate of Merit (Student) for The 2014 International Conference of Mechanical Engineering".
http://www.iaeng.org/WCE2014/congress_awards.html.by presenting a paper (Al-Kayiem A., Yu, Z., Design of a traveling wave thermoacoustic engine driven cooler with hybrid configuration, proceeding of the World congress on engineering 2014, Vol II,WCE 2014, July 2-4, 2014, London, U.K) at "International Conference of Mechanical Engineering 2014 in London"

Appendix Five: Calibration of pressure sensors

A5.1: Calibration of pressure sensors 1:

CALIBRATION CERTIFICATE

Model: 113B27
Serial #: 24484
Description: Pressure Sensor
Type: ICP
Time Constant: 2.7 sec

Date: 9/29/2012
By: David Kimmel, Cal. Tech.
Station: 903 Pulse #3 (Test procedure AT601-6)

Sensitivity*: 53.16 mV/PSI
7.710 mV/kPa

Temp: 71 deg F (22deg C)
Humidity: 39 %

Linearity*: 0.08% FS
Uncertainty**: +/- 1 %

Cert #: 452045

Bias: 8.2 VDC

* Zero based, least-squares straight line.

** Measurement uncertainty represented using a coverage factor of k=2 which provides a level of confidence of approximately 95 %.

Condition of Unit:
As Found: Not applicable
As Left: In tolerance, new unit

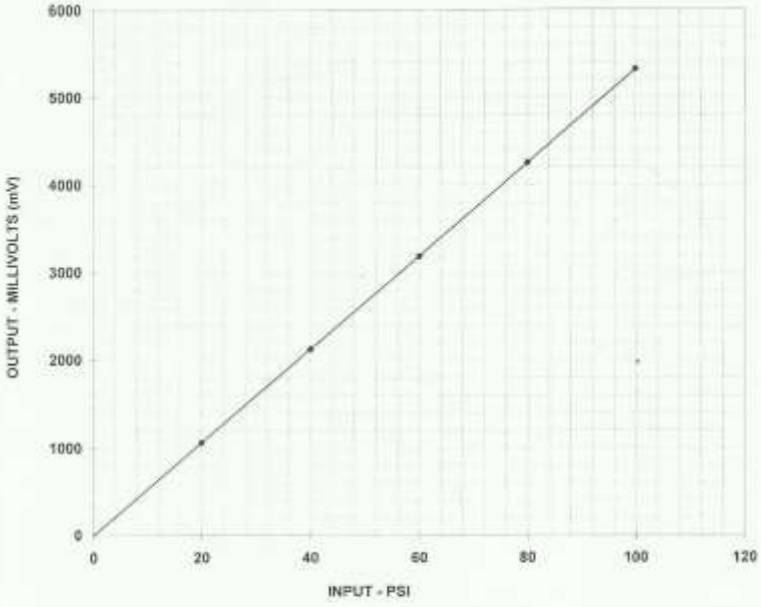

TEST DATA

INPUT (PSI)	OUTPUT (mV)
20.0	1063
40.0	2124
60.0	3186
80.0	4252
100	5320

Notes:
1 Station #15
2 Calibration is traceable to NIST and is accredited to ISO 17025 and ANSI/NCSL Z540-1-1994.
3 NIST traceability through PCB control # CA1296A.
4 This certificate may not be reproduced, except in full, without written approval from PCB Piezotronics, Inc.

ACCREDITED
CALIBRATION CERT #1962.01

PCB PIEZOTRONICS

Tel: 716-684-0001 Fax: 716-684-0987 Email: sales@pcb.com
3425 Walden Avenue, Depew NY 14043

ISO 9001 CERTIFIED

Page 1 of 1

A5.2: Calibration of pressure sensors 2:

CALIBRATION CERTIFICATE

Model: 113B27
Serial #: 24463
Description: Pressure Sensor
Type: ICP

Time Constant: 2.9 sec

Date: 9/29/2012
By: David Kimmel, Cal. Tech
Station: 903 Pulse #3 (Test procedure AT601-6)

Sensitivity*: 52.33 mV/PSI
7.590 mV/kPa

Temp: 71 deg F [22deg C]
Humidity: 39 %

Linearity*: 0.08% FS
Uncertainty**: +/- 1 %

Cert #: 452044

Bias: 8.2 VDC

* Zero based, least-squares straight line.

** Measurement uncertainty represented using a coverage factor of k=2 which provides a level of confidence of approximately 95 %.

Condition of Unit:
As Found: Not applicable
As Left: In tolerance, new unit

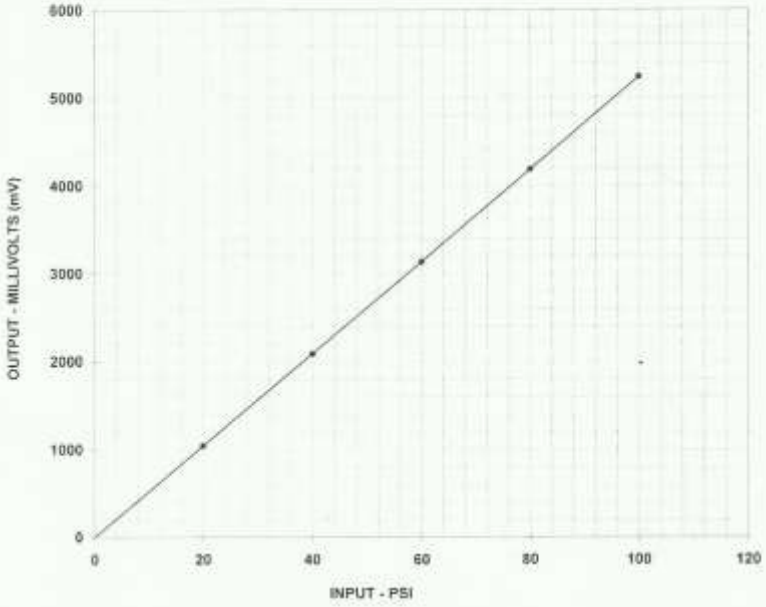

TEST DATA

INPUT (PSI)	OUTPUT (mV)
20.0	1047
40.0	2090
60.0	3137
80.0	4186
100	5237

Notes:
1. Station #15
2. Calibration is traceable to NIST and is accredited to ISO 17025 and ANSI/NCSL Z540-1-1994.
3. NIST traceability through PCB control # CA1296A.
4. This certificate may not be reproduced, except in full, without written approval from PCB Piezotronics, Inc.

ACCREDITED
CALIBRATION CERT #1852.01

PCB PIEZOTRONICS

Tel: 716-684-0001 Fax: 716-684-0987 Email: sales@pcb.com
3425 Walden Avenue, Depew NY 14043

ISO 9001 CERTIFIED

Page 1 of 1

A5.3: Calibration of pressure sensors 3:

CALIBRATION CERTIFICATE

Model: 113B27
Serial #: 27390
Description: Pressure Sensor
Type: ICP
Time Constant: 3.5 sec

Date: 4/8/2014
By: Eric Kachermeyer, Cal. Tech.
Station: 903 Pulse #2 (Test procedure AT601-6)

Sensitivity*: 52.26 mV/PSI
7.579 mV/kPa

Temp: 74 deg F [23deg C]
Humidity: 52 %

Linearity*: 0.08% FS
Uncertainty:** +/- 1 %

Cert #: 517275

Bias: 8.8 VDC

* Zero based, least-squares straight line.

** Measurement uncertainty represented using a coverage factor of k=2 which provides a level of confidence of approximately 95 %.

Condition of Unit:
As Found: Not applicable
As Left: In tolerance, new unit

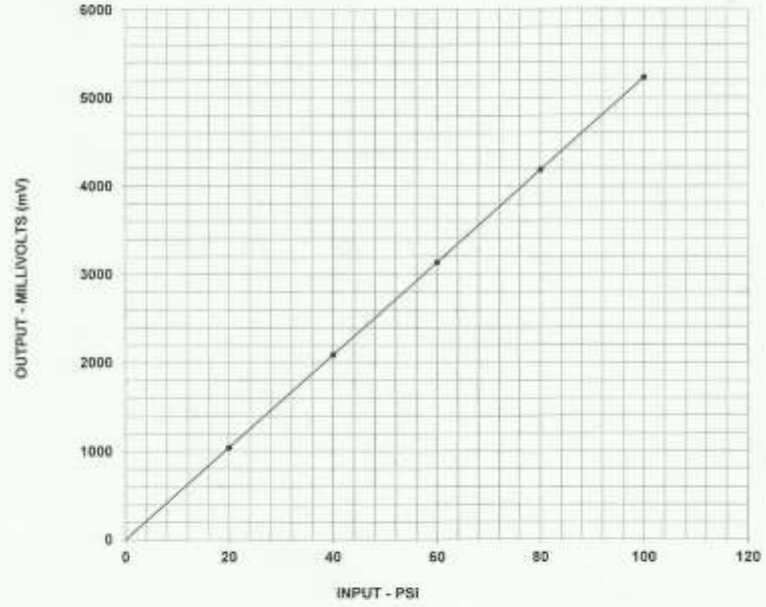

TEST DATA

INPUT (PSI)	OUTPUT (mV)
20.0	1042
40.0	2089
60.0	3134
80.0	4181
100	5227

Notes:
1 STATION #17
2 Calibration is traceable to NIST and is accredited to ISO 17025 and ANSI/NCSL Z540.3.
3 NIST traceability through PCB control # ME127.
4 This certificate may not be reproduced, except in full, without written approval from PCB Piezotronics, Inc.

ACCREDITED
CALIBRATION CERT #1662.01

PCB PIEZOTRONICS
Tel: 716-684-0001 Fax: 716-684-0987 Email: sales@pcb.com
3425 Walden Avenue, Depew NY 14043

ISO 9001 CERTIFIED

Page 1 of 1

List of References

References

[1] Abduljalil ASA. Investigation of thermoacoustic processes in a travelling-wave looped-tube thermoacoustic engine. PhD thesis, Mancheter University 2012.

[2] www.aster-thermoacoustics.com

[3] Tijani MEH. Loudspeaker-driven thermo-acoustic refrigeration. PhD thesis, Technische Universiteit Eindhoven, Netherlands 2001.

[4] Swift GW. Thermoacoustic engines and refrigerators. Physics today 1995; 48(7).

[5] Akhavanbazaz M. Design, analysis, testing and development of a thermoacoustics system for refrigeration applications. Master thesis, Mechanical and Industrial Engineering, Concordia University, Canada 2004.

[6] Strutt JW, Rayleigh B, Lindsay RB, MA, FRS. The theory of sound. vol.1, Dover New York 1945.

[7] Saechan P. Application of thermoacoustic technologies for meeting the refrigeration needs of remote and rural communities in developing countries. PhD thesis, University of Leicester 2014.

[8] http://Wikipedia.org (accessed 2017).

[9] Tijani MEH, Zeegers JCH Waeli TAM. The optimal stack spacing for thermoacoustic refrigeration. The Journal of the Acoustical Society of America 2002; 112(1): 128-133.

[10] Backhaus S, Swift GW. A thermoacoustic-Stirling heat engine: detailed study.J Acoust Soc Am 2000; 107: 3148-3166.

[11] Backhaus S, Swift GW . New varieties of thermoacoustic engines. Proceedings of the Ninth International Congress on Sound and Vibration 2002. www.lanl.gov/thermoacoustics/Pubs/ICSV9.pdf.

[12] Yu Z, Al-Kayiem A. Numerical Analysis of a Thermally Driven Thermoacoustic Heat Pump for Low-Grade Heat Recovery. Computational Thermal Sciences 2014; 6(4): 317-327.

[13] Tijani MEH, Vanapalli S, Spoelstra S. Design of a mechanical resonator to be coupled to a thermoacoustic stirling-engine. In: Proceedings of ASME 2010 3rd Joint US-European Fluids Engineering Summer Meeting and 8th Inter-national Conference on Nanochannels, Microchannels, and Minichannels. Canada 2010.

[14] Ward B, Clark J, Swift G. Design environment for low-amplitude thermoacousticenergy conversion, DELTAEC version 6.2: users guide. Los Alamos National Laboratory 2008. http://www.lanl.gov/thermoacoustics/DeltaEC.html.

[15] Abbott A, Putnam, Dennis WR. Survey of Organ-Pipe Oscillations in Combustion Systems. The Journal of the Acoustical Society of America 1956; 28:246.

[16] Sondhauss C. Ueber die Schallschwingungen der Luft in erhitzten Glasröhren und in gedeckten Pfeifen von ungleicher Weite. Annalen der Physik 1850; 155(1): 1-34.

[17] Feldman KT, JR. Review of the literature on Rijke thermoacoustic phenomena. Journal of Sound and Vibration 1968; 7(1): 83-89.

[18] Telesz MP. Design and Testing of a Thermoacoustic Power Converter. Master thesis, School of Mechanical Engineering, Georgia Institute of Technology 2006.

[19] Kramers HA. Vibrations of a gas column. Physica 1949; 15(11-12): 971-989.

[20] Hartley RVL. Electric power source. U.S. Patent No. 2,549,464; 1951.

[21] Marrison WA. Heat-controlled acoustic wave system. U.S. Patent No. 2,836,033; 1958.

[22] In't panhuis PHMW. Mathematical Aspects of Thermoacoustics. PhD thesis, Eindhoven University; 2009.

[23] Rott N. Damped and thermally driven acoustic oscillations in wide and narrow tubes. Journal of Applied Mathematics and Physics 20 (1969); 230–243.

[24] Rott N. Thermally driven acoustic oscillations. Part II: Stability limit for helium. Journal of Applied Mathematics and Physics 24 (1973); 54–72.

[25] Rott N. The influence of heat conduction on acoustic streaming. Journal of Applied Mathematics and Physics 25 (1974); 417–421.

[26] Rott N. Thermally driven acoustic oscillations, Part III: Second-order heat flux. Journal of AppliedMathematics and Physics 26 (1975); 43–49.

[27] Rott N, Zouzoulas G. Thermally driven acoustic oscillations, Part IV: Tubes with variable cross-section. Journal of Applied Mathematics and Physics 27 (1976); 197–224.

[28] Rott N, Zouzoulas G. Thermally driven acoustic oscillations, part V: Gas-liquid oscillations. Journal of Applied Mathematics and Physics 27 (1976); 325–334.

[29] Merkli P, Thomann H. Thermoacoustic effects in a resonance tube. Journal of fluid mechanics 1975; 70(1): 161-177.

[30] Ceperley PH. A pistonless Stirling engine-The traveling wave heat engine. J Acoust Soc Am 1979; 66: 1508.

[31] Ceperley PH. Gain and efficiency of a short traveling wave heat engine. J Acoust Soc Am 1985; 77: 1239.

[32] De Blok K. Novel 4-stage traveling wave thermoacoustic power generator. In:Paper FEDSM2010-ICNMM2010-30527 in proc ASME 3rd joint US-European fluids engineering summer meeting and 8th international conference on nanochannels, microchannels, and minichannels, Montreal, Canada; 2010. August 2-4.

[33] Collard S. Design and Assembly of a Thermoacoustic Engine Prototype. Helsinki Metropolia University of Applied Sciences 2012.

[34] Swift GW. Thermoacoustic engines. The Journal of the Acoustical Society of America 1988; 84: 1145.

[35] Olson JR, Swift GW. A loaded thermoacoustic engine. J Acoust Soc Am, Vol.98, No. 5, Pt. 1, November 1995.

[36] Yazaki T, Iwata A, Maekawa T, Tominaga A. Traveling wave thermoacoustic engine in a looped tube. Phys Rev Lett 1998; 81(15): 3128-3131.

[37] Backhaus S, Swift GW. A thermoacoustic Stirling heat engine. Nature 1999; 399: 335-338.

[38] Boa R, Chen GB, Tang K, Jia ZZ, Cao WH. Effect of RC load on performance of thermoacoustic engine. Cryogenics 2006; 46: 666–671.

[39] De Blok K. Low operating temperature integral thermo acoustic devices for solar cooling and waste heat recovery. J Acoust Soc Am 2008; 123(5): 3541. And the presentation associated with this paper available on, http://www.aster-thermoacoustics.com.

[40] De Blok K. Multi-stage traveling wave thermoacoustics in practice. The 19th International Conference on Sound and Vibration (ICSV19); July 8-12 2012. Vilnius, Lithuania.

[41] Hofler TJ. Thermoacoustic refrigerator design and performance. PhD thesis, Physics department, University of California, San Diego 1986.

[42] Hofler TJ. High-efficiency heat-driven acoustic cooling engine with no moving parts. U.S.Patent, Editor.The United States of America as represented by Secretary of the Navy, washington D.C. United States of America 1999.

[43] Adeff JA, Hofler TJ. Design and construction of a solar-powdered, thermoacoustically driven, thermoacoustic refrigerator. The Journal of the Acoustical Society of America 2000;107(6): L37-L42.

[44] Chen R-L. Design, construction, and measurement of a large solar powered thermoacoustic cooler. PhD thesis, the Graduate School Graduate Program in Acoustics, the Pennsylvania State University 2001.

[45] Poese ME, Smith RWM, Garrett SL, Gerwen R, Gosselin P. Thermoacoustic refrigeration for ice cream sales. In: 6th IIR Gustav Lorentzen conference 2004.

[46] Dai W, Luo E, Zhang Y, Ling H. Detailed study of a traveling wave thermoacoustic refrigerator driven by a traveling wave thermoacoustic engine. The Journal of the Acoustical Society of America 2006; 119: 2686-2692.

[47] Tijani MEH, Spoelstra S. Study of a coaxial thermoacoustic-Stirling cooler. Cryogenics 2008; 48: 77-82.

[48] Yu Z. Design and Analysis of a Thermally Driven Thermoacoustic Air Conditioner for Low Grade Heat Recovery. In: 13th UK Heat Transfer Conference. Imperial College London; 2013.

[49] Xu J, Hu J, Zhang L, Dai W, Luo E. Effect of coupling position on a looped three-stage thermoacoustically-driven pulse tube cryocooler. Energy 2015; 93(Part1): 994-998.

[50] Xu J, Zhang L, Hu J, Wu Z, Bi T, Dai W, Luo E. An efficient looped multiple-stage thermoacoustically-driven cryocooler for liquefaction and recondensation of natural gas. Energy 2016; 101: 427-433.

[51] Backhaus S, Tward E, Petach M: Traveling-wave thermoacoustic electric generator. Applied Physics Letters 2004; 85(6):1085-1087.

[52] Yu Z, Jaworski A, Backhaus S. A low-cost electricity generator for rural areas using a travelling-wave looped-tube thermoacoustic engine. Proceedings of the Institution of Mechanical Engineers, Part A: Journal of Power and Energy 2010; 224(6): 787-795.

[53] Wu Z, Man M, Luo E, Dai W, Zhou Y. Experimental investigation of a 500 W traveling-wave thermoacoustic electricity generator. Chin Sci Bull 2011; 56: 1975-1977.

[54] Yu Z, Saechan P, Jaworski AJ. A method of characterising performance of audio loudspeakers for linear alternator applications in low-cost thermoacoustic electricity generator. Applied Acoustics 2011; 72: 260–267.

[55] Wu Z, Dai W, Man M, Luo E. A solar-powered traveling-wave thermoacoustic electricity generator. Sol Energy 2012; 86: 2376-2382.

[56] Yu Z, Jaworski AJ, Backhaus S. Travelling-wave thermoacoustic electricity generator using an ultra-compliant alternator for utilization of low-grade thermal energy. Applied Energy 2012; 99:135-145.

[57] Chen BM, Riley PH, Abakr YA, Hann DB. Development of thermoacoustic engine operating by waste heat from cooking stove. AIP Conf Proc 2012; 1440: 532-540.

[58] Chen BM, Yousif YA, Riley PH, Hann DB. Development and assessment of thermoacoustic generators operating by waste heat from cooking stove. Engineering 2012; 4: 894-902.

[59] Sun D, Wang K, Zhang X, Guo Y, Xu Y, Qiu L. A traveling-wave thermoacoustic electric generator with a variable electric R-C load. Appl Energy 2013; 106: 377-382.

[60] Wu Z, Zhang L, Dai W, Luo E. Investigation on a 1 kW traveling-wave thermoacoustic electrical Generator. Appl Energy 2014; 124: 140-147.

[61] Wu Z, Yu G, Zhang L, Dai W. Development of a 3 kW double-acting thermoacoustic stirling electric generator. Appl Energy 2014; 136: 866-872.

[62] Wang K, Sun D, Zhang J, Xu Y, Zou J, Wu K, Qui L, Huang Z. Operating characteristics and performance improvements of a 500 W traveling-wave thermoacoustic electric generator. Appl Energy 2015; 160: 853-862.

[63] Kang H, Cheng P, Yu Z, Zheng H. A two-stage traveling-wave thermoacoustic electric generator with loudspeakers as alternators. Appl Energy 2015; 137: 9-17.

[64] Bi T, Wu Z, Zhang L, Yu G, Luo E, Dai W. Development of a 5 kW travelingwave thermoacoustic electric generator. Appl Energy 2016; 185: 1355-1361.

[65] Wang K, Sun D, Zhang J, Xu Y, Luo K, Zhang N, Zou J,Qiu L. An acoustically matched traveling-wave thermoacoustic generator achieving 750 W electric power. Energy 2016; 103: 313-321.

[66] Hu JY, Ren J, Luo EC, Dai W. Study on the inertance tube and double-inlet phase shifting modes in pulse tube refrigerators. Energy Conver Manag 2011; 52(2): 1077-1085.

[67] Gardner DL, Swift GW. Use of inertance in orifice pulse tube refrigerators. Cryogenics 1997; 37(2): 117-121.

[68] Dai W, Hu J, Luo E. Comparison of two different ways of using inertance tube in a pulse tube cooler. Cryogenics 2006; 46: 273–277.

[69] Luo E, Radebaugh R, Lewis M. Inertance tube models and their experimental verification. AIP Conf Proc 2004; 710: 1485-1492.

[70] Zhang X, Chang J, Cai S, Hu J. A multi-stage travelling wave thermoacoustic engine driven refrigerator and operation features for utilizing low grade energy. Energy Convers Manag 2016; 114: 224-233.

[71] Yazaki T, Biwa T, Tominaga A. A pistonless stirling cooler. Applied Physics Letters 2002;80:157–159.

[72] Al-Kayiem A, Yu Z. Using a side-branched volume to tune the acoustic field in a looped-tube travelling wave thermoacoustic engine with a RC load. Energy Conversion and Management 150 (2017): 814-821.

[73] Fusco AM, William C, Ward, Swift GW. Two-sensor power measurements in lossy ducts. J. Acoust Soc Am 1992; 91 (4); Pt. 1.

[74] Swift GW. Thermoacoustics: A Unifying Perspective for Some Engines and Refrigerators. New York, Acoustical Society of America 2002.

[75] Thombare DG, Verma SK. Technological development in the Stirling cycle engines. Renewable and Sustainable Energy Reviews 2008; 12: 1-38.

[76] Yu Z, Jaworski AJ. Impact of acoustic impedance and flow resistance on the power output capacity of the regenerators in travelling-wave thermoacoustic engines. Energy Convers Manag 2010; 51(2): 350-359.

[77] Garrett S. Thermoacoustic engines and refrigerators. American Journal of Physics 2004; 72: 11–17.

[78] Rietdijk F. Thermoacoustic refrigeration using a standing-wave device. SP Technical Research Institute of Sweden. Energy Technology, Acoustics 2010.

[79] Swift GW, Ward WC. Simple harmonic analysis of regenerators. J Thermophys Heat Transf 1996;10(4): 652-662.

[80] Yu Z, Jaworski AJ. Design of a low-cost thermoacoustic electricity generator and its experimental verification. Proceedings of the ASME 2010 10th Biennial Conference on Engineering Systems Design and Analysis ESDA July 12-14, 2010, Istanbul, Turkey.

[81] Chinn DG. Piezoelectrically-Driven Thermoacoustic Refrigerator. Master thesis, University of Maryland 2010.

[82] Kays WM, London AL. Compact heat exchangers. New York: Mcgraw-Hill; 1964.

[83] Mitchell E. A lumped element model for an inline thermoacoustic chiller. Master thesis, the Pennsylvania State University, the Graduate School 2012.

[84] B&C Speakers. Data sheet of 6PS38. http://www.bcspeakers.com.

[85] Oriti SM,. Schifer NA. Recent Stirling conversion technology developments and operational measurements at NASA Glenn research centre. 7th International energy conversion and engineering conference (IECEC 2009); Denver, CO, August 2-5.

[86] De Blok K. Acoustic power measurements in thermoacoustic systems. Aster thermoacoustics 2013.

[87] De Blok K. On the design of near atmospheric air operated thermoacoustic engines. Aster thermoacoustics 2013.

[88] Tijani MEH, Spoelstra S. A high performance thermoacoustic engine. J Appl Phys 2011; 110: 093519.

[89] Swift GW.Analysis and performance of a large thermoacoustic engine. Journal of Acoustical Society of America 1992; 92: 1551–1563.

[90] Gardner DL, Swift GW. A cascade thermoacoustic engine. J Acoust Soc Am 2003; 114 (4): Pt 1.

[91] Al-Kayiem A, Yu Z. Using side-branched Helmholtz resonator to tune phase in looped-tube travelling wave thermoacoustic engine. The ASME-ATI-UIT 2015 Conference on Thermal Energy Systems: Production, Storage, Utilization and the Environment". 17th -20th May, 2015, Napoli, Italy.

[92] Garrett S, Adeff AJ, Hofler TJ. Thermoacoustic refrigerator for space applications. Journal of Thermophysics and Heat Transfer 1993; 7: 595–599.

[93] Garrett S. Non-dissipative lumped parameter systems. In The Pennsylvania State University 2012: 1-62.

[94] Garrett S, Backhauss S. The power of sound. American Scientist 2000;88:516–525.

[95] Garrett S. Deltaec as a teaching tool in the classroom and laboratory. 17th International Congress on Sound and Vibration (ICSV17), Cairo, Egypt, 18-22 July 2010.

[96] Piccolo A. Optimization of thermoacoustic refrigerators using second law analysis. Appl Energy 2013; 103: 358-367.

[97] Yazaki T, Tominaga A, Narahara Y. Stability limit for thermally driven acoustic oscillations. Cryogenics1979; 19: 393–396.

[98] Yazaki T, Tominaga A, Narahara Y. Experiments on Thermally Driven Acoustic-Oscillations of Gaseous Helium. Journal of Low Temperature Physics 1980;41(1-2): 45-60.

[99] Yazaki T, Tominaga A, Narahara Y. Thermally Driven Acoustic-Oscillations - 2nd Harmonic. Physics Letters A 1980; 79(5-6): 407-409.

[100] Yazaki T, Biwa T, Tominaga A. A pistonless stirling cooler. Applied Physics Letters 2002; 80: 157–159.

[101] Swift GW.Analysis and performance of a large thermoacoustic engine. Journal of Acoustical Society of America 1992; 92: 1551–1563.

[102] Swift GW.Thermoacoustic natural gas liquefier. Proceedings of the Department of Energy Natural Gas Conference (1997), http://www.netl.doe.gov/publications/proceedings/97/97ng/ng97_pdf/NG7-1.PDF.

[103] Swift GW, Wollan J. Thermoacoustics for liquefaction of natural gas. Los Alamos National Laboratory 2002; 21–26. http://www.lanl.gov/thermoacoustics/Pubs/GasTIPS.pdf.

[104] Swift GW. What is thermoacoustics. Los Alamos National Laboratory 2004.

[105] Backhaus S, Swift GW. A thermoacoustic Stirling heat engine. Nature 1999; 399: 335-338.

[106] Tijani MEH, Spoelstra S. A hot air driven thermoacoustic-Stirling engine. Applied Thermal Engineering 2013; 61: 866-870.

[107] Tijani MEH, Spoelstra S. High temperature thermoacoustic heat pump. Presented at the 19th International Congress on Sound and Vibration (ICSV19), Vilinius, Litouwen, July 8-12, 2012.

[108] Vanapalli S,Tijani MEH, Spoelstra S. Thermoacoustic-Stirling heat pump for domestic applications. Proceedings of ASME 2010 3rd Joint US-European Fluids Engineering Summer Meeting and 8th International Conference on Nanochannels, Mircochannels, and Minichannels, August 1-5, 2010, Montreal, Canada.

[109] Yang Z, Zhuo Y, Luo EC, Yuan Z. Travelling-wave thermoacoustic hightemperature heat pump for industrial waste heat recovery. Energy 2014; 77: 397-402.

[110] Chen BM, Riley PH, Abakr YA, Pullen K, Hann DB, Johnson CM. Design and development of a low-cost, electricity-generating cooking Score-Stove™. Proc Inst Mech Eng Part A J Power Energy 2013; 227(7): 803-813.

[111] Verma SS. Eco-friendly alternative refrigeration systems. Resonance 2001; 6(10): 57-67.

[112] Thombare DG, Verma SK. Technological development in the Stirling cycle engines. Renewable and Sustainable Energy Reviews 2008; 12: 1-38.

[113] Sastry S. A Thermoacoustic Engine Refrigerator System for Space Exploration Mission. PhD thesis, Department of Mechanical and Aerospace Engineering, Case Western Reserve University 2011.

[114] Petach M, Tward E, Backhaus S. Design and testing of a thermal to electric power converter based on thermoacoustic technology. In: 2nd International energy conversion engineering conference. Providence, Rhode Island: The American Institute of Aeronautics and Astronautics; 2004. August 16-19.

[115] Kongtragool B, Wongwises S. Thermodynamic analysis of a Stirling engine including dead volumes of hot space, cold space and regenerator. Renew Energy 2006; 31: 345-359.

[116] Desjouy C, Penelet G, Lotton P. Active control of thermoacoustic amplification in an annular engine. J Appl Phys 2010; 108: 114904.

[117] Ali R. Self-powered thermoacoustic sensor for in-pile nuclear reactor monitoring. Master thesis,The Pennsylvania State University 2013.

[118] G. Walker, Stirling engines, Clarendon, Oxford 1960.

[119] Schroeder M, Rossing TD, Dunn F, Hartmann WM, Campbell DM, Fletcher NH. Springer handbook of acoustics. Springer 2007.

[120] Kinsler L, Fre A, Coppens A, Sanders J. Fundamentals of Acoustics. 3rd Edition. John Wiley and Sons Publishing 1982.

[121] Feldman KT, JR. Review of the literature on sondhauss thermoacoustic phenomena. Journal of Sound and Vibration 1968; 7: 71–82.

[122] Tao J, Jiale H, Ye f, Rui Y, Ke T, Ray R. Thermoacoustic prime movers and refrigerators: Thermally powered engines without moving components. Energy 2015; 93: 828-853.

[123] Luo E, Wu Z, Dai W, Li S, Zhou Y. A 100 W-class traveling-wave thermoacoustic electricity generator. Chinese Science Bulletin 2008; 53 (9): 1453-1456.

[124] Zhao Y, Chen Y, Yu G, Luo E, Zhou Y. Experimental Investigation on a Linear-compressor driven travelling-wave thermoacoustic heat pump. Energy Procedia 2015; 75: 1844–1849.

[125] www.Losalamosnationallaboratory.com

[126] www.qdrive.com

[127] Omega® www.omega.com (accessed 2015).

[128] PCB Piezotronics Inc. Model 105C12. www.pcb.com (accessed 2015).

[129] http://www.score.uk.com/. [Accessed 2015].

[130] Al-Kayiem A, Yu Z. Numerical investigation of a looped-tube travelling-wave thermoacoustic engine with a by-pass pipe. Energy 112 (2016):111-120.

[131] Al-Kayiem A, Yu Z. Design of a traveling wave thermoacoustic engine driven cooler with hybrid configuration. Proceeding of the World congress on engineering 2014 Vol II, WCE 2014, July 2- 4, 2014, London, U.K.

[132] Al-Kayiem A. Numerical investigation of a two-stage travelling-wave thermoacoustic engine driven heat pump with a hybrid configuration. UK Heat Transfer Conference 2015; Edinburgh 7th-8th September.

[133] Al-Kayiem A, Yu Z. Numerical investigation of the effects of a side-branched Helmholtz resonator on a looped-tube travelling wave thermoacoustic engine,

The 4th Sustainable Thermal Energy Management International Conference (SusTEM 2017), 28th – 30th June, Netherlands.

[134] Al-Kayiem A, Yu Z. Numerical investigation of a looped-tube traveling-wave thermoacoustic generator with a by-pass pipe, Cardiff to Host 9th International Conference on Applied Energy (ICAE-2017), 21st - 24th August, Cardiff, UK.